



# Elastic waves in complex conditions : from the onset of rupture to viscous dispersion in foams

Johannes Aichele

## ► To cite this version:

Johannes Aichele. Elastic waves in complex conditions : from the onset of rupture to viscous dispersion in foams. Acoustics [physics.class-ph]. Université de Lyon, 2019. English. NNT : 2019LYSE1217 . tel-02481746

**HAL Id: tel-02481746**

**<https://theses.hal.science/tel-02481746>**

Submitted on 17 Feb 2020

**HAL** is a multi-disciplinary open access archive for the deposit and dissemination of scientific research documents, whether they are published or not. The documents may come from teaching and research institutions in France or abroad, or from public or private research centers.

L'archive ouverte pluridisciplinaire **HAL**, est destinée au dépôt et à la diffusion de documents scientifiques de niveau recherche, publiés ou non, émanant des établissements d'enseignement et de recherche français ou étrangers, des laboratoires publics ou privés.



LYON UNIVERSITÉ CLAUDE BERNARD

*École doctorale N°205*

Interdisciplinaire Sciences Santé

THÈSE DE DOCTORAT D' ACOUSTIQUE PHYSIQUE

---

# Elastic waves in complex conditions: From the onset of rupture to viscous dispersion in foams

---

*Par:*

Johannes AICHELE

*Dirigée par*

Dr. Stefan CATHELIN

Dr. Philippe ROUX

*Devant un jury composé de:*

Mme. Marie Muller	Assistant Professor , NC State University, USA	Rapporteuse
M. Chris Marone	Professor, PennState University, USA	Rapporteur
M. Matthias Fink	Professeur sur la chaire Georges Charpak, ESPCI , Université de Sorbonne	Examinateur
Mme. Soumaya Latour	Maître de conférences, Université Paul Sabatier Toulouse	Examinatrice
M. Hervé Liebgott	Professeur, CREATIS - Université Lyon 1	Examinateur
M. Stefan Catheline	Directeur de recherche, LabTAU, Université Lyon 1	Directeur de thèse
M. Philippe Roux	Professeur, ISTERRE, Université Grenoble Alpes	Co-directeur de thèse

Présentée et soutenue publiquement le 14 10 2019





The main insight learned from interdisciplinary studies is the return to  
specialization

George Stigler

Well, I am a dilettante. It's only in England that dilettantism is considered a bad  
thing. In other countries it's called interdisciplinary research.

Brian Eno



# Summary

This thesis is part of the research at Labtau (Laboratory of therapeutic applications of ultrasound) and ISTerre (Institut des sciences de la terre - earth science institute) at the interface of medical imaging and seismology, two research disciplines that are based on the propagation of elastic waves. It investigates the nature of elastic wave propagation in complex conditions by ultrafast ultrasound imaging, also known as transient elastography or shear wave imaging. This medical imaging technique allows for retrieval of the dynamic shear wave field inside a soft elastic material and is commonly applied in hospitals for elasticity mapping in, e.g., the liver and breast. In the present manuscript, two research questions of interest for bio- and geophysics are tackled. The first part treats elastic wave propagation in porous materials. The dispersion of the shear and secondary compression wave in lung-mimicking materials is analyzed experimentally and compared to Biot's theory of poro-elasticity. The results show a good agreement for the shear wave and qualitative agreement for the secondary compression wave. This has direct implications for elasticity imaging: the properties of the viscous fluid govern the shear wave dispersion in highly porous soft elastic materials. The thesis thus contributes to the emerging branch of lung elasticity imaging. The results could have clinical implications for other organs as well. The liver and spleen contain a high percentage of blood, a non-Newtonian fluid which exposes a highly varying viscosity. The conclusions drawn from the comparison of the experimental results and poro-elastic theory imply, that the role of the pore-filling fluid should be investigated in liver elastography: The clinically observed dispersion of shear waves in the liver remains partly unexplained by purely visco-elastic models.

Furthermore, the experimental proof of the secondary compression wave is of general interest for poroelasticity. Originally, this wave has been the object of geophysical studies and has scarcely been shown experimentally. In the second part, the ultrafast ultrasound shear wave imaging technique is applied to a geophysical research question. What does the elastic wavefield, which is emitted by a frictional instability, reveal about the nature of dynamic rupture propagation? How does rupture, the process behind earthquakes, nucleate? By mapping the shear wave-field during rupture of a granular asperity at the source point and in the medium, unique insights into rupture nucleation are gained. The experimental setup, which relies on soft elastic phantoms, is shown to reproduce many characteristics of sliding friction that have been shown for real rocks in the earth and the laboratory. These include supershear and sub-Rayleigh rupture propagation, a nucleation phase and stick-slip friction. Neither a singular-force nor a double-couple source mechanism explain the entirety of observed rupture modes. Finally, in order to statistically analyze the complex spatio-temporal evolution of the presented experiment, a semi-automated data

analysis workflow, taking advantage of image segmentation and computer vision, is suggested.

**Keywords** Elastic wave propagation; near-field; rupture nucleation; stick-slip; Biot theory; shear wave imaging; transient elastography; porous medium; secondary compression wave; slow wave.

# Résumé

Ces travaux s'inscrivent dans la continuité des recherches académiques du Labtau (Laboratory of therapeutic applications of ultrasound) et de l'ISTerre (Institut des sciences de la terre) à l'interface entre imagerie médicale et sismologie, deux disciplines reposant sur la propagation des ondes élastiques. La nature de la propagation des ondes élastiques dans des milieux complexes est étudiée à travers l'imagerie ultrasonore ultrarapide - également connue sous le nom d'imagerie d'ondes de cisaillement. Cette technique d'imagerie médicale permet de récupérer un champ d'onde de cisaillement se propageant dans un milieu élastique mou. Elle est habituellement utilisée comme modalité d'imagerie cartographiant les élasticités d'organes tels que le foie ou le sein.

La première partie se penche sur le comportement des ondes dans des milieux poreux. La dispersion de l'onde de cisaillement et de l'onde de compression secondaire dans des matériaux imitant le poumon est analysées expérimentalement, puis comparées à la théorie de poro-élasticité de Biot. Les résultats quant à l'onde de cisaillement sont conformes à la théorie, et ceux de l'onde de compression y correspondent qualitativement. Pour conclure, dans le cas des milieux mous, poreux et élastiques, la dispersion des ondes élastiques est gouvernée par les propriétés du fluide visqueux. Ainsi, les résultats présentés au cours de cette thèse pourraient consolider la théorie nécessaire à une imagerie de l'élasticité pulmonaire. Potentiellement d'autres organes pourraient en bénéficier : en effet, le foie et la rate sont constitués d'un pourcentage élevé de sang. Ce fluide non-Newtonien présente une forte variabilité de la viscosité. Celle-ci implique la nécessité d'étudier le rôle du sang vis-à-vis de l'élastographie du foie, pas encore expliquée par les modèles visco-élastique. En outre, la preuve expérimentale de l'onde de compression secondaire est utile dans l'étude de la propagation d'ondes poro-élastiques. Il est important de noter que l'onde de compression secondaire a été objet principal d'études approfondies en géophysique et n'a été observée que dans quelques rares cas.

La partie suivante s'intéresse à une problématique de la géophysique explorée au moyen de l'imagerie de l'onde de cisaillement :

Que pourrait révéler sur la nature de la rupture dynamique d'une instabilité de friction l'étude du champs d'onde élastique ?

Comment la rupture, le processus responsable des tremblements de terre, est générée? En observant la carte du champ d'onde de cisaillement pendant la rupture d'une aspérité granulaire au point source et dans le milieu, il est possible d'acquérir une meilleure compréhension de la propagation de la rupture. L'expérience qui se base sur l'utilisation de fantômes mous et élastiques montre une multitude de phénomènes qui sont aussi présents dans la friction des roches en laboratoire, ainsi que dans la Terre. Par exemple, les ruptures supershear, sub-Rayleigh, une phase

de nucléation et la friction du type stick-slip ont été observés. Toutefois, ni un mécanisme de source d'une force unique, ni un double-couple n'arrivent à expliquer l'ensemble des ruptures observées. De plus, pour analyser la complexité spatio-temporelle des ruptures de cette expérience, un workflow semi-automatique intégrant la segmentation d'image et la vision numérique est suggéré.

**Mots-clés** Propagation des ondes élastiques; champ proche; nucleation de la rupture; stick-slip; theorie de Biot; imagerie d'onde de cisaillement; elastography transient; milieu poreux; onde de compression secondaire; onde lente.

# Acknowledgements

In order to be able to start this doctoral thesis many people influenced my development, of which I want to thank a few by name. First of all, my parents that always encouraged me to ask questions, read books and go my own way. Curiosity is an absolute prerequisite for science and encouraging a child to search for answers and challenge the reasoning behind them is a gift I was spoiled with. As an older brother I had the chance to test my pedagogical skills on my two sisters, not always to their delight. Sorry for that. For finding joy in writing science, I have to thank my master thesis supervisor, Florian Wellmann, who taught me the importance of thinking in words. Having an engineer turned writer who still publishes at the age of ninety as a grandfather might also have had its share in providing a role model. Starting with a geology degree, my taste for physics was deepened during the Joint Master in Applied Geophysics from TU Delft, ETH Zurich and RWTH Aachen. Thank all who keep this program alive for this excellent experience. The present work would not have been possible without my colleagues in Lyon, Grenoble and from the WAVES program. First of all, my supervisors, Stefan Catheline and Philippe Roux developed my understanding for physics through their excellent and complimentary pedagogical skills. Without their instinct to ask the right questions, this work would probably be much less interesting. Thank you Philippe for all of your splendid ideas. Sometimes I left a single discussion with more than I could possibly test in several months. Thank you Stefan for always answering each of my questions, however naive, in the beautiful and elegant physical way which is so characteristic of you. Thank you both for enduring my flair of argument in combination with my stubbornness. I am inclined to believe that a little bit less disposition for challenging your ideas from my side might have made your life as a supervisor much easier. At different stages of my thesis many discussions and collaborations with different colleagues formed my scientific mind. Thanks to Remy Souchon, Ali Zorgani, Perry Naughton, Felix Gerick, Chadi Zemzemi, Victor Barrère, Victor Delattre, Loic Daunizeau, Jaques Rivière, Tobias van Baarsel, Jaques Brives, Paul Greiller and Christophe Voisin. Among those I especially want to mention the co-authors of our publication in Physical Review Letters: Bruno Giammarinaro, Michael Reinwald and Goulven LeMoign. Goulven, after the disappointment in discovering that your supervisor is not Joanne but Johannes, I think we were a good team in capturing elastic waves in porous tissues. Michael's combined numerical and physics skills as well as critical and immediate manuscript corrections were of crucial value. Thank you and I hope we will continue to collaborate. Last, Bruno was and is my irreplaceable discussion partner concerning anything from physics to politics. Without his mathematical skills one or the other error made during my thesis might have stayed undetected. I hope I can soon call you professor and would be honored to continue to work with you. I although want to thank all the members at ISTERRE and Labtau I forgot to mention



as well as my 14 PHD colleagues from the WAVES program. The workshops and seminars with you were always fun, instructive and I hope we will be able to stay in contact. A big Thank you! especially to Patrick and Theo with whom I shared eight respectively five years of higher education as well as a two bedroom flat in Zurich. My very regular stays in Grenoble would not have been possible without the effort of a multitude of people. Thanks to Leila Guessoum I got reimbursed for my travels, which was not as evident as it might seem given the INSERM administrative rules. Thanks to Raphael, Charlotte, Guillaume and Mathilde I always had a couch which prevented me from spending my whole funding on hotels in the first few months. When moving to Chambéry, Benoit, Lola, Justine and Greg equally hosted me at my former base in Lyon. Thank you, as well as Paul Greiller, Jacques Brives, Amber Zanandel and Max Solazzo all indefinitely for your hospitality. Experimental work requires a lot of challenging technical work. The laboratory had quite some problems with the technical follow up and sadly enough I am a much less talented craftsman than my forefathers. Luckily, Max Solazzo came along to give the motor its final polish! Thank you for your work, the discussions on anything from bikes to permaculture and your couch as well. Finally, the most important person throughout these nearly four years has been my girlfriend Veronika. She endured all my frustration, bad moods and exhaustion that I otherwise kept to myself while always reminding me that even though at times it might appear otherwise, a thesis is not the most important thing in the world.

# Contents

<b>Summary</b>	<b>iii</b>
<b>Résumé</b>	<b>v</b>
<b>Acknowledgements</b>	<b>vii</b>
<b>1 Introduction</b>	<b>1</b>
1.1 Shear wave imaging across the disciplines . . . . .	1
1.2 Outline of this thesis . . . . .	2
<b>2 Shear wave imaging</b>	<b>5</b>
2.1 The development of shear wave imaging . . . . .	5
2.2 Equipment . . . . .	11
2.3 Correlation algorithm . . . . .	11
<b>3 Poro-elastic wave dispersion</b>	<b>15</b>
3.1 Introduction . . . . .	15
3.2 Biot theory . . . . .	17
3.2.1 Idealized fluid: Wave propagation in the absence of viscosity . .	18
3.2.2 Inertial coupling - nonviscous fluid . . . . .	19
3.2.3 Viscous fluid: Wave propagation in the presence of dissipation .	20
3.2.4 Wavespeed calculation . . . . .	20
3.3 Saturated Foam . . . . .	23
3.3.1 Experimental setup . . . . .	23
3.3.2 Wave propagation . . . . .	24
3.3.3 Comparison to Biot theory . . . . .	29
3.3.4 Attenuation & Kramers-Kronig . . . . .	30
3.3.5 Conclusion . . . . .	32
3.4 Ex-vivo lung experiments . . . . .	33
3.4.1 Excised pig lung saturated in water . . . . .	33
3.4.2 Conserved pig lung in air . . . . .	36
3.4.2.a Comparison to Biot theory . . . . .	39
3.5 The possible role of fluid viscosity in clinical applications . . . . .	40
3.5.1 Lung elasticity investigation . . . . .	40
3.5.2 Blood-rich organs . . . . .	40
<b>4 Laboratory rupture observation</b>	<b>45</b>
4.1 Introduction . . . . .	45
4.2 Background . . . . .	46
4.2.1 Historical studies - The friction coefficient . . . . .	46
4.2.2 Dynamic rupture observations - Laboratory earthquakes . . . . .	48
4.2.2.a Elastic rebound theory . . . . .	48
4.2.2.b Stick-slip . . . . .	50

4.2.2.c Pulse-like propagation . . . . .	52
4.2.2.d Real contact area dynamics . . . . .	53
4.2.2.e Supershear rupture propagation . . . . .	55
4.2.3 Slow slip . . . . .	59
4.2.3.a Granular friction . . . . .	60
4.2.3.b Ultrasound wave propagation imaging . . . . .	64
4.2.3.c And the real world? . . . . .	64
4.2.4 Kinematic source models . . . . .	67
4.2.4.a Point dislocation source . . . . .	69
4.2.4.b Double couple source . . . . .	70
4.2.4.c Non-double-couples and damage terms . . . . .	71
4.2.5 Summary . . . . .	72
4.3 Experimental setup . . . . .	74
4.3.1 Samples . . . . .	75
4.3.2 Friction bench . . . . .	76
4.3.3 Asperity . . . . .	76
4.3.4 Imaging device . . . . .	76
4.3.5 Imaging method . . . . .	79
4.3.6 Workflow . . . . .	80
4.4 Results . . . . .	82
4.4.1 Rupture seen from above the fault . . . . .	83
4.4.1.a Experiment 1 - Passing supershear front . . . . .	84
4.4.1.b Experiment 2 - Nucleation of a rupture front . . . . .	96
4.4.2 Rupture seen parallel to the fault . . . . .	101
4.4.2.a Experiment 1 - Small asperity . . . . .	101
4.4.2.b Experiment 2 - Larger asperity . . . . .	109
4.4.2.c Experiment 3 - Coarse sand . . . . .	117
4.4.3 Gel-gel rupture . . . . .	120
4.5 Work in progress: 2D wavefield detection . . . . .	125
4.6 Conclusion . . . . .	127
4.7 Relevance for real-world cases . . . . .	128
<b>5 Conclusion</b>	<b>131</b>
<b>A Biot theory</b>	<b>133</b>
A.1 Idealized fluid: Wave propagation in the absence of viscosity . . . . .	133
A.1.1 Stress-strain relations . . . . .	133
A.1.2 Poroelastic coefficients - Gedankenexperimente . . . . .	134
A.1.3 Inertial coupling - nonviscous fluid . . . . .	135
A.1.4 Equations of motion . . . . .	136
A.1.5 Wave equations . . . . .	137
A.2 Viscous fluid: Wave propagation in the presence of dissipation . . . . .	138
A.2.1 Wavespeed calculation . . . . .	140
A.3 Crossover frequency between high and low frequency range . . . . .	142
A.4 High frequency approximation . . . . .	142
<b>B Appendix Sensitivity Analysis</b>	<b>145</b>

---

<b>C Further experimental results</b>	<b>147</b>
C.1 Further rupture examples . . . . .	147
C.2 2D wavefield detection . . . . .	149
C.3 Frequency content . . . . .	151
C.4 K-means . . . . .	153
<b>D Simulation sources</b>	<b>157</b>
<b>E Accepted article - <a href="https://arxiv.org/abs/1907.11276">https://arxiv.org/abs/1907.11276</a></b>	<b>161</b>
<b>Bibliography</b>	<b>167</b>



# List of Figures

2.1.1 US imaging principles . . . . .	8
2.1.2 PiV example . . . . .	10
2.3.1 Shear wave imaging schema . . . . .	13
3.3.1 Experimental setup . . . . .	24
3.3.2 Experimental wave-fields . . . . .	26
3.3.3 Experimental vs. theoretical dispersion . . . . .	27
3.3.4 Simulation linear elastic solid . . . . .	28
3.3.5 Wave dispersion Biot vs. experiment . . . . .	30
3.3.6 Attenuation curves . . . . .	32
3.4.1 Setup for water-saturated porcine lung . . . . .	34
3.4.2 Wave propagation in ex-vivo pig lung . . . . .	34
3.4.3 Surface dispersion in ex-vivo pig lung . . . . .	35
3.4.4 Optical Snapshots of the lung surface . . . . .	36
3.4.5 Attenuation in ex-vivo pig lung . . . . .	37
3.4.6 Lung in air - dispersion . . . . .	38
3.4.7 Theoretical dispersion - foam in air . . . . .	39
3.5.1 Sensitivity analysis and theoretical poro-elastic liver dispersion . . . . .	44
4.1.1 Leonardo da Vinci's friction bench . . . . .	46
4.2.1 Sketch by Coulomb (1781) . . . . .	48
4.2.2 Faults and Folds . . . . .	49
4.2.3 Reid's Jelly experiments . . . . .	50
4.2.4 Burridge-Knopoff model . . . . .	51
4.2.5 Crack modes . . . . .	51
4.2.6 Rate and state friction . . . . .	52
4.2.7 Schallamach wave . . . . .	53
4.2.8 Crack-like vs. pulse-like rupture . . . . .	53
4.2.9 Contact area measurement . . . . .	54
4.2.10 Photo-elasticity experiment . . . . .	58
4.2.11 Fault gouge . . . . .	60
4.2.12 Force chains . . . . .	62
4.2.13 Double shear setup and results from Johnson et al. (2013) . . . . .	63
4.2.14 AE sources . . . . .	66
4.2.15 Haskell's unilateral rupture model . . . . .	68
4.2.16 Force couples - Seismic moment tensor . . . . .	69
4.2.17 Double-couple radiation pattern . . . . .	72
4.3.1 Experimental Setup . . . . .	77
4.3.2 Photos experimental setup . . . . .	78
4.3.3 Schematic observation planes . . . . .	79
4.3.4 Sketch visualizing the available data . . . . .	80
4.3.5 Experimental workflow . . . . .	81
4.4.1 Photos experimental setup . . . . .	84

4.4.2 Particle velocity snapshots . . . . .	85
4.4.3 Simulation vs. experiment: 1 source . . . . .	86
4.4.4 Simulation vs. experiment: Moving source . . . . .	87
4.4.5 Simulation vs. experiment: Moving DC-source . . . . .	88
4.4.6 Shear wave time of flight . . . . .	89
4.4.7 Example of Hough detection . . . . .	89
4.4.8 Time of flight for a rupture . . . . .	90
4.4.9 Speed measurements from correlation . . . . .	91
4.4.10 Displacement during one rupture . . . . .	92
4.4.11 Displacement curves - full experiment . . . . .	93
4.4.12 Displacement curves - 1 rupture . . . . .	93
4.4.13 Final displacement . . . . .	94
4.4.14 Andrews and Ben-Zion: Simulation . . . . .	94
4.4.15 Explanatory sketch - Hough transform . . . . .	95
4.4.16 Snapshots for a rupture nucleation . . . . .	97
4.4.17 Simulation vs. experiment: 1 DC-source . . . . .	98
4.4.18 Displacement against time . . . . .	99
4.4.19 Simulation vs. experiment . . . . .	100
4.4.20 Photo of the experimental setup . . . . .	101
4.4.21 Wavefield for one cycle . . . . .	103
4.4.22 Simulations - Horizontal plane . . . . .	104
4.4.23 Displacement plot . . . . .	105
4.4.24 Seismogram detection examples . . . . .	106
4.4.25 Speed profile . . . . .	107
4.4.26 Variance based event classification . . . . .	109
4.4.27 Wavefield snapshots for one rupture . . . . .	110
4.4.28 Wavefield snapshots for a 2nd rupture . . . . .	111
4.4.29 Particle acceleration snapshots 3rd rupture . . . . .	112
4.4.30 Total displacement against time . . . . .	113
4.4.31 Displacement zoom . . . . .	113
4.4.32 Rupture detections 1D . . . . .	114
4.4.33 Seismograms for detection . . . . .	115
4.4.34 Speed profile . . . . .	117
4.4.35 Displacement curves coarse sand . . . . .	119
4.4.36 Ultrasound reflection image gel-gel . . . . .	120
4.4.37 Wavefield gel-gel rupture . . . . .	122
4.4.38 Waveforms for the gel-gel rupture . . . . .	122
4.4.39 Experimental-analytical comparison gel-gel . . . . .	124
4.5.1 Wavelet transform detection . . . . .	126
4.6.1 Schematic of 3D US acquisition . . . . .	128
C.1.1 Further rupture examples . . . . .	148
C.2.1 Parabolic fit attempt . . . . .	150
C.3.1 Spectrogram Section 4.4.2.a . . . . .	151
C.3.2 Power spectra Section 4.4.2.b . . . . .	152
C.3.3 Power spectra averageSection 4.4.2.b . . . . .	152
C.3.4 Spectrograms Section 4.4.2.b . . . . .	153
C.4.1 K-means Section 4.4.2.b . . . . .	154
C.4.2 Example snapshots K-means . . . . .	155
D.0.1 Source function for Fig. 4.4.19 . . . . .	157

---

D.0.2 Source function for the singular-force simulations in Section 4.4.1.a . .	158
D.0.3 Source function for the DC simulations in Section 4.4.1.a . . . . .	159
D.0.4 Source function for the simulations in Section 4.4.3 . . . . .	160





# List of Tables

3.1 Liver - poro-elastic literature values . . . . .	43
4.1 Evolution of the friction bench . . . . .	77
4.2 Experimental parameters . . . . .	83
B.1 Sensitivity analysis . . . . .	145



# List of Abbreviations

<b>PI</b>	Primary compression wave
<b>PII</b>	Secondary compression wave
<b>PVA</b>	PolyVinylAlcohol
<b>RF</b>	RadioFrequency
<b>IQ</b>	Transformation of polar ampliude and phase data to a cartesian coordinate system
<b>DC</b>	Double Couple
<b>LEFM</b>	Linear Elastic Fracture Mechanics
<b>ROI</b>	Region Of Interest



## Chapter 1

# Introduction

### 1.1 Shear wave imaging across the disciplines

Ultrasound imaging, by its nature, has historically focused on acoustic wave propagation. Applied in medical imaging and nondestructive testing, travel-time and amplitude information of these compression waves are exploited to map biological tissue and monitor engineering structures. The exploitation of shear waves for imaging purposes has for a long time been reserved to geophysics, where the difference of arrival times of P- and S-waves led Oldham to postulate a core at the center of the earth as early as 1906 (Oldham, 1906). The realization that soft matter also support shear waves, led to the emergence of shear wave imaging or transient elastography. Enabled by the development of fast ultrasound scanners, it took more than 90 years from Oldham's use of shear waves for earth imaging to shear wave imaging in the medical field. It is a fairly recent imaging method which allows to image shear wave propagation inside soft matter and retrieve a high resolution map of the local shear wave speed in situ. Motivated by seismology, which exploits seismic waves to infer the earth's structure from travel-times, transient elastography uses changes in shear wave speed to resolve local changes in elasticity. This is possible because the stiffness of tissue, which was historically investigated by doctors through palpation, is primarily related to shear elasticity. Hence, the familiar surname often used for transient elastography: *Seismology of the human body*. Its benefit lies in detecting elasticity contrasts which classical ultrasound reflection images, relying on impedance contrasts, are unable to detect. Furthermore, by directly observing the dynamic shear wave field inside the body of interest, one can visualize complex wave propagation and processes that otherwise could only be visualized through numerical modeling. It is this latter property, resolving dynamic properties of wave propagation, that I will tackle in this thesis.

Firstly, I will show that through transient elastography we are able to directly observe the shear and secondary compression wave in a highly porous soft foam. These results have direct implications for transient elastography since the used foams expose a similar complex structure as the human lung, an organ that only recently

has drawn the attention of the ultrasound community. The secondary compression wave is known from geophysics as Biot's slow wave. In earth sciences, porous media have for long incited the curiosity of hydrocarbon and environmental geophysics alike. However, the secondary compression wave has scarcely been observed. The presented experiment offers a new way of high quality slow wave imaging and is of general interest for physicists interested in porous wave propagation.

Secondly, I will present the application of shear wave imaging to a geophysical research question - the complex processes of rupture nucleation and propagation in an earthquake mimicking laboratory experiment. I thus present an original method of rupture observation that allows the retrieval of the dynamic wave-field and accumulated displacement created by a propagating rupture in situ a 3D laboratory sample. The nature of the highly resolved  $x - y - t$  and  $x - z - t$  data allows for application of imaging processing routines that automate the exploitation of laboratory stick-slip events. My observations show that the used laboratory setup reproduces many aspects of natural earthquakes and more realistic laboratory earthquakes, e.g., supershear rupture, sub-Rayleigh rupture, stick-slip and rupture regime stabilization. The results are not only relevant for earthquake physics - they are probably even more easily extrapolated to other rupture processes such as glacier stick-slip.

I hope that apart from the scientific results, this manuscript illustrates how much the two fields of medical imaging and geophysics stimulate each other, if they use a common language.

## 1.2 Outline of this thesis

This work is divided into four main parts. After this general introduction, Chapter 2 gives an overview of transient elastography or shear wave imaging, including recent developments and the methods behind the technique. For the reader that has not been introduced to ultrafast ultrasound imaging this chapter gives the necessary background for the following chapters. Chapters 3 and 4 are the core of this thesis and to the reader who is familiar with transient elastography, each of them stands alone.

Chapter 3 shows the first shear and slow compression wave propagation in soft porous materials. The experimentally observed dispersion is compared to Biot's theory of poro-elastic wave propagation and the relevance of the results for medical imaging is discussed.

Chapter 4 presents experimental observations of laboratory earthquakes by use of shear wave imaging. This imaging technology reveals the near field of a nucleation rupture in outstanding resolution and sheds a new light on source mechanism and rupture mode of laboratory earthquakes. A general introduction to laboratory

friction experiments gives the necessary background to rupture nucleation and the results are discussed with regard to their relevance for natural phenomena. Additional information for Chapter 3 is found in Appendices A and B and Appendices C and D contains additional information on Chapter 4.

Section 3.3 was submitted in a more concise form to physical review letters and accepted for publication. The preprint version can be read independently in Appendix E or at <https://arxiv.org/abs/1907.11276>.





## Chapter 2

# Shear wave imaging

In this chapter, shear wave imaging or transient elastography is reviewed. It starts with a brief overview of the developments in medical imaging that led to its emergence, followed by the methods and materials relevant to this thesis.

### 2.1 The development of shear wave imaging

**Motivation** Ultrasound shear wave imaging is inherently linked to the medical field. It's main application is to give physicians a quantitative measure of the elasticity of human tissues and organs in order to distinguish malign from healthy tissue. It can thus be seen as a further development of the ancient medical practice of palpation. In palpation, the physician estimates the stiffness as an indicator for healthy or malign tissue using his fingertips. In short, he feels the resistance of human tissue by pushing and shearing the relevant body part of a patient. First written reports of this practice date back to the Ebers and Edwin Smith papyruses of ancient Egypt (*Wundenbuch Papyrus Smith*; Selin, 2016; Wells et al., 2011) dated to the 16th century BC which are possibly transcriptions of the 3rd millennium BC. Further reports of palpation come from traditional Chinese medicine (5th century BC) (Selin, 2016; Wells et al., 2011), Indian Ayurveda (Selin, 2016) and Hippocrates (Cantisani et al., 2014). Nowadays palpation is still used as one of the first qualitative diagnostic tools every medical practitioner possesses (Wells et al., 2011). First scientific studies aimed at estimating the properties felt by palpation on a more quantitative basis date back to the 1950s. Nearly 40 years before the first ultrasonic shear wave imaging studies, Oestreicher (1951) and Gierke et al. (1952) analyzed shear wave propagation in soft tissue with medical applications in mind. Gierke et al. (1952) used an optical method on surface waves of the human thigh and arm which allowed them to give an estimate of the shear modulus, the physical quantity underlying what is called stiffness in palpation. It is remarkable that they already noticed the very low speed of the shear wave compared to the compression wave. This is an essential property required for shear wave imaging to work. It took until the 1980s and the advent of ultrasound imaging however, to awake a continuous interest in quantitative elasticity measurements in biological tissue. In contrast to optical methods, which are

limited to surface measurements, ultrasound assesses tissue in-depth. This property makes it the tool of choice for a variety of clinical applications. Standard reflection ultrasound imaging (see Infobox 2.1) however cannot inherently be used to estimate elasticity. The image is based on impedance contrasts, which are not directly correlated to elasticity contrasts. Tissues of varying elasticity can for example expose no measurable impedance contrast at all.

**Beginnings** In parallel to the evolution of ultrasound Doppler imaging in the 1980s arose the idea of using ultrasound to estimate elasticity. Stress ( $\sigma_{ij}$ ) and strain ( $e_{kl}$ ) in linear elastic materials are related through the elasticity tensor ( $c_{ijkl}$ ) by the linear form of Hooke's law<sup>1</sup>:

$$\sigma_{ij} = c_{ijkl}e_{kl} \quad (2.1)$$

Hence, measuring all components of tissue deformation (strain) or displacement induced by known vibrations or static compression would give the elasticity tensor. Ultrasound, with its capability of imaging tissue in-depth was thus the method of choice. First attempts to measure motion and vibration through correlation of pulsed ultrasound echos were done by Wilson et al. (1982) and Dickinson et al. (1982). Birnholz et al. (1985) suggested to evaluate the maturity of fetus lungs by measuring their compressibility using ultrasound. Eisenscher et al. (1983) were probably the first to invoke the parallels to geophysics by employing the word echosismography for the echo-graphic rhythmic palpation they proposed. Cox et al., 1987 and Holen et al. (1985) used the Doppler spectrum to measure vibration amplitudes in the heart and fish hearing organ respectively. Despite the optical works of Oestreicher (1951) and Gierke et al. (1952) the early ultrasound literature seems to largely ignore the importance of the shear modulus in palpation. Instead it focuses on calculating the Young's modulus as the measure of stiffness.

First steps to quantitatively estimate stiffness by using ultrasound and shear waves were made by Krouskop et al. (1987). Using a single transducer, they applied pulsed Doppler to determine the motion gradient induced by a vibration device. Assuming isotropy and incompressibility of the tissue they calculated an elastic modulus  $E$ :

$$E = \frac{3}{2}\rho\omega^2 \frac{u_2(x_3 - x_1)}{\frac{u_1 - u_2}{x_2 - x_1} - \frac{u_2 - u_3}{x_3 - x_2}}$$

where  $u$  are the displacement amplitudes,  $x$  the corresponding depths,  $\rho$  is density and  $\omega$  is the excitation frequency. First attempts of 2D stiffness imaging were undertaken shortly afterwards by Lerner et al. (1990) and Parker et al. (1990). They

---

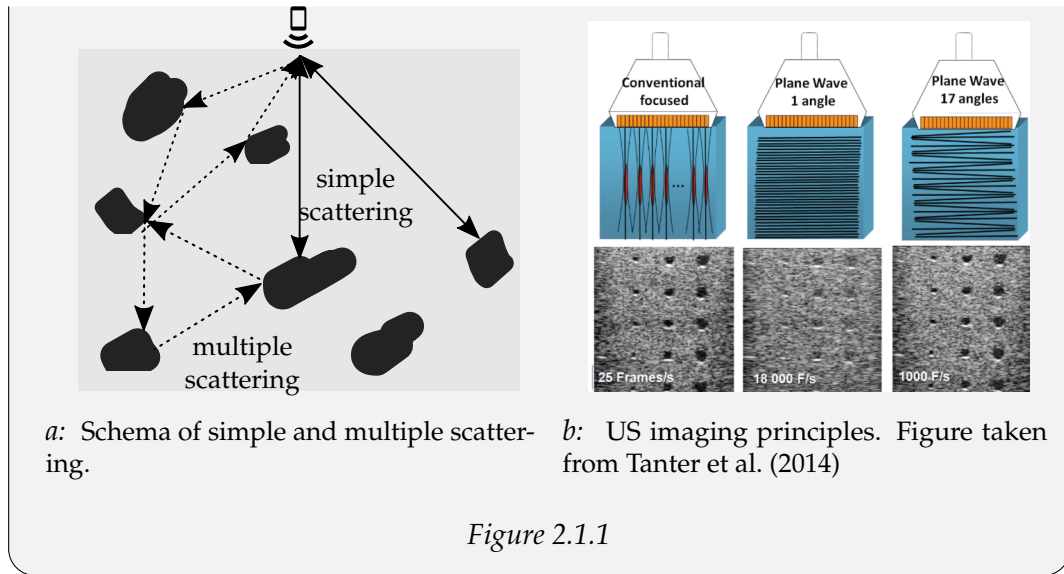
<sup>1</sup>Stated in Einstein summation convention where repeated indexes get summed.

proposed Vibration amplitude sonoelastography to differentiate regions of varying stiffness in soft tissue. The method relies on the ultrasound Doppler spectrum of mechanically induced low frequency excitation (20- 1000 Hz).

Ophir et al. (1991) presented a method for static strain imaging by ultrasound that framed the term elastography, which today is used for static and transient techniques alike. In their setup, they compute a strain profile from the cross-correlation of an ultrasound image prior- and post-compression of the region of interest. The strain and the applied stresses are used to compute an elastic modulus estimation throughout the image. One drawback of this method is that the stress and strain fields in soft tissues are not uniform. Since in ultrasound imaging only the strain component along the axis of ultrasound propagation is measured, the reconstruction of the complex strain tensor can at best be approximated.

#### **Infobox 2.1 Ultrasound echography**

The basis for shear wave imaging is the ultrasound reflection image, commonly known as echography. An array of piezoelectric elements emits and receives an ultrasonic pulse. The central frequency used in tissues is commonly in the MHz range. The signal gets reflected wherever impedance contrasts are present inside the body of interest. These contrasts which consist of groups of scatterers are needed to reflect the signal at each imaging depth. At the same time, the simple scattering approximation needs to be fulfilled: The majority of the reflected energy comes from a direct reflection and not from multiple scattering (see Fig. 2.1.1a). Beamforming algorithms (Van Veen et al., 1988) allow then to attribute the received energy at each element and each point in time to a specific group of scatterers, commonly named speckle. Historically these images are constructed line by line, with one element going through an emit-receive cycle after the other, focusing at the depth of interest. The development of phased arrays or plane wave compounding permitted plane wave imaging with similar image quality (Tanter et al., 2014). Therefore, a small delay is introduced from one element to the next, such that the wave-fronts superpose with an angle relative to the probe surface. Plane wave imaging has the advantage that the emit-receive cycle only takes a fraction of the time which line-by-line imaging requires.



**State of the Art** Shear wave imaging or transient elastography was developed to overcome this difficulty. By imaging the dynamic wave field, shear wave imaging directly accesses the local wave speed, which is closely related to elasticity. Based on the elastic Green's functions, well known by Geophysicists since the 1960s (Aki et al., 2009), the method acknowledges the vector nature of shear body waves. It thus overcomes the limitations which the amplitude-focused previous methods faced. The slow speed of the shear wave in soft tissue already recognized by Gierke et al. (1952) was not taken advantage of until the works the late 1990s (Sarvazyan et al., 1998; Catheline, 1998; Catheline et al., 1999). Sarvazyan et al. (1998) use acoustic radiation force to locally induce a shear wave inside a soft tissue and image the displacement of the shear wave front through Magnetic Resonance Imaging (MRI). In parallel, Catheline (1998) and Sandrin et al. (1999a) developed transient elastography. The displacements induced by a propagating (hence the name transient) shear wave inside soft tissue are measured via cross-correlation of ultrasonic signals. In comparison with Magnetic Resonance Imaging the temporal resolution achieved by ultrasound is orders of magnitude higher. First presented in 1D along one transducer axis (Catheline, 1998), it was soon extended to 2D: By using ultra-fast plane wave imaging (see Fig. 2.1.1b) Sandrin et al. (1999a) filmed a propagating shear wave at 2000 frames per second. This was made possible due to hard- and software developments. Increased storage and processing capacity allowed to profit from the large speed ratio of compression and shear wave already noted by Gierke et al. (1952). By emitting and receiving with all probe elements simultaneously, one emit-receive cycle only takes the two-way travel-time of the ultrasound signal at approximately  $1480 \text{ m s}^{-1}$ . Because shear waves in biological tissue commonly travel at  $1$  to  $10 \text{ m s}^{-1}$ , the propagation of a shear wave front between two consecutive ultrasonic images is small. Consequently, the ultrasound frame-rate is well above the shear wave's Nyquist frequency. Applying cross-correlation of consequent ultrasonic reflection

signals then allows for tracking the relative particle displacement induced by the shear wave. This method, commonly known as speckle tracking was motivated by optics, a field that already used correlation methods in Particle Imaging Velocimetry (PIV) of fluid flow (Raffael et al., 2007) as well as Digital Image Correlation in satellite or airborne Imaging for geographic and geologic applications (Anuta, 1970)<sup>2</sup>. For an intuitive example of optical image correlation by Particle Image Velocimetry see Infobox 2.2.

The particle velocity maps retrieved through cross-correlation allowed Sandrin et al. (1999a) to calculate the time of flight and thus the group velocity of a propagating shear wave front. In soft tissues, Lamé's first parameter is large compared with the shear modulus due to the incompressibility of soft tissue. Consequentially, elasticity can be estimated from the shear wave speed using what is often called the elastography approximation (Gennisson et al., 2003):

$$C_s = \sqrt{\frac{\mu}{\rho}} \quad (2.2)$$

$$E = \frac{\mu(3\lambda + 2\mu)}{\lambda + \mu} \quad (2.3)$$

$$E \cong 3\mu \quad , \quad \lambda \gg \mu. \quad (2.4)$$

Transient elastography was first commercialized for liver elasticity estimation (Fibroscan<sup>TM</sup>) and later extended to further organs such as the breast or muscle (Wells et al., 2011; Sarvazyan et al., 2011; Gennisson et al., 2013). The standard in hospitals at this time is 2D transient elastography using high-frame rate plane wave imaging and excitation of the shear wave through acoustic radiation force. Because high-frame rate scanners are relatively expensive and deep organs are difficult to reach, supplementary elastography methods are currently being investigated. In passive elastography, the noise inherently present in a body of interest is used as the imaging source. The method is once again a development motivated by geophysics. In geophysics, tides and volcanic tremors have been proven to be effective noise source for imaging and monitoring. Apart from not needing an active source, the big advantage of passive methods is that by using the diffuse noise field they do not require a high temporal resolution. Thus, elastography becomes possible with standard low frequency scanners (Sabra et al., 2007; Gallot et al., 2011; Catheline et al., 2013).

---

<sup>2</sup>It is noteworthy, that first attempts to qualitatively visualize motion for scientific purposes were already done in the early days of photography by Marey (1893), Mach (1896), Marey (1901), Ahlborn (1902a), and Ahlborn (1902b). The most famous experiments are probably those by Mach, after whom the Mach cone - created by a source traveling faster than the waves it is emitting - is named.

### Infobox 2.2 Particle Image Velocimetry

The two photos in the top of Fig. 2.1.2 show a group of particles at two timesteps  $t_1$  and  $t_2$ . From  $t_1$  to  $t_2$ , the particles undergo a uniform translation in  $y$ -direction. To retrieve the translation, the images  $t_1$  and  $t_2$  are split into windows, as indicated by one example window (white box) in  $t_1$ . Each window of  $t_1$  is then cross-correlated with each window of  $t_2$ . The result is the correlation map of Fig. 2.1.2c). The space lag of the maximum amplitude peak gives the shift and thus the distance traveled by the particles. From the peak and the magnitude map in Fig. 2.1.2c, we see that the translation is about 60 pixel per timestep. The bottom row of Fig. 2.1.2 gives the more complex example of a vortex. Additionally some particles vanish from the light sheet (illumination plane) by traveling in  $z$ -direction. The green arrows in  $t_1$  and  $t_2$  are the displacement vectors retrieved through cross-correlation.

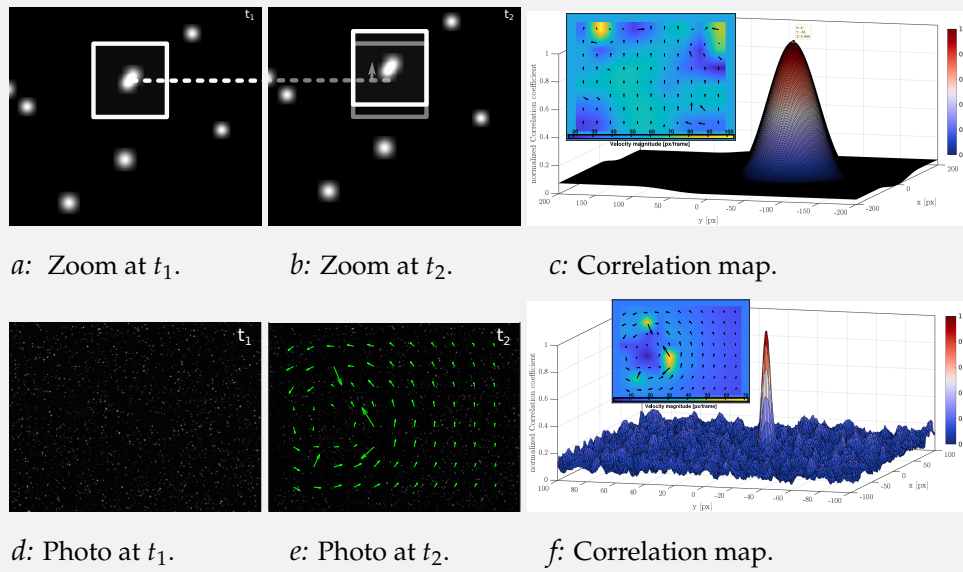


*Figure 2.1.2:* PiV examples for a simple translation in  $y$  (top) and a more complicated rotation (bottom) on synthetic photos. The dimensions of the unzoomed photos are 1600x1200 px (top) and 800x600 px (bottom). Arrows denote the displacement vectors retrieved through cross-correlation. The insets in the correlation maps show a total magnitude map. Generated and calculated through Pivlab (Thielicke, 2014; Thielicke et al., 2019)

The fundamentals of imaging and processing are the same in optics and ultrasound. It is however important to keep in mind, that for most applications optics are limited to the material surface while ultrasound assesses the inside of the material.

The utility of ultrasound elastography outside medical physics was soon realized by Catheline et al. (2003) in imaging shear shock waves in a soft elastic medium. Recently, non-medical research questions were tackled by Latour et al. (2011b), Latour et al. (2011a), and Latour et al. (2013b) as well as Gallot et al. (2013). The first presented imaging of rupture nucleation as an earthquake analogy experiment, and the

second used ultra-fast ultrasound imaging for measuring flow variations in sheared fluids. Chapter 4 of this work is a direct follow up of the works of Latour et al.

## 2.2 Equipment

The ultrasound imaging device used throughout this thesis is a 128-element L7-4 (Philips) ultrasound probe centered at 5 MHz. The probe is connected to a non-clinical high-frame rate ultrasound scanner (Verasonics Vantage™) which works at up to 10 000 frames per second. For our applications the effective limit of temporal resolution is not the pulse repetition frequency of the scanner but the ultrasound speed. At very fast rates, the penetration depth of the ultrasound before two consequent pulses interfere is too small for our purposes. This is a basic limitation not encountered in optical methods. There, it is the frame-rate of the camera posing the effective limit, since the speed of light is the physical limit of temporal resolution. Sequence programming is undertaken via a Matlab interface. All sequences were developed at Labtau and ISTerre, based on example codes by Verasonics and previous sequences by Remy Souchon and Ali Zorgani. The reconstruction algorithms implemented by Verasonics already provide the user with complex IQ-Data. IQ is basically a Cartesian representation of the polar magnitude and phase information, that is used due to advantages in hardware construction (NI, 2018). Consequently, magnitude and phase of the beamformed signal are available to the user after the reconstruction. This offers the advantage that phase shift estimation becomes feasible. Phase shift estimation allows for faster data processing and higher image resolution than speckle tracking which requires windowing for cross-correlation.

## 2.3 Correlation algorithm

We use a phase shift estimation algorithm in the Fourier domain. Phase shift methods are well known in Doppler imaging and are closely related to phase correlation, a technique developed for image processing. Following Thoduka et al. (2017), the method was introduced by Kuglin et al. (1975). Two images having identical information but shifted coordinates, e.g., show the same motif but are shifted up-, down-, or side-wards, will only differ in phase. Hence, their Fourier transform will have identical magnitude but differing phase information. This phase shift or phase difference can be expressed through the Fourier shift theorem. The theorem states, that a signal  $x(t)$  delayed by  $dt$  has a Fourier transform that equals the Fourier transform of  $x(t)$  multiplied by  $e^{-j\omega dt}$ . Hence,  $x(t - dt) \leftrightarrow e^{-j\omega dt} \hat{x}(\omega)$ .

Thus, for a 2D-image  $f_1$  shifted in its coordinates  $x$  and  $y$ :



$$f_2(x, y) = f_1(x - dx, y - dy) \quad (2.5)$$

$$\hat{f}_2(\xi, \eta) = e^{-j2\pi(\xi dx + \eta dy)} \hat{f}_1(\xi, \eta) \quad (2.6)$$

Because for ultrasound reflection images, only displacements in direction of the plane ultrasound wave can be recorded, the translation of the ultrasound reflection images is one-dimensional. The spatial coordinates along the axis ultrasound propagation are actually inferred from the ultrasonic travel-time and the central frequency of the probe. Hence, with one spatial dimension  $x$  held constant and the other,  $y$ , being expressed through travel-time  $\tau$  ( $y \rightarrow \tau$ ), the 2D phase shift of equation 2.5 becomes a 1D phase shift:

$$f_2(x, \tau) = f_1(x, \tau - d\tau) \quad (2.7)$$

$$\hat{f}_2(\xi, \omega) = e^{-j2\pi(\xi d\tau)} \hat{f}_1(\xi, \omega) \quad (2.8)$$

Hence, for two beamformed ultrasound reflection images ( $IQ$ ) that are recorded with a time difference  $d\tau$  at  $t_1$  and  $t_2$ , which are identical in magnitude but shifted in phase, the theorem reads:

$$IQ(x, \tau, t_2) = IQ(x, \tau - d\tau, t_1) \quad (2.9)$$

$$\hat{IQ}_2(\xi, \omega, t_2) = e^{-j2\pi(\omega d\tau)} \hat{IQ}(\xi, \omega, t_1) \quad (2.10)$$

The phase shift  $e^{-j2\pi(\omega d\tau)}$  can be calculated by using the normalized cross power spectrum, which is retrieved through multiplication with the complex conjugate in the Fourier domain.

$$e^{-j2\pi(\omega d\tau)} = \frac{\hat{IQ}(\xi, \omega, t_1) \hat{IQ}^*(\xi, \omega, t_2)}{|\hat{IQ}(\xi, \omega, t_1) \hat{IQ}(\xi, \omega, t_2)|} \quad (2.11)$$

The argument of equation 2.11 gives thus the relative displacement between two images in radians.

The particle velocity is then:

$$v_p(x, \tau) = \frac{c_0}{(4\pi f_c)} \arg(e^{-j2\pi(\omega d\tau)}) \quad (2.12)$$

- with  $\tau$  being related to the spatial coordinate  $y$  by  $\lambda = \frac{c_0}{f_c}$  and  $y$  being resolved by the imaging system at four points per wavelength.

- with  $c_0$  being the speed of ultrasound, approximately  $1480 \text{ m s}^{-1}$  (speed of sound in water) in soft matter, and  $f_c$  being the central frequency of the probe.

A more sophisticated algorithm suitable for elastography is Loupas algorithm. While equation 2.11 calculates the time shift in the ultrasound signal assuming a constant central frequency of the probe, Loupas algorithm incorporates frequency changes of the reflected ultrasound signal with depth (Pinton et al., 2005).

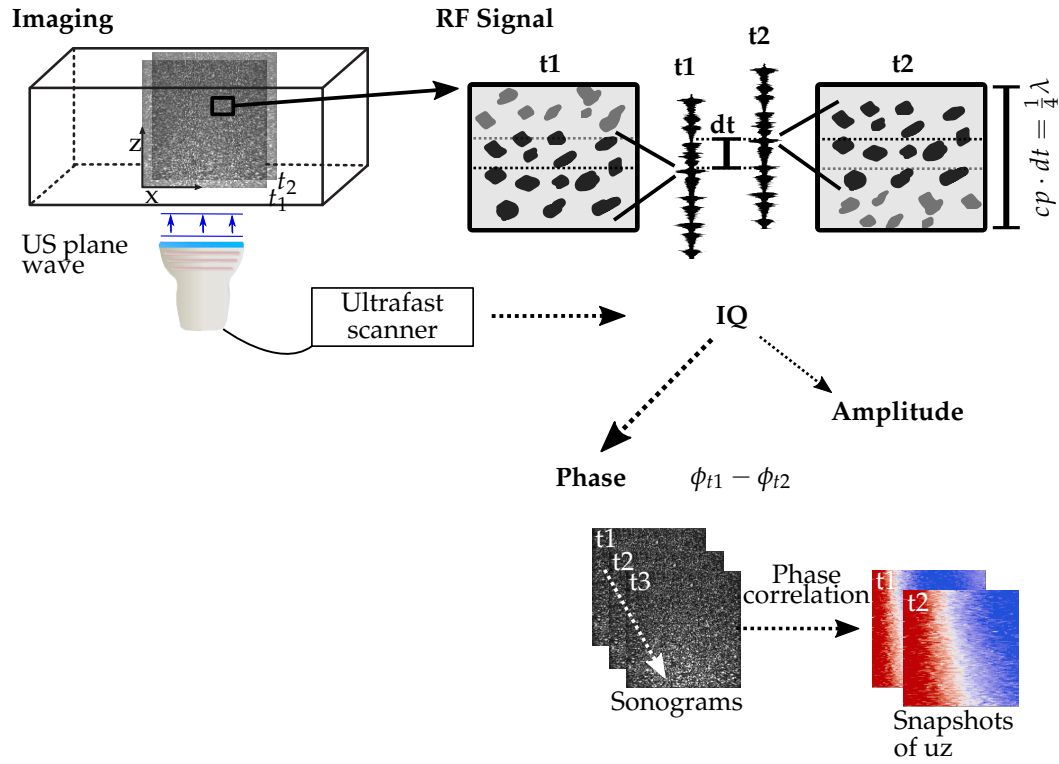


Figure 2.3.1: Schema of the elastography principle. The top left shows an exemplary beamformed ultrasound reflection image retrieved through plane wave emission of the indicated ultrasound probe. The top right shows the schematic elastography principle: A passing shear wave displaces the speckle pattern which is reflected in a time-shift of the ultrasound reflection signal (one transducer line is shown as an example). This time shift can be retrieved through speckle tracking or phase correlation which is schematically shown in the bottom right.



## Chapter 3

# Poro-elastic wave dispersion

This chapter reports our results on dispersive elastic wave propagation in soft porous materials. The chapter presents several studies in different soft porous materials, but emphasis is put on:

- High-frame rate ultrasound imaging in a water saturated melamine foam.

It is under the controlled conditions of the manufactured Melamine foam, that the physics of soft porous materials are best accessed. The chapter starts with a general introduction that quickly reviews the development of porous wave propagation theories and states the main results of the Melamine experiment. It is followed by the principal equations resulting from Biot's theory of elastic wave propagation and the detailed description and discussion of elastic wave propagation in the Melamine foam. This part can be found in the more concise form of a letter in Appendix E. Additionally, two experiments in ex-vivo porcine lungs are presented to get an idea of the wave propagation in a real lung:

- High-frame rate ultrasound ex-vivo imaging in a saturated porcine lung.
- High-frame rate optical ex-vivo imaging in a conserved porcine lung.

At last, possible implications for wave dispersion analysis in-vivo are discussed.

### 3.1 Introduction

The characterization of wave propagation in porous materials finds a wide range of applications in various fields at different scales. In contrast to classical elastic materials, poro-elastic materials support three types of elastic waves and exhibit a distinctive dispersion in the presence of viscous fluids (Biot, 1956c; Plona, 1980; Lauriks et al., 2005).

The existence of a secondary compression wave (PII-wave) in addition to the the first compression wave (PI-wave) and shear wave (S-wave) has been an issue of debate until its first unambiguous experimental proof by Plona (1980). However, first experimental reports that mention the possibility of a frame- and a fluid-borne

compression wave date back to the 1940s and 1950s. Beranek (1947) reports two waves, with "... one primarily airborne and the other primarily structure-borne". Oura (1952) measured sound waves in snow and stated, that: "...the sound wave is propagated mainly by air in snow and its icy structure only interferes with the propagation" (Carcione, 2015).

Paterson (1956) find that two volume expansion waves, named frame-wave, air-wave or liquid-wave, are propagating in porous granular aggregates and that these involve coupled displacements of both constituents.

The first theoretical analysis of the secondary compression wave is attributed to J. Frenkel (Frenkel, 1944; Frenkel, 2005). Following from Darcy's law and the equation of motion he finds two longitudinal velocities corresponding to one wave with small and one wave with heavy damping. For very low permeabilities they become identical. However, using a scalar theory, Zwikker et al. (1941) already derive the existence of an air-borne and skeleton-borne compression wave (further details see Zwikker et al. (1949)).

The first thorough theoretical description of poro-elasticity including dispersion and a secondary or slow compression wave (PII-wave) was developed by Biot (Biot, 1956c; Biot, 1956b), hence it is often named Biot slow wave. The theory was soon applied in the field at geophysical scale for hydrocarbon exploration (Geerstma et al., 2005). The theory incorporates viscous effects, but neglects thermal effects. For water and oil, the main fluids encountered by geophysicists, the approximation is good enough, but for air-filled pores an extension of the theory incorporating thermal effects was needed. Hence, models of sound transmission through air-filled foams (Melon et al., 1998) and bone (Haire et al., 1999) often incorporate fluid-equivalent models based on the Johnson–Koplik–Dashen (Johnson et al., 1987) and Johnson–Champoux–Allard (Johnson et al., 1987; Champoux et al., 1991) models, that assume a rigid skeleton.

Biot's theory was later extended and applied at the laboratory scale for bone and lung characterization using numerical modeling and medical imaging (Allard et al., 2009; Johnson et al., 1987; Champoux et al., 1991; Fellah et al., 2008; Mizuno et al., 2009; Dai et al., 2014a). While poro-elastic models have been used to characterize materials and fabrics such as textiles (Álvarez-Arenas et al., 2008), anisotropic composites (Castagnede et al., 1998), snow (Gerling et al., 2017) and sound absorbing materials (Boeckx et al., 2005), experimental detection of the PII-wave remains scarce (Plona, 1980; Smeulders, 2005). In medical imaging, the characterization of the porous surface and shear wave (S-wave) has only recently been brought to attention (Dai et al., 2014b; Nguyen et al., 2013; Zhou et al., 2018). The high attenuation of poro-elastic S- and PII-waves and the diffuse behavior below a critical frequency of the PII-wave pose crucial difficulties for experimental detection (Biot, 1956c; Yang et al., 2016; Smeulders, 2005).

We overcome this challenge by using high frame rate ultrasound imaging for wave tracking (Sandrin et al., 1999b) inside saturated, highly porous melamine foams. High frame rate ultrasound imaging is also the technique underlying transient elastography (Sandrin et al., 1999b; Gennisson et al., 2003; Catheline, 2006; Gennisson et al., 2013). A very dense grid of virtual receivers is placed inside the sample through image correlation of ultrasonic backscattered images, enabling the recovery of the particle velocity field of elastic waves. The elastic waves are thus sampled at super-resolution in the sense that the resolution is determined by the wavelength of the tracking waves. At ultrasonic frequencies this wavelength is several orders of magnitude lower than the wavelength of the tracked low-frequency waves (Catheline et al., 2004; Gennisson et al., 2013). To this end, two requirements need to be fulfilled. Firstly, simple scattering of ultrasonic waves assures the ultrasound reflection image. Secondly, the imaged elastic waves propagate several times slower ( $< 40 \text{ m s}^{-1}$ ) than the ultrasonic waves ( $\approx 1500 \text{ m s}^{-1}$ ). In water-saturated melamine foams, both assumptions are satisfied, allowing us to visualize the S- and PII-wave propagation. Consequently, investigation of their speeds and attenuations becomes possible, which, to the best of our knowledge, has not been done before. The measured low frequency speeds are in agreement with a first approximation that views the foam as a biphasic elastic medium and ignores coupling effects. The approximation predicts a ratio of  $\sqrt{2}$  between the S-wave and the PII-wave. To take into account coupling of the fluid and solid phase, we compare the measured speeds and attenuations of both waves with the analytic results of Biot's theory. We find a good quantitative prediction of the S-wave results and the predicted Biot slow wave shows a qualitative agreement with the measured PII-wave. The porous material we investigate (melamine resin foam) has already been used to simulate the acousto-elastic properties of pulmonary tissue due to its common highly porous soft structure (Mohanty et al., 2016; Lauriks et al., 2005; Zhou et al., 2018). Furthermore, first in-vivo tests of surface wave lung elastography have been reported (Zhang et al., 2016). We thus postulate that our results have possible future implications for lung characterization by ultrasound imaging. This is supported by two additional experiments with Ex-vivo pig lungs that we present at last. The first shows that shear wave dispersion can be observed in a water-saturated defrosted Ex-vivo pig lung. The second shows the absence of the shear wave dispersion in an air-filled, conserved Ex-vivo pig lung.

### 3.2 Biot theory

The first theory thoroughly describing a secondary longitudinal wave in porous media due to the existence of a fluid phase was developed by Biot in several papers (Biot, 1955; Biot, 1956c; Biot, 1956b) for water saturated rocks. Geophysicists and geotechnical engineers had a particular interest in porous media due to the exploration of hydrocarbon resources and the characterization of soil behaviour in civil

engineering. Biot's theory of poroelasticity uses macroscopic quantities such as permeability, viscosity and porosity to describe the medium, which is regarded as a solid matrix saturated by a viscous fluid. It assumes infinitesimal strain theory and local fluid motion governed by Darcy's law. A representative elementary volume is small compared to the elastic wavelengths and infinitesimal strain theory holds true. The fluid and solid displacement are coupled which leads to the existence of a secondary compression wave and the dispersion of the P- and S-waves for a viscous fluid filling the pores (Biot, 1956c; Biot, 1956b; Biot, 1962; Carcione, 2015; Vogelaar, 2009; Morency et al., 2008; Mavko et al., 2009; Allard et al., 2009). Based on porosity ( $\phi$ ), Bulk moduli of the solid ( $K_s$ ), drained frame ( $K_{fr}$ ) and fluid ( $K_{fl}$ ), Biot's formulation of poroelasticity takes into account the coupled pore pressure, porosity and volumetric changes in the fluid and solid constituent.

Using a Lagrangian model, Biot derives the equations of motion including dissipation due to a viscous fluid from the potential energy of deformation, invoking Hamilton's principle (Carcione, 2015). For a complete step-by-step derivation see Appendix A. Here we will state the fundamental equations and the resulting expressions for the wave-speeds, which we use later to calculate the theoretical shear and slow wave speed in a porous material.

### 3.2.1 Idealized fluid: Wave propagation in the absence of viscosity

Similar to the wave equation in an elastic solid, the wave equation for a porous aggregate can be defined. First, the equations of motion are developed for a fluid-solid aggregate represented by an elementary cube (REV). In contrast to classical linear elasticity, inertial coupling has to be taken into account. For simplicity, we start with an ideal fluid and will derive the role of viscosity at a later point.

As for the notation:

$$\mathbf{u} = u(\mathbf{r}) = (u_x \ u_y \ u_z) = u_i \text{ and } \sum_{i=1}^3 u_i U_i = u_i U_i = u_1 U_1 + u_2 U_2 + u_3 U_3.$$

**Stress-strain relations** The total displacement of the elementary cube is divided into two components: the average displacements of the solid  $u(\mathbf{r}, t)$  and of the fluid  $U(\mathbf{r}, t)$ .

Biot takes into account that the fluid stress tensor resulting from the forces acting on the fluid parts of the cube is a diagonal tensor comprising the fluid pressure  $p$  scaled by porosity: ( $\phi p \delta_{ij}$ ). The stress-strain relations for an isotropic material can then be expressed as:

$$\begin{aligned} \sigma^s_{ij} &= 2Ne_{ij} + Ae_{kk}\delta_{ij} + Qe_{kk}\delta_{ij} \quad ; \quad A = P - 2N \\ \sigma^f_{ij} &= -\phi p \delta_{ij} = (Qe_{kk} + Re_{kk})\delta_{ij}, \end{aligned} \tag{3.1}$$

where  $e_{ij} = \frac{1}{2}(\frac{\partial u_i}{\partial x_j} + \frac{\partial u_j}{\partial x_i})$ ,  $e_{ij} = e_{ji}$  and  $\epsilon_{kk} = \frac{\partial U_x}{\partial x} + \frac{\partial U_y}{\partial y} + \frac{\partial U_z}{\partial z}$ .

$P, Q$  and  $N$  are Biot's poroelastic coefficients and are a function of the fluid as well as the solid properties.  $P - 2N$  and  $N$  represent the Lamé parameters.  $R$  expresses the pressure needed for the fluid to enter the aggregate without change in total volume.  $Q$  expresses the coupling between the volume of the solid and fluid phases. In practice, the coefficients are calculated using Gedankenexperimente (*thought experiments*), presented by Biot et al. (1957) (see Appendix A). Since fluids do not support shear motion,  $N$  is equal to the shear modulus of the frame.

### 3.2.2 Inertial coupling - nonviscous fluid

For a solid-fluid aggregate the acceleration of one phase creates an inertial force or a drag on the other phase. This effect holds true for an idealized fluid without viscosity as well and is known as added mass or apparent weight. It states that a body moving in a fluid moves in the same way in which the same body, but with an added mass, would move in vacuum (Landau and Lifshitz, 1987; Oman et al., 2016). The added mass has to be taken into account in energy considerations and consequently the kinetic energy of a porous material cannot simply be expressed by the sum of the fluid and solid macroscopic accelerations. Instead:

$$E_c = \frac{1}{2}\rho_{11}|\dot{\mathbf{u}}|^2 + \rho_{12}\dot{\mathbf{u}}\dot{\mathbf{U}} + \frac{1}{2}\rho_{22}|\dot{\mathbf{U}}|^2. \quad (3.2)$$

The added mass and thus the mass coefficients  $\rho_{11}, \rho_{12}, \rho_{22}$  depend on the frame and fluid densities and the pore geometry.

The three mass parameters can be expressed in terms of porosity ( $\phi$ ) and the densities of the frame and fluid ( $\rho_{fr}$  and  $\rho_{fl}$ ):

$$\begin{aligned} \phi\rho_{fl} &= \rho_{22} + \rho_{12} \\ \rho_{fr} &= \rho_{11} + \rho_{12}. \end{aligned} \quad (3.3)$$

**Equations of motion** Next, we state the porous equations of motion for a non-viscous fluid through stress gradients:

$$\begin{aligned} \nabla_j \sigma_{ij}^s &= \frac{\partial^2}{\partial t^2}(\rho_{11}u_i + \rho_{12}U_i); \quad \nabla_j = \frac{\partial}{\partial x_j} \\ \nabla_j \sigma_{ij}^f &= \frac{\partial^2}{\partial t^2}(\rho_{12}u_i + \rho_{22}U_i). \end{aligned} \quad (3.4)$$

Making use of Eq. (3.1), which relates stress  $\sigma$  to displacement  $u$ , we can derive the equations depending on the poroelastic coefficients  $N, A, Q, R$ :



$$\begin{aligned}
N\nabla^2 u_i + (A + N) \frac{\partial e_{kk}}{\partial x_i} + Q \frac{\partial \epsilon_{kk}}{\partial x_i} &= \frac{\partial^2}{\partial t^2} (\rho_{11} u_i + \rho_{12} U_i) ; A = P - 2N \\
Q \frac{\partial e_{kk}}{\partial x_i} + R \frac{\partial \epsilon_{kk}}{\partial x_i} &= \frac{\partial^2}{\partial t^2} (\rho_{12} u_i + \rho_{22} U_i).
\end{aligned} \tag{3.5}$$

### 3.2.3 Viscous fluid: Wave propagation in the presence of dissipation

To account for dissipation Biot assumes Poiseuille flow to hold true in a low frequency regime defined by a cross-over frequency  $f_c$  (see Appendix A.3). Above, Poiseuille flow breaks down. Assuming isotropy and that the flow in microscopic pores is completely determined by the velocities  $u_i$  and  $U_i$ , Biot defines a dissipation function  $D_{visc}$ :

$$\begin{aligned}
2D_{visc} &= b \left[ \sum_{i=1}^3 (\dot{u}_i - \dot{U}_i)^2 \right] \\
b &= \eta_f \frac{\phi^2}{\kappa}
\end{aligned} \tag{3.6}$$

There are thus two additional parameters for the two phase system where  $\eta_f$  is fluid viscosity and  $\kappa$  is permeability. The permeability characterizes how well the solid allows for fluid flow. It is independent of the fluid and measured in  $m^2$ . Next, we add the dissipation function into the inertial framework, which leads to the new equations of motion including viscosity:

$$\begin{aligned}
N\nabla^2 u_i + (A + N) \frac{\partial e_{kk}}{\partial x_i} + Q \frac{\partial \epsilon_{kk}}{\partial x_i} &= \frac{\partial^2}{\partial t^2} (\rho_{11} u_i + \rho_{12} U_i) + b \frac{\partial}{\partial t} (u_i - U_i) ; A = P - 2N \\
Q \frac{\partial e_{kk}}{\partial x_i} + R \frac{\partial \epsilon_{kk}}{\partial x_i} &= \frac{\partial^2}{\partial t^2} (\rho_{12} u_i + \rho_{22} U_i) - b \frac{\partial}{\partial t} (u_i - U_i).
\end{aligned} \tag{3.7}$$

Spatially differentiating the equations of motion leads to the dilatational wave equations and applying the curl operation to the rotational wave equation.

### 3.2.4 Wavespeed calculation

For the calculation of Biot's wavespeed in this manuscript we use a formulation that employs a slightly different notation from Biot's original paper. For practical applications Biot (1956a) and Biot et al. (1957) introduce a new set of variables. Biot et al. (1957) gives a linear strain energy formulation, which for uniform porosity results in equations of motion equivalent to Eq. (3.7). The wave equations then depend on the new coefficients  $H, M, C, \mu_{fr}$  instead of  $P, Q, R, N$ . Instead of the mass coefficients  $p_{11}, p_{12}, p_{22}$ , the mass of the fluid ( $\rho_{fl}$ ) and solid ( $\rho_s$ ) or frame ( $\rho_{fr}$ ) as well

as the tortuosity ( $\alpha$ ) are used. Furthermore,  $\zeta$ , which is the volumetric change of fluid content is introduced (Biot, 1956a):

$$\begin{aligned}
 H &= P + 2Q + R \\
 \mu_{fr} &= N \\
 M &= \frac{R}{\phi^2} \\
 C &= B_W M \\
 B_W &= \left( \frac{Q + R}{R} \phi \right) \\
 \zeta &= \phi \nabla \cdot (\dot{\mathbf{u}} - \dot{\mathbf{U}}) \\
 m &= \alpha \frac{\rho_{fl}}{\phi} \\
 \rho &= (1 - \phi) \rho_s + \phi \rho_{fl}
 \end{aligned} \tag{3.8}$$

where  $B_W$  is known as the Biot-Willis coefficient. Note that the purely geometric tortuosity factor  $\alpha$  can be related to the mass coupling coefficient by  $\rho_{12} = -(\alpha - 1)\phi\rho_f$  (Berryman, 1980).

Following Biot (1962), Stoll et al. (1970), Buchanan (2005), and Berryman (1980) the dilatational equations then read:

$$\begin{aligned}
 \nabla^2 (He_{kk} - C\zeta) &= \frac{\partial}{\partial t^2} (\rho e_{kk} - \rho_{fl} \zeta) \\
 \nabla^2 (Ce_{kk} - M\zeta) &= \frac{\partial}{\partial t^2} (\rho_{fl} e_{kk} - m\zeta) - \frac{\eta}{\kappa} \frac{\partial \zeta}{\partial t}.
 \end{aligned} \tag{3.9}$$

The rotational wave equations read:

$$\begin{aligned}
 \mu \nabla^2 \nabla \times \mathbf{u} &= \frac{\partial}{\partial t^2} (\rho \nabla \times \mathbf{u} - \rho_{fl} \nabla \times \mathbf{U}) \\
 -\frac{\eta}{\kappa} \frac{\partial \nabla \times \mathbf{U}}{\partial t} &= \frac{\partial^2}{\partial t^2} (\rho_{fl} \nabla \times \mathbf{u} + m \nabla \times \mathbf{U}),
 \end{aligned} \tag{3.10}$$

The frequency dependent velocity  $v = \frac{\omega}{k}$  is calculated from the the dispersion relation in the frequency domain (Berryman, 1980; Mavko et al., 2009; Stoll, 1974):

$$\left( \frac{\omega_p}{k_p} \right)^{-2} = \frac{-(Hq + M\rho - 2C\rho_{fl}) \pm \sqrt{(Hq + M\rho - 2C\rho_{fl})^2 - 4(C^2 - MH)(\rho_{fl}^2 - \rho q)}}{2(C^2 - MH)} \tag{3.11}$$

$$\left( \frac{\omega_s}{k_s} \right)^{-2} = \frac{q\rho - \rho_{fl}^2}{q\mu_{fr}}, \tag{3.12}$$

where the different terms can be expressed in term of the solid, fluid and porous parameters as:

$$\begin{aligned}
 q &= \frac{\alpha \rho_{fl}}{\phi} - \frac{i\eta F(\zeta)}{\omega \kappa} \\
 H &= \frac{(K_s - K_{fr}) * (K_s - K_{fr})}{D - K_{fr}} + K_{fr} + \frac{4}{3}\mu_{fr} \\
 C &= K_s \frac{K_s - K_{fr}}{D - K_{fr}} \\
 M &= K_s \frac{K_s}{D - K_{fr}} \\
 D &= K_s(1 + \phi(\frac{K_s}{K_f} - 1)).
 \end{aligned} \tag{3.13}$$

$F(\zeta)$  expresses the frequency dependence of the viscosity. Under the assumption of Poiseuille flow, which is assumed in Biot's low frequency range,  $F(\zeta)$  is one. For the differentiation of the low and high frequency regimes and the high frequency expression see Appendix A.

### 3.3 Saturated Foam

#### 3.3.1 Experimental setup

We use a rectangular Basotect<sup>®</sup> melamine resin foam of dimensions  $x = 30$  cm,  $y = 18$  cm,  $z = 12$  cm, which is fully immersed in water to ensure complete saturation. The foam exhibits a porosity between 96.7 and 99.7%, a tortuosity between 1 and 1.02, a permeability between  $1.28 \times 10^{-9}$  and  $2.85 \times 10^{-9}$  m<sup>2</sup> and a density of  $8.8 \pm 1$  kg m<sup>-3</sup>. The viscous length  $\sigma$  is between  $1.124 \times 10^{-4}$  and  $1.302 \times 10^{-4}$   $\mu$ m as indicated in the microscopic photo of the foam at the top of Fig. 3.3.1. The foam parameters were measured using the acoustic impedance tube method (Niskanen et al., 2017) and a Johnson-Champoux-Allard-Lafarge model (Johnson et al., 1987; Champoux et al., 1991; Lafarge et al., 1997; Niskanen et al., 2017). These measurements are independent of the presented water-saturated experiment and serve as input to the analytic Biot model. Fig. 3.3.1 shows the setups for the S-wave (a) and PII-wave (b) experiments. A piston (ModalShop Inc. K2004E01), displayed at the top, excites the waves. In a), a rigid metal rod which is pierced through the sponge ensures coupling between the rod and foam as well as transverse polarization ( $u_z$ ) of the wave. Shear wave excitation is achieved in two ways. Firstly, through a pulse and secondly, through a frequency sweep from 60 to 650 Hz. The excited S-wave propagates along x-dimension ( $k_x$ ) exposing a slight angle due to imperfect alignment of the rod during excitation. In b), a rigid plastic plate at the end of a rod excites the compression wave on the upper foam surface and ensures longitudinal polarization. The induced vibration is a Heaviside step function with a hold down time larger than measurement time. We undertake three realizations of the experiment with different amplitudes of the step function. In both setups, particle motion and motion of the rod are along the z-dimension. The imaging device is a 128-element L7-4 (Philips) ultrasound probe centered at 5 MHz. Fig. 3.3.1c) schematically indicates the probe position below the foam and the z-polarization of the ultrasonic waves. The probe is connected to a high-frame rate ultrasound scanner (Verasonics Vantage<sup>TM</sup>) which works at 3000 (S-wave) and 2000 (PII-wave) frames per second. Each frame is obtained through emission of plane waves as in (Sandrin et al., 1999b) and beam-forming of the backscattered signals. In order to visualize the wave propagation, we apply phase-based motion estimation (Pinton et al., 2005) on subsequent beam-formed ultrasound frames. Similar to ultrasound Doppler techniques, the retrieved phase difference gives the relative displacement in the micrometer range. Due to the finite size of our sample, boundary effects are present. Hence, we apply a directional filter (Buttkus, 2000) in the  $k_x - k_y - f$  domain of the full 2D wavefield (Deffieux et al., 2011). The resulting relative displacement for setup 3.3.1a) is a superposition of the primary compression wave (PI) and the PII-wave. Thus, we additionally apply

a spatial gradient in  $z$ -direction to isolate the PII-wave displacement for dispersion measurements.

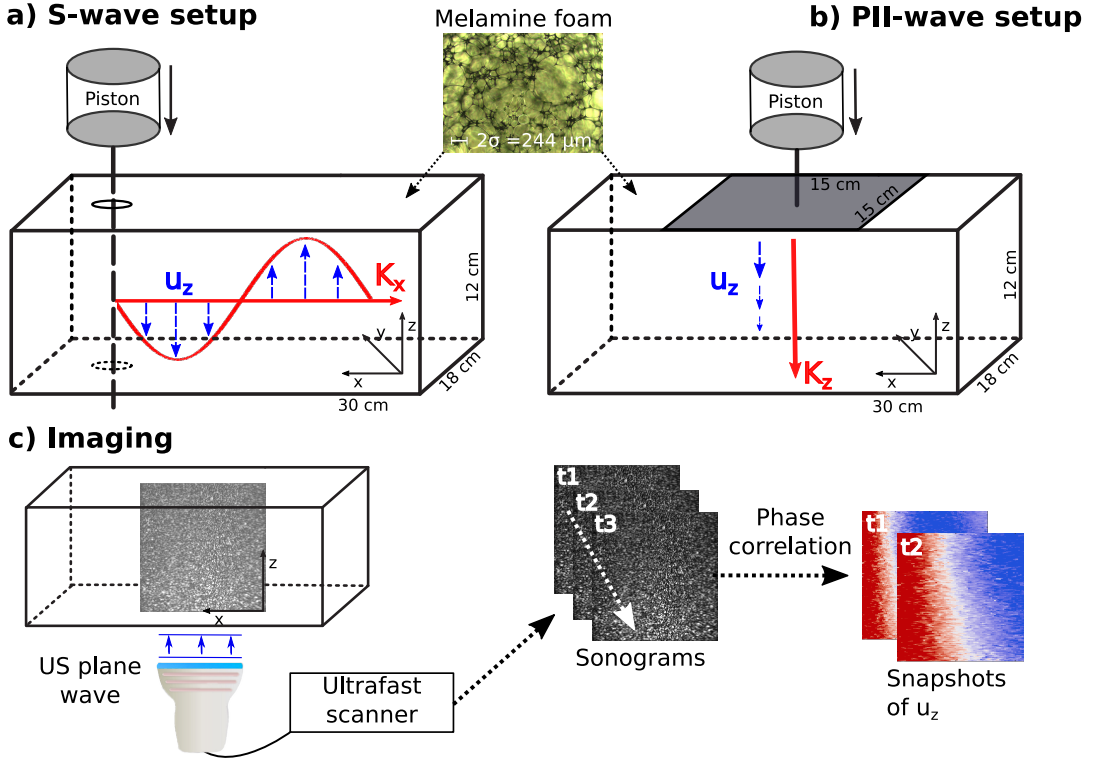


Figure 3.3.1: Schematic experimental setups of the S-wave excitation (a) and PII-wave excitation (b). Blue arrows signify the polarization of particle motion and red arrows the direction of wave propagation. At the center top, a microscopic photo of a sample of the investigated melamine foam is displayed. c) High frame rate ultrasound imaging principle: The particle velocity maps are retrieved through correlation of subsequent ultrasound images.

### 3.3.2 Wave propagation

Three displacement snapshots of the S- and PII-wave are shown in Fig. 3.3.2a). The top row is an example of the wave propagation induced by shear excitation as schematically shown in Fig. 3.3.1a). Blue color signifies particle motion  $u_z$  towards the probe. A comparison of the wave-fields shows that the plane wave front is propagating and attenuated in positive  $x$ -direction ( $k_x$ ). The bottom row displays the PII-wave for 6, 7 and 8 ms. It is excited at the top and the plane wave front propagates with decreasing amplitude in positive  $z$ -direction ( $k_z$ ). A summation along the  $z$ -dimension for the transverse setup, and along the  $x$ -dimension for the longitudinal setup give the resulting space-time representations in Fig. 3.3.2b). They show that the S- and PII-wave are propagating over the whole length of the sample at near constant speed. The PII-wave (PII) is well separated and of opposite polarity from the direct arrival (PI) at 2.5 ms. A time-of-flight measurement through slope fitting

gives a group velocity of  $14.7 \text{ m s}^{-1}$  (S-wave) and  $14.4 \text{ m s}^{-1}$  (PII-wave). The central frequency is approximately 220 Hz for the S-wave, and 120 Hz for the PII-wave. These values suggest that both speed are governed by the low elastic modulus of the foam. The most simple porous model for the foam is an uncoupled biphasic medium with a weak frame supporting the S- and PII-wave. In this case, the PI-wave is supported by an in-compressible fluid, which circulates freely through the open pores. The compressibility of the solid phase is that of the foam matrix and the first isotropic Lamé parameter  $\lambda_0$  is very small compared to the shear modulus  $\mu_0$ . Hence, the compression wave speeds  $v_{p1,2}$  become:

$$\begin{cases} v_{p1} = \sqrt{\frac{\lambda_f}{\rho_f}} & ; \lambda_f \gg \mu_f \\ v_{p2} = \sqrt{\frac{(\lambda_0 + 2\mu_0)}{\rho_0}} \approx \sqrt{\frac{2\mu_0}{\rho_0}} \approx \sqrt{2}v_s & ; \lambda_0 \ll \mu_0 \end{cases} \quad (3.14)$$

with  $\lambda_0$ ,  $\mu_0$  and  $\lambda_f$ ,  $\mu_f$  being the first and second Lamé parameters of the drained sponge and the fluid.  $\rho_0 = \rho_{\text{mineral}}(1 - \phi)$  is the density of the the drained sponge,  $\rho_f$  the fluid density,  $v_s$  the S-wave speed and  $\phi$  is porosity. This approximation is in accordance with Tanaka et al. (1973) who investigated the quasi-static behaviour of hydrogels. To assess the velocity dispersion of the two elastic waves, we apply a fast Fourier transformation and recover the phase velocity and attenuation from the imaginary and real part of the complex signal. For the S-wave, we use the frequency sweep. For the PII-wave, reflections from the boundaries and mode conversions prohibit the exploitation of a chirp and we use the Heaviside displayed in Fig. 3.3.2. Its bandwidth is limited from 50 to 150 Hz for power spectral density values larger than  $-10 \text{ dB}$ . The phase velocity is directly deduced from a linear fit of the phase value along the spatial propagation dimension. In order to achieve a reliable fit, we use a Ransac algorithm (Torr et al., 2000) and display values with a  $R^2$  of 0.98 and minimum 70 % inliers. The results for the speed measurements of the S- and PII-wave in their shared frequency band are displayed in Fig. 3.3.3. Both speeds are monotonously increasing with frequency. In order to verify Equation 3.14 we use a sixth-order polynomial fit (blue line) and its 95 % confidence interval as input data. The resulting PII-wave speeds (black line) and its 95 % confidence interval (gray zone) show that the PII-wave experimental data lie within the prediction of Equation 3.14, and keep a ratio of approximately  $\sqrt{2}$  with the S-wave speeds. Fig. 3.3.5 shows, that over the entire investigated frequency range the measured S-wave speeds increase monotonously and triple in value.

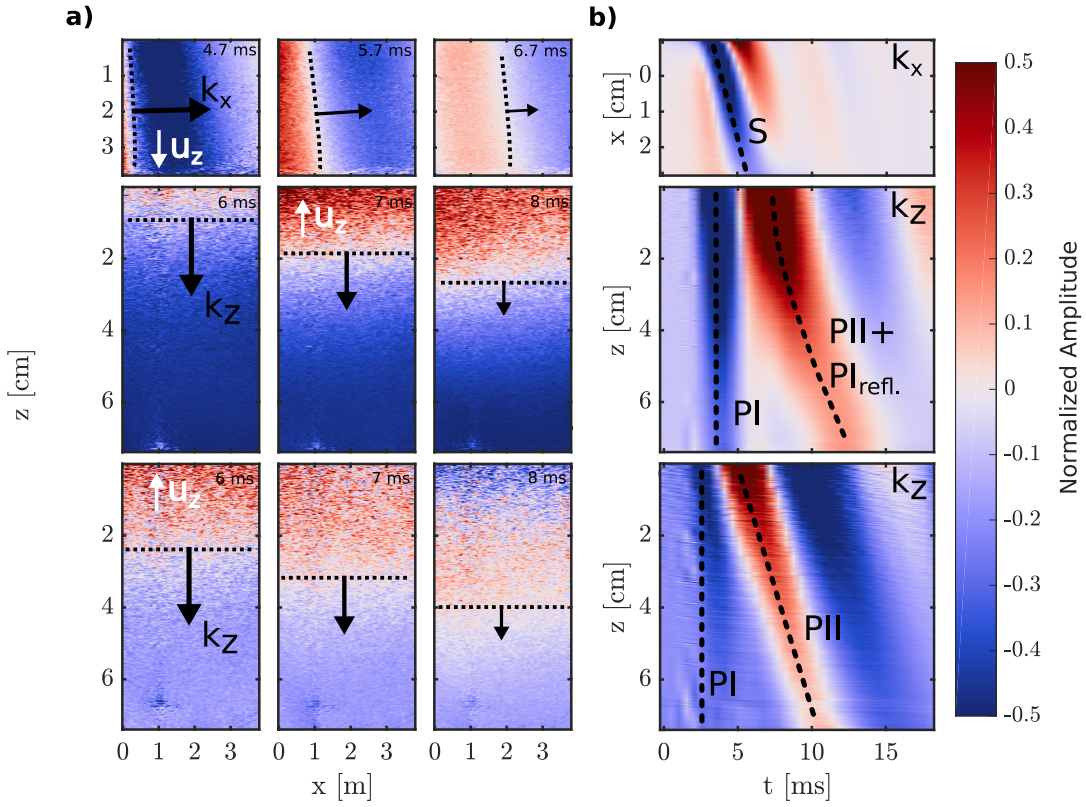


Figure 3.3.2: Experimental wave-fields for the two setups in Fig. 1. a) Snapshots at three time-steps of a propagating S-wave pulse (top row) and PII-wave step (middle and bottom row). The top and middle row show the particle velocity and the bottom row shows the z-gradient of the particle velocity. The gradient cancels the PI-wave and its reflection because their displacements are retrieved as nearly constant (PI-wave travels at the same speed as the tracking ultrasound) b) Corresponding time-space representation by summation orthogonal to  $x$  (top) and  $z$  (middle and bottom). In the top row, the S-wave (S) and in the middle and bottom row, the first (PI) and secondary compression wave (PII) can be identified.  $u_z$  - Direction of particle motion.  $k_{x/z}$  - Direction of wave propagation.

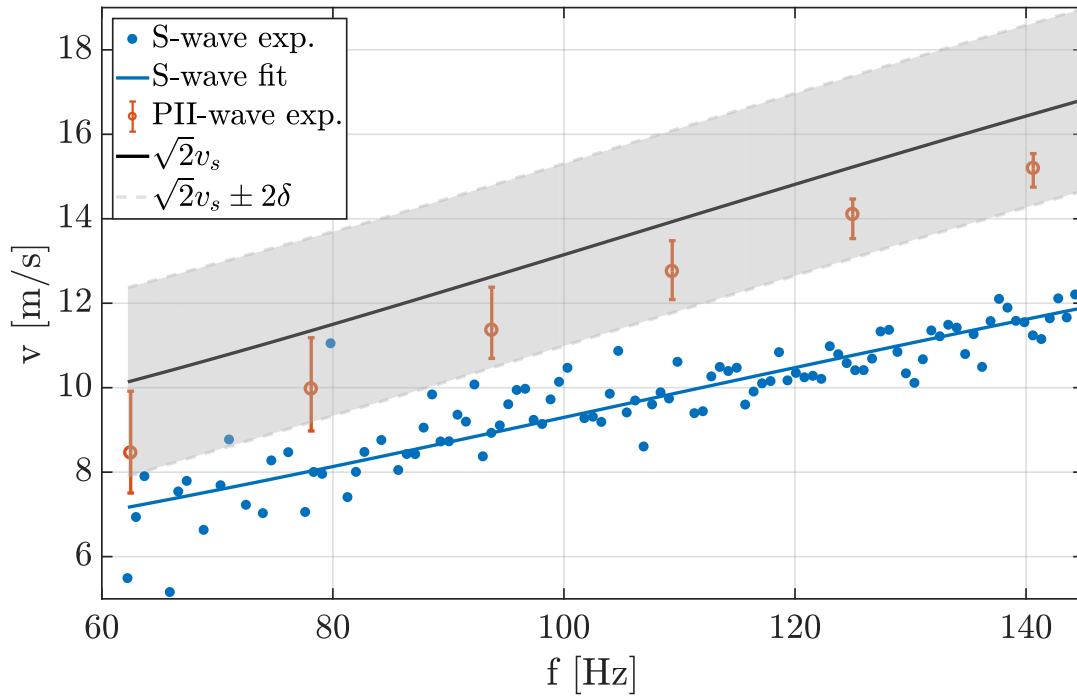


Figure 3.3.3: Experimental and theoretical dispersion. Experimental S-wave (blue dots) and PII-wave (red circles) speeds. A sixth order polynomial fit (blue solid line) of the total available frequency band and its 95 % confidence interval give  $v_s$  for Equation 3.14. The resulting PII-wave speeds (black solid line) and its 95 % confidence interval (gray zone) are displayed. The PII-wave measurements are the average of three realizations with the maximum deviation indicated by the error bars.



**Infobox 3.1 PII-wave verification**

We have long been thinking that guided waves could explain what we now interpret as a PII-wave. In particular, Rayleigh/Scholte waves on the sidewalls could interfere and form a S0-mode, also called a bar or rod wave. Our two main arguments within the manuscript to exclude the presence of this mode are:

1. The polarity of the observed wave which is opposite to the excitation and not expected by a S0 rod wave.
2. The strong positive positive velocity dispersion retrieved in the phase velocity analysis which is in opposition to the weak negative dispersion expected by a S0 rod-wave.

In addition, we ran a 2D finite element simulation for a linear elastic solid with wavespeeds and geometric dimensions as in the experiment (see Fig. 3.3.4). The P-wave velocity was set to 1500 meter/s and the S-wave velocity to 14 meter/s. In this medium, a classical soft solid, only one P-wave and the S-wave are present. As expected, the Rayleigh waves traveling on the surface radiate inwards. However, at the frequencies observed in elastography, they do not form a coherent wavefront parallel to the excitation plate and no S0-mode of the vertical boundaries is observed. Furthermore, they reach the region imaged by the ultrasound probe (0.08 m - 1.12 m) several milliseconds after the excitation. In contrast to that, the PII-wave in our experiment arrives directly after the PI-wave and no down-going waves coming from the top corners are observed. As a conclusion of this finite element simulation in an elastic incompressible medium, a standard elastic S0 mode (rod wave) has to be excluded.

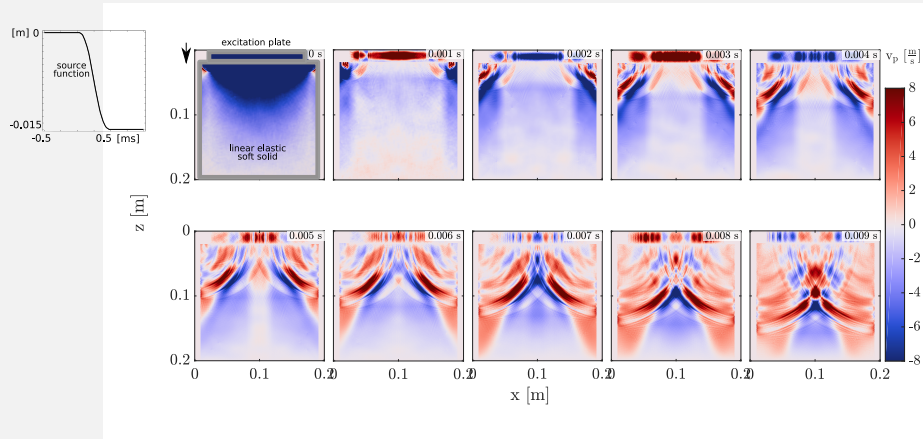


*Figure 3.3.4:* 2D finite element simulation using Comsol Multiphysics®. A solid plate is pushed downwards and coupled to a linear soft elastic medium. The source function is a ramp with a rise time of 1 ms. Blue color corresponds to negative particle velocity and signifies downwards particle movement.

For the shear wave excitation, surface waves do not pose a problem since the excited surface wave, a Rayleigh wave, travels nearly at the speed of the shear wave. Section 3.3.4 gives further proof because guided waves do not observe the dispersion relation.

### 3.3.3 Comparison to Biot theory

The elastic model for Eq. (3.14) cannot account for viscous dissipation. Consequently, we compare the measured dispersion with Biot theory (Biot, 1956c), as introduced in Section 3.2. The PII- and S-wave dispersion predictions result then from the coupling of fluid and solid. (Biot, 1956c; Biot, 1956b; Biot, 1962; Carcione, 2015; Vogelaar, 2009; Morency et al., 2008; Mavko et al., 2009; Allard et al., 2009). One drawback of the theory is that it requires nine porous and elastic parameters. While we use the measured porous and fluid parameters  $\phi = 0.99\%$ ,  $\alpha_\infty = 1.02$ ,  $k_0 = 1.276 \times 10^{-9} \text{ m}^2$ ,  $\rho = 8.8 \text{ kg m}^{-3} \pm 1 \text{ kg m}^{-3}$ ,  $BW = \phi$  (Biot-Willis coefficient),  $E_{fl} = 2.15 \times 10^9 \text{ kPa}$  (fluid Young's modulus) and fluid viscosity  $\eta_f = 0.0013 \text{ Pa s}$ , we rely on literature values for the elastic parameters. They range from 0.276 to 0.44 for the Poisson's ratio and from 30 to 400 kPa for the Young's modulus (Geebelen et al., 2007; Allard et al., 2009; Deverge et al., 2008; Ogam et al., 2011; Boeckx et al., 2005). Optimization by least-squares of the misfit of the experimental and theoretical speeds within the literature bounds gives the analytic dispersion for the S-wave and the PII-wave in Fig. 3.3.5. The resulting Poisson's ratio is 0.39 and the Young's modulus 303 kPa. However, the PII-wave is sensitive towards Poisson's ratio with a  $R^2$  of 0.783. In contrast to that, both waves behave similar with respect to changes in Young's modulus. A 10 % increase in Young's modulus results in a  $R^2$  of 0.975 for the S-wave curves and a  $R^2$  of 0.979 for the PII-wave curves. For a detailed sensitivity analysis see Appendix B. The analytic S-wave curve in Fig. 3.3.5 shows good agreement ( $R^2 = 0.808$ ) with the experimental values between 120 and 600 Hz. Below, wave guiding, present if the wavelength exceeds the dimension of particle motion (Royer et al., 1996), and not taken into account by Biot's infinite medium, might lower the measured speeds. The PII-wave measured and theoretical speeds exhibit the same trend but the Biot model overestimates the PII-speeds. Furthermore, it predicts that the PII-displacements of the solid and fluid constituent are of opposite sign while they are locked together for the PI-wave (Biot, 1956c; Geerits, 1996). This leads the PI and PII arrivals to be out-of-phase (Nakagawa et al., 2001; Bouzidi et al., 2009), which is confirmed by the time-space representation of Fig. 3.3.2b). Ultrasound imaging measures the solid displacement only, hence the solid displacement of PI (blue) and PII (red), are out-of-phase. The phase opposition of PI and PII (Nakagawa et al., 2001), and the measured positive PII-dispersion are a strong argument to exclude the possibility of a bar wave ( $S_0$ -mode) masking the PII-wave. It should be pointed out, that there is a crucial difference in the interpretation of the PII-wave between historic applications, laboratory detections (Plona, 1980; Nakagawa et al., 2001; Bouzidi et al., 2009), and this study. In geophysics and bone characterization, the PII-wave speed is close to that of the pore liquid and the PI-wave propagates at the speed of the rigid skeleton. In contrast to that, our results indicate that the speed of the PII-wave is governed by the weak frame of the foam and the PI-wave propagates at the speed of sound in

water. An equivalent interpretation was given by Smeulders (2005) for experiments in porous granular media (Paterson, 1956).

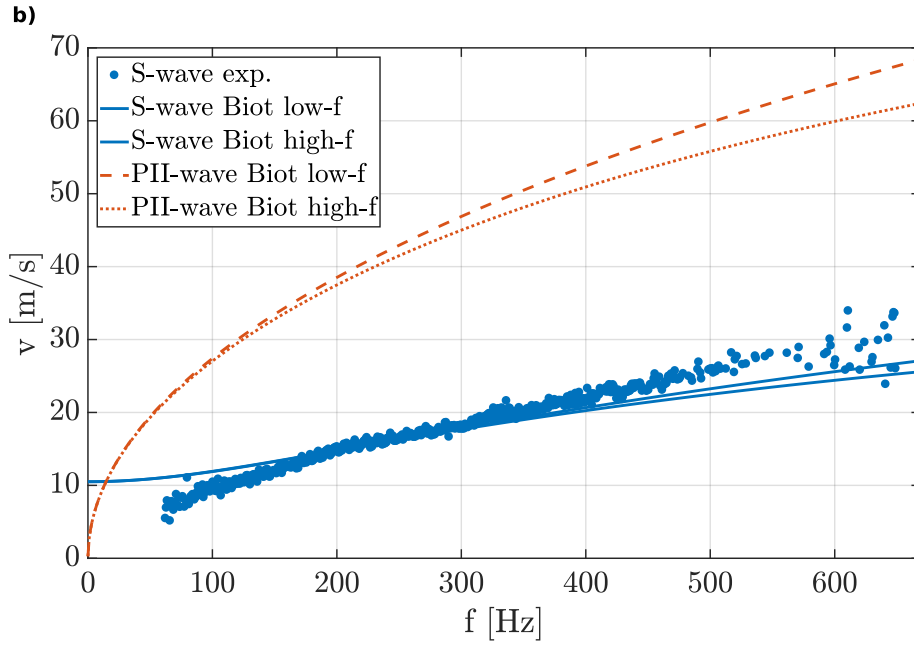


Figure 3.3.5: Experimental S-wave (blue dots) and analytic Biot S- (blue line) and PII-wave (red lines). The small difference between high frequency and low frequency approximations shows that the frequency dependence of the viscosity is negligible.

### 3.3.4 Attenuation & Kramers-Kronig

**Attenuation** To verify the dispersion results we compare them to attenuation, which for plane waves is described by (Catheline et al., 2004):

$$A(x + \Delta x) = A(x)e^{-\alpha(\omega)\Delta x}, \quad (3.15)$$

where  $\omega$  is angular frequency,  $\alpha(\omega)$  is attenuation coefficient,  $A$  is amplitude and  $x$  is measurement direction. The top left insert in Fig. 3.3.6 shows the logarithmic amplitude decrease with distance at one exemplary frequency of the S-wave. The bottom right insert shows the decrease at the central frequency of the PII-wave. The observed difference between these experimental curves and the expected linear decrease reflects the difficulties to conduct attenuation measurement by high frame rate ultrasound imaging (Catheline et al., 2004). We apply a logarithmic fit of the amplitude with distance to retrieve the attenuation coefficient at each frequency, using the RANSAC algorithm described earlier. The resulting attenuation, displayed in Fig. 3.3.6, monotonously increases with frequency.

**Kramers-Kronig** Attenuation and velocity of plane waves can be related through the bidirectional Kramers-Kronig (K-K) relations. They relate the real and imaginary part of any complex causal response function (Toll, 1956), which we use to verify our experimental results. While the original relations are integral functions that require a signal of infinite bandwidth, O'Donnell et al. (1981), Waters et al. (2003), and Waters et al. (2005) developed a derivative form that is applicable on band-limited data and has previously successfully been applied by Urban et al. (2009) on S-wave dispersion. Following Catheline et al. (2004) and Holm et al. (2014), the dispersion and attenuation in complex media is observed to follow a frequency power law:

$$\alpha(\omega) = \alpha_0 + \alpha_1 \omega^y \quad (3.16)$$

and can be related to velocity by (Waters et al., 2003; Waters et al., 2005):

$$\frac{1}{c(\omega)} - \frac{1}{c(\omega_0)} = \begin{cases} \alpha_1 \tan\left(\frac{\pi}{2}y\right)(\omega^{y-1} - \omega_0^{y-1}) & ; 0 \leq y \leq 2 \\ \frac{-2}{\pi} \alpha_1 \ln \frac{\omega}{\omega_0} & ; y = 1 \end{cases} \quad (3.17)$$

where  $\omega_0$  is a reference frequency,  $\alpha_1$  and  $y$  are fitting parameters and  $\alpha_0$  is an offset, typically observed in soft tissues (Szabo et al., 2000; Urban et al., 2009). Since velocity measurements by high frame rate ultrasound imaging are less error prone than attenuation measurements (Catheline et al., 2004), we use Equation 3.17 to predict attenuation from velocity. A least squares fit gives the exponent  $y$  and the attenuation constant  $\alpha_1$  that minimizes Equation 3.17 for different reference frequencies. The resulting attenuation model is  $\alpha(\omega) = 21 * \omega^{0.29}$  [Np m<sup>-1</sup>], with a reference frequency of 413 Hz and a  $R^2$  larger 0.98 for frequencies between 120 Hz and 650 Hz. In contrast to PI attenuation, which is commonly larger than one, the exponent  $y = 0.29$  is a typical value for S-waves in biological tissues (Nasholm et al., 2012; Holm et al., 2014). The K-K relations do not take into account the offset  $\alpha_0$ . It is introduced by minimizing the least squares of Equation 3.16 and the attenuation measurements. The resulting attenuation curve with  $\alpha_0 = -119$  Np m<sup>-1</sup> is displayed in Fig. 3.3.6. It shows a good agreement ( $R^2 = 0.9016$ ) with the measured attenuation and a very good agreement ( $R^2 = 0.9274$ ) with the calculated Biot attenuation. It follows from the successful K-K prediction and its causal nature, that guided waves do not significantly influence our measurements above 120 Hz. The remaining misfit might stem from out-of-plane particle motion, which can introduce an error on amplitude measures by high frame rate ultrasound imaging (Catheline et al., 2004). Furthermore, the low frequency elastic wave is imaged in the near-field, where the wave-field does not show a power law amplitude decrease due to the coupling of transverse and rotational particle motion (Sandrin, 2004). The good agreement between the experimental and theoretical S-wave dispersion and attenuation indicates that the

observed S-wave attenuation is due to the interaction between the solid and the viscous fluid. The PII-wave attenuation measurements of the three experimental realizations converge at the central frequency of 120 Hz only ( $\approx 16 \text{ Np m}^{-1}$ ). Below, the measurements are taken on less than two wavelengths of wave propagation and consequently, the exponential amplitude decrease cannot be assured (Sandrin, 2004). A reason for the failure of the Biot theory to quantitatively predict the observed PII-wave dispersion could be viscoelasticity and anisotropy of the foam matrix itself (Deverge et al., 2008; Melon et al., 1998). The Biot theory and the model of Equation 3.14 have different implications at low frequencies. The Biot PII-wave disappears, whereas it persists as a decoupled frame-borne wave in Eq. (3.14). While velocity and attenuation measurements at lower frequencies would be needed to make a definite statement, the results presented in Fig. 3.3.3 support a decoupling into a frame- and fluid-borne wave.

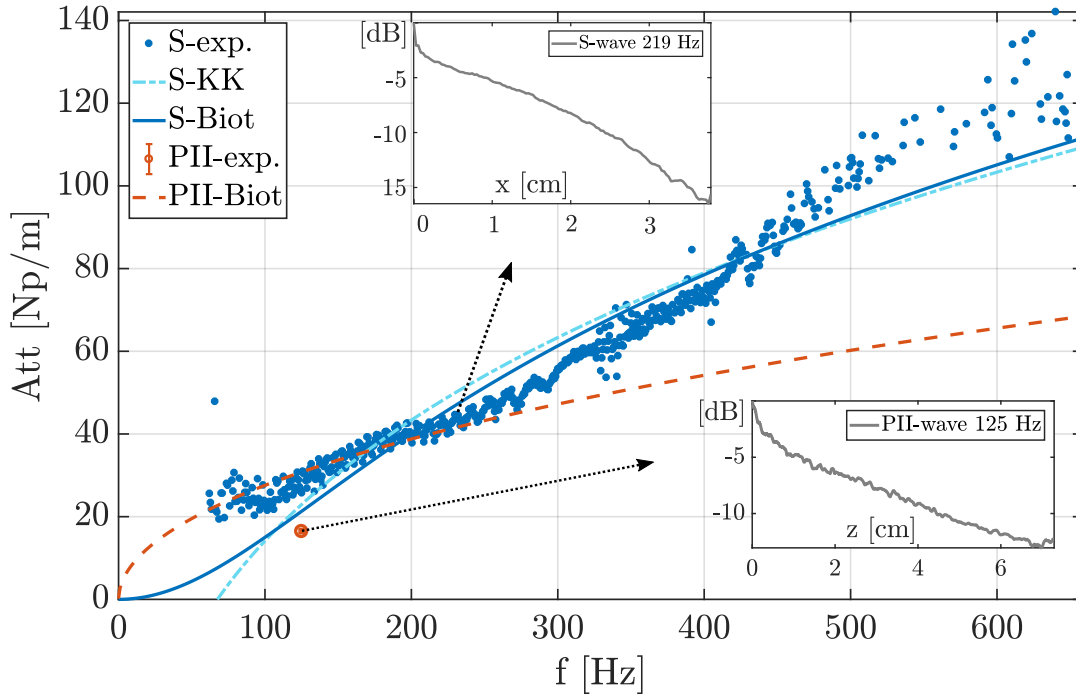


Figure 3.3.6: Attenuation measurements, K-K and Biot predictions. The inserts show the exemplary amplitude decrease of the S-wave (left) and PII-wave (right). Dots are attenuation measurements, solid blue and dashed red lines are the Biot predictions and the dashed blue line is the S-wave K-K prediction for Equation 3.16:  $\alpha(\omega) = -119 + 21 * \omega^{0.29} \text{ [Np m}^{-1}\text{]}$ .

### 3.3.5 Conclusion

In conclusion, we have shown the first direct observation of elastic wave propagation inside a poroelastic medium. The recorded compression wave of the second kind (PII-wave) propagates at  $\sqrt{2}$  times the shear wave speed and is of opposite polarization compared to the first compression wave (PI-wave). Finally, the measured shear wave

dispersion (S-wave) and attenuation are closely related to the pore-filling fluid. These results might have important consequences in medical physics for characterizing porous organs such as the lung or the liver.

### 3.4 Ex-vivo lung experiments

In order to get an idea about the wave propagation in an actual lung we performed experiments on two types of porcine lungs ex-vivo. First, we took an excised pig lung purchased from a butcher, immersed it in water and measured the elastic wave speed similar as in Section 3.3. Second, we took a conserved pig lung (ENasco, Fort Atkinson, WI) and studied the elastic wave propagation under different air pressure levels using an optical correlation method.

#### 3.4.1 Excised pig lung saturated in water

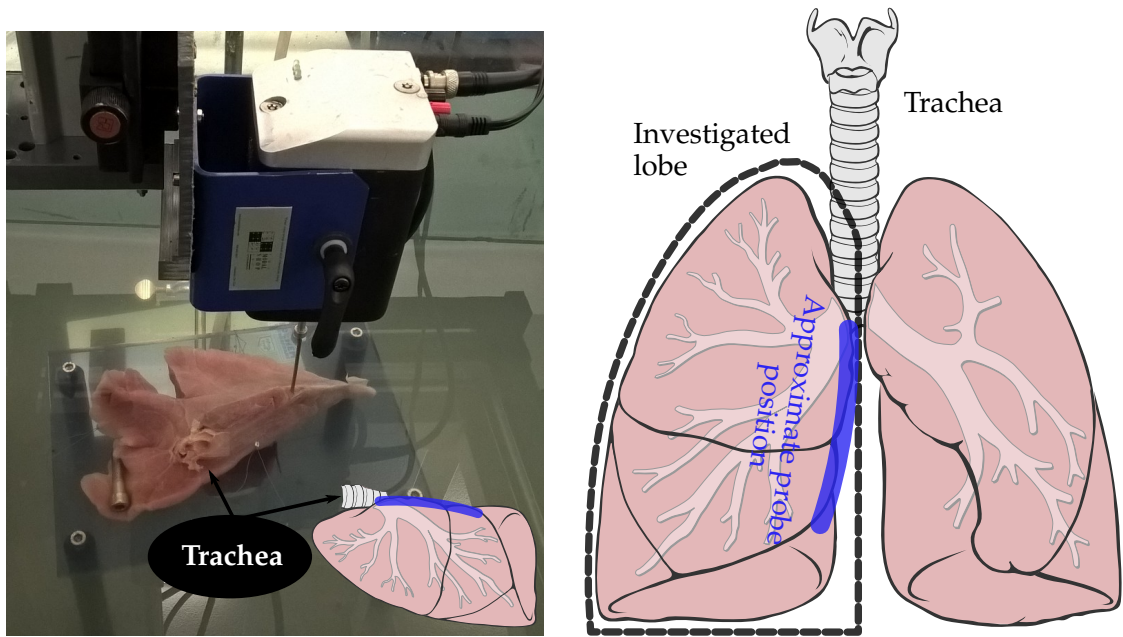
As a proof of concept we fully immersed a defrosted porcine lung in the water tank presented in Section 3.3.1. A photo of the lung and experimental setup is shown in Fig. 3.4.1a. Exemplary snapshots for wave propagation in the upper part of the lung are shown in Fig. 3.4.2. The investigation depth as well the image quality are worse than in the melamine foam. The porcine lung was much more difficult to degas than the melamine foam and the reminiscence of air bubbles worsens the ultrasound quality.

We performed two experiments at difference excitation frequencies. The velocity dispersion for a low frequency sweep from 10 to 500 Hz is displayed by the blue markers in Fig. 3.4.3. A monochromatic excitation at 500 Hz is represented by red markers in the same figure. The geometry of the lung might introduce various effects such as wave guiding and reflections. While the datasets expose the least error in the frequency range induced by the piston, frequencies beyond the range of the source excitation are excited in both experiments. The two experiments expose the same trend, increasing from values around  $1 \text{ m s}^{-1}$  to more than  $15 \text{ m s}^{-1}$  at 500 Hz. The difference in phase velocity of the two sets might stem from the different geometry, difference in remaining air content or different elastic properties of the ex-vivo lung tissue.

Fig. 3.4.1a shows that the ex-vivo lung exposes a complex geometry. The lobes on the side thin out to less than 1 cm, while the central part is a few centimeters thick. Due to this complex geometry, guided waves and modes are highly likely to be present.

---

<sup>1</sup>Medical illustrator, CC BY 2.5, <https://commons.wikimedia.org/w/index.php?curid=1496628>



a: Photo showing the experimental setup for the water-saturated ex-vivo pig lung. The entry of the trachea into the lung tissue is clearly visible. Note that the water-saturated lung takes less volume than the schematic drawing of an in-vivo lung on the right suggests. Consequently, the excised lobe is thinner than an air-inflated lung would be.

b: Schematic drawing of the lung. The investigated lobe (black dashed line) and the approximate investigation zone (blue straight line) are indicated. Adapted from Patrick J. Lynch, medical illustrator - Patrick J. Lynch<sup>1</sup>

Figure 3.4.1: Setup for the water-saturated ex-vivo porcine lung.

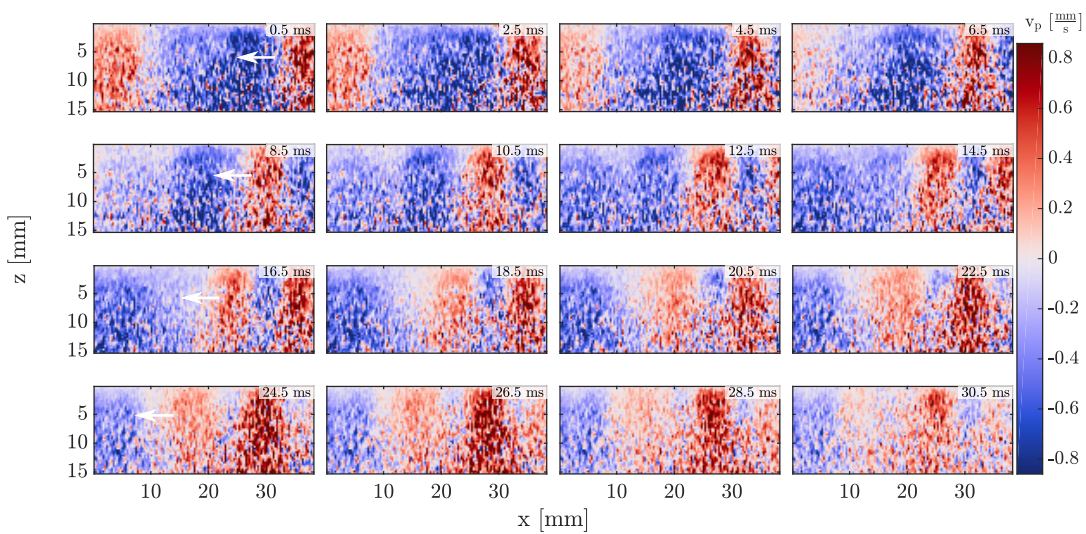


Figure 3.4.2: Snapshots for the wave propagation in the upper part of the ex-vivo pig lung. Note the time of flight of the waves propagating at the lung surface indicated by the white arrows is less than  $1 \text{ m s}^{-1}$ .



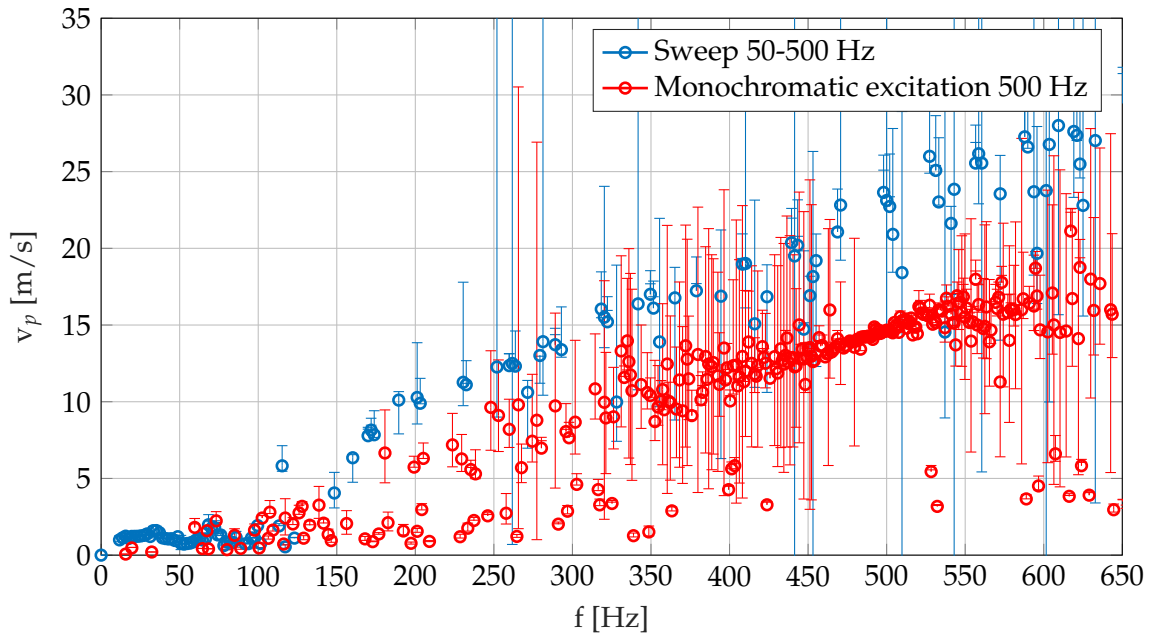


Figure 3.4.3: Phase speed measurements for two experiments in the water-saturated ex-vivo porcine lung. Red markers represent a monochromatic source excitation at 500 Hz. Blue markers represent a low frequency sweep from 10 to 500 Hz. The error associated with each data point is indicated<sup>a</sup>.

<sup>a</sup>The maximum error indicated by the error bars is estimated from the difference of the Ransac linear fit and a simple linear fit along the whole ultrasound probe length.



### 3.4.2 Conserved pig lung in air

For the second ex-vivo experiment we purchased a preserved pig lung (ENasco, Fort Atkinson, WI, USA). It is connected to an artificial ventilation device to control the pressure inside the lung. Imaging is undertaken with a high-frame rate optical camera (Chronos 1.4, Krontech, Burnaby, BC, Canada). Fig. 3.4.4 shows exemplary snapshots of the lung surface for each experiment. The elastic wave-field is retrieved analogous to the previously presented ultrasound phase correlation. The ultrasonic speckle is replaced by the optical speckle, but the same phase correlation algorithm as presented in Section 2.3 is used to retrieve the particle velocity maps.

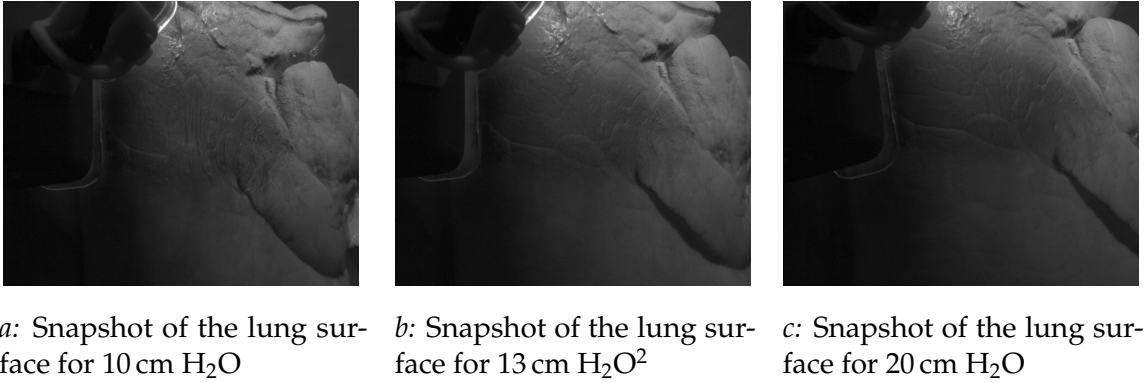


*Figure 3.4.4:* Exemplary snapshots for the inflated conserved ex-vivo lung.

No secondary compression wave is observed in the wave propagation film. This is in accordance with Dai et al. (2014b), who did not measure a slow wave on freshly excised and blood drained pig lungs<sup>3</sup>. The coupling of the fluid and solid phase at low frequencies is expected to be weak, suggesting a decoupling into a frame and fluid-borne wave (Bardot et al., 1996). Bardot et al. (1996) further present a case of air-saturation, where at low frequencies a mixing of these two waves leaves the frame nearly motionless. In this case, no slow wave can be observed by our optical method, which relies on the frame motion, either.

The phase velocities of the retrieved frequencies for different air pressures are displayed in Fig. 3.4.6. The comparison of the three curves for different air pressures indicates that the wavespeed of the lung frame is strongly depending on the inflation of the lung. The more the lung is inflated, the faster the measured wave speeds. One possible explanation is that the inflation of the lung results in an extension and thus stiffening of the lung matrix. Consequently the elastic modulus and the shear wave speed would increase with inflation. Furthermore, the peak at 140 Hz in Fig. 3.4.6a indicates the presence of a mode or resonance. Fig. 3.4.5 shows the amplitude measurements retrieved in the same way as presented in Section 3.3.4. In comparison to

<sup>2</sup>Pressure unit used in clinical applications. 1 cmH<sub>2</sub>O is the equivalent of 98.01 Pa.

<sup>3</sup>They relied on a one point measurement, using a laser Doppler vibrometer

the phase velocity measurements, only a few frequencies expose a reliable RANSAC fit which is reflected in the scarcity of measures displayed in Fig. 3.4.5. The poor quality of the logarithmic attenuation fits indicate that the amplitude decrease does not follow a power law. The present amplitude decrease could be explained if the observed waves were guided waves and not shear body waves. The velocity differences for different air pressures would then depend on the effective plate thickness for a Lamb mode, which might change with pressure. Furthermore, geometric effects of the not perfectly homogeneous lung surface (see Fig. 3.4.4) could also change with pressure. I hypothesize that the observed changes in velocity with inflation result from a combination of stiffening of the matrix and changing effective plate thickness on the thinner parts of the lung.

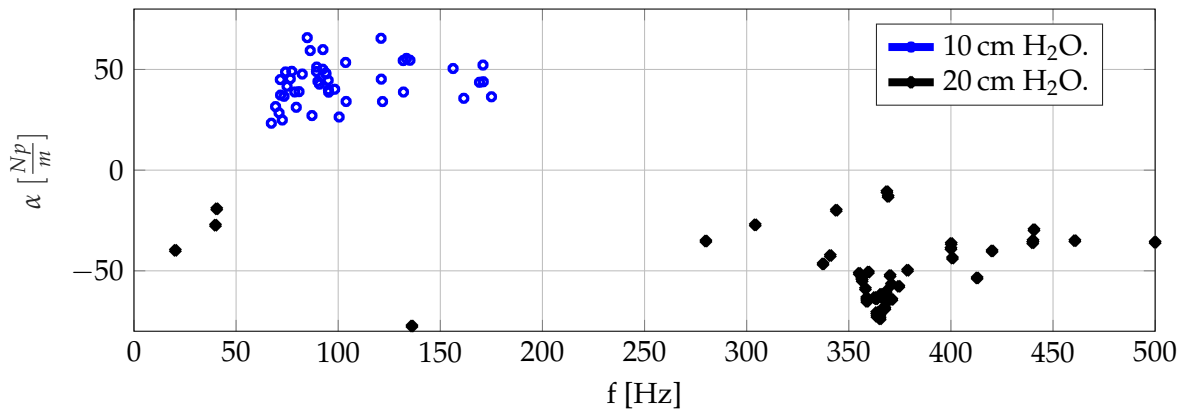
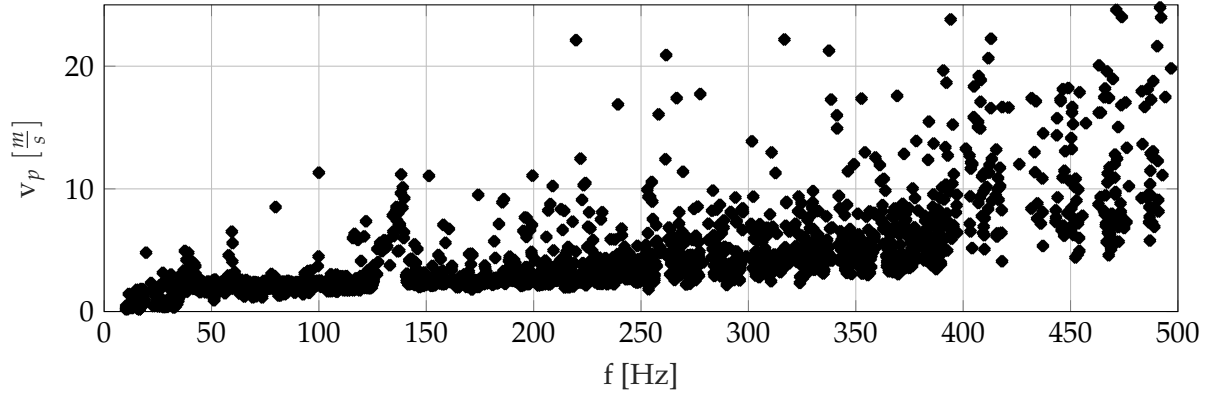
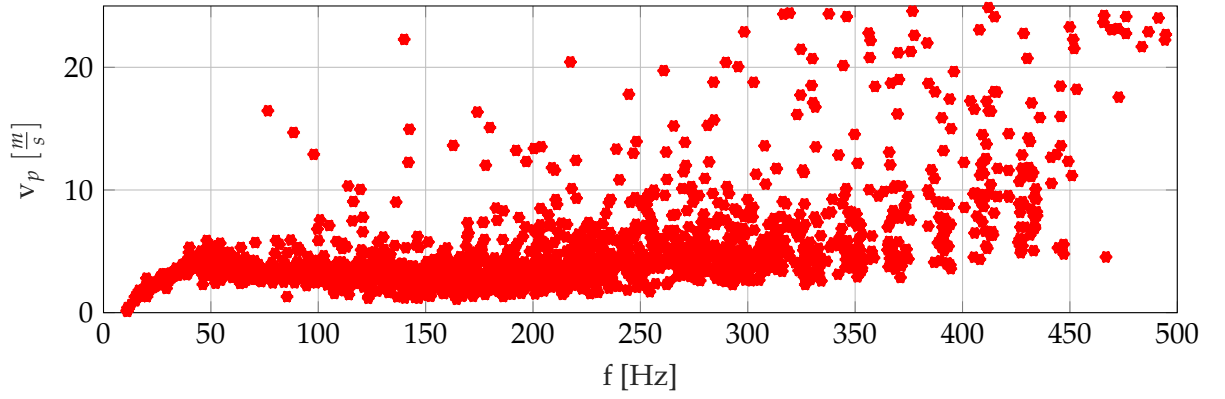


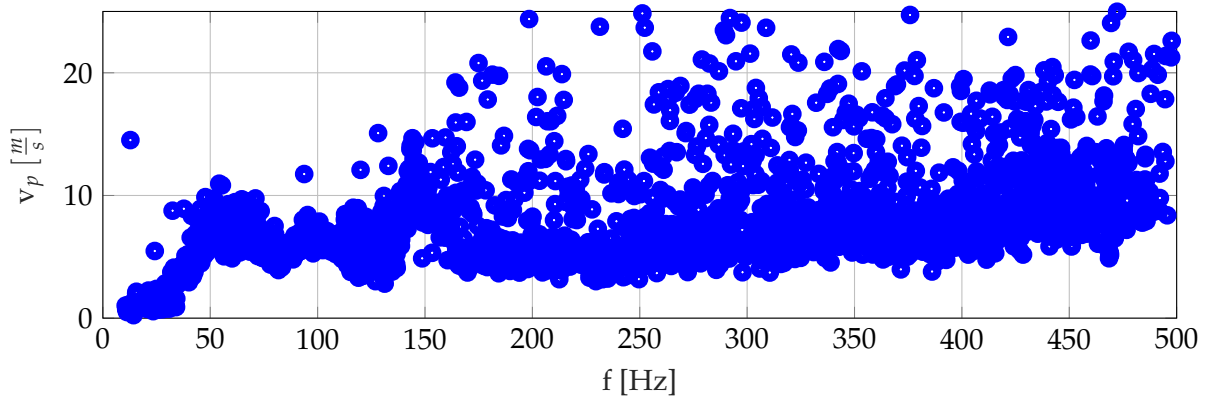
Figure 3.4.5: Attenuation against frequency for 10 and 20 cm  $\text{H}_2\text{O}$ . At 13 cm  $\text{H}_2\text{O}$ , the  $R^2$  did not exceed the cut-off value of 0.95 or less than 60 % of measurement points were used for the RANSAC linear fit.



a: Dispersion for 10 cm H<sub>2</sub>O.



b: Dispersion for 13 cm H<sub>2</sub>O



c: Dispersion for 20 cm H<sub>2</sub>O.

Figure 3.4.6: Dispersion results for the inflated conserved ex-vivo lung

### 3.4.2.a Comparison to Biot theory

Figure 3.4.7 shows the results of classical Biot theory for the Melamine foam filled by air. As in the water filled model, the slower compression wave is highly dispersive. Again, the faster compression wave travels close to the speed of the pore-filling fluid. In the water-saturated experiment that was the speed of sound in water. Now, the fast compression wave speed is close the the speed of sound in air. There is one qualitative difference though. The solution for the primary compression wave, which resulted in the fast wave before, now gives the solution of the slower wave. The secondary compression wave is thus in this case the faster wave. Hence, the terms primary and secondary wave are more suited than fast and slow wave for general cases<sup>4</sup>. The shear wave is predicted to be nearly non-dispersive at more than 100 m s<sup>-1</sup>, much faster than in the water-saturated foam. This confirms that the shear wave speed is strongly influenced by the pore-filling fluid, due to inertial and viscous effects. The median elastic modulus of healthy lung tissue is expected to be lower than that of the foam with  $E = 0.14$  kPa and  $\mu = 0.5$  kPa (Liu et al., 2011), which could explain why we measure much lower wave speeds in Section 3.4.2.

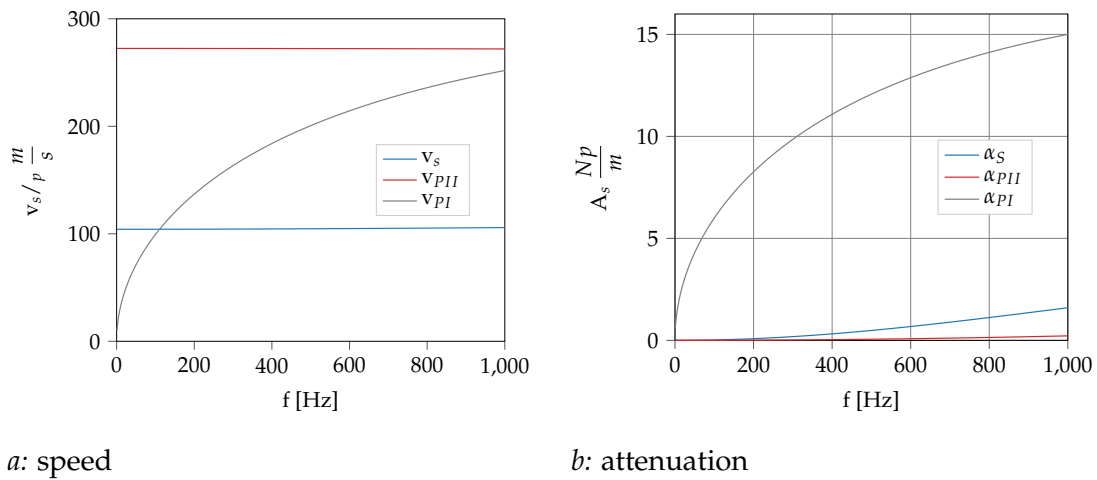


Figure 3.4.7: Biot theory dispersion curves for the melamine foam of Section 3.3 saturated by air.

It should be noted that a purely poro-elastic model, while sufficient for water-filled pores, is not well suited to model the velocity dispersion for the air-filled foam or the lung. At the high compressibility of air, heat exchanges should be included. This can be done by implementing the Champoux et al. (1991) model as indicated in Bardot et al. (1996). Nevertheless, the poro-elastic model gives a first approximation, guiding the interpretation of our preliminary experiments. For accurate description of an in-vivo lung, a mixture theory is probably needed, since blood, vessels, a wet layer surrounding the lung (pleura) and air-filled pores are present in a healthy lung.

<sup>4</sup>Primary and secondary are also the terms chosen by Biot in his 1956 paper

### 3.5 The possible role of fluid viscosity in clinical applications

This section is highly speculative and presents some thought experiments that investigate the possible implications of our results on future studies and clinical applications.

#### 3.5.1 Lung elasticity investigation

Many pulmonary diseases, e.g., Bronchiectasis and pulmonary obstructive disease affect the elastic properties of the lung airways (Williamson et al., 2011). Fibrotic lung tissue has been shown to be exposed to a three-fold increased average elastance<sup>5</sup> compared to healthy tissue (Dolhnikoff et al., 1999). Locally this value can go up to 30 times the median value of healthy tissue (Liu et al., 2011). Optical coherence tomography has been suggested for invasive analysis of pulmonary tissue by Williamson et al. (2011). Quirk et al. (2011) found that using a saline solution to saturate the pulmonary tissue increased the image quality of the optical coherence tomography. Using a saline solution to locally flush the lung is also a clinically established practice in bronchoalveolar lavage and used to test for interstitial lung disease (Meyer et al., 2012; Boccon-Gibod et al., 1997). Another clinical practice which involves saturation of the lung is whole lung flushing (Wasserman et al., 1968), where one entire lung is flushed with a saline solution for therapeutical applications.

Ultrasound elastography might be an additional tool to access the elastic properties of saturated lung tissues. While it would not be non-invasive due to required flushing of the lung, it has the advantage that employment of an invasive probe is not an a priori requirement. Our results show that the properties of the saturating fluid would need to be taken into account when interpreting the elastic properties of a highly porous medium such as the lung from wave speed measurements.

#### 3.5.2 Blood-rich organs

By comparing our experimental results in the melamine foam to Biot's theory we assumed Poiseuille flow of the fluid. Poiseuille was a physicist as well as a physiologist and the studies that led to his formulation of Poiseuille flow were motivated by the flow of blood through capillaries (Joseph-Léonard-Marie Poiseuille, 1835; Suter et al., 1993). It thus seems reasonable to investigate the influence of blood viscosity on elasticity in blood-rich organs. The most natural organ to inspect would be the liver. The liver is drawn through by a network of very narrow blood vessels. These vessels could be regarded as a network of connected pores and the liver thus be modeled as a poro-elastic medium. Furthermore, shear wave elastography in the liver is

---

<sup>5</sup>Elastance - inverse of lung compliance, is a clinical measure describes the ability of lung tissue to expand. It is measured in cm H<sub>2</sub>O/mL and describes thus a change of Volume induced by a pressure change.

an established clinical practice and the FibroScan™ device (Echosens, Paris, France) for liver elasticity estimation was the first commercialized application of shear wave elastography. Another blood-rich porous organ is the spleen, for which in-vivo elastography measurements have recently been reported (Pawluś et al., 2016; Stefanescu et al., 2011).

Blood is a non-Newtonian fluid, that exposes a stress dependent viscosity. However, even under the approximation of a Newtonian fluid, blood viscosity is highly variable. It varies significantly between patients as well as for a single individual depending on different factors, such as fitness, hydration and medicament taken. Furthermore, it is sensitive to different pathologies (Fedosov et al., 2011) like liver cirrhosis and non-alcoholic fatty liver disease (Yu et al., 2014; Jang et al., 2016). Rand et al. (1963) give viscosity values for human blood ranging from approximately 3 to 60 mPa s. Hence, it is worthwhile to investigate the role of blood viscosity on shear wave dispersion in the liver. In the following thought experiment we will take the available literature values for the porous, elastic and fluid parameters of the liver and analyze the dependency of the shear wave speed dispersion on these parameters. Our sensitivity measure will be the simple difference of the shear wave speed calculated by Biot theory at 500 Hz and 50 Hz.

**Literature values** The principal parameters of interest are porosity  $\phi$ , permeability  $\kappa$ , blood viscosity  $\eta$  and Young's modulus  $E$ . Care has to be taken about the actual meaning of each reported value. The porosity of interest is that of the *open* pores, e.i., the pores which allow an exchange of fluid. Because the liver is a complex organ, classification is not evident. While the major blood vessels can safely be assumed as open pores, each capillary vessel is a semi-permeable membrane and a simple classification in open and closed is futile. For example, the sinusoidal liver porosity is reported as low as 12 % (Smye et al., 2007) and the decellularized<sup>6</sup> porosity of both spleen and liver as high as 80 % (Xiang et al., 2015). Peeters et al. (2015) model a healthy liver with 14.3 % and a cirrhotic liver with 24.6 % sinusoidal porosity. The permeability defies a simple expression even more. In clinical research the term permeability does not have the same significance as in Darcy or Biot theory<sup>7</sup>. We thus limit our thought experiment to the reported permeability values in Darcy's sense, i.e., expressed in square meter. However, the permeability in a complex organ such as the lung is far from being as isotropic and homogeneous as in our foam model. For example, permeability in the portal vein parallel to blood flow differs significantly from that across the hepatic sinusoids. Even for the sinusoidal permeability alone Debbaut et al., 2012; Debbaut et al., 2014 use a permeability tensor.

Table 3.1 lists the values for the porous liver parameters and their sources that we use in the thought experiment. The author is no physician and does not presume

<sup>6</sup>Decellulaization - Isolating the extracellular matrix and small blood vessels from the organ

the list to be exhaustive, but for the intended thought experiment the values are sufficient. The very high permeability values of the portal vein are excluded from the sensitivity analysis because they represent a very localized characteristic. However, it should be noted that in Biot's model very high ( $\gtrsim 10 \times 10^{-8} \text{ m}^2$ ) as well as very low permeability ( $\lesssim 10 \times 10^{-11} \text{ m}^2$ ) results in shear wave dispersion which is independent of blood viscosity.

Since the aim of this thought experiment is to investigate if porous theory would have a measurable influence on elasticity estimates from shear wave measurements, and by no means do an exact calculation, we assume an isotropic, homogeneous material.

**Theoretical poro-elastic liver dispersion** The sensitivity analysis shows that the shear wave speed as predicted by Biot theory is sensitive to porosity, permeability and blood viscosity. The first two are parameters that are eligible to alteration by illnesses, e.g., cirrhosis (Peeters et al., 2015). The most important influential factor in the large range that was given is permeability. This is not surprising for the several orders of magnitude the literature values span. It is however interesting, that it exposes a high total order component<sup>8</sup>, indicating that it is interacting notably with the viscosity, the second most influential factor. The dependence of the shear wave speed on viscosity is thus not a simple linear one, but depends on the combined changes of permeability and viscosity. The maximum wave speed difference of all 60 000 calculations from the Sensitivity Analysis is  $0.26 \text{ m s}^{-1}$ . This might not seem a large value, but represents about 10 % of the shear wave speed at the higher frequency. Blood viscosity is a highly variable factor, even for healthy patients. It is thus interesting to compare the dispersion curves of a liver with the parameters that give the highest deviation in the sensitivity analysis and the end members of the viscosity range. Fig. 3.5.1b depicts the shear wave dispersion curves for the lowest and highest viscosity given by Rand et al. (1963)<sup>9</sup>. Fig. 3.5.1b shows, that while very low and higher frequencies expose similar velocity values, the shape of the dispersion curve highly depends on the chosen viscosity. This is significant, because the frequency range where the variation is highest is exactly the frequency range investigated in shear wave elastography. The parameter values resulting in the dispersion curves of Fig. 3.5.1b are close to the values given by White et al. (2016). We thus conclude from our thought experiment that poro-elasticity might play a measurable role for the shear wave dispersion in the liver. Here we tested a purely

<sup>7</sup>The U.S. national library defines capillary permeability as: *The property of blood capillary Endothelium that allows for the selective exchange of substances between the blood and surrounding tissues and through membranous barriers such as the Blood-air barrier; blood-aqueous barrier; blood-brain barrier; blood-nerve barrier; blood-retinal barrier; and blood-testis barrier.* - <https://meshb.nlm.nih.gov/record/ui?name=VASCULAR%20PERMEABILITY>

<sup>8</sup>For details on the type of sensitivity analysis employed, see Appendix B.

<sup>9</sup>Measured ex-vivo. Similar values are reported by Jang et al. (2016) for in-vivo measurements.

Table 3.1: Literature values for the poro-elastatic parameters of the liver.  $\phi$  is porosity,  $\kappa$  is permeability,  $\eta$  is viscosity,  $\alpha$  is tortuosity,  $E$  is Young's modulus and  $\nu$  is Poisson's ratio.

Source	Type	$\phi$ [%]	$\kappa$ [m <sup>2</sup> ]	$\eta$ [Pa s]	$\alpha$ []	$E$ [Pa]	$\nu$ []
White et al. (2016)	Tissue	29.8	$1.4 - 2.5 \times 10^{-9}$	$3.5 \times 10^{-3}$			
White et al. (2016)	Vascular		$5.9 \times 10^{-9}$				
Rattanadecho et al. (2013)	Vascular	60 - 70	$7.7 \times 10^{-11} - 2.2 \times 10^{-10}$				
Debbaut et al. (2012)	3D Sinusoidal	14.3	$7.0 \times 10^{-16} - 1.1 \times 10^{-14}$				
Peeters et al. (2015)	3D Sinusoidal Cirrhotic	24.6	$1.1 \times 10^{-14} - 7.7 \times 10^{-13}$				
Bonfiglio et al. (2010)	2D Sinusoidal	12	$7.0 \times 10^{-16} - 3.3 \times 10^{-13}$	$4.0 \times 10^{-3}$		1230 <sup>a</sup>	0.43 - 0.47 <sup>b</sup>
Komatsu et al. (1990)	Sinusoidal (rat)				1.04 - 1.11		
Jang et al. (2016)	Fibroscan			$3.3 \times 10^{-3} - 2.2 \times 10^{-2}$		2669 - 76497	
Meyer (2013)	Portal Vein		$5.5 \times 10^{-5} - 1.3 \times 10^{-3c}$				
Rand et al. (1963)	Hematocrit 20 - 80 <sup>d</sup>			$3.9 \times 10^{-3} - 5.3 \times 10^{-2}$			
Sensitivity Analysis	Author's choice	0.12 - 0.3	$7 \times 10^{-16} - 9 \times 10^{-9}$	$3.3 \times 10^{-3} - 5.3 \times 10^{-2}$	1.04 - 1.11	20 000	0.3 - 0.49

<sup>a</sup>Based on Chui et al. (2004)

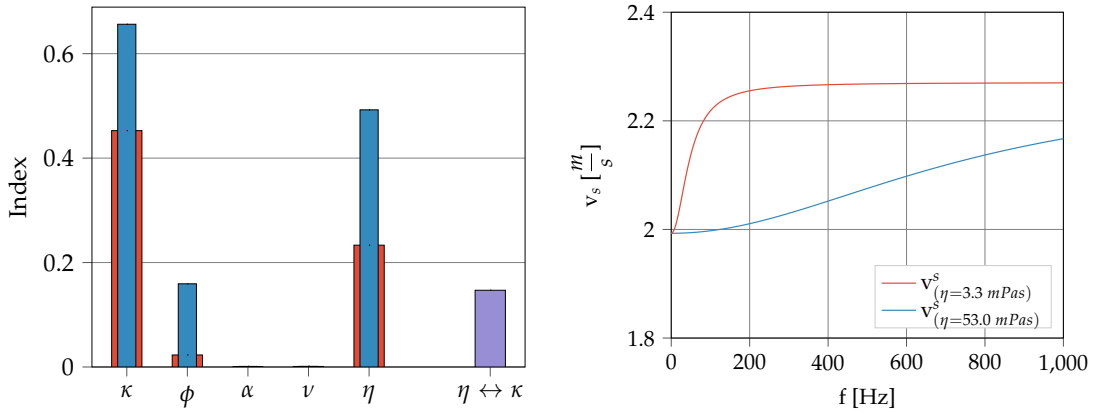
<sup>b</sup>Based on Chui et al. (2004), who measured in pig livers. Note that the Poisson's ratio employed in our calculations is a property of the frame. It might this be slightly different from Chui's.

<sup>c</sup>Calculated from flow speed and geometry in Meyer (2013) using Darcy's law.

<sup>d</sup>Represents the extreme values of Hematocrit for human blood



poro-elastic model. Previous studies, e.g., Muller et al. (2009), Tang et al. (2015), Nightingale et al. (2015), and Barry et al. (2012), focused on modeling the liver as a visco-elastic tissue. However, the purely visco-elastic models used have not shown conclusive agreement with the measured variety of shear wave dispersion. For the future, we suggest to combine visco-elasticity and poro-elasticity in a poro-visco-elastic model to test if the observed unexplained dispersion of the shear wave in the liver could be explained by poro-visco-elasticity. While a detailed liver model should incorporate anisotropy and heterogeneity comparing an isotropic, homogeneous poro-visco-elastic model with experimental results would be a worthwhile first step.



*a:* Sensitivity analysis for the liver literature values from Table 3.1.  $\phi$  is porosity,  $\kappa$  is permeability,  $\eta$  is viscosity,  $\alpha$  is tortuosity,  $E$  is Young's modulus and  $\nu$  is Poisson's ratio.  $\eta \leftrightarrow \kappa$  represents the interaction of viscosity and permeability. The sensitivity measure is the difference in shear wave speed at 50 and 500 Hz.

*b:* Theoretical dispersion curve for the poro-elastic shear wave. The parameter values are  $\kappa = 3.42 \times 10^{-9} \text{ m}^2$ ,  $\phi = 29.87$ ,  $\alpha = 1.04$ , and  $\nu = 3.44 \times 10^{-1}$ . The fluid viscosity  $\eta$  is indicated in mPa s.

Figure 3.5.1: Dispersion and sensitivity analysis for a liver modeled by Biot poro-elasticity.

## Chapter 4

# Laboratory rupture observation

### 4.1 Introduction

Frictional sliding and the onset of rupture govern a multitude of phenomena of interest for the natural and engineering sciences alike. The breaking of a car, sliding of a ski, lighting of a matchstick and movement of a joint are all examples of sliding friction. The scales relevant in frictional sliding range from the micro scale to the global scale. In Earth's sciences, friction is essential to the understanding of earthquake nucleation which can have global devastating consequences. For example, the 2004 tsunami in the Indian ocean, was created by an underwater earthquake and was responsible for more than 200,000 deaths. The deadly water wave was created by the displacement of the ocean during the earthquake. Similar to earthquake nucleation, friction also governs more localized geophysical phenomena such as landslides, avalanches and glacier break-offs.

From Leonardo da Vinci's tribology experiments (see Fig. 4.1.1) to today's high-resolution asperity models, our understanding of friction has deepened, but a thorough understanding of the underlying processes under laboratory conditions and thereupon in the field has yet to be gained. Through better understanding the laws that govern sliding friction and the onset of rupture, geophysicists can improve earthquake rupture models in the hope to ultimately be able to predict earthquake nucleation.

This work focuses on the elastic wave propagation associated with the onset of rupture and stick-slip motion. The elastic wave-field created by rupture propagation is of particular interest to seismologists, because they rely primarily on the elastic waves recorded on the Earth's surface to infer the location, strength and nucleation mechanism of earthquakes.

Geophysical field observations are nearly always limited to surface motion, which is a superposition of the elastic waves created during the complex rupture process. Furthermore, it depends on the media which the elastic waves are traveling through from the earthquake source position to the surface. Hence, the need for, computationally intensive, inverse modeling in seismology. In the inversion of real earthquake data, the aim is to retrieve the slip history causing the observed waveforms. It is

thus a kinematic approach. The slip itself however is an intrinsically dynamic process. It results from the physical laws governing the slip interface (the fault), and the surrounding rock. Earthquake mimicking laboratory experiments allow for investigating the physical processes at the small scale by controlling the material properties at work. However, the temporal and spatial scales that ultimately govern frictional processes defy most experimental techniques and linking them to the elastic wave radiation and ultimately ground motion is not a trivial task.

The present work tackles this challenge by using high frame rate ultrasound imaging as described in Chapter 2 to register the shear wave field resulting from the onset of rupture in situ, i.e., inside a 3D laboratory sample. The technique allows for an extremely dense array of virtual seismometers inside a sheared elastic material. The drawback of the method, the inability to use real rocks and thus reproduce field conditions in the lab, is compensated by the richness of the data, which in quality and resolution is only equaled by numerical simulations.

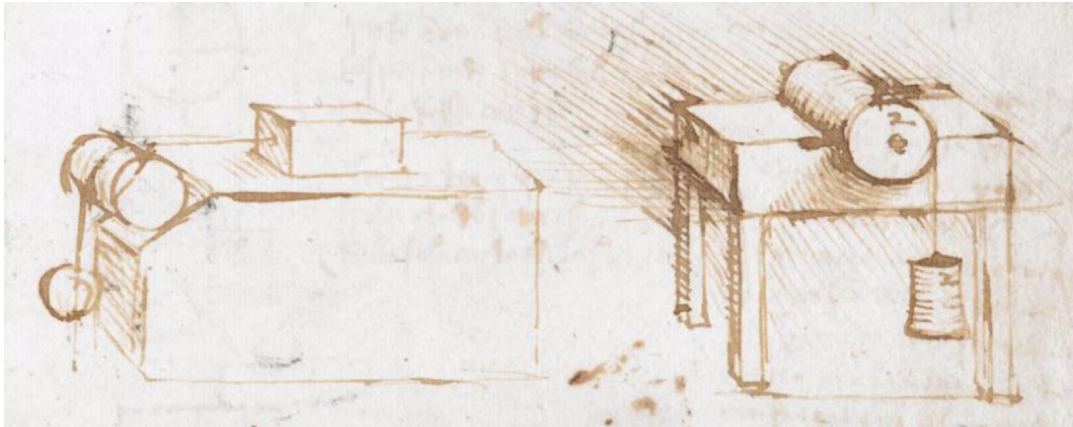


Figure 4.1.1: Sketch by Leonardo da Vinci which illustrates the experimental setup he designed. From Codex Arundel, British Library, London (Arundel folio 41r c. 1500–05)

## 4.2 Background

### 4.2.1 Historical studies - The friction coefficient

Friction has naturally been used by mankind for thousands of years. The neolithic use of firestones and the fire drill (128 000–30 000 B.C. ), arctic sledges (7000 B.C. ) and the Sumerian wheel (3500 B.C. ) are examples where the increase or decrease of frictional resistance is put to use (Feeny et al., 1997; Feeny et al., 1998). The realization that friction is a force opposing a moving body can at least be dated back to the central book of the Chinese Mohist school of thought, the *Mo Ching* or *Mo Zi* (5th–3rd century BC), and the collection of Aristotle's (4th century B.C. ) writings known as *Physics* (see e.g. Aristotle et al. (1936)) (Selin, 2016; Feeny et al., 1997; Feeny

et al., 1998). Themistius (4th century A.D. ) realizes that sliding friction is different from static friction (stiction): "For what is spherical moves easily, and those bodies which are least stable and have the smallest surface of contact are easily furthered in their motion. Generally it is easier to further the motion of a moving body than to move a body at rest" (Sambursky, 1962). A pioneer in experimental tribology as well as the formulation of friction laws is Leonardo Da Vinci. Through various sketches (see Fig. 4.1.1) and notes we know that from 1493 to 1515 he conceived various experimental setups and discovered the two fundamental friction laws named after Amontons (Amontons, 1699), who rediscovered them 200 years later.

- The friction force is directly proportional to the applied load.
- At the same load, the friction force is independent of the apparent area of contact.

These laws give the expression for the coefficient of friction

$$\mu = \frac{F_F}{F_N} \quad (4.1)$$

where  $F_F$  is the frictional force and  $F_N$  is the normal force.

Furthermore, Leonardo already recognized that the friction coefficient depends on the nature of the material although he mostly used a value of 0.25 in his calculations (Hutchings, 2016). Da Vinci, who wrote his notes in mirror mode, kept his discovery secret and it took until the works of Amontons (1699) and Coulomb (1781) for the friction laws to get published. Coulomb, motivated by naval applications, conducted experiments on wood and metal realizing that:

- For most materials, the friction coefficient is independent of the sliding velocity
- Friction arises from the engaging of the asperities of two surfaces *as the hairs of two brushes do* (Feeny et al., 1997) (see Fig. 4.2.1).

The first statement applies to dry friction between two idealized solids. It is different in the case of lubricated surfaces or wet friction. John Leslie notes that the asperities postulated by Coulomb get modified by a sliding body and friction should thus be seen as a time-dependent process (John Leslie, 1804). It took until the works of Bowden et al. (1939) for a physical explanation to be found for the Amontons-Coulomb friction laws. We have to look at the microscopic scale to realize that the real contact area is much smaller than the apparent contact area: 0.1 % for many materials (Rubinstein et al., 2009). Speaking in Coulomb's metaphor, only a few of the hairs of the brush are actually in contact and when the load gets increased, more hairs enter into contact. Under load, contacting asperities get deformed plastically and/or elastically. The pressure on single contacts can thus be much higher than the mean pressure on the apparent surface area. In contrast, increasing the apparent

surface area does not increase the actual contact area and the friction force stays constant.

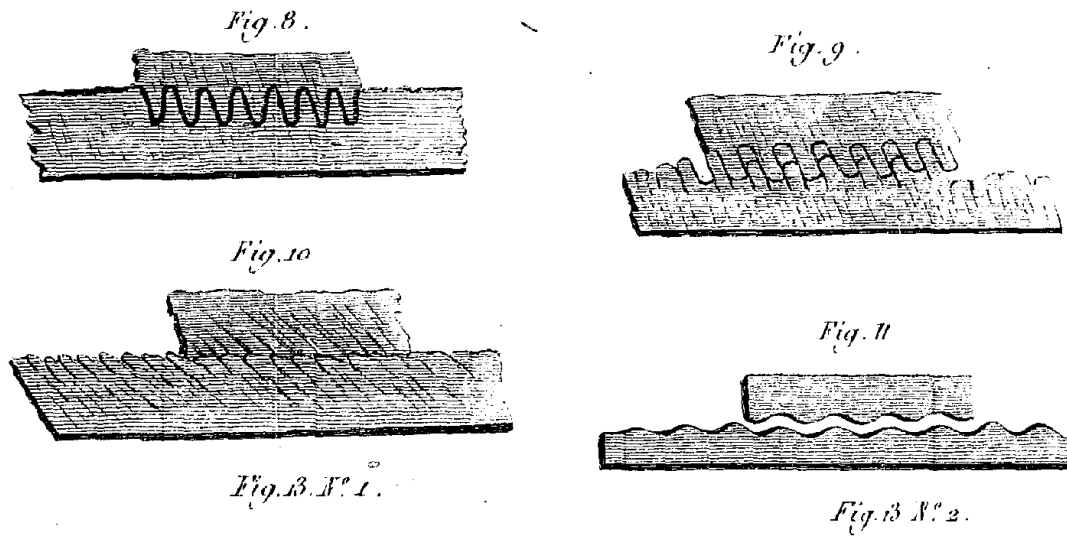


Figure 4.2.1: Sketch by Coulomb (1781), showing how he imagined the surfaces of two frictional bodies.

**Summary** Early friction studies led to the conclusion that friction is the force needed to resist a relative movement. It is a resulting, path-dependent, non-fundamental force and many empirical models exist to describe it. Historically, the friction coefficient is a material parameter characterizing the material frictional properties. It takes different values for a moving and a static body. Sliding of a body sets in when the ratio of shear stress to normal stress exceeds the static friction coefficient. During sliding, the friction coefficient holds a lower value: the kinetic friction coefficient.

## 4.2.2 Dynamic rupture observations - Laboratory earthquakes

The field of tribology spans various fields in physics and engineering and a complete review exceeds the scope of the present manuscript. We thus focus on experimental setups mimicking seismic events that are most relevant to our work. For further reading the reader is referred to the literature cited hereafter. A selection of reviews and books is given below <sup>1</sup>.

### 4.2.2.a Elastic rebound theory

The basis for much of the later work were the observations of the 1906 California earthquake that led Reid (1910) to define the elastic rebound theory: The elastic rock on both sides of a fault deforms until slip is initiated through strain release. The

<sup>1</sup>Marone (1998), Scholz (1998), Bizzarri (2011), TenCate (2011), and Rosakis et al. (2007), Ohnaka (2013), Kanamori et al. (2004), Rice (1980), Olsen et al. (2002), and Rosenau et al. (2017), Scholz (2002), Daub et al. (2010), Svetlizky et al. (2019), and Persson (2000)

result is a block displacement along the fault. For an example of such displacement along a fault line, see the satellite image in Fig. 4.2.2a of the Piqiang fault in China. Accumulated slip has displaced the two halves of a previously continuous mountain range by 3 km. Reid supported his rebound theory by laboratory experiments on stiff jelly mimicking the elastic rock. To a non-geologist jelly might seem the most unlikely analogue for rocks due to the ease at which it can be deformed. However, the pressure and temperature in the earth are high enough to deform rocks in analogue to the jelly. This becomes evident by looking at folds outcrops in mountainous regions, such as the one of the Chartreuse mountain in Fig. 4.2.2b. The limestone was originally sedimented flat and then deformed due to the stress-field of the the African-European continent collision that formed the alps. Now, Reid sheared his jelly parallel to a pre-cut fault plane (Zoback, 2006) as shown in the original sketches in Fig. 4.2.3. By drawing lines on the jelly before deformation, after deformation but before slip and after slip Reid was able to conclude that the total slip distance equaled the distortion distance of the deformation.



*a:* Satellite photo of the Piqiang fault (25.10.2018, China)<sup>2</sup>.



*b:* Example of rock deformation by a fold in the Chartreuse mountains, France (Creative Commons from [https://commons.wikimedia.org/wiki/File:%C3%89coutoux-La\\_Frette.jpg?uselang=fr](https://commons.wikimedia.org/wiki/File:%C3%89coutoux-La_Frette.jpg?uselang=fr)).

*Figure 4.2.2*

---

<sup>2</sup>retrieved from <https://landsatlook.usgs.gov/sentinel2/viewer/> on 14.07.2019 14 : 03 : 54 CEST

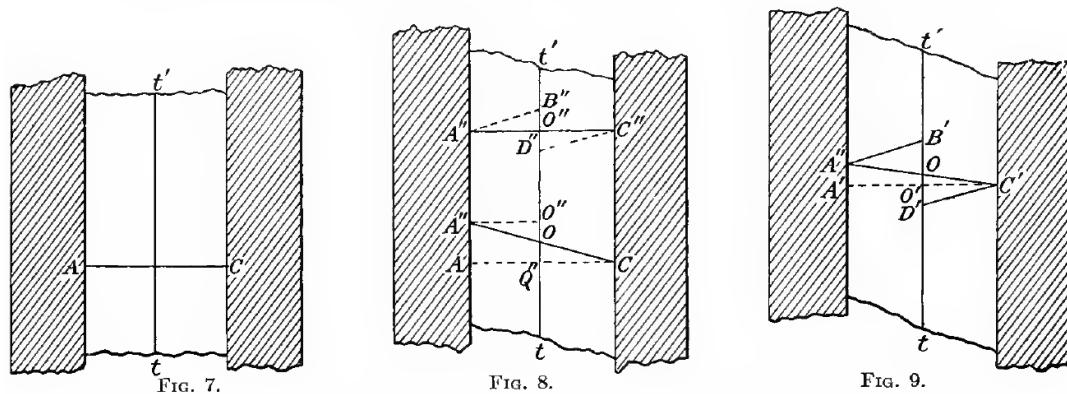


Figure 4.2.3: Original drawings from Reid (1910), showing schematically his experiments in jelly. Two pieces of wood hold the pre-cut jelly. The cut is along  $tt'$ . Left: The line  $AC$  was drawn on the jelly at rest. Middle: Under deformation, the line gets distorted into  $A''C''$ . After slip, the segments  $A''O$  and  $CO$  straighten to the lines  $A''O''$  and  $CQ''$ .  $A''O''C''$  is drawn after deformation but before slip. After slip, the line is broken into the segments  $A''B''$  and  $C''D''$ . Right:  $A'C'$  is drawn after distortion of the jelly but is then further distorted into  $A''C'$ . After slip and breaking of the segments the total slip distance  $D'B'$  equals the total distortion distance applied on the jelly by the wood.

#### 4.2.2.b Stick-slip

In laboratory experiments with rocks, frictional sliding often occurs through oscillation between a stick and a slip phase rather than a smooth sliding (Persson, 2000). Byerlee et al. (1966) were among the first to link stick-slip to earthquake mechanisms. Previous criticism of Reid's theory stated that sliding is unlikely in dry friction and fracture alone does not release sufficient energy. Byerlee et al. (1966) reason that energy release through stick-slip is at the origin of the observed wave radiation of earthquakes and in agreement with the elastic rebound theory.

**Stick-slip models: Springs, cracks and slip weakening** Burridge et al. (1967) introduced a simple spring slider model for stick-slip. The elastic body and the frictional contacts are separate entities connected by simple springs as depicted in Fig. 4.2.4. The model met some success, also because its predictions fit the famous Gutenberg-Richter law<sup>3</sup>, which nowadays has been shown to be a very robust property fitting a variety of different friction models (Persson, 2000).

As a result from granite shearing experiments Johnson et al. (1973) and Johnson et al. (1976) were the first to postulate that the transition from static friction to kinetic friction happens at a rupture front, similar to crack propagation in Linear Elastic Fracture Mechanics (LEFM - see Infobox 4.2 and Fig. 4.2.5). Dieterich (1972) and Dieterich (1978) experimentally found a time dependence of static friction suggesting

<sup>3</sup>The Gutenberg-Richter law relates the total number of earthquakes to their magnitude in geographical region.

a model in which the interface gets weakened during slip and strengthened or healed during stick. The initial model by Dieterich led Rice et al. (1983) to the formulation of the Dieterich-Ruina-Rice rate and state constitutive law that expresses friction as a function of rate and state variables (see Infobox 4.1).

Figure 4.2.4: 2D spring-block model of Burridge and Knopoff. The frictional contacts are connected to each other via springs (spring constant  $k_1$ ). The upper interface surface is connected to the frictional contacts by a second set of springs ( $k_2$ ).

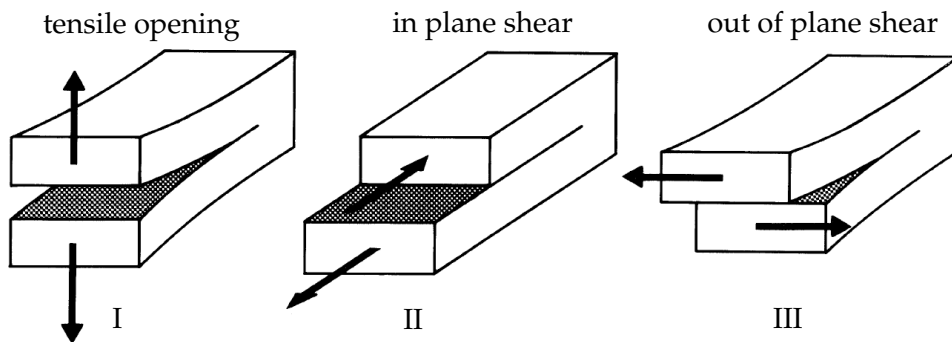
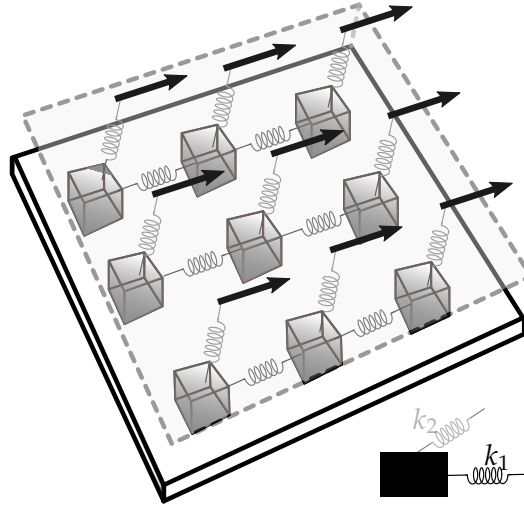


Figure 4.2.5: The three basic crack modes from LEFM. In seismology, only modes II and III are assumed, since mode I seems highly unlikely due to the high pressures inside the earth (Latour et al., 2011a). Figure created based on (Scholz, 1998)



**Infobox 4.1 Rate and state friction**

Rate and state friction models the shear strength depending on the sliding velocity and the time-dependant properties of frictional contacts. In the form of Dieterich-Ruina-Rice it is also called *slowness law*:

$$\tau = (\mu_0 + a \ln\left(\frac{V}{V_0}\right) + b \ln\left(\frac{V_0 \theta}{\mathcal{L}}\right)) \bar{\sigma} \quad (4.2)$$

$$\frac{d\theta}{dt} = 1 - \frac{\theta V}{\mathcal{L}} \quad (4.3)$$

The variables are slip velocity  $V$ , reference velocity  $V_0$ , critical slip distance  $\mathcal{L}$ , shear ( $\tau$ ) and effective normal ( $\bar{\sigma}$ ) stress, material parameters  $a$  and  $b$  and a state variable  $\theta$ , describing the time evolution (Scholz, 1998). The state variable  $\theta$  can be interpreted as the characteristic lifetime of the frictional contacts (Marone, 1998). The variable  $\mathcal{L}$  is the critical slip distance needed for the shear stress on the fault to reduce to a residual shear stress. In other words, if the patch on the fault slipping is smaller than  $\mathcal{L}$ , no stick-slip instability develops. Ohnaka (2004b) gives an estimation for about 1 m for a magnitude 8 earthquake. The larger the earthquake, the larger  $\mathcal{L}$ . The constitutive law shows, that the differentiation into a static and kinetic friction coefficient gets abandoned in favor of a continuum of friction values. Rate and state models have been successfully applied on various materials such as granite (Dieterich, 1978), PMMA (Baumberger et al., 1999) and granular fault gouge (Mair et al., 1999).

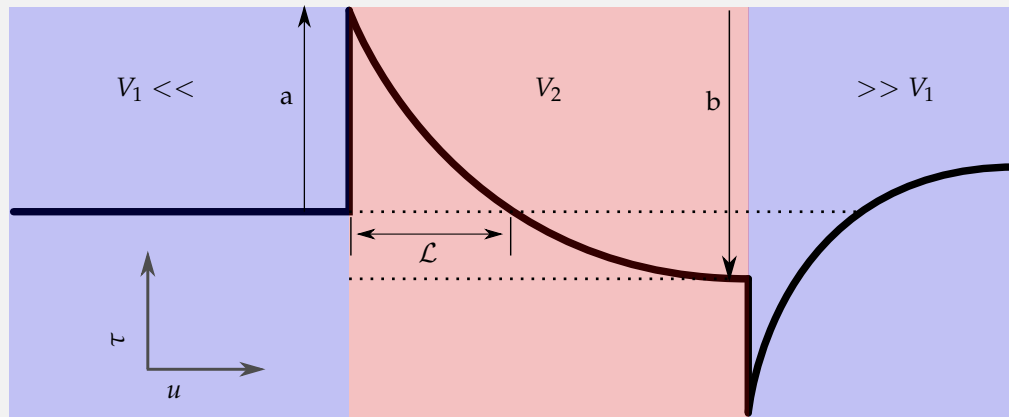


Figure 4.2.6: Schematic development of shear stress under rate and state friction for a sliding velocity  $V$  changing from slow  $V_1$  to fast  $V_2$  to slow. Figure modified after Scholz (2002).

**4.2.2.c Pulse-like propagation**

Schallamach (1971) were probably the first to observe, that besides uniform sliding, macroscopic displacement between two frictional bodies can also take the form of detachment waves. In their experiment of rubber on glass, the motion of the detachment wave is similar to a propagating wrinkle in a carpet (Andrews et al., 1997). Brune et al. (1991) and Brune et al. (1993) obtained similar detachment fronts during

stick-slip of foam rubber on foam rubber sliding. Weertman (1980) showed theoretically that for bimaterial interfaces unstable slip or a *localized group of fast moving dislocations* can exist under the Amontons-Coulomb friction law. Kinematic models, which assume that slip takes place in a short time after the passing of the rupture front, match seismological data well (Aki, 1968; Heaton, 1990). Based on his analysis of earthquake waveforms, Heaton (1990) speculated that moving dislocation models are successful because self-healing slip-pulses might be the process governing interface failure for earthquakes.

Figure 4.2.7: Distortion of the surface of a transparent rubber slab by a spherical slider. The initially regular, rectangular grid shows a distortion like the wrinkle in a carpet. Photo from Schallamach (1971).

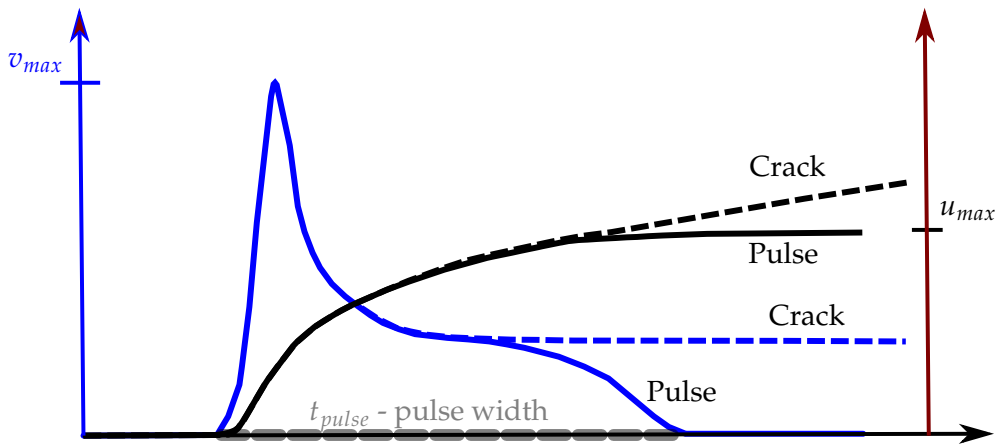
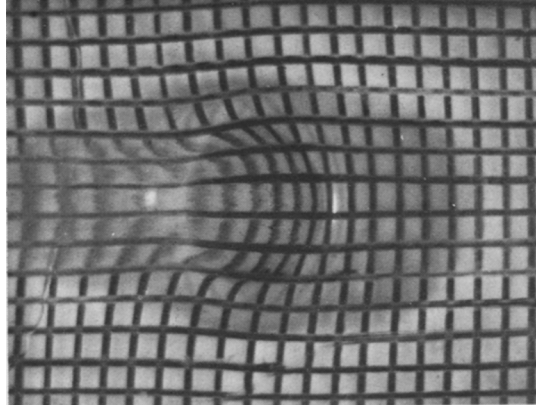


Figure 4.2.8: Displacement  $u$  and rupture velocity  $v$  against rupture time  $t$  for a crack-like and pulse-like rupture model. Modified from Bizzarri (2011)

#### 4.2.2.d Real contact area dynamics

Many friction studies assume either a perfect rigid body (Coulomb-Amontons) or an elastic body and rigid contacts (Burridge-Knopoff spring-block) during frictional sliding. However, both assumption are easily shown not to hold true in ice. In experiments where ice is sliding on a granite surface, it is observed that the ice itself deforms elastically (Persson, 2000). The interfacial strength is larger than the shear strength of ice and the stress required for stick-slip to set in is actually a measure of the material strength (Persson, 2000). Furthermore, small applied stresses

already lead to deformation of the frictional contacts, due to the high creep rate of ice (Persson, 2000). Thus, ice shows that the concept of a truly static friction coefficient is misleading. How do these findings relate interfaces without material contrast? Recent experiments by Ben-David et al. (2010) in PMMA (Plexiglass, acrylic glass) show that the local static friction coefficient at one asperity can far exceed the macroscopically measured friction coefficient without slip setting in. Furthermore, the macroscopic friction coefficient can vary with loading conditions. This leads to the conclusion that the ratio of shear and normal stress at which sliding sets in is not a pure material constant (Ben-David et al., 2011). If the rigid body assumption is not valid, simple one spring and slider models cannot be representative of rupture dynamics. In fact, the high resolution contact area measurements by Ben-David et al. (2010), Ben-David et al. (2011), and Rubinstein et al. (2004) (see Fig. 4.2.9) show that spatio-temporal dynamics are at play in frictional sliding. In this context, slip is not seen as the detachment of a whole sliding surface, but is nucleated at specific points in space and time followed by propagation as a rupture front. In homogeneous materials there are two types of consecutive rupture fronts. The first one does not traverse the entire interface, but gets arrested before. These arrested ruptures can precede a second type, a rupture that breaks the entire interface after which overall sliding sets in. It is the second type which releases the elastic energy stored in tectonically loaded rocks that causes the ground motion observed in the wake of earthquakes (Svetlizky et al., 2019).

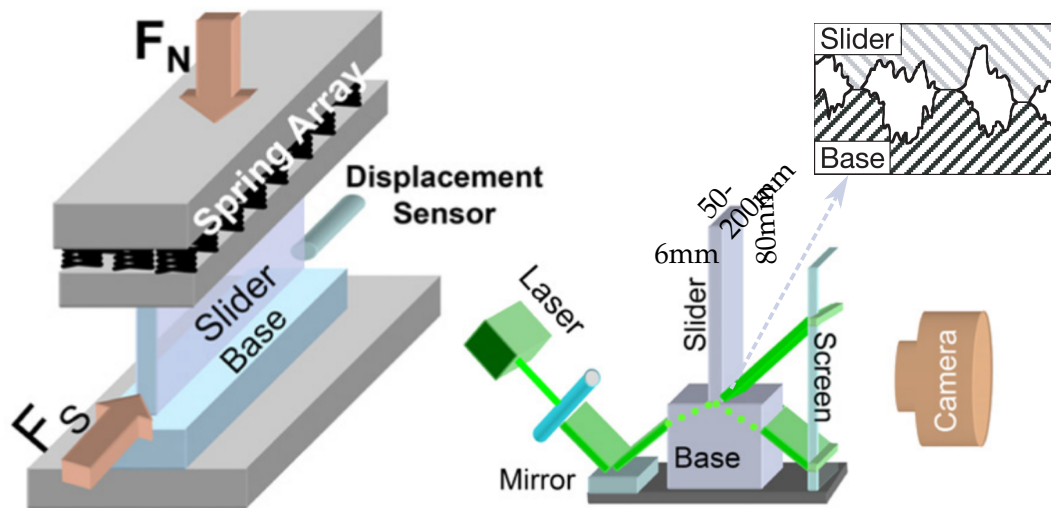


Figure 4.2.9: Setup of quasi-one-dimensional frictional contact area measurements by the group of Fineberg at the Racah Institute of Physics (e.g. (Shlomai et al., 2016; Svetlizky et al., 2019)). Adapted from Rubinstein et al. (2004) and Rubinstein et al. (2009)

**Infobox 4.2 Linear elastic fracture mechanics - LEFM**

Rupture propagation in homogeneous materials can be described through linear elastic fracture mechanics (LEFM), a continuum mechanics approach. In this context, rupture propagation is described by the propagation of a shear crack, where the crack is idealized as perfectly flat, cohesionless plane in a linear elastic medium. It has its basics in the work of Griffith (1921) who investigated the failure of steel during World War I. Realizing that brittle materials fail under stresses below the values of their atomic strength, he developed an energy criterion for an initial crack (a pre-existing material weakness) to extend. Crack propagation is sustained through external forces against the cohesive forces of the unbroken material and leads to an increase of the crack surface energy, while the mechanical energy of the material decreases (Scholz, 2002). Three basic modes describe the LEFM crack mechanism. Tensile opening (mode I), in-plane shear (mode II) and anti-plane shear (see Fig. 4.2.5) (Scholz, 2002). Under the assumptions of a plane, sharp, cohesionless interface, the stress and displacement find a simple analytic expression for which I refer the interested reader to Scholz (2002) p.10-12. The propagating crack has a stress singularity at the crack tip. Rupture propagation is sustained as long as the kinetic and elastic strain energy flux to the tip are sufficient to rupture the frictional contacts (exceeding the local friction coefficient) and create new crack surfaces (Xia et al., 2004; Rosakis et al., 1999).

It should be pointed out that the LEFM theory does not properly describe the crack tip in experiments with polyacrylamide gels. This is probably due to the nonlinear elastic behavior of gels at the crack tip (Livne et al., 2008; Boué et al., 2015). Since the hydrogels used in elastography expose similar properties as polyacrylamide gels, this probably holds true for the experiments in the present manuscript as well. LEFM has also faced criticism in terms of its applicability to real-world faults. In comparison to laboratory experiments they are heterogeneous and often show a bi-material contrast. Furthermore, the frictional interface of faults exhibit cohesive forces that vary along the interface. In the words of Ohnaka (2004b) "*no such unrealistic stress singularity*" exists, but a zone behind the rupture tip over which shear stress decreases. Dugdale (1960) and Barenblatt (1962) developed a cohesive zone model (CZM), in which cohesive forces are considered. When the two walls of the interface are pulled or sheared apart there is cohesive fracture zone in front of the crack tip, instead of a stress-singularity at the crack-tip.

**4.2.2.e Supershear rupture propagation**

**Theoretical prediction** In the LEFM context, the maximum crack propagation speed for a perfectly linear elastic material and crack mode III is the Rayleigh wave speed. Beyond, no energy would arrive at the tip because only shear stresses are present at the rupture tip (direction of propagation orthogonal to shearing). Ruptures propagating faster than this limiting Rayleigh wave speed have been predicted by Burridge (1973) and Andrews (1976) for mode II cracks. In their framework, an initial crack accelerates towards the Rayleigh wave speed and the rupture tip then nucleates a

secondary rupture at supershear speed. Furthermore, they showed that stable rupture speeds in fracture mechanics are either inferior to the Raleigh wave speed or superior to  $\sqrt{2}V_s$ , where  $V_s$  is the shear wave speed. Freund (1979) found that a mode II crack tip singularity in the intersonic range  $\sqrt{2}V_s < V_r < V_p$ <sup>4</sup> is only greater than the subsonic singularity for the speed  $\sqrt{2}V_s$ . The only stable intersonic rupture speed is thus  $\sqrt{2}V_s$ . Eshelby (1949) found the same limiting speeds for an edge dislocation moving at constant speed in an elastic isotropic material taking into account the atomic structure. The limiting velocity is the Rayleigh wave speed but an isolated solution for a supershear speed exists at  $\sqrt{2}V_s$ . However, it cannot be reached from sub-Rayleigh speeds. The existence of this singular solution is due to the fact that the moving dislocation is radiation free at this speed. For a supershear rupture moving at exactly that speed, the shear Mach cone would thus vanish (Mello et al., 2016).

**Experimental proof** Archuleta (1982) inferred possible supershear speeds for crustal earthquakes, but the existence of supershear ruptures remained a disputed question until the first experimental proof in the 1990s.

The first direct observation for supershear rupture on a bi-material interface without application of stress at the crack tip itself is reported by Rosakis et al. (1998). They use photo-elasticity and high-speed imaging to visualize a 2D rupture propagating faster than the shear wave speed of the softer material (see Fig. 4.2.10a). Using the same technique, Rosakis et al. (1999) show that supershear ruptures can be sustained in homogeneous materials as well. Following up on the insights from these laboratory experiments, Bouchon et al. (2001) report supershear propagation on a 200 km segment for two 1999 earthquakes in Turkey.

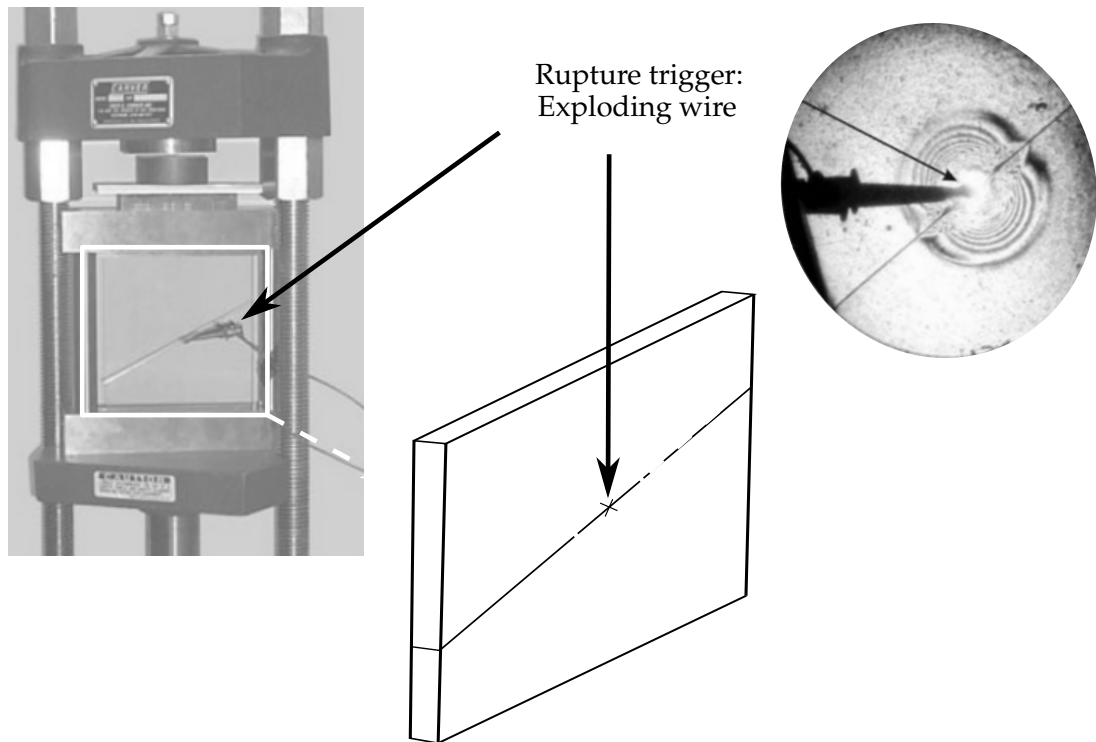
In contrast to the described crack-like ruptures in homogeneous materials, bi-materials favor pulse-like ruptures. They are pulse-like, because only a small area of the interface behind the rupture tip is sliding and heals before the rupture has traversed the entire interface. The sliding thus takes place step-by-step. Using contact area and strain measurements, Shlomai et al. (2016) show that ruptures in bi-materials have a preferred direction of propagation. This direction is the direction of slip of the material with the lower wave speed. These ruptures propagate pulse-like and at a well-defined speed, which is equivalent to the shear wave speed of the softer material. Secondary pulses exist and contact area and stress across the interface continuously evolve, thus no steady-state rupture is reached. In the opposite direction, the direction of relative motion of the stiffer material, the ruptures take two forms. Either, they propagate like cracks at sub-Rayleigh speed, similar to rupture propagation in homogeneous materials, or as supershear cracks. The occurrence of supershear ruptures dominates in this direction. The contact area decreases during rupture for homogeneous as well as bi material systems. However, in the direction of the motion

<sup>4</sup> $V_r$  - rupture speed;  $V_p$  - compression wave speed

of the softer material, the real area of contact can drop to 3 % after an increase just before the rupture arrives. In the opposite direction and in homogeneous materials the contact area does not reach values below 60 %. In a different setup of Polystyrene on glass Weber et al. (2019) find that the real contact area in their experiments increases during sliding. They measure the contact area using fluorescent molecules that, if confined by a real contact of sphere and glass, emit an increased fluorescence intensity. Their result implies, that a mechanical weakening of the asperities and thus a decrease in the interface strength must compensate the increase in contact area to allow for sliding.

Supershear propagation in rocks has been investigated by Passelegue et al. (2013) on an upper-crust mimicking triaxial granite on granite experiment. They measured supershear propagation speeds ( $\neq \sqrt{2}V_s$ ) using the Mach front arrivals times at different acoustic sensors along the fault line. They show a transition from sub-Rayleigh to supershear speed on a few centimeters. The average rupture velocity is correlated to the ratio of initial shear stress ( $\tau_0$ ) and normal stress ( $\sigma_N$ ) as well as the final stress drop. For sub-Rayleigh ruptures the ratio is  $\frac{\tau_0}{\sigma_N} < 0.6$  and the stress drop lower 1.5 MPa. For supershear ruptures the ratio is  $\frac{\tau_0}{\sigma_N} > 0.7$ , and the stress drop is larger than 3 MPa. These results are coherent with the experimental results of Ben-David et al. (2010) on polymers, as well as results for the Kunlunshan supershear earthquake (Robinson et al., 2006). The authors point out, that in contrast to field observations, supershear is a common phenomenon in their setup. Possible reasons are the smoothness of the plane fault and high normal stresses. Real faults kink and exhibit a gouge layer. Furthermore, energy dissipation at the rupture front producing off-fault damage could play a bigger role in real-world faults. The short transition length for supershear ruptures in these experiments indicate that supershear might be a common phenomenon at asperity size. Using the same experimental setup, Marty et al. (2019) back-projected the measured energy and revealed that high-frequency radiation stems from a zone close behind the rupture front and travels along with it. Higher normal stress and higher rupture velocity lead to an increase in high frequency radiation. This is consistent with field observations, where high frequency energy release corresponds to deeper portions of the fault. Possible reasons for the high frequency emissions are off-fault damage in the vicinity of the rupture front or accelerations and decelerations of the rupture front.

**Supershear across scales** Abraham et al. (2000) and Abraham (2001) showed that atomic/molecular dynamics simulations can also describe secondary supershear crack nucleation from sub-Rayleigh crack propagation. In their simulations, the crack accelerates up to sonic speed. Gao et al. (2001) compared these atomic simulations to elastic continuum simulations and found very good agreement. The characteristics of crack propagation seem thus to be comparable from the atomistic to the fault scale, over 11 orders of magnitude (Gao et al., 1999). Ruptures propagating faster than the



*a:* Experimental setup: A pre-cut PMMA plate is vertically confined under controlled stress conditions. A rupture is induced by an exploding wire at the indicated point. The rupture propagation is filmed by photo-elasticity. Original figures from Xia et al. (2004)

*b:* Photo-elasticity snapshot of a left traveling supershear rupture. The supershear cone, its angle to the fault line, the spherical shear wave front and a trailing sub-Rayleigh rupture are indicated. Figure from Mello et al. (2016)

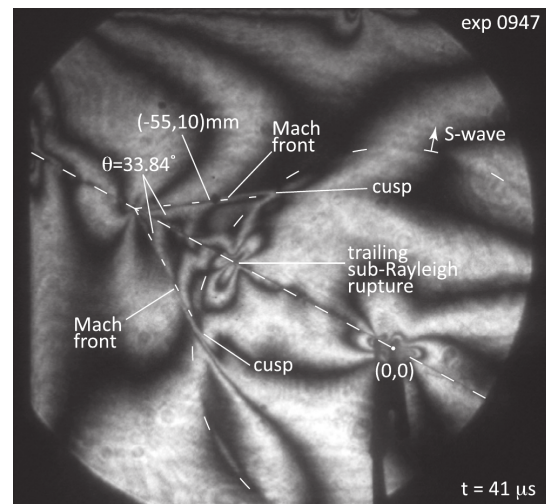


Figure 4.2.10: Setup and example of the rupture experiments by the group of Rosakis et al. at the California Institute of Technology.

$\sqrt{2}V_s$  speed have also been observed in the laboratory by Xia et al. (2004), Rubinstein et al. (2004), and Latour et al. (2011b). Their experiments indicate that weak interfaces favor faster supershear ruptures due to energy dissipation.

### 4.2.3 Slow slip

So far, we have seen experiments modeling the rapid energy release of earthquakes through fast frictional sliding. This has been the main priority of rock mechanics and seismologists for decades since it is responsible for what we experience as an earthquake: The strong ground motion associated with the arrival of elastic waves at the surface. However, this is not the only mechanism through which faults release energy. Observation of creep, i.e., very slow motion on faults, can at least be traced back to Tocher (1960) and Steinbrugge et al. (1960). These events are also called aseismic events because in contrast to fast events they are not accompanied by seismic wave radiation. However, the results of, e.g., King et al. (1973) indicated that they release large amounts of strain energy, comparable to large magnitude earthquakes. Kato et al. (1991) performed the first rock on rock sliding experiments I am aware of. The results indicated that these slow-slip, slow earthquake or creep events are likely to occur in the lower crust and the upper mantle. Heslot et al. (1994) studied slow slip of paper on paper and found, similar to rock mechanics, that creep is governing the slow process. Furthermore, they defined a crossover from the creep regime to an inertial regime when the velocity dependent friction coefficient changes from slip weakening to slip strengthening. Voisin et al. (2008) experimentally modeled a subduction zone and found that with further displacement, the acoustic emissions in their experiment evolve from strong and short signals (comparable to seismic signals of fast earthquakes) to small and long signals. Kaproth et al. (2013) sheared Serpentine, a fault zone material, and observed slow stick-slip events. Their slips are independent of fault stiffness and indicate that slow slip could depend on the friction characteristics of the fault gouge (see Fig. 4.2.11 for an example of fault gouge). Furthermore, they observed changes in acoustic travel-time through the fault zone indicating wave speed changes of up to 21 %. This is of particular interest for monitoring of real faults. The mechanisms of slow slip remain even more elusive than those of fast slip. For Ide (2014) slow earthquakes are qualitatively different from fast earthquakes while for Voisin et al. (2008) and Peng et al. (2010) the fast and slow modes present a slip continuum.

**Nucleation phase** Ohnaka et al. (1990) and Ohnaka et al. (1999a) observed that rupture nucleation on pre-existing laboratory faults can be divided into a quasi static phase and an acceleration phase. Furthermore, the observed shear ruptures highly depended on the surface geometry. Latour et al. (2013a) also found two phases for experiments in polycarbonate using photo-elasticity and acoustic emissions for



monitoring. However, the rupture velocity grows exponentially during the quasi-static nucleation phase in their experiments which is in contrast to the claimed steady growth of previous observations. The difference might actually not be due to a different process but due to higher resolution of their data revealing an exponential growth which appeared as apparently linear previously. They define a characteristic time of the nucleation phase  $t_c = L_0 / V_{0r}$ , where  $L_0$  and  $v_{r0}$  are the nucleation zone length and velocity at the time of transition from the quasi-static to the acceleration phase. The characteristic time scales inverse to the slip weakening rate and becomes shorter with growing observation scale due to fault heterogeneity. Rubinstein et al. (2006) observe that slow rupture fronts (2 order of magnitude below the Rayleigh wave speed) are present in all their PMMA contact area measurements. They are emitted upon arrest of sub-Rayleigh fronts and can be arrested or traverse the entire frictional interface. In the last case they account for a quarter of the observed overall sliding. These slow fronts on PMMA scale well with the nucleation phase observed by Ohnaka et al. (1999a) and might thus be a universal mechanism. Trømborg et al. (2014) suggest that slow fronts are connected to slow slip in the following way: Slow slip occurs immediately after normal rupture front arrest and loads the front tip so that the rupture front continues slowly to propagate instead of being arrested completely.

#### 4.2.3.a Granular friction

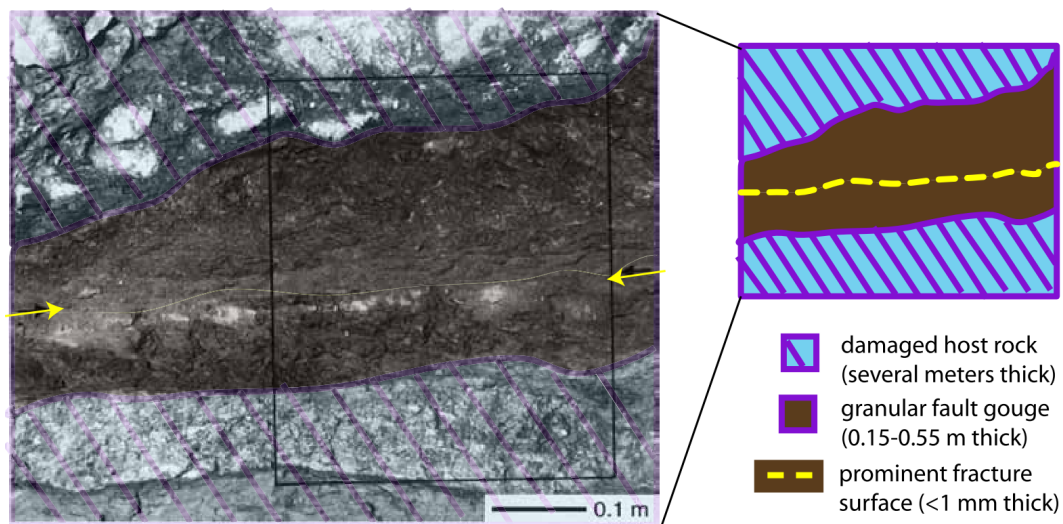


Figure 4.2.11: Field observations from an exhumed fault. The fault contains a layer of a finely crushed fault gouge (dark material), and the slip in the gouge is localized in a narrow shear band (yellow arrows). Figure from Daub et al. (2010), fig.4.

Earthquakes occur along fault lines, but these faults are not perfect planes. They rather consist of layer of granular material, the fault gouge, separating two rock bodies. Fig. 4.2.11 shows an example of a fault, where the granular gouge material can be identified between the two solid rock blocks of the fault. A granular material, the ice stream till, is also present in observed ice stream stick-slip (Leeman et al., 2016). In the laboratory, stick-slip friction has been observed to be a common phenomenon for sheared granular layers. Scotti et al. (1994) undertook a double-direct-shear experiment, which showed that the apparent friction coefficient depends on the thickness of the gouge layer. Gu et al. (1994) observed that in a sheared ultra fine quartz layer localization of shear took place before sliding was initiated and is a condition for stick-slip.

**Particle rearrangements** Granular media do not behave linearly elastic under load. The responsible process are microscopic particle rearrangements leading to the formation of force chains. Force chains form in a granular medium under compression, because the stresses are only transferred via individual particle contacts and not via the bulk material. A chain of particles supports the load while others can be completely unstressed. This leads to a hardening of the material for small deformations. Only when the stresses are high enough for more and more particles to enter into contact, the material enters a linearly elastic regime (Hidalgo et al., 2002). Using photo-elastic particles, Daniels et al. (2008) imaged the force chains developing in a deforming granular medium as an analogue to fault gouge deformation. Fig. 4.2.12 shows their observation: The deformation in the granular fault model is accompanied by a rearrangement of the particles which carry most of the load. This rearrangement occurs prior to stick-slip setting in. Daub et al. (2010) describe a model of shear transformation zones (STZ). Rearrangement of the grains under shear produces plastic strain. The strain is localized and deformation takes place in a small zone/band and not throughout the whole material. Simulations with the STZ model reproduce crack, pulse and supershear ruptures (Daub et al., 2010). Through STZ modeling of laboratory data, Lieou et al. (2017) connect the STZ-theory to rate and state friction laws.

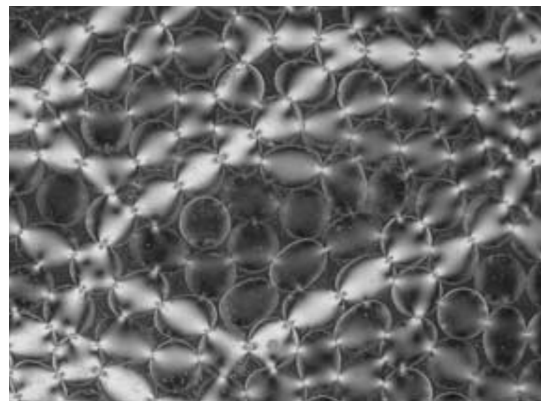
**Acoustic emissions from granular friction** The earth is never quiet. Acoustic sensors placed on its surface always register a background noise, that can stem from sources as various as tides, rivers, cars and even elephants. However, this background can also contain useful signals. Acoustic emissions, have long been linked to the cracking of brittle materials as well as to the failure of soils (Koerner et al., 1976) and the initiation of landslides (Cadman et al., 1967). Soil is a granular material, which becomes evident if one looks at the Unified Soil Classification System, where soils are classified according to particle form and grain size (Astm et al., 2006). More recently, Herwijnen et al. (2011) showed the presence of acoustic emissions

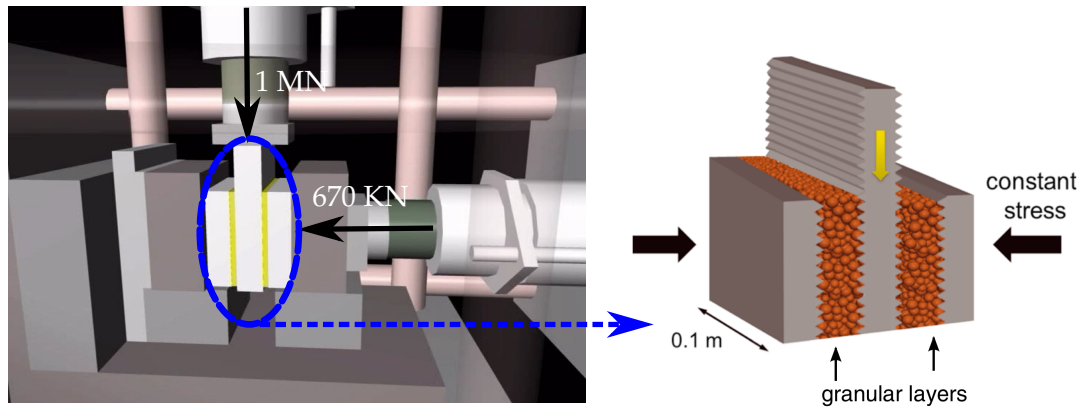
at the onset of avalanche rupture. In avalanches, slab avalanches are responsible for most casualties. In many cases, a small layer of angular grains, formed under specific weather conditions, is responsible for the mechanical failure of the snow pack. The first to show a clear link between acoustic emissions and the displacement of granular particles in the forming and breaking of force chains in the laboratory were, to my knowledge, Hidalgo et al. (2002). They measured the acoustic emissions of glass beads under load and found a good agreement of their proposed model of rearrangement and the experimental results.

In the laboratory, slip precursors to major slip events have been reported that can be related to acoustic emissions from granular materials. Ferdowsi et al. (2013) report microslips before the onset of major slip from 3D discrete finite element simulations. Johnson et al. (2013) showed the same mechanism experimentally in a biaxial setup through shear stress measurements. They combined the shear stress measurements with recordings of acoustic signals and showed that slip events are not only preceded by microslip but also by coincident acoustic emission precursors.

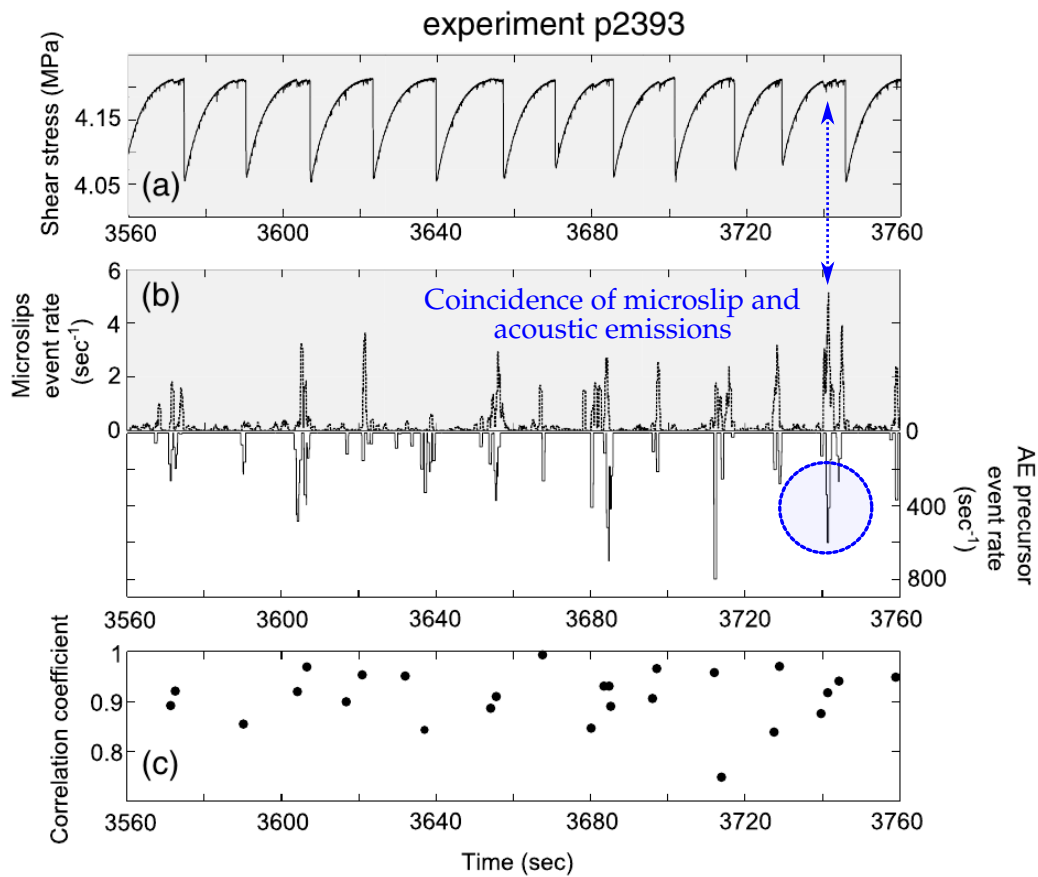
**Triggering** Johnson et al. (2016) report that gouge material is essential to earthquake triggering. Using the biaxial apparatus in Fig. 4.2.13a they find that a critically stressed fault can instantaneously fail at the arrival of an acoustic pulse. The failure is accorded to the fact that the wave breaks the intergranular force chains, weakening the material.

*Figure 4.2.12:* Photo-elastic evidence of force chains from Daniels et al. (2008). The stress is concentrated along lines of rearranged grains (brighter grains). The grains outside the chains (dark grains) can be completely free of stress, without contacting each other. The higher the stress, the more grains enter into contact. The material approaches the elastic behavior of the bulk material when all grains are in contact.





*a*: Left: The bi-axial double shear apparatus with maximum force indicated. Adapted from <https://www.rockmechanics.psu.edu/apparatus.html>. Right: Schema of the central part from Johnson et al. (2013).



*b*: Results of Johnson et al. (2013) for a granular double-shear experiment as shown in Fig. 4.2.13a. The shear stress curve in (a) of the original Figure shows that each major slip event is preceded by microslips (indicated by blue arrow). The rate of acoustic emissions (AE) in (b) shows an increase coincident with the measured microslip, as becomes evident through the correlation coefficient plot in (c). Adapted from Johnson et al. (2013).

Figure 4.2.13: Double shear setup and results from Johnson et al. (2013)

#### 4.2.3.b Ultrasound wave propagation imaging

Apart from the photo-elasticity experiments by Rosakis et al., all previous laboratory set-ups are based on strain gauges, acoustic emissions or contact area measurements but none bridges the gap between rupture creation and the associated elastic wave radiation. Direct observation of shear waves from a propagating rupture has only been done in the 2D setup of Rosakis et al., where the propagating wavefront is filmed with a high-speed camera. Latour et al. (2011a), Latour et al. (2011b), and Latour et al. (2013b) used ultrafast ultrasonic speckle interferometry or high frame-rate ultrasound imaging to image the elastic wavefield inside a 3D sample during interface failure. They performed three types of experiments:

- Hydrogel on sandpaper
- Hydrogel on a single layer of sand on a glass-plate
- Hydrogel on glass plate with large pebbles as asperities.

For the sandpaper they found abrasion of the gel and linked the depinning of sandpaper-gel contacts to slow slip and tremor. The observed waves were well modeled by a unidirectional point source and the elastic Green's function in an isotropic, homogeneous, elastic medium. For the sand mono-layer they found exclusively supershear ruptures. They accord this to a very homogeneous interface between the glass plate and the sand pebbles. They assume that the sliding friction is between the sand pebbles, that are stuck to the gel by hydrostatic forces, and the glass plate. In the asperity setup, they relieve that on a heterogeneous interface the rupture and wave radiation depend strongly on the barrier (asperity) type. A barrier can stop a rupture, increase or lower its velocity and a sub- to supershear transition can be induced. Under equal conditions the ruptures may vary for the same interface. These experiments were the first experiments done on friction using high frame rate ultrasound imaging. To our knowledge they were also the first to directly image a 3D rupture in a 2D imaging plane in situ an elastic body.

#### 4.2.3.c And the real world?

One of the main issues associated with laboratory earthquakes experiments is scalability. To which extend are earthquakes and rupture propagation self-similar? Seismic faults are not smooth homogeneous layers as is the case for many laboratory experiments. They exhibit asperities or barriers on which strain accumulates and it is their breaking that releases large amounts of elastic energy (Ohnaka, 2004a). However, the above reported laboratory experiments show that a number of characteristics found in real-world earthquakes can be reproduced in the laboratory. These include for example supershear, creep, stick-slip and fault healing (Marone, 1998).

As already mentioned, kinematic models of a moving dislocation fit a large number of earthquake records surprisingly well. Among the first to show this were Aki (1968) for the 1968 Parkfield earthquake. This fit is an indicator for the **slip-pulse** mechanism in earthquakes (Heaton, 1990). Lu et al. (2010) suggested that a low stress level along faults may support pulse-like behavior (Rosenau et al., 2017).

The sub-Rayleigh and supershear dichotomy known from **crack-like** rupture propagation was shown by Bouchon et al. (2001) and Bouchon et al. (2002) for the 1999 Izmit and Düzce earthquakes in Turkey. On a nearly planar part of the fault (less than one meter wide), the rupture speed was inferred to be supershear and close to the prediction by Freund (1979) of  $\sqrt{2}V_s$ . On a more complex part of the fault, the rupture was inferred to have propagated at sub-Rayleigh speed. Furthermore, the two sides of the fault exhibit a material contrast. For the 2001 Kunlunshan earthquake, Bouchon et al. (2003) inferred a sub-Rayleigh to supershear transition during the first 100 km of a 400 km long surface rupture. These results fit the experimental results of Rosakis et al. (1998) and Rosakis et al. (1999) astonishingly well. From experimental evidence (e.g. (Latour et al., 2013b; Latour et al., 2011a)) it was suggested that fault heterogeneity inhibit supershear while homogeneous faults facilitate it. This relation seems to hold true for real faults as well. The observed supershear ruptures for real-world earthquakes happened on smooth, planar fault segments (Bouchon et al., 2010). The granite experiments by Passelegue et al. (2013) presented earlier were reproduced successfully using dynamic rupture simulations originally applied at the large real-world scale. This is another indicator for self-similarity of supershear rupture propagation.

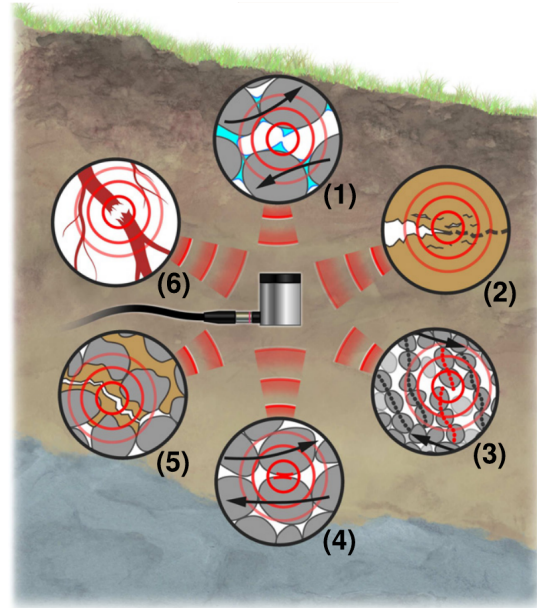
Several earthquakes have been showed to be dynamically **triggered**, even over large distances. The 1992 Landers earthquake (magnitude 7.3) and the 1999 Hector Mine earthquake (magnitude 7.1), triggered earthquakes in the same locations (Gomberg et al., 2001). For the Landers event triggering as far as 280 km away from the fault has been shown (Scholz, 2002).

The presence of a **nucleation phase**, as shown in the laboratory by Ohnaka et al. (1999b), was discussed for real-world earthquakes by Beroza et al. (1996), Iio (1995), and Latour et al. (2013b). Bouchon et al. (2011) found a precursor phase for the 1999 Izmit earthquake. The earthquake was preceded for 44 minutes by a phase of **slow slip** occurring at the base of the brittle crust. This slip accelerated slowly at the start and then rapidly accelerated in the 2 minutes preceding the earthquake. A slow slip just before a fast event was also observed by Kato et al. (2012) for the 2011 Tohoku-Oku earthquake. Early detections of slow earthquakes in the field depended on the use of strainmeters, buried for example in borehole at the San Andreas fault (Linde et al., 1996). The number of detections grew quickly when GPS stations for fault monitoring were introduced. Thus, Rogers et al. (2003) could reveal that small seismic signals (tremor) correlate with slow crustal slip in a subduction zone. Although slow earthquakes themselves are not a natural risk, they happen in the

same areas as fast earthquakes and, because they result in stress changes, likely play a role in triggering fast earthquakes.

As already mentioned, **acoustic emissions** are indicators for landslide and avalanche failure (Michlmayr et al., 2012). Kwiatek et al. (2013) used acoustic emission sensors in boreholes in the frequency range from 1 to 60 kHz to monitor aftershock sequences of a magnitude 1.9 earthquake. The results indicated a large number of events with a tensile component. Thus, the source mechanism strongly deviated from the pure mode II or III crack idealization.

*Figure 4.2.14: AE sources for geologic materials from Michlmayr et al. (2012): (1) liquid bridge rupture, (2) crack development, (3) release of force chains, (4) grain friction, (5) grain cementation fracture, and (6) rupture of soil fiber*



In recent years, stick-slip has been shown to be present in other geophysical sliding events than earthquakes. **Glacier stick-slip** has been reported for Antarctica (Anandakrishnan et al., 1993; Walter et al., 2015), Greenland, (Nettles et al., 2003) and possibly for alpine glaciers (Helmstetter et al., 2015). For the case of basal sliding, the material contrast of ice to the glacial till and underlying rock is much stronger than for seismic faults. This fact is of particular interest for us, since most of the friction experiments presented in this work also exhibit a strong bi-material contrast. Walter et al. (2015) directly compared laboratory experiments with homogeneous, solid sliding PMMA blocks to seismic data from the antarctic Whillans Ice plain. The simple laboratory setup reproduces several features of the bi-daily ice stick-slip. In the field, the observed rupture nucleates below the Rayleigh wave speed and slows down during propagation. In the laboratory experiment it nucleates around the Rayleigh wave speed and slows down during propagation. The sub-Rayleigh rupture velocity covaries with loading conditions in both case. In the ice plain the varying loading conditions are due to the ocean tides. Both, high and low tides nucleate rupture. The stress-dependence is in agreement with the LEFM description of ruptures. The author's accord the successful matching of laboratory and field experiments to the fact that the ice plain is an isolated system of homogeneous

material. In contrast to earthquake faults, which exhibit branches and a complex geometry, it is a simple plane. Furthermore, triggering by seismic events from nearby fault segments can be excluded. Lipovsky et al. (2017) use a rate and state friction law to model the slow slip on the the same ice plain. When the fault dimension of the Whillans ice plain is approximately equal to the nucleation length, they reproduce slip occurring as slow slip similar to subduction zone slow-slip events.

#### 4.2.4 Kinematic source models

Seismologists have historically tried to relate the seismic waveforms observed by seismometers in the far-field to the source mechanism of the earthquake. In contrast to the laboratory, real-world seismology until recently entirely relied on recording elastic waves<sup>5</sup>. The complex dynamic rupture propagation is thus approximated by kinematic models which reproduce the observed elastic wavefield. Kinematic rupture propagation is a first approximation that ignores stress dependence and only includes the space-time development of a displacement continuity on the rupture surface. It links the displacements in the body of interest to the physical quantity which created it. These are body forces, frictional forces and displacement. As we know from classic elasticity, the equation of motion for an external force in an isotropic, elastic medium is (Landau et al., 1986; Aki et al., 2009; Pujol, 2003):

$$\rho \ddot{\mathbf{u}} = (\lambda + 2\mu) \nabla \nabla \cdot \mathbf{u} - \mu \nabla \times (\nabla \times \mathbf{u}) + \mathbf{f}, \quad (4.4)$$

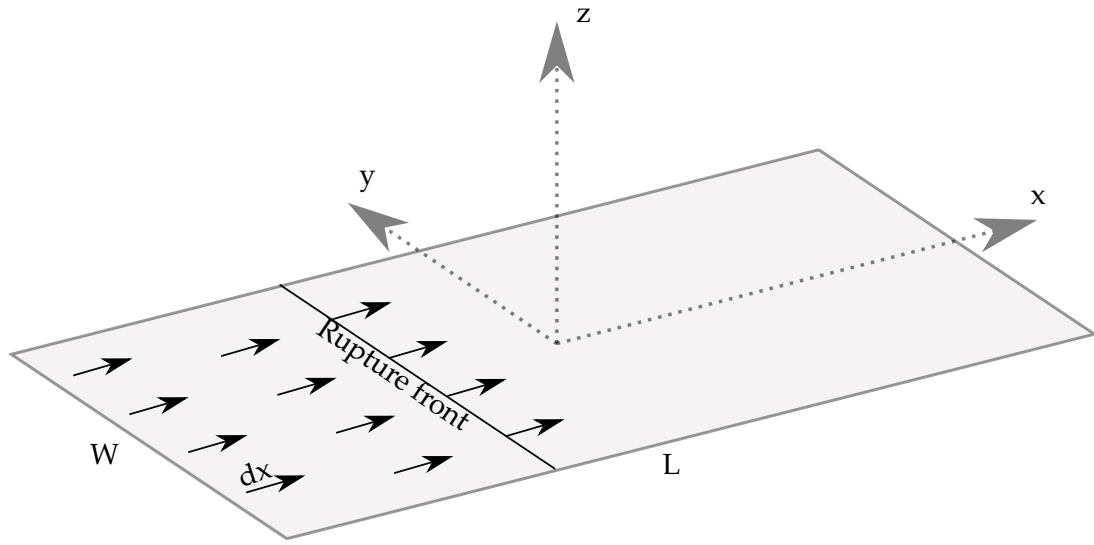
where  $\rho$  is density,  $\mu$  is shear modulus,  $\lambda$  is Lamé's first parameter,  $\mathbf{u}$  is the displacement vector and  $\mathbf{f}$  is the force term. Before detailed rupture models were available, seismologists, aware that earthquakes happen along fault planes, faced the following question: "What is the equivalent body force that in the absence of the fault will cause exactly the same displacement field as slip on the fault?" (Pujol, 2003). The solution is the famous double-couple and was derived in the 1960s by T (1963), Haskell (1964), and Burridge et al. (2003). It is the force equivalent in space and time for the earthquake source which creates the observed displacement and radiation pattern. For details see also Box 4.3.

An intuitive kinematic rupture model used to describe seismic waveforms in the far-field is Haskell's unidirectional rupture model of a propagating dislocation, schematically shown in Fig. 4.2.15a. The parameters at the source responsible for the elastic displacement in the medium in Haskell's model are the fault length, fault width ( $\ll$  length), permanent slip distance, rise time and a constant rupture velocity (Aki et al., 2009). Numerically the model can be represented by a point source moving along the discretized rupture length  $L$  at a constant speed  $v_r$ . The elastic wavefield in

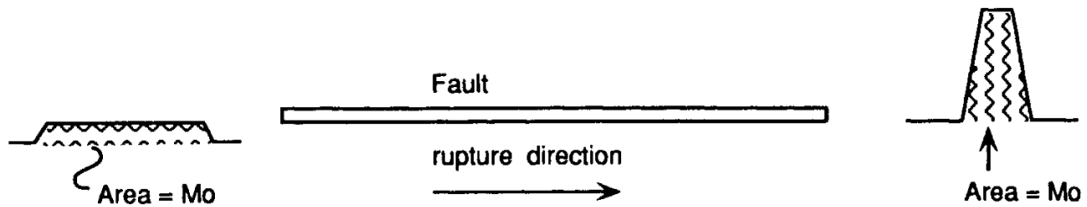
<sup>5</sup>In recent years, deformation measurements through GPS stations near natural faults enrich the available seismology data



the medium of interest can be calculated by convolution of the point source function with the Green's function of the medium and summation in space and time. One of the first to do so for a rectangular fault model with double and simple couple sources was Ben-Menahem (1961). In the next section I will first present the Green's function for a unidirectional point force as the equivalent to a point dislocation source. Since natural strike-slip earthquakes are however better described by a double couple as the equivalent body force we then present the Green's function for a double couple source.



*a*: Schema of a fault in Haskell's model.  $W$  is the fault's width,  $L$  the length,  $dx$  is the slip distance in the ruptured part of the fault.



*b*: Azimuthal variability of the source time function for a unilaterally rupturing fault. The duration changes, but the area of the source time function is the seismic moment and is independent of azimuth. Extracted from Figure 9.9 in Lay et al. (1995).

Figure 4.2.15: Haskell's unilateral rupture model.

**Infobox 4.3 Seismic moment tensor**

In global seismology the rupture complexity is often further reduced by collecting the properties of the rupturing fault in the seismic moment tensor that describes the slip mechanism in terms of a nine independent force (couples) shown in Fig. 4.2.16. The equivalent surface force for an infinitesimal surface element can always be expressed as a combination of these nine couples (Aki et al., 2009).

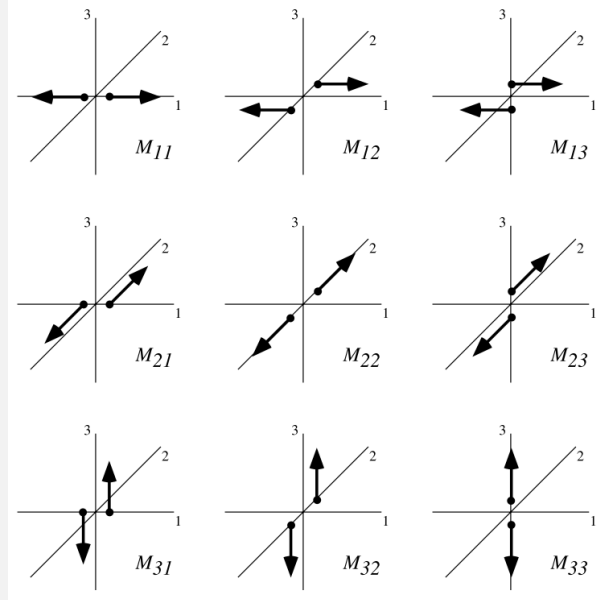


Figure 4.2.16: Illustration of the force couples that make up the seismic moment tensor. From Shearer (2009)

The energy radiated through the elastic wavefield is described by the scalar seismic moment, which is defined as the product of the rupturing surface  $A$ , the slip length  $l$  and the local shear modulus  $\mu$ :

$M_0 = A\mu l$ . The seismic moment and moment tensor are related through  $M_0 = \frac{1}{\sqrt{2}}(\sum_{ij} M_{ij}^2)^{\frac{1}{2}}$ .

For an explosive source the moment tensor is  $\begin{vmatrix} M_0 & 0 & 0 \\ 0 & M_0 & 0 \\ 0 & 0 & M_0 \end{vmatrix}$ , and for a double couple

$\begin{vmatrix} 0 & M_0 & 0 \\ M_0 & 0 & 0 \\ 0 & 0 & 0 \end{vmatrix}$ . Through the moment tensor, the earthquake source is thus approximated as a point source with a specific radiation pattern.

**4.2.4.a Point dislocation source**

The displacement field for a Delta function is the elastodynamic impulse response or Green's function. As can be observed on earthquake outcrops, ruptures are directional and as such the displacement at a Receiver at a point in time and space  $u(x, t)$  depends on Source direction and Receiver polarization. The Green's function is thus

a tensor  $G_{ij}(x, t; \zeta, \tau)$  where  $i$  is the displacement in direction  $i$  due to an impulse in direction  $j$ ,  $t$  is the arrival time,  $\tau$  the source time and  $\zeta$  the source location. Following Haskell's model of a unilaterally rupturing fault, the earthquake source function is not a delta function but a time dependent displacement. A simple appropriate source in terms of displacement is thus a ramp, leading to particle-velocities as depicted in Fig. 4.2.15b. Due to the inherent property of the delta function

$$\int_{-\infty}^{+\infty} f(x)\delta(t - \tau)dt = f(\tau), \quad (4.5)$$

the displacement  $u_{ij}(x, t)$  due to the Source function  $X_0(t)$  in  $x_j$ -direction at the source position becomes:

$$\begin{aligned} u_i(x, t) &= X_0 * G_{ij} \\ &= \frac{1}{4\pi\rho} (3\gamma_i\gamma_j - \delta_{ij}) \frac{1}{r^3} \int_a^r \tau X_0(t - \tau) d\tau \\ &\quad + \frac{1}{4\pi\rho\alpha^2} \gamma_i\gamma_j \frac{1}{r} X_0(t - \frac{r}{\alpha}) \\ &\quad - \frac{1}{4\pi\rho\beta^2} (\gamma_i\gamma_j - \delta_{ij}) \frac{1}{r} X_0(t - \frac{r}{\beta}), \end{aligned} \quad (4.6)$$

where  $r$  is the distance from the source to the receiver,  $\rho$  is density,  $\alpha$  and  $\beta$  are the compression and shear wave speeds,  $r$  is distance to the source and  $\gamma$  is a direction cosine defined as  $\gamma_i = \frac{x_i}{r} = \frac{\delta r}{\delta x_i}$ . A thorough derivation is given in Aki et al. (2009) Chapter 3 and 4.

#### 4.2.4.b Double couple source

The kinematic source that best models Seismic waves observed in the far field has been an open question for a long time (Pujol, 2003). A simple shear point force as given in Eq. (4.6) does not explain the seismic radiation patterns observed from most fault slips. Under the approximation that earthquakes are caused by pure shear faulting, the equivalent force system for an isotropic medium causing the shear displacement are two force couples with no net torque. This leads to the widely used double couple (DC) point source expression that well explains a displacement continuity across a fault plane buried in a 3D-body in the far field (see Fig. 4.2.17). Here the source is modeled as two force couples acting on the surfaces of the fault plane. The displacement continuity across the fault can thus be given equivalently as the surface force acting on an infinitesimal surface element. This force in turn can be described by a combination of nine force couples.

In the case of a strike-slip event in an isotropic body the two couples are sufficient to describe the radiation pattern and the displacement continuity can be described by a double-couple.

The convolution of a force with a Green's function has its equivalent in the convolution of the moment tensor with the derivative of the Green's function. This gives the force-displacement equivalent. With  $X_0$  being the amplitude of a force in  $p$  direction we find that:

$$u_n(\mathbf{x}, t) = X_0 * G_{np} = F_p * G_{np} = M_{pq} * G_{np,q}. \quad (4.7)$$

Hence, the displacement field induced by a shear dislocation can be described as a convolution of the seismic Moment tensor with the Green's function which in polar coordinates gives:

$$\begin{aligned} u_n &= M_{pq} * G_{np,q} \\ u(\mathbf{x}, t) &= \frac{1}{4\pi\rho} A^N \frac{1}{r^4} \int_{\frac{r}{\alpha}}^{\frac{r}{\beta}} \tau M_0(t - \tau) d\tau \\ &\quad + \frac{1}{4\pi\rho\alpha^2} A^{IP} \frac{1}{r^2} M_0(t - \frac{r}{\alpha}) + \frac{1}{4\pi\rho\beta^2} A^{IS} \frac{1}{r^2} M_0(t - \frac{r}{\beta}) \\ &\quad + \frac{1}{4\pi\rho\alpha^3} A^{FP} \frac{1}{r} \dot{M}_0(t - \frac{r}{\alpha}) + \frac{1}{4\pi\rho\beta^3} A^{FS} \frac{1}{r} \dot{M}_0(t - \frac{r}{\beta}), \end{aligned} \quad (4.8)$$

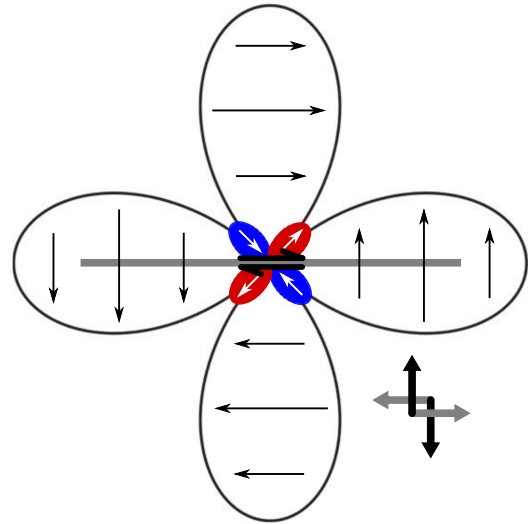
where the radiation patterns of the near, far and intermediate field terms are described by:

$$\begin{aligned} A^N &= 9 \sin 2\theta \cos \phi \hat{\mathbf{r}} - 6(\cos 2\theta \cos \phi \hat{\boldsymbol{\theta}} - \cos \theta \sin \phi \hat{\boldsymbol{\phi}}) \\ A^{IP} &= 4 \sin 2\theta \cos \phi \hat{\mathbf{r}} - 2(\cos 2\theta \cos \phi \hat{\boldsymbol{\theta}} - \cos \theta \sin \phi \hat{\boldsymbol{\phi}}) \\ A^{IS} &= -3 \sin 2\theta \cos \phi \hat{\mathbf{r}} - 3(\cos 2\theta \cos \phi \hat{\boldsymbol{\theta}} - \cos \theta \sin \phi \hat{\boldsymbol{\phi}}) \\ A^{FP} &= \sin 2\theta \cos \phi \hat{\mathbf{r}} \\ A^{FS} &= \cos 2\theta \cos \phi \hat{\boldsymbol{\theta}} - \cos \theta \sin \phi \hat{\boldsymbol{\phi}}. \end{aligned}$$

#### 4.2.4.c Non-double-couples and damage terms

DC sources are routinely used for earthquake modeling. However, in many cases non DC-sources might be more appropriate. Such examples include landslides and volcanic earthquakes as well as earthquakes in the upper mantle (Julian et al., 1998). Ben-zion et al. (2009) find that changes in elastic moduli of the source region contribute additionally to the classic moment term. For, example a decrease due to brittle fracture increases seismic energy radiation into the bulk. They argue that the energy stemming from this change can even be larger than the energy stemming from the classic moment tensor. Although I do not tackle these questions in the present manuscript, they are noteworthy. Because shear wave imaging is a unique tool to investigate the near-field, our experimental setup is ideal to investigate these questions. Even more so, if elasticity mapping as is done in the medical field was included through, e.g., passive elastography (Catheline et al., 2013).

Figure 4.2.17: Radiation pattern of the double-couple point source in the *far field*. The direction of particle movement, displacement and force are indicated by arrows. Adapted from Aki et al. (2009) and Igel (2017). Note that in ultrasound shear wave imaging one often retrieves what seismologist call the *near field*.



#### 4.2.5 Summary

The presented works show, that seismic rupture is inherently a dynamic process, depending on material properties and their stress history. This conclusion derives mainly from the laboratory. At the real world scale seismologist rely largely on the rupture models developed in theory and the laboratory. However, dynamic rupture simulation is computationally expensive, especially at a fault's scale. Hence, the developed models representing the seismic source in real world seismology were and still predominantly are simpler kinematic models. Acknowledging that many rupture phenomenon are scale invariant, one could ask the question if global seismology numeric models should not be scaled to and validated in the laboratory before applying them on the earth's scale. The work presented by Latour et al. (2011a) bridges the gap between laboratory friction experiments that seldom examine the emitted elastic wavefield and global seismology data which is nearly entirely far-field elastic wave data. In this work we build on the preceding works of Latour et al. (2011a), Latour et al. (2011b), and Latour et al. (2013b) using new methodology, hard- and software as well as new experimental setups. Using ultrafast ultrasonic imaging we exploit the fact that we can investigate 3D experimental setups in-situ. While many experimental configurations are possible and worthwhile exploring, we concentrate on the case of a small frictional patch on an otherwise smooth interface. This allows us to image the elastic wavefield during the rupture as well as its propagation in the wake of the rupture. Furthermore, by keeping a distance between the frictional patch and the boundaries we isolate it as much as possible from these boundaries. The spatial isolation allows us to reduce the variation of rupture processes in a single experiment. These variations are for example caused by the not perfectly homogeneous interface and material. Thus, we facilitate detection and statistical analysis of rupture events. Finally, this setup is truly three-dimensional, and plane-stress or

---

plane-strain assumptions do not hold inside the gel. If we want to draw a comparison to earthquake language we would describe this as an asperity on a smooth fault.

### 4.3 Experimental setup

Following the work by Latour et al. (2011a) we build a strike-slip fault mimicking experiment. The basic idea is that an elastic 3D-sample is sheared until slip initiates and the resulting wave-field is imaged through shear wave imaging. Shearing is assured through a glass plate driven by a stepper motor. The sample is confined except for a small part close to the shearing surface that is left free to allow for deformation. A layer of sand which gives rise to granular friction is posed in between the glass plate and the sample to ensure frictional sliding.

The main changes compared to the previous setup by Latour et al. are:

#### Hardware

- New stepper motor
- New imaging system: Verasonics<sup>TM</sup> Vantage, ability to use up to 10000 frames per second and compounding (angular plane wave emission) for better illumination.

#### Software

- User friendly Matlab interface, allowing for acquisition and data treatment in the same environment
- Separation of acquisition, reconstruction and data treatment allows for repeated execution without breaks
- Fast reconstruction through the built-in beamforming which results in high quality, complex IQ-data
- Phase correlation instead of speckle tracking → retrieval of total displacement<sup>6</sup> from particle velocity ( $\int_{t_0}^{t_{end}} v_p dt$ ).

---

<sup>6</sup> The tracking algorithms used by Latour et al. (2011a) used windowing functions to retrieve the particle velocity. While they work perfectly fine for particle velocity imaging they are known to have limitations in retrieving the total displacement. By loosing the high spatial resolution of the ultrasound through the averaging done by the windowing, errors accumulate when integrating over time. This explains why Latour et al. (2011a) relied on an optical sensor to retrieve the gel displacement on one extremity of the gel. There is one main difference of displacement measurements by an optical sensor or by ultrasound. While the optical sensor retrieves the true displacement of one physical point in the Lagrangian sense, the ultrasound measures from an Eulerian point of view. For the particle velocity this is generally negligible, since the displacement between two time-steps is very small. Throughout the entire experiment however, displacement in the gel is in the millimeter range. Strictly speaking we see the displacement passing through a spatial coordinate, not the displacement of a physical point.

## Setup

- Small, isolated sand patch that does not cover the entire gel surface to reduce boundary effects and isolate the rupture → Equivalent to an asperity on a smooth fault
- Gel-on-plate and gel-on-gel sliding.

In the following I present the sample preparation, friction bench, asperity, imaging device and the experimental workflow.

### 4.3.1 Samples

We use homemade polyvinyl-alcohol (PVA) hydrogels. These gels are commonly used to mimic biological tissue. In comparison with gelatin and agar-gels they have the advantage of a much longer lifetime if stored in water. The production process consist the following steps:

- Solution of PVA-powder in hot water under constant stirring.
- Addition of 0.1-0.5 % of graphite powder to introduce the scatterers that assure the ultrasonic speckle.
- Rapid cool-down in an ice-bath of the viscous solution until gelification sets in.
- Freezing at  $-18^{\circ}\text{C}$  until complete gelification is reached.
- Complete thawing of the gel.

The last two steps are repeated until the gel has the desired elasticity. In experiments requiring large investigation depth it is essential to degas the solution before solidification. Less air means less scattering and can lead to a gain of several centimeters with the 5 MHz ultrasound probe. Many more hydrogels are possible. These include gelatin, agar-agar, cellulose and polyacrylamide gels. In this manuscript we do not tackle the question of brittle versus elastic versus ductile material and consequently the relevant property for us is the average shear wave speed. Most presented experiments are gel-on glass experiments in which the material contrast of the gel and the glass is orders of magnitude above the difference in elastic parameters of the gels. It should be noted, that the homemade gels are not homogeneous. During the production of the large samples required for the setup, incomplete solution of the PVA-powder could not be avoided and the long time needed for complete solidification led to deposition of graphite and PVA-powder at the bottom of the gel. An example of an inhomogeneous hydrogel is shown in Fig. 4.4.1 of Section 4.4.1.a.



### 4.3.2 Friction bench

The motor is a Kollmorgen® AKM™ stepper motor, depicted in Figs. 4.3.2a and 4.3.3. It is piloted through a LabVIEW (National Instruments) interface which ensures synchronization with the imaging device. The motor drives an endless screw, which in turn drives a glass plate through a wagon that is sliding on low-resistance bills on two rails. The motor controls the rotation rate of the screw and thus the driving speed of the wagon. It can be driven at constant speed or user specified speed profiles. In this work we focus on a constant driving speed. The movement of the glass plate and the friction of the asperity lead to deformation of a hydrogel, which is hold in a fixed position on the friction bench. A force gauge in between the driving unit of the endless screw and the wagon allows the measurement of the total average force on the glass plate. For the longest time of the work the friction bench was badly aligned, the motor introduced lateral movement in the system and the force gauge(s) were broken. It took until the end of the third year to overcome these experimental issues. Table 4.1 gives a quick overview of the development of the friction bench and the imaging system. It serves the reader as a reference of the state of the experimental setup in which the data-sets presented in this manuscript were acquired.

### 4.3.3 Asperity

In contrast to the work of Latour et al. (2011a) I concentrate on a spatially limited sand asperity that gives rise to granular friction. A small patch of fine to medium sand ( $<0.5$  mm), and in the case of Section 4.4.2.c, coarse sand is placed on the glass plate in the center of the hydrogel position. The sand is not completely dry, because PVA hydrogels loose water, especially under stress. In the case of the fine sand this becomes evident in the cohesion of sand grains after the experiment (see, e.g., Fig. 4.4.1b).

### 4.3.4 Imaging device

The imaging probe is a 128-element L7-4 (Philips) ultrasound probe centered at 5 MHz. A photo of the probe is shown in Fig. 4.3.2b during an experiment where a  $x - z$ -plane inside a hydrogel is imaged. The probe is connected to a high-frame rate ultrasound scanner (Verasonics Vantage™)<sup>7</sup> which works at up to 10 000 frames per second. Fig. 4.3.2c shows the scanner with its host computer. The host computer ensures sequence programming as well as registration and treatment of the acquired data through a Matlab™ interface. Each ultrasound frame is obtained through emission of plane waves as in Sandrin et al., 1999b and beamforming of the backscattered signals. In addition to emission of plane waves with a propagation angle of  $90^\circ$  to the probe surface, the setup allows for compound imaging with up to  $20^\circ$  offset. To

<sup>7</sup>See also Section 2.2

achieve this, an emission delay is introduced from one element to the next. The superposition of the waves emitted by each element is then a plane wave propagating with an angle relative to the probe surface. For coherent results an impair number of angles is emitted, one at  $0^\circ$  and two for each required angle value. The effected pulse repetition frequency (PRF) is thus the emitted PRF divided by the number of angle values.

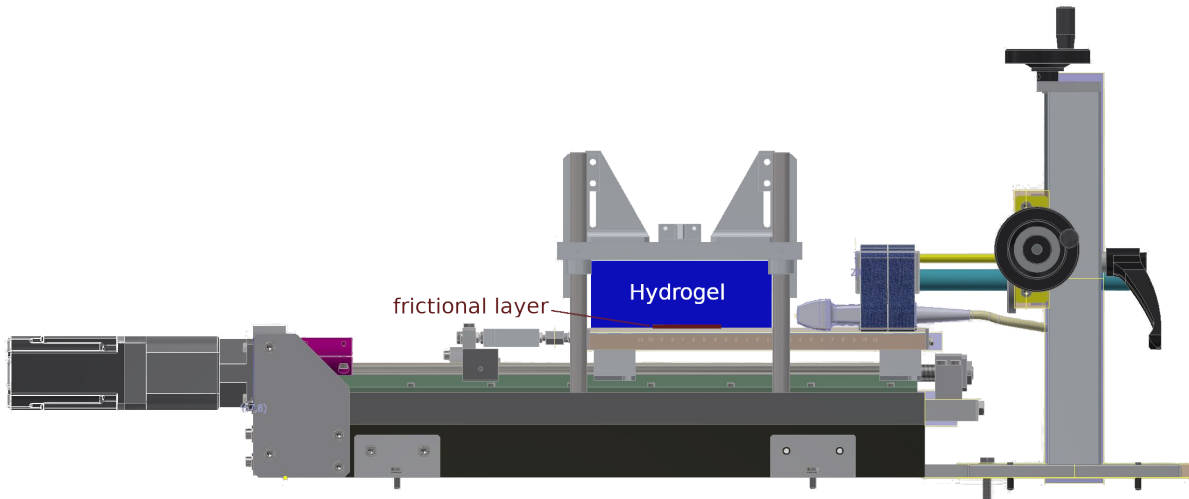
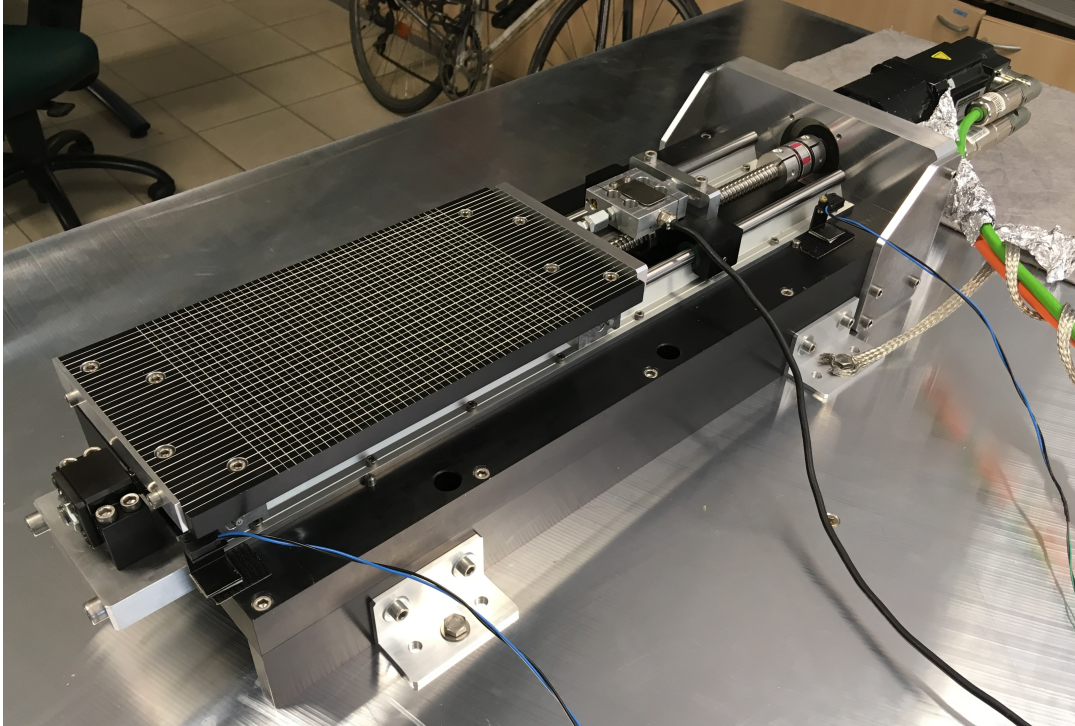


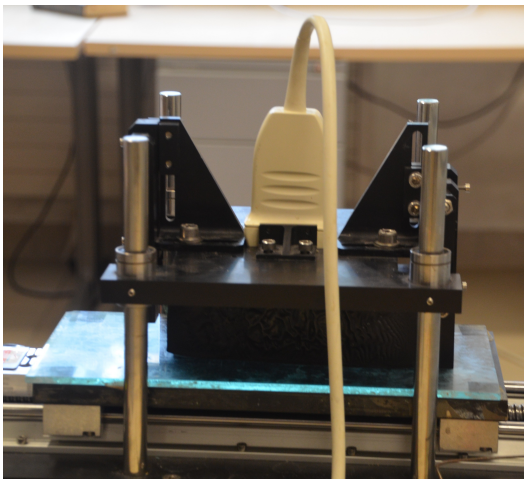
*Figure 4.3.1:* Experimental setup of the friction bench. From left to right: A stepper motor drives an endless screw which displaces a strain gauge connected to the wagon with the glass plate. A hydrogel is posed on the glass plate with a frictional layer of sand in between. Normal load is applied on top via weights. The gel is blocked in the direction of movement of the plate and a small part at the bottom is left free to deform. The strain gauge continuously measures the force exerted on the glass plate to induce the demanded movement. An ultrasound imaging probe is placed on the side or top of the gel with a layer of echography gel in-between to ensure coupling and omit stress induced by the probe.

*Table 4.1:* Evolution of the friction bench

2016	no security no synchronization force gauge broken mechanical noise: movement in the bench	electronic noise complicated workflow speckle tracking	
2017	synchronization security force gauge eventually working mechanical noise: movement in the bench	electronic noise removed phase correlation simplified workflow	Section 4.4.1.a Section 4.4.1.b Section 4.4.3 Section 4.4.2.a
2018	new frame → no mechanical noise force gauge working		Section 4.4.2.b Section 4.4.2.c
2019 in production	frame for well-aligned, fast US-probe positioning		



*a:* The friction bench with the motor, strain gauge, wagon and the glass plate.



*b:* Vertical probe position



*c:* Ultrafast ultrasound scanner

*Figure 4.3.2:* Photos of the experimental setup. In *a*, the new version of the friction bench is shown.

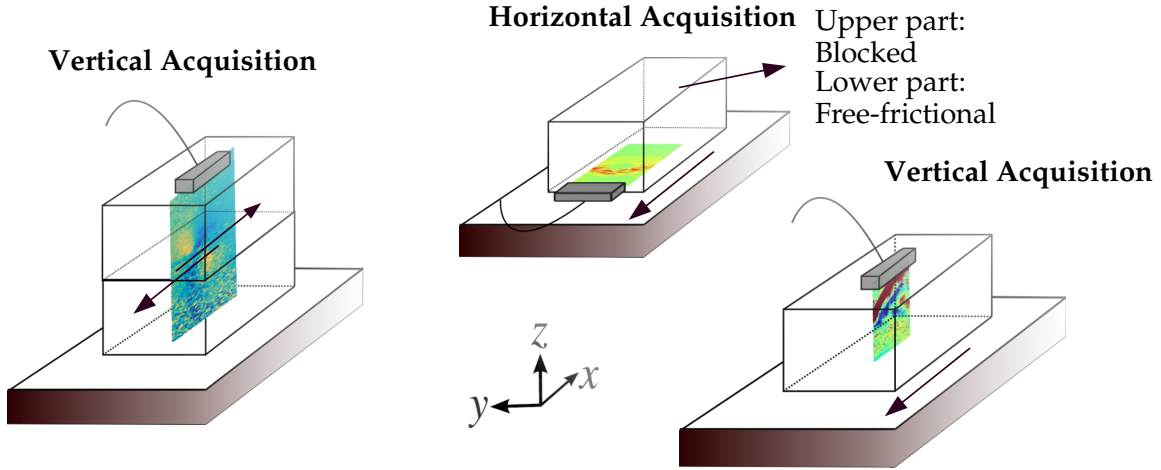


Figure 4.3.3: Schema visualizing the investigated observation configurations. Left: Gel on gel sliding. Two blocks of gel are superposed with a sand layer in-between. The lower gel is moved synchronous with the glass plate. Both gels deform and stick-slip is observed by the probe, which is positioned on top of the gels. The  $z$ -component of the particle velocity shows a higher quality above the sand layer. Although the ultrasound has to pass the sand barrier, some information can be retrieved in the lower halfspace. Middle: Horizontal observation for gel on glass with a sand layer in-between. The  $x$ -component of the particle velocity is retrieved. Right: Same as left but with gel on glass instead of gel on gel sliding.

### 4.3.5 Imaging method

In order to visualize the wave propagation, we apply phase-based motion estimation (Pinton et al., 2005) on subsequent beamformed ultrasound frames. Similar to ultrasound Doppler techniques, the retrieved phase difference gives the relative displacement in the micrometer range. For details on the algorithm, see Section 2.3. It should be noted that in terms of computational efficiency this is a large advantage over classic speckle tracking methods, because the beamforming performed by the Verasonics software results in complex IQ-Data. The correlation becomes a simple point by point multiplication in the frequency domain and time-consuming windowing is not required.

Due to the very high resolution of the probing ultrasound waves of  $3 \times 10^{-5}$  m and the high frame rate, the retrieved particle velocity can be locally integrated over time to get the total displacement along the ultrasound propagation direction. Furthermore, taking the spatial gradient of the accumulated displacement allows for estimation of one component of the strain tensor. Likewise, time differentiation leads to particle acceleration which is advantageous when continuous deformation masks simultaneous wave propagation. In Fig. 4.3.4, particle velocity snapshot of a wave-field and the corresponding particle velocity ( $v_z(t)$ ), displacement ( $u_z(t)$ ) and  $z$ -strain ( $\frac{\partial}{\partial z} u_z(t)$ ) waveforms in one space location are plotted against time.

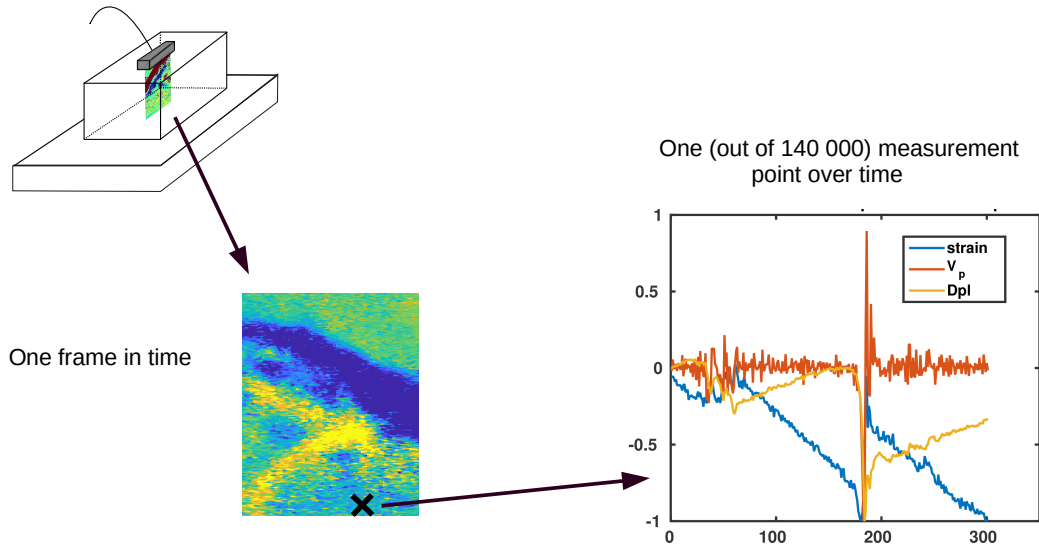


Figure 4.3.4: A timesnap of a propagating wave-field, imaged in the vertical configuration, is displayed. The snapshot is composed of 140 000 measurement points. The normalized particle velocity, displacement and z-strain in one measurement point are displayed on the right.

#### 4.3.6 Workflow

The Acquisition of raw RF-Data, beamforming and phase correlation can each be undertaken independently. This permits rapid succession of experiments. The length of the experiment is hereby only limited by the frame size of the raw data and the available memory of the host computer. The total time needed for one experiment is not limited by data treatment but by the time needed to transfer the raw data frames to the hard-disk of the host-computer. Hence, automated acquirement of multiple experiments is possible. The beamforming and phase correlation are done equally automated in a second and third step. The complete workflow is schematically indicated in Fig. 4.3.5

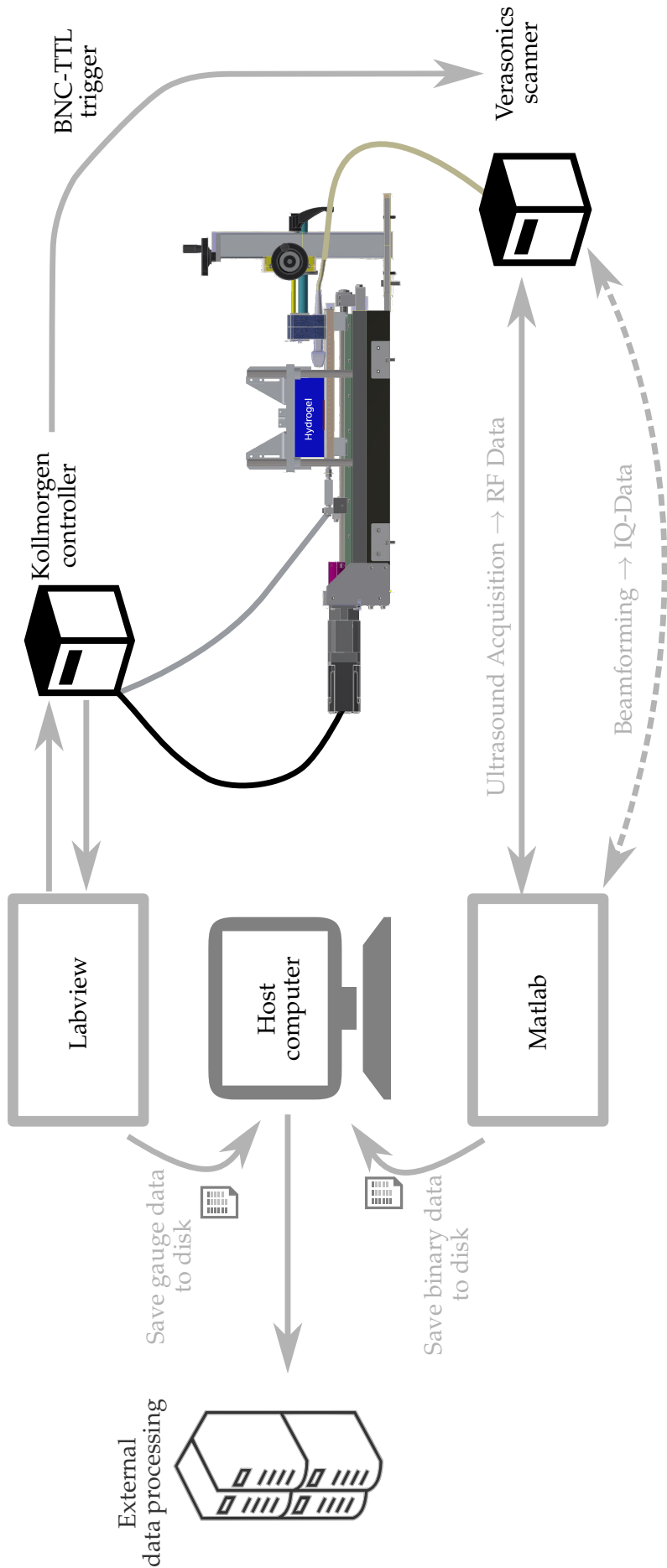


Figure 4.3.5: Experimental workflow: Raw-data acquisition, beamforming and post-processing are separate processes. Labview pilots the motor and triggers the ultrafast scanner via a BNC-TTL trigger.



## 4.4 Results

Some representative experimental which illuminate the variety of phenomena observable with ultrafast ultrasound imaging. are shown. The section is structured by observation mode. First, the vertical or fault-normal observation mode is presented, followed by the horizontal or fault-parallel observation mode. Each observation mode is subdivided into different experiments which illuminate different rupture phenomena. Table 4.2 shows an overview of the parameters of each experiment presented in the present manuscript. To help the interpretation of the observed fields, some of the experimental results are confronted with the analytic results for a moving point source as presented in Section 4.2.4. These comparisons are purely qualitative and intended to guide the physical interpretation of the experimental results. The simulation parameters can be found in Appendix D. For most experiments, a preliminary version of the friction bench was used. The alignment of the wagon and rails and the stability of the bench were not optimal, leading to movement in the system. The temporal evolution of the system might thus be biased by the experimental setup. For the last two experiments presented, the new friction bench with properly aligned rails and a stable case for the motor has been used.

With the current experimental setup, tens of experiments, each containing numerous rupture events can be performed in a single day. A robust workflow is a prerequisite for a statistical analysis of these ruptures. I started investigating possibilities of automated image treatment and data analysis. The preliminary results are presented following the respective experiment from which they were acquired.

Furthermore, the interested reader finds a selection of further observations and ideas in Appendix C.

**Infobox 4.4 Color code**

**Blue** is defined as the negative phase difference of two consequent ultrasound images. Consequently it represents particle movement **towards** the probe. Hence, if the probe is positioned on top of the gel, blue represents upwards particle movement. **Red** represents particle movement **away** from the probe. We thus choose the same convention as astrophysics. Like for the redshift in an expanding universe, red in our experiments signifies elongating movement.

Table 4.2: Summary experimental parameters

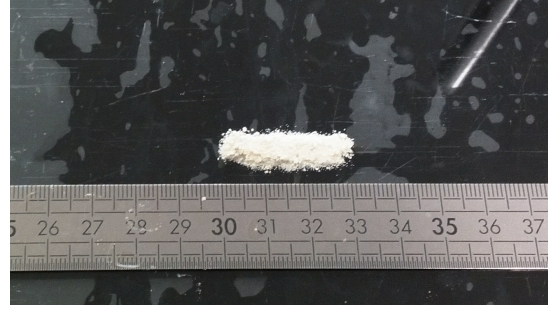
Experiment Ref.	Gel Nr.	PRF [ $\frac{frame}{s}$ ]	Angles [-]	Drive speed [ $\frac{mm}{s}$ ]	Normal load [kg]	Duration [s]
Section 4.4.1.a	Gel 2	3000	1	1	$\approx 4.0$	2
Section 4.4.1.b	Gel 2	2000	3	2	$\approx 2.75$	3
Section 4.4.3	Gel 2+4	3000	1	2	$\approx 2.5$	3
Section 4.4.2.a	Gel 4	3000	1	3	$\approx 4.0$	3
Section 4.4.2.b	Gel 4	3000	1	2	$\approx 4.0$	2
Section 4.4.2.c	Gel 4	3000	1	3	3.1	2

**4.4.1 Rupture seen from above the fault**

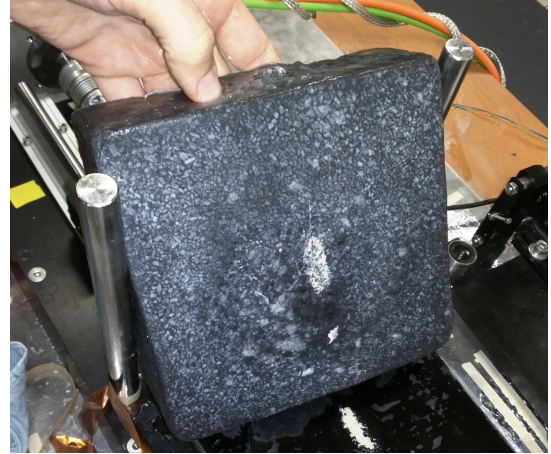
In this section we will see rupture observations imaged in the  $(x - z)$  plane. The ultrasound probe is hold in a fixed position on top of the hydrogel by the friction bench frame as shown in Fig. 4.3.2b. The gel is placed on the glass plate with a sand asperity in-between. It is blocked on the side opposite to glass-plate motion, with a small part close to the glass plate left free to deform. Normal load is induced by weights that are placed on top of the frame which hold the hydrogel in position. The setup is thus the one depicted in Fig. 4.3.3 on the right and the elastic wave radiation is recovered through the fault normal particle velocity. The most significant change in the experimental setup compared to the work of Latour et al. (2011a) is the frictional interface. I concentrate on a small patch of fine to medium sand ( $<0.5$  mm) placed in the center of the imaging plane. An example of such a sand patch before and after an experiment is shown in Fig. 4.4.1.



*Figure 4.4.1: Photos of the experimental setup. Note the inhomogeneity of the gel due to insufficient solution of PVA-particles that get deposited during the first freeze-thaw cycle when the gel is not yet solidified.*



*a: Sand patch before the experiment*



*b: Sand patch after the experiment*

#### 4.4.1.a Experiment 1 - Passing supershear front

**Setup** The sand patch in-between the glass plate and the hydrogel is no more than 1 cm wide (y-axis). The length (along  $x$ ) of the sand patch slightly exceeds the probe length. Normal loading was  $\approx 2.75$  kg, shearing speed was  $1 \text{ mm s}^{-1}$ <sup>8</sup> and total duration of the experiment was 3 s.

**Wavefield** The snapshots in Fig. 4.4.2 show one example of a slip event. The direction of plate movement is indicated by a black arrow in the first snapshot. Four events can be identified: Two weak localized events at 2 ms (Event 1 and 18 ms (Event 3) and one strong localized event at 6 ms (Event 2) precede a rupture front that passes the whole probe length at 22 ms (Event 4). The rupture nucleation spot of the event 4 lies just outside the imaging region. This becomes evident in the dilatational field lobe, which can be identified at 22 ms. Subsequently, a high amplitude wavefront is traversing the entire imaging plane. It is nearly linear, suggesting wavefront superposition similar to a Mach cone and thus supershear rupture. In total, during the three second long experiment 22 supershear fronts are identified. While event 4 traverses the entire asperity, the other events are much shorter in time

<sup>8</sup>The minimum speed which resulted in seismic wave radiation under the conditions which I tested.

and space. Event 1 and 3 happen each 4 ms before the next event and a manual investigation of the entire wave propagation film shows that large ruptures are always preceded by smaller events. This raises the question if the low amplitude events could be a sign of the following large amplitude events and thus a type of precursor.

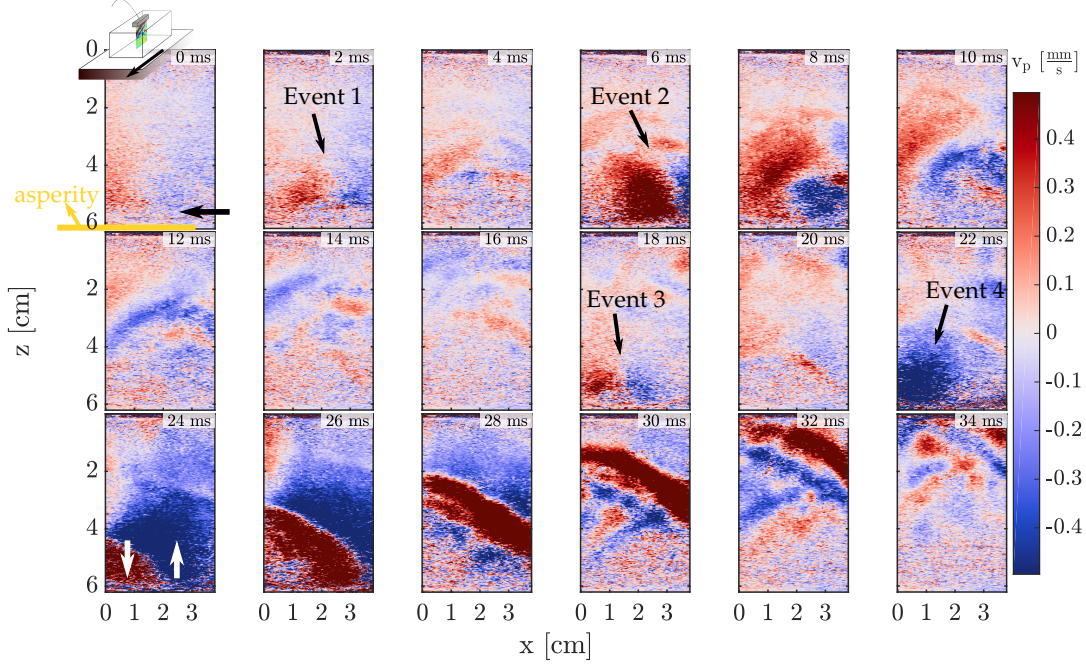


Figure 4.4.2: Particle velocity snapshots of a 34 ms long extract of the experiment. The direction of plate movement is indicated by a black arrow in the first snapshot. The schematic experimental setup with the probe position is indicated by the inset in the same snapshot. Note that blue color denotes upwards polarization of the z-component of the particle velocity and red denotes downwards polarization of the z-component of the particle velocity.

In order to analyze the mechanism of event 1 and 3, event 3 is compared to a simulation in Fig. 4.4.3. The source is a Gaussian point force in positive x-direction. It gets convolved with the Green's function of Eq. (4.6)<sup>9</sup>. The top row shows the particle velocity scaled by its maximum, the bottom row the displacement and the middle row shows event 3 of Fig. 4.4.2. The qualitative fit of the polarization of the field indicates that the source mechanism is well described by a force directed in positive x-direction. All four events show the same polarization of the leading field lobe. The events could thus be microslips that do not develop into a full rupture of the asperity. They could be due to rearrangements of grains in the sand layer or small slips of the gel, induced by stress conditions that are not elevated enough to break the entire asperity.

It is interesting to note, that the simulated displacement qualitatively fits the particle velocity data better than the simulated particle velocity. The reason might be the difference of the source between the analytical solution and the experiment. Eq. (4.6) convolves an elastic source with the corresponding Green's function. However, if the

small event actually is a microslip which exposes a continuous displacement at the source, an elastic source of the Dirac or Gaussian type is physically not justified. If the physical source in the experiment is better described by, e.g., a ramp, this could partly explain why the time-integral of the Gaussian force maps the wavefield better than the Gaussian force itself.

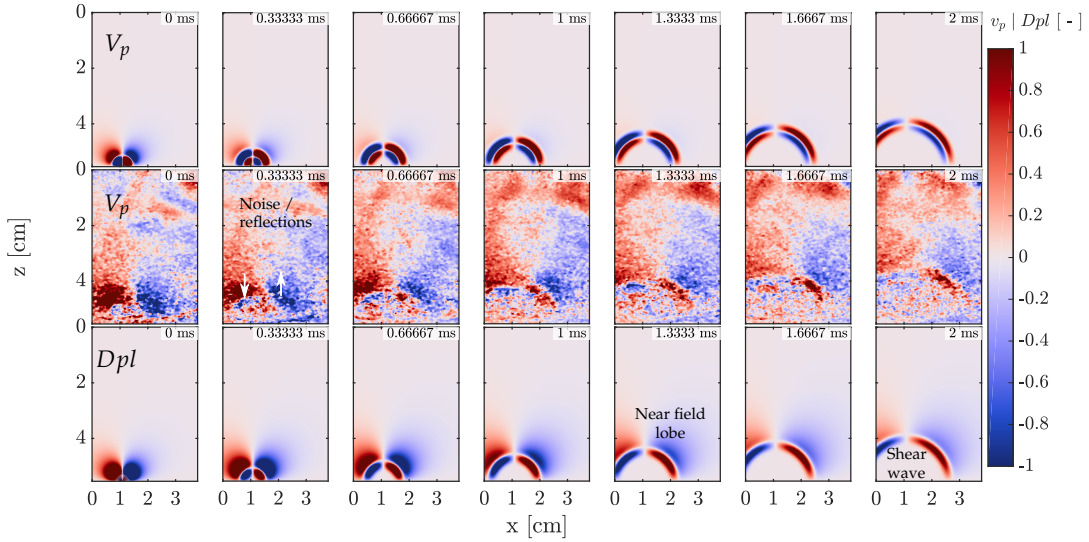


Figure 4.4.3: Particle velocity snapshots event 3 at 18 ms in Fig. 4.4.2 compared to a simulation with a Gaussian force source function in x-direction. The top row shows simulated particle velocity and the bottom row shows the simulated displacement. The middle row shows the experimental particle velocity. A median filter was applied to visually highlight the coherent wavefronts. All values are scaled by their extreme values.

The supershear interpretation of event 4 is justified by the qualitative comparison with the analytical solution of a Gaussian directional force moving at supershear speed displayed in Fig. 4.4.4 top and bottom. Although the rupture speed of the simulation was arbitrarily chosen to propagate at  $\sqrt{2}v_s$ , the simulation qualitatively fits the experimental result. Apart from the supershear rupture, the near-field lobe containing dilatational components and a rupture arrest front can be identified in both, simulation and experiment. Again, as for the singular source, the experimental data seems to be better mapped by the simulated displacement than the simulated particle velocity.

While Eq. (4.6) is simulated with a Gaussian force, Eq. (4.8) uses the displacement discontinuity  $\leftrightarrow$  body force equivalent for a pure shear slip to convolve a displacement source function with the denoted Green's function. How does this double couple (DC) of forces equivalent to a shear slip compare to our experiments?

The superposition of a moving double couple source is shown in Fig. 4.4.5. For both, experiment and simulation the particle velocity is shown. The near field lobe,

<sup>9</sup>For details on the source parameters of this and the following simulations, see Appendix D.

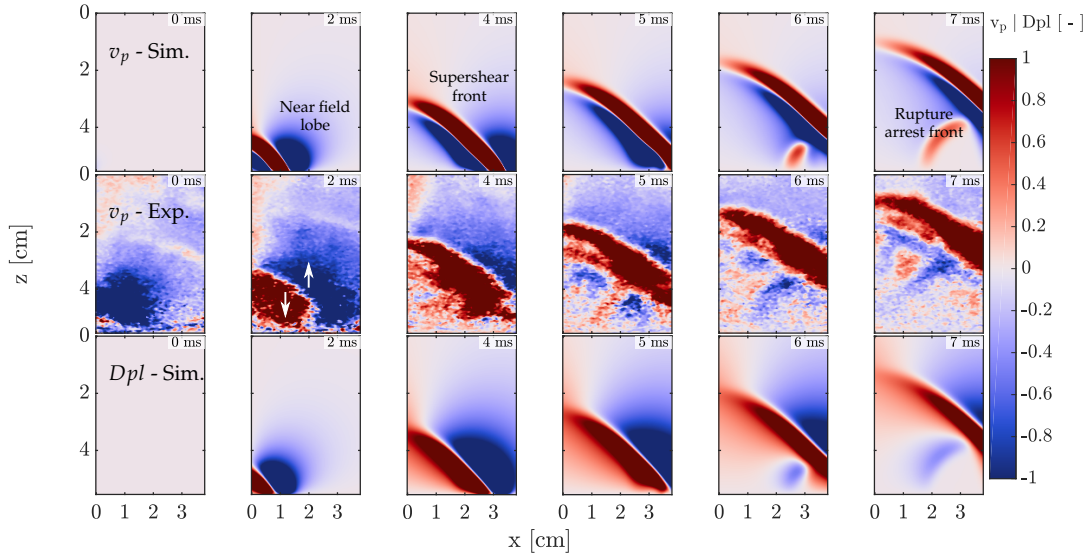


Figure 4.4.4: Particle velocity snapshots of the event starting at 18 ms in Fig. 4.4.2 compared to a simulation with a x-directional Gaussian force moving in x-direction just above  $\sqrt{2}v_s$ . The top row shows simulated particle velocity and the bottom row shows the simulated displacement. The middle row shows the experimental particle velocity. A median filter was applied to visually highlight the coherent wavefronts. All values are normalized by their extreme values.

supershear front and rupture arrest wave from the experiment are present in the simulation. The qualitative fit is good, also the first part of near-field in the DC-simulation which is downwards polarized (red) seems missing in the experiment. One physical reason for this could be that the gel is not in a static state but gets continuously deformed. The global deformation happens fast enough to be retrieved by the correlation and in parallel to the elastic wave propagation. This becomes obvious when considering that the average of the particle velocity in our snapshots is non-zero, even when no wavefield is present. Since the near field is not a sharp and well defined wavefront, it might get masked in the global deformation. The DC-field as well as the experiment show more complexity behind the supershear front than the Gaussian force field. Furthermore, the DC field which uses a ramp-displacement source shows a fit for the particle velocities while it is the integral of the particle velocity that fits the experimental data best for the Gaussian force. The double-couple being a combination of four forces, the true source mechanism might neither be one or the other but a combination of directional forces.

**Rupture speed** In order to measure the average rupture speed of a supershear rupture it is sufficient to know its angle to the horizontal and the shear wave speed. Both are related by:

$$\sin \beta = \frac{c_s}{v_r}, \quad (4.9)$$



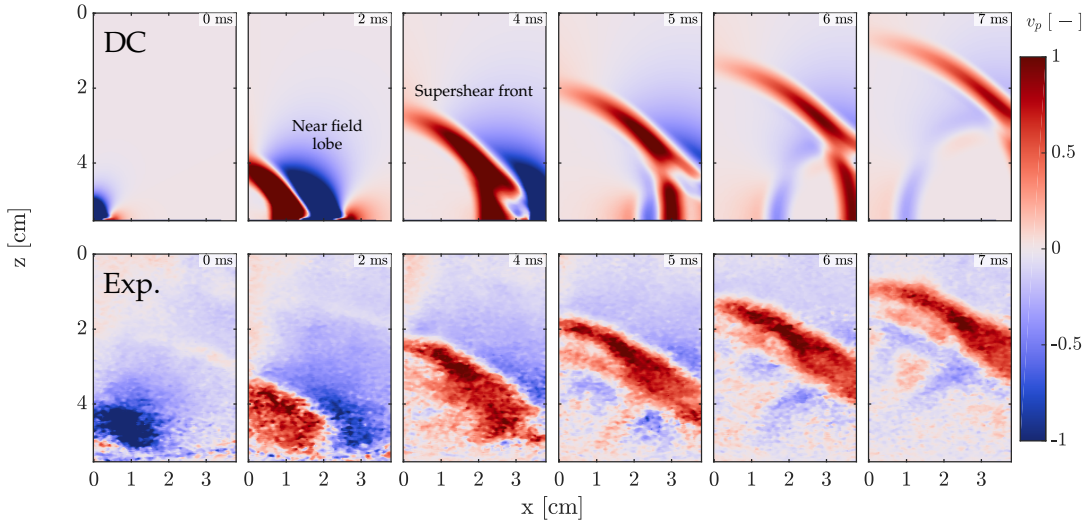


Figure 4.4.5: Particle velocity snapshots of the event starting at 18 ms in Fig. 4.4.2 compared to a simulation with a x-directional Double-couple moving in x-direction just above  $\sqrt{2}v_s$ . The top row shows simulated particle velocity and the bottom row shows the experimental particle velocity. A median filter was applied to visually highlight the coherent wavefronts. All values are normalized by their extreme values.

where  $\beta$  is the front angle to the horizontal,  $c_s$  is the shear wave speed and  $v_r$  is the average rupture speed.

The time of flight of one of Event 3 in 4.4.2 allows us to calculate the average shear wave speed of the gel, which we assume in the following to be constant in time. Any possible non-linear effects due to the deformation of the gel are thus neglected. Fig. 4.4.6 shows a combined representation of two snapshots in time of a precursory event<sup>10</sup>. Below the white dashed line the data belongs to snapshot  $t_1$ . Above the white line to snapshot  $t_2$ . The resulting time of flight gives a shear wave speed of  $6.9 \text{ m s}^{-1}$ .

We employed a linear Hough transform (Hough, 1962; Duda et al., 1972) on the snapshots of the particle velocity to automatically measure the angle of the supershear front. Fig. 4.4.7 shows an example of image segmentation and successful detection of a rupture front using the Hough transform<sup>11</sup>. For each rupture event the supershear front is detected for several consequent snapshots. The measured angle varies slightly from early to late snapshots in one rupture, but the median angle of the different snapshots stays constant for all ruptures. All detected events expose an angle of  $21.8^\circ$ . It follows from Eq. (4.9), that the apparent rupture velocity  $v_r$  is  $18.6 \text{ m s}^{-1}$  or  $2.7v_s$ .

<sup>10</sup>Precursory in the sense that it is happening prior to the passing of the main rupture front that breaks the entire asperity. This does not imply that it has to be a precursor in the sense of an earthquake precursor

<sup>11</sup>For more information on the Hough transform see Infobox 4.5

Figure 4.4.6: Example of the time of flight measurement of the shear wave speed on a composite image of two snapshots. The part below the white line shows a snapshot at  $t_1$  and the upper part shows a snapshot at  $t_2$ . The shear wave speed is calculated from  $v_s = \frac{dr}{t_2 - t_1}$  as  $6.9 \text{ m s}^{-1}$ .

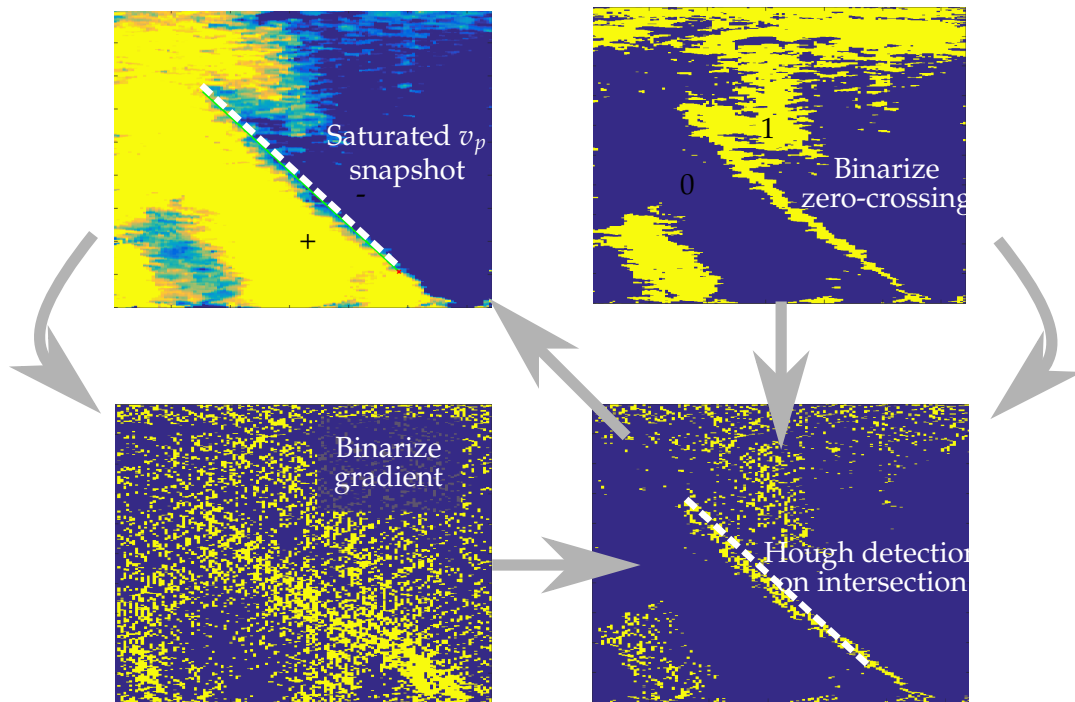
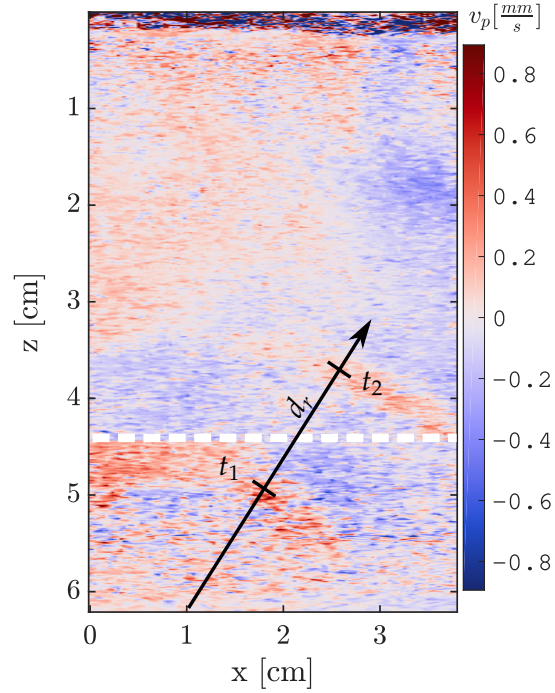
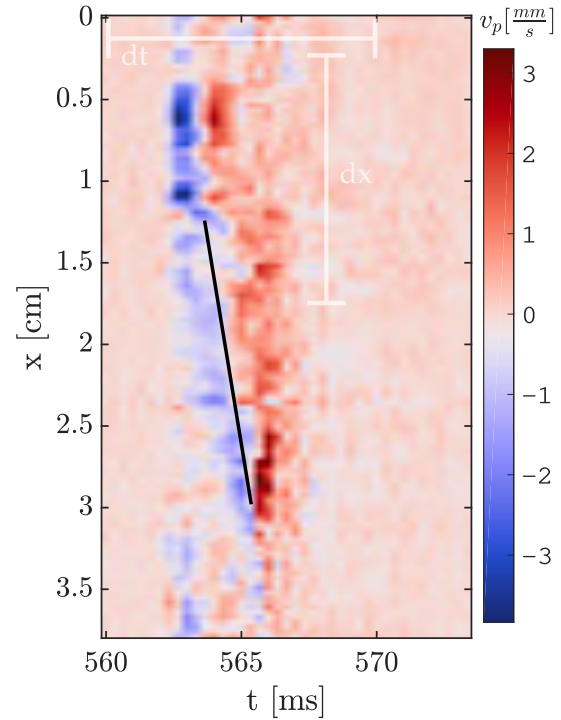


Figure 4.4.7: Example for a detection by applying the linear Hough transform. A zero crossing and gradient thresholding are applied to retrieve two binarized maps. The hough transform is run on the binarized snapshot and the slope is extracted from the coordinates of the Hough transform line.

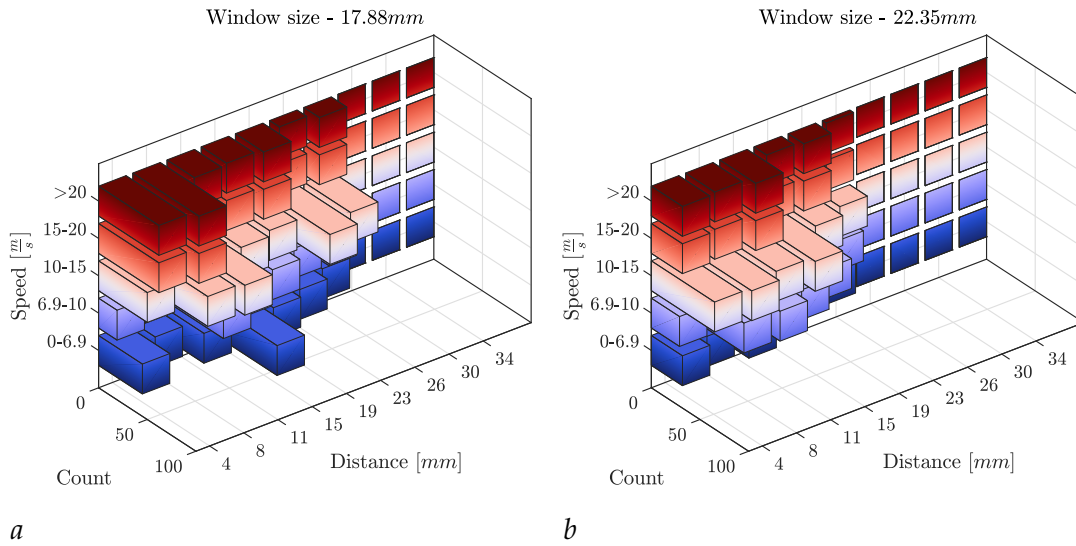
Close to the fault surface, the rupture tip can be followed through the energy it is radiating. In a measurement point close to the tip, the displacement is measured directly at the source of the emitted elastic waves. Thus, rupture speed can also be measured from a seismogram parallel to the fault surface. Fig. 4.4.8 shows an example of such a seismogram. The rupture does not propagate at a constant speed. On the first segment at the top, the rupture speed seems to defy the temporal resolution and it appears as occurring immediately. On the second segment the measured speed is  $10.6 \pm 1 \text{ m s}^{-1}$ . Because the rupture is traveling from left to right (in positive  $x$ -direction) the measurements indicate that the rupture travels faster in the beginning and continues with a speed in the vicinity of  $\sqrt{2}v_s$ .

Figure 4.4.8: Example of the time of flight measurement of the rupture speed. The speed along the profile is not constant. The rupture speed on the indicated segment is calculated from:  $v_r = \frac{dx}{(t_2 - t_1)}$ , as  $10.6 \text{ m s}^{-1}$ . The white transparent bars indicate the time and space-window correlation size for Fig. 4.4.9.



We additionally tested a second method for rupture speed detection. We take the seismogram and correlate the temporal 1D waveforms of the measurement points along  $x$ . Thus, we extract the time lag between the different arrival times of the rupture front at different  $x$ -positions. The velocity is then calculated as a time of flight from the lag and the distance. The method is limited by the ultrasound imaging frequency. Very fast ruptures or ruptures that would nucleate inside the imaging plane and propagate both ways are thus difficult to measure. The minimum window size was set to  $8.9 \text{ mm}$ , because below, the error introduced by the time discretization of  $dt = 0.3 \text{ ms}$  is too large. Furthermore, the recorded bandwidth of the elastic waves radiation might limit the available resolution. Fig. 4.4.9 shows the resulting speed measurements of the 22 ruptures in a histogram plot. Five bins, subshear, supershear  $< \sqrt{2}v_s$ , supershear  $10 - 15 \text{ m s}^{-1}$  and supershear  $> 20 \text{ m s}^{-1}$  have been chosen. The fault segment was divided into 10 bins and the speed measures were counted for each  $x$ -segment and speed bin. The  $x$ -axis denotes the start point of the measured

segment. The total segment is thus the startpoint plus the indicated window size. In contrast to the supershear angle measurement, the result is not robust, with measurements varying according to window-size and seismogram segment. In general, larger window sizes seem to favor faster speeds. We assign this to the fact, that the smaller window sizes are not robust enough for a successful correlation. As for the exemplary seismogram in Fig. 4.4.8, Figs. 4.4.9a and 4.4.9b show that supershear speeds  $> \sqrt{2}v_s$  concentrate on the early segments of the seismogram. The bin for  $v_s$  to  $\sqrt{2}v_s$  shows a lower count than higher speeds. This would be in agreement with the forbidden zone for a stable speed predicted by LEFM. Sub-shear speeds do not show a clear trend. For the smaller window size there is a high count at 15 mm, but it is completely missing in the higher window size. It is thus likely due to erroneous correlations on a small part of the segment which get smoothed out in the larger window size..



Speed measurements from correlation of  $x$ -segments as indicated in Fig. 4.4.8 in time. The window size indicates the length of the segments which are correlated with each other over the time indicated in Fig. 4.4.8.

Figure 4.4.9

**How does it slip? Displacement over time** Fig. 4.4.10 shows the local time integral<sup>12</sup> of the data in Fig. 4.4.2 relative to  $-2.3$  ms. The gel gets continuously deformed and the events 1-3 nucleate at the point where the sign of the deformation changes, an indication for the point of stress concentration. For the supershear rupture this is not the case. It nucleates presumably outside or right at the limit of the imaging plane as a comparison of the snapshots at 21.7 and 23 ms shows.

The long term temporal dynamics of this experiment become more evident in Fig. 4.4.11. The cumulative displacement ( $u_z$ ) in three points close to the fault surface

<sup>12</sup>Local in the sense that the integration is done over a short time interval only. Hence,  $t_0^{integral} \neq t_0$



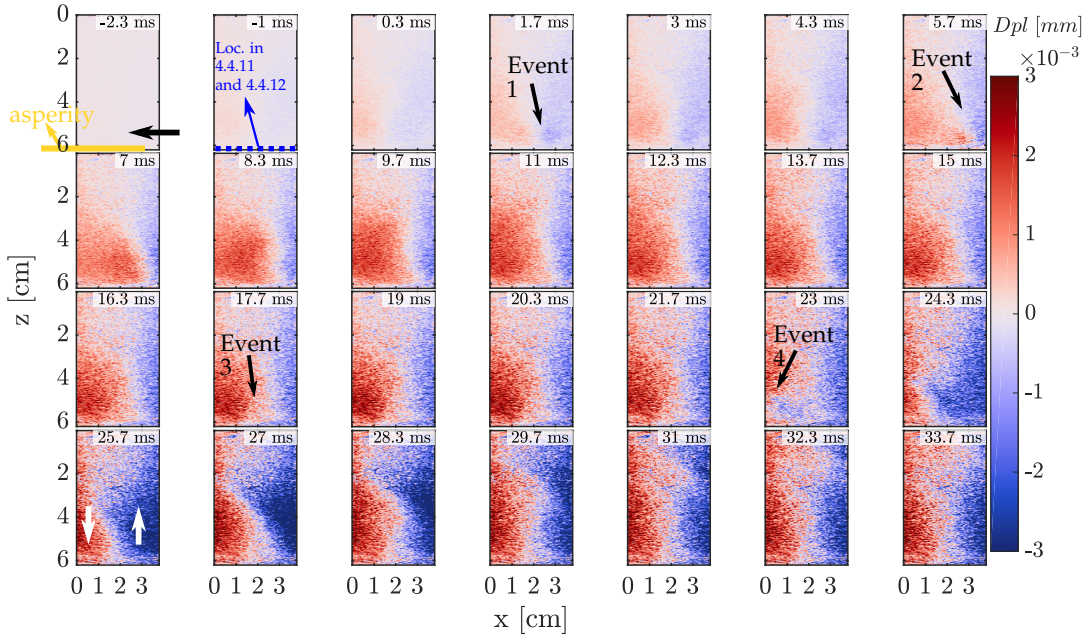


Figure 4.4.10: The cumulative displacement of the rupture cycle of Fig. 4.4.2 relative to  $-2.3$  ms. The blue points in snapshot 2 indicate the approximate locations of the 1D displacement curves in Figs. 4.4.11 and 4.4.12. The three precursory events nucleate at the point of stress concentration, where the fault normal displacement changes sign. The supershear rupture however nucleates outside the imaging region and possibly not at a visible point of stress nucleation.

is plotted against time. The overall trend is a slow increase in displacement on the left part of the fault, interrupted by rapid events of negative displacement that appear as a characteristic sawtooth pattern. The trend is opposite on the right part of the fault. Thus, while the left part globally gets compressed, the right part gets lifted or stretched away from the fault. The final 2D displacement in  $z$ -direction shows that the gel is folded. I explain this folding due to the varying boundary conditions along the  $z$ -axis. At the side opposite to the motor (and charging), the gel is free at the bottom and blocked at the top. At the side from which it gets charged, it is free. The bottom part of the gel moves away from the motor and entrails the deformation of the rest of the gel. The global trend of increasing deformation reveals the non-elastic deformation due the induced shear stress. It is not surprising that this stress, which is applied by the stepper motor in  $x$ -direction, gets transferred to the  $z$ -axis. In hydrogels, one nearly always faces the full stress and strain tensors and plane stress or strain assumptions are rarely justified.

Each sawtooth corresponds to the passing of a supershear rupture front, where curvature represents charging and the vertical part represents slip. The displacement pattern is thus a typical stick-slip pattern.

Fig. 4.4.12 shows a zoom on the displacements at the times presented in Figs. 4.4.2 and 4.4.10. Comparing the slips at different  $x$ -positions shows a small delay in

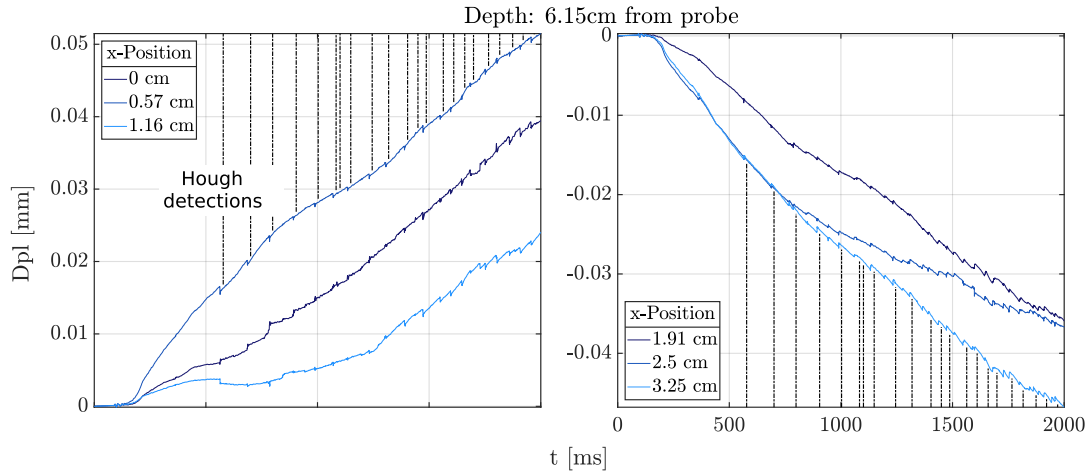
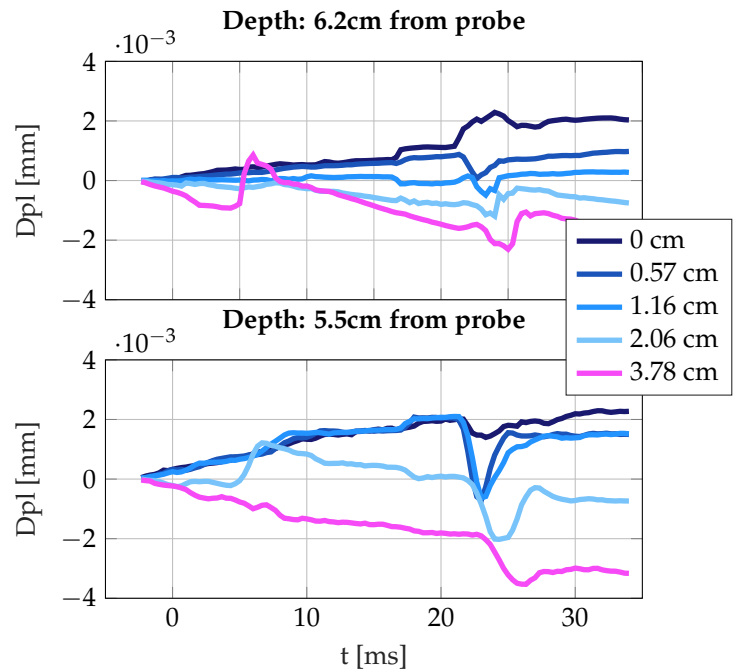


Figure 4.4.11: Displacement curves of the entire experimental time for selected points on the rupture surface. Positive is downwards displacement, away from the probe as in Fig. 4.4.10. The overall trend is continuous deformation of the gel. The black dashed lines indicate successful supershear front detections by image segmentation and the Hough transform (see Infobox 4.5). Each sawtooth in the displacement curves represents thus a rupture as in Fig. 4.4.12.

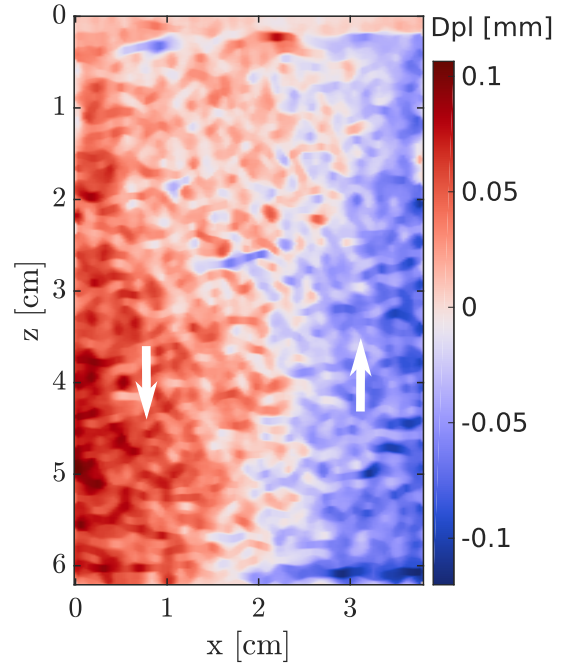
displacement. This indicates that the rupture is propagating pulse-like (see Fig. 4.2.8) and slip is thus segment per segment. The PVA-gel is a soft elastic solid, similar to the rubber investigated by Schallamach (1971). It is thus suggesting, that the observed ruptures expose a similar mechanism.

Figure 4.4.12: Displacement against time for several points along  $x$  on the rupture surface. The points are as close as possible to the fault, possibly partly inside the granular material. Positive is downwards displacement, away from the probe as in Fig. 4.4.10. The cycle from Fig. 4.4.10 is shown. In the displacement, the time-space evolution of the slip becomes evident. The first measurement point shows charging but no slip, indicating that the nucleation point of the rupture at 22 ms appears to lie in the first few millimeters of the imaged fault. Note the event at  $x=3.78$  cm and 6 ms. It represents Event 2 of Figs. 4.4.2 and 4.4.10.



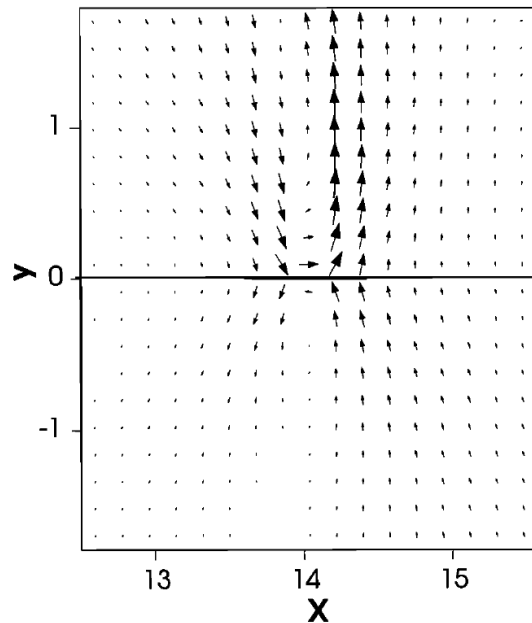
Andrews et al. (1997) numerically modeled such wrinkle-like slip pulses on a rupturing asperity in a bimaterial with 20 % material contrast. During slip, the softer

Figure 4.4.13: Snapshot of the total accumulated displacement at the end of the experiment. At the free side of the gel, it gets lifted/stretched.



medium moves away from the fault, like a wrinkle in a carpet. This effect is visualized in the 2D particle velocity snapshot of Fig. 4.4.14, where the 1D fault extends along  $x$ . At the center of the slip pulse, the polarization of the fault-normal particle velocity changes sign. The particle velocity (Fig. 4.4.2) and displacement (Fig. 4.4.10) data presented in this chapter suggest the same mechanism. Especially the snapshots at 21.7 to 28.3 ms show the propagation of this polarity change. The reasoning that slipping occurs pulse-like is in accordance with Baumberger et al. (2003), who found this mode for another hydrogel friction experiment. They observed gelatin on glass sliding. Likewise, Latour et al. (2013b) already deduced the same mechanism from observations in the  $x - y$  plane 8 mm above the interface.

Figure 4.4.14: Figure 6 from Andrews et al. (1997): Particle velocities of selected points interpolated in a two-dimensional computational grid at a given time. The thick line along the fault at  $y = 0$  marks the current extent of slip pulse propagating to the right.



**Infobox 4.5 Hough transform**

The Hough transform is a pattern recognition method commonly used in computer vision. While the original formulation was intended for detection of straight lines in 2D bubble chamber photographs and patented by Hough (1962), Duda et al. (1972) proposed a more general form. In the simple case of the detection of straight lines, a parameter space in which each line can be represented by the parameters  $r$  and  $\theta$  is created.  $r$  is the shortest line connecting the origin of the coordinate axis with the line of interest and  $\theta$  is the angle of the line to the  $x$ -axis (see Fig. 4.4.15a). The basic idea is, that finding a straight line in an image is identical to finding the largest number of pixels of a certain characteristic (color, intensity threshold) on a straight line. In a binarized image, the problem is thus to find the largest number of pixels with value 1 lying on a common straight line. Fig. 4.4.15b shows an example of the principle behind the Hough transform: Through each point of the image lines with different orientations are drawn. As soon as two points lie on the same line, e.g., the blue and red circle, this line gets a count. The higher the count of a line, the more points lie thus on the line. The lines with most counts get identified as straight lines in the image.

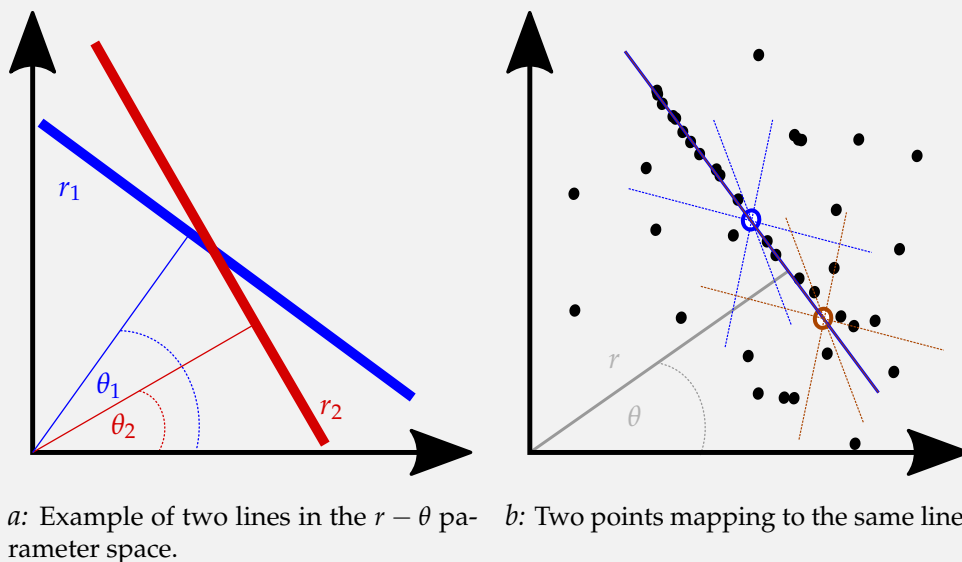


Figure 4.4.15: Explanatory sketches for the Hough transform

**Outlook** A generalized form of the Hough transform, applicable on ellipses and circles exist. I started implementation of automatic detection of the precursory events, but so far did not succeed in reliable fits. A reason might be the much lower signal-to-noise level of the precursory events. It demands more elaborate data processing than the simple gradient threshold used for the detection of the supershear events<sup>13</sup>.

<sup>13</sup>A promising method for image segmentation is presented in Section 4.5.

#### 4.4.1.b Experiment 2 - Nucleation of a rupture front

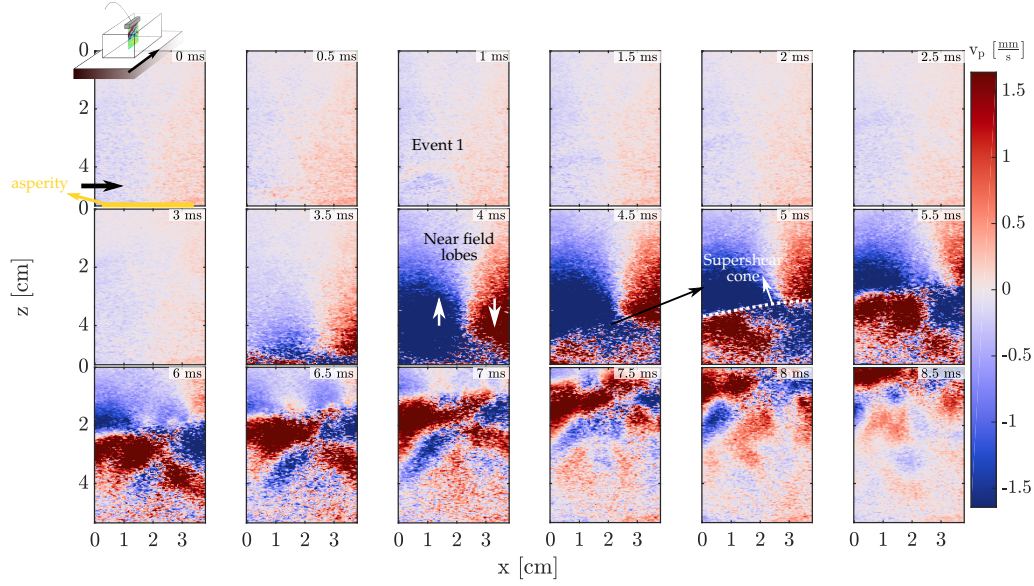
**Setup** For this experiment, setup and observation plane are similar to the previous experiment. The sand patch is no more than 1 cm wide (y-axis) and the length (along x) of the sand patch is approximately equal to the probe length. Normal loading is  $\approx 2.75$  kg, shearing speed is  $2 \text{ mm s}^{-1}$  and duration is 3 s. In contrast to Section 4.4.1.a, the probe is positioned directly above the preferred rupture nucleation position. We are thus able to observe the nucleation of the supershear rupture. Furthermore, each snapshot acquired is a superposition of three angles emitted in the compound mode. Consequentially, The displayed z-component of the particle component is an average of  $-20^\circ$ ,  $0^\circ$ , and  $20^\circ$  and reveals more details of the shear wave field.

**Wavefield** Fig. 4.4.16 shows the retrieved particle displacement for one rupture. Event 1 results from a reflection at the top of the gel, which was created in a previous rupture a (see Infobox 4.6). The main rupture is identified by the very flat supershear wavefront and appears to nucleate at about 3 cm. In contrast to the previous experiment, which showed a single near-field lobe of a supershear rupture which nucleated outside the imaging plane, both near field lobes and three polarizations of the wavefield can be identified. The near-field lobe is followed by two wavefronts of alternating polarity (see Fig. 4.4.16 6 ms). This is what we would expect for a single source double-couple source mechanism as the simulation of the vertical component of the particle velocity for a point double couple source in Fig. 4.4.17b shows. In contrast to the directional force in Eq. (4.6), the double couple solution contains three near field terms, where two terms, the purely shear and purely dilatational near field, are often called intermediate field terms. The separate parts of the field are indicated in Fig. 4.4.17. Fig. 4.4.16b exemplifies a strong folding of the gel similar to the previous experiment. It starts before rupture nucleation, intensifies with the near field and does not get totally released by the supershear rupture front.

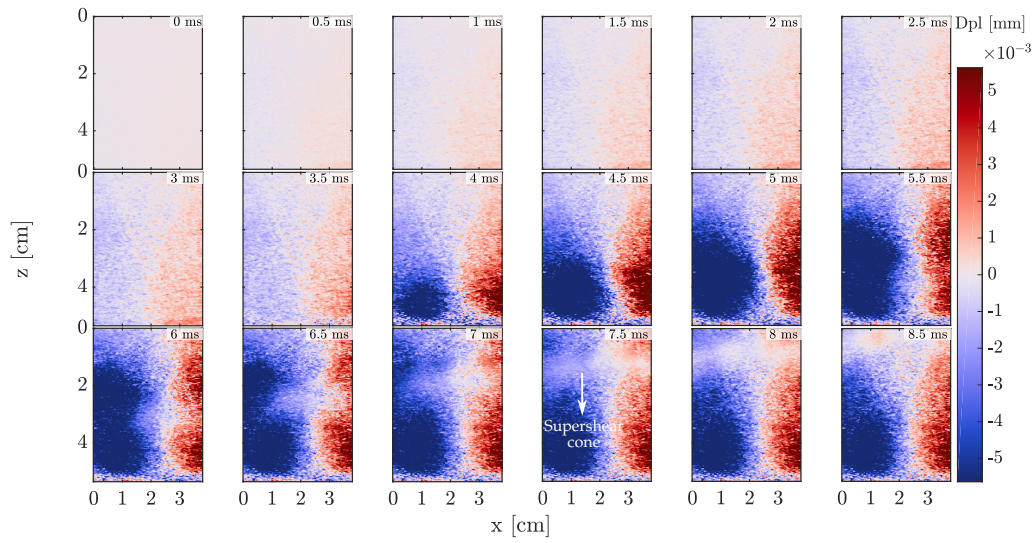
The improvement in image quality becomes evident by comparing the near field lobes in the displacement snapshots with the previous experiment. They appear much sharper.

**Temporal evolution** The displacement in Fig. 4.4.16b shows the charging of the gel. At about 2 cm, the direction of cumulative displacement changes from up to downwards. Qualitatively the pattern is clear. The imaging plane is split into two parts, one of upwards and one of downwards particle movement. The gel gets deformed, with stress concentrating at the center of the imaging plane. The global evolution is thus similar to the local evolution observed in Fig. 4.4.16b. Since the normal stress is hold constant by the weight, this deformation in the vertical component shows that the stress is not transferred parallel to the fault plane. It contains large components in z-dimension, as in the previous experiment.



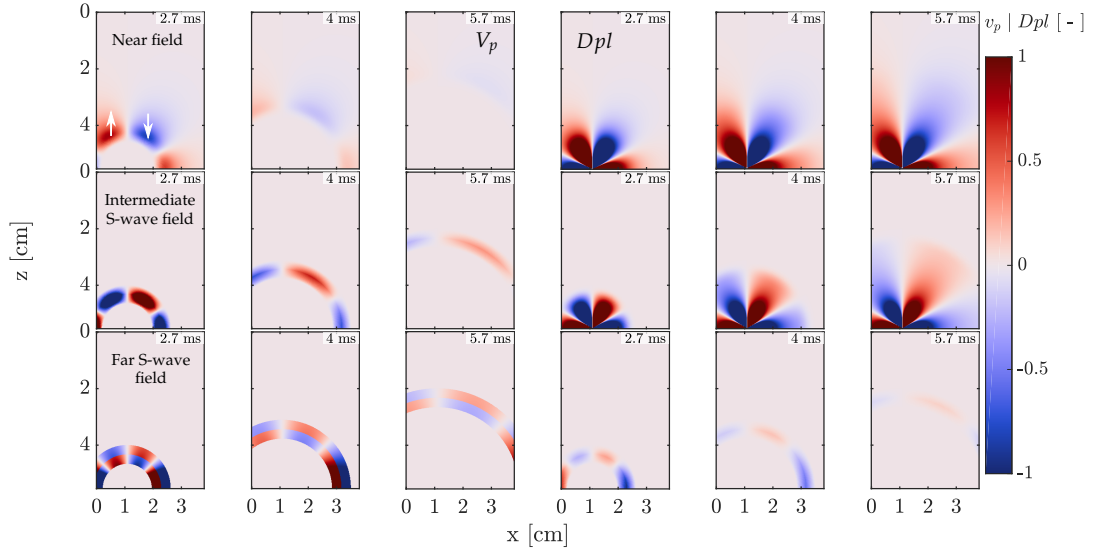


a: Particle velocity snapshots

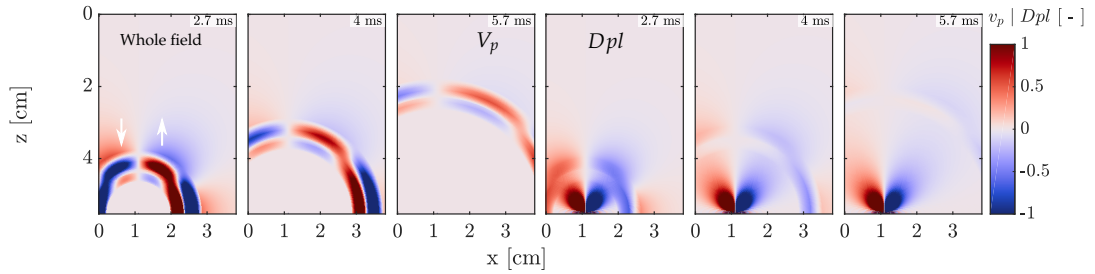


b: Displacement snapshots

Figure 4.4.16: Example of the nucleation of a rupture directly below the ultrasound probe.



*a*: Double-couple terms containing a transverse component. Top: Near-field term; Middle: Intermediate field shear wave term; Bottom: Far field shear wave term.



*b*: Double-couple full field, including the compressional terms.

*Figure 4.4.17*: Particle velocity and displacement snapshots for a double-couple point source. The left shows particle velocity and the right shows displacement. A cut-off amplitude has been introduced for each sub-dataset to highlight the weak elements of the field. The values are normalized by these cut-off amplitudes.

In total we count 59 slip events, as can be seen from the saw-teeth in the displacement curves in Fig. 4.4.18 left. The slip-rate increases with time and the total displacement seems to approach a plateau after about 1.6 s, where the slip rate stabilizes. The well-defined saw-teeth of the individual stick-slip events might for one part be attributed to the better imaging technique and for the other part to the changed loading conditions. The faster shear loading probably favors large repetitive events. The right of Fig. 4.4.18 shows a zoom on the displacement curves. They are smooth for the right part of the imaging plane (bottom right in Fig. 4.4.18) suggesting that the rupture process is a single slip event. On the left side of the imaging plane (top right in Fig. 4.4.18) an oscillation immediately after the slip is visible. Comparing with Fig. 4.4.16 we see that this oscillation corresponds to the complex wavefield that follows the supershear rupture. The absence of this wave-field at the probe position of 3.25 cm indicates that the rupture nucleates in the vicinity of this point.

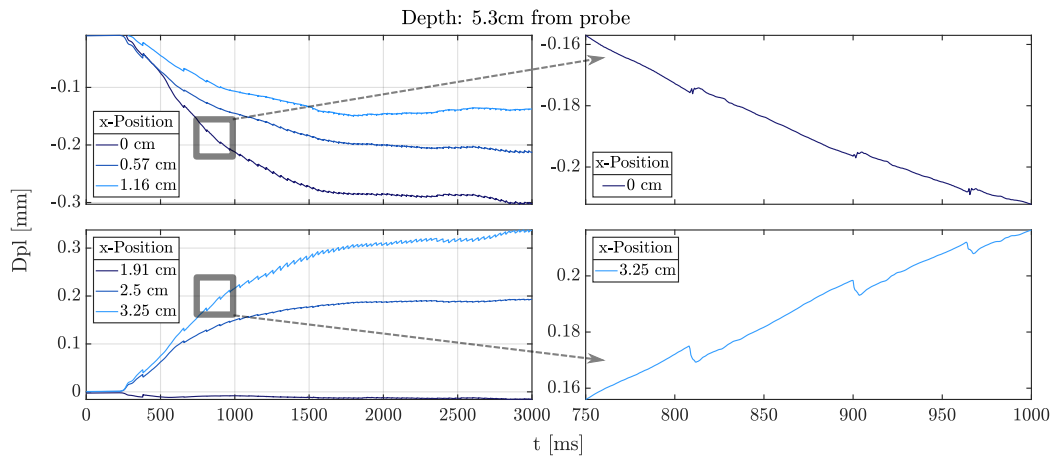


Figure 4.4.18: Displacement ( $u_z$ ) over time for three points along the fault. Each sawtooth represents an event similar to the one depicted in Fig. 4.4.16. The lifting/stretching is strongest at the edge of the asperity and nearly zero in the center.



**Infobox 4.6 Note on event 1**

The low-amplitude wave (event 1) appears similar to the depinning events already denoted by Latour et al. (2011b). However, the comparison with the Green's function of a directional point force indicates that the force of this event has a vertical component. This becomes evident in the qualitative comparison of Fig. 4.4.19. Here, the Green's function simulation was performed with a source oriented in  $z$ -direction. The top row shows an upwards directed source and the bottom row a downwards directed source. The first wavefront of the experimental data (middle row) cannot unambiguously be identified. I interpret the polarity of the first arrival as the near-field term of a downwards directed force. The deviation with the simulation right above the nucleation center might stem from the fact that in the experiment the average of three angles is displayed while the simulation contains only the  $0^\circ$  angle to the vertical. A manual investigation of the entire particle velocity film confirms the downwards-directed force hypothesis. The event appears to happen at a constant time interval before each rupture. However, a close look at the first events, temporally more elongated than later ones, shows that it is actually happening at a constant time interval after the previous rupture. It results from a reflection of the upper gel boundary. Consequently, the downwards directed source is the proper mechanism. The time-of-flight of the event is  $7.0 \text{ m s}^{-1}$ , which shows that in the four month between the experiment in Section 4.4.1.a and this experiment the characteristic time of flight has not changed.

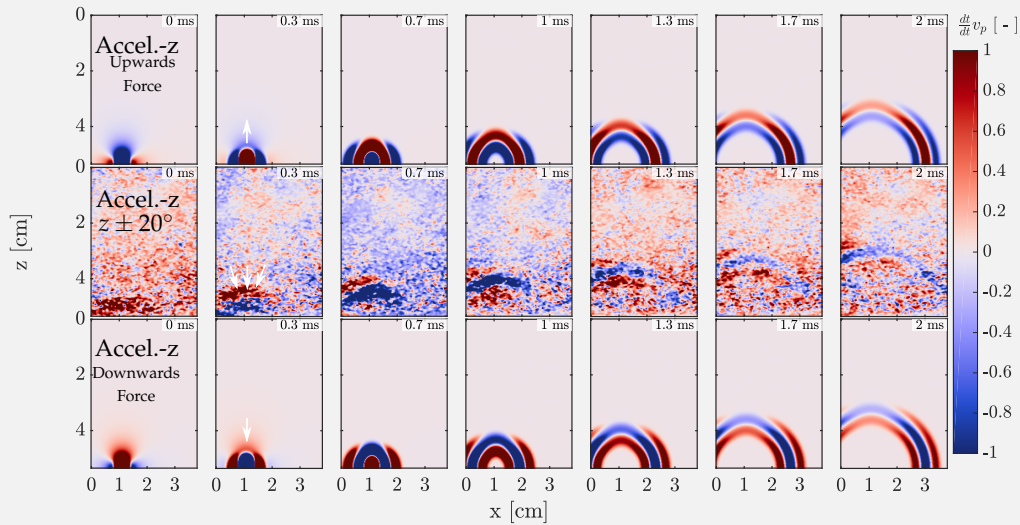


Figure 4.4.19: Comparison of the particle acceleration of Event 1 at 0.5 ms in Fig. 4.4.16 with a vertical Gaussian force simulation. The top row shows a Gaussian force directed towards the probe and the bottom row shows a Gaussian force directed away from the probe. Note that while the simulations show the pure  $z$ -component of the acceleration, the experimental data was acquired using compounding, e.i., three angles at  $-20^\circ$ ,  $0^\circ$  and  $20^\circ$  were emitted.

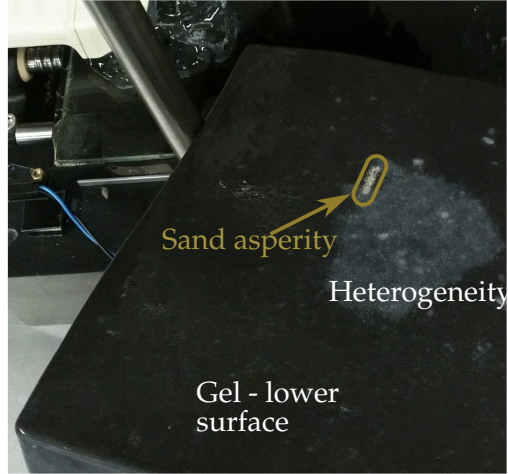
### 4.4.2 Rupture seen parallel to the fault

In this section, the observation plane is parallel to the glass plate. The rupture is imaged in the  $x - y$  plane, as depicted in the center of Fig. 4.3.3. Its  $z$ -position is 0.5 to 1 cm above the glass plate, the lowermost possible position. The retrieved component of the particle velocity is thus the  $x$ -component, the fault parallel particle velocity. We will see three different experiments, with the main distinction among them being the nature of the asperity.

#### 4.4.2.a Experiment 1 - Small asperity

**Setup** The sand patch is short and narrow with dimensions of  $\approx 0.5 \times 2$  cm, as shown in Fig. 4.4.20. This geometry allows for isolation of the rupture induced wavefields from its reflections off the gel borders. Normal load is 4 kg and the plate is driven at  $3 \text{ mm s}^{-1}$  for three seconds.

*Figure 4.4.20: Photo of the lower gel surface and the sand asperity. The asperity is located as far from each border as the ultrasound penetration depth allows.*



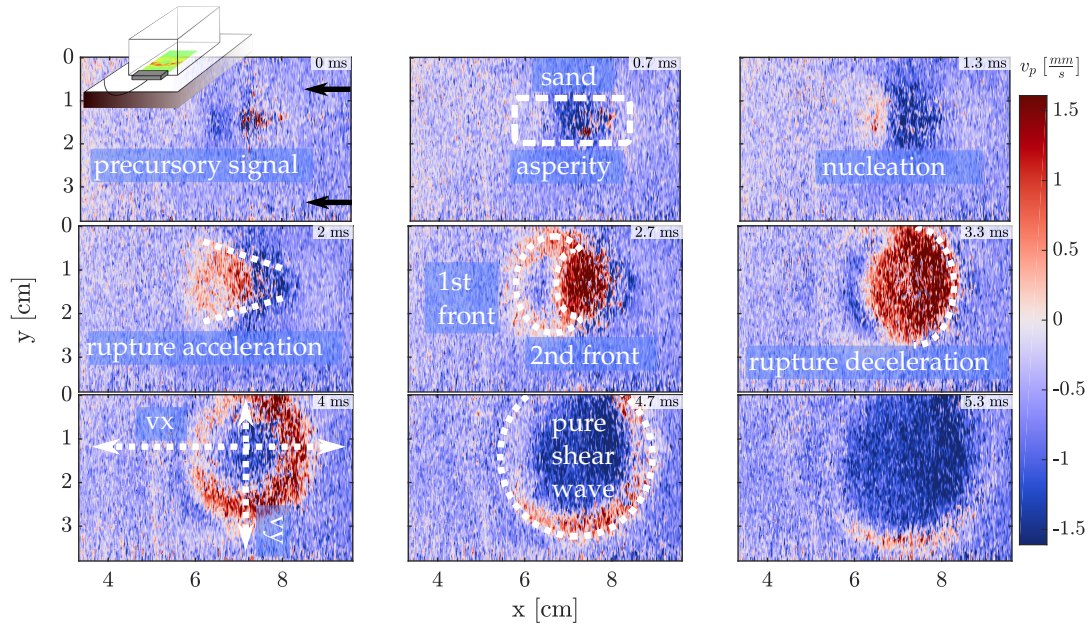
**Wavefield** Fig. 4.4.21 shows an example of a rupture cycle via particle velocity, accumulated displacement and the  $x$ -derivative of the displacement. A precursory signal consisting of very localized (a few pixel), very large amplitude events of varying polarization precedes the rupture. The first two milliseconds show, that slip is preceded by a charging phase. As the strain and displacement in Fig. 4.4.21c show, the stress concentrates at about  $x=7$  cm, in the center of the asperity. Slip starts at 2 ms and reaches its final value 1.7 ms later, when the rupture passed the entire asperity. Afterwards, the continued movement of the plate re-deforms the gel until the next rupture. Some interpretations of the rupture characteristic are indicated in the snapshots. At 2 ms, the wavefield takes a cone-like shape. At 2.7 and 3.3 ms, two wavefronts can be identified in negative  $x$ -direction. These are the rupture initiation and rupture arrest fronts. From their distance and the shear wave speed, one could calculate the average rupture speed, knowing the length of the asperity - and vice-versa. The slowing down or end of the rupture can be identified at 3.3 ms. The

wavefront is neither cone-like nor circular but ellipsoidal: The shear waves are catching up with the rupture tip. The axis of rupture propagation can also be identified in the post-rupture pure shear wave field at 5.3 ms. The amplitudes of the circular waves are stronger in  $y$ -direction, the exact property acoustic radiation force imaging takes advantage of in medical imaging.

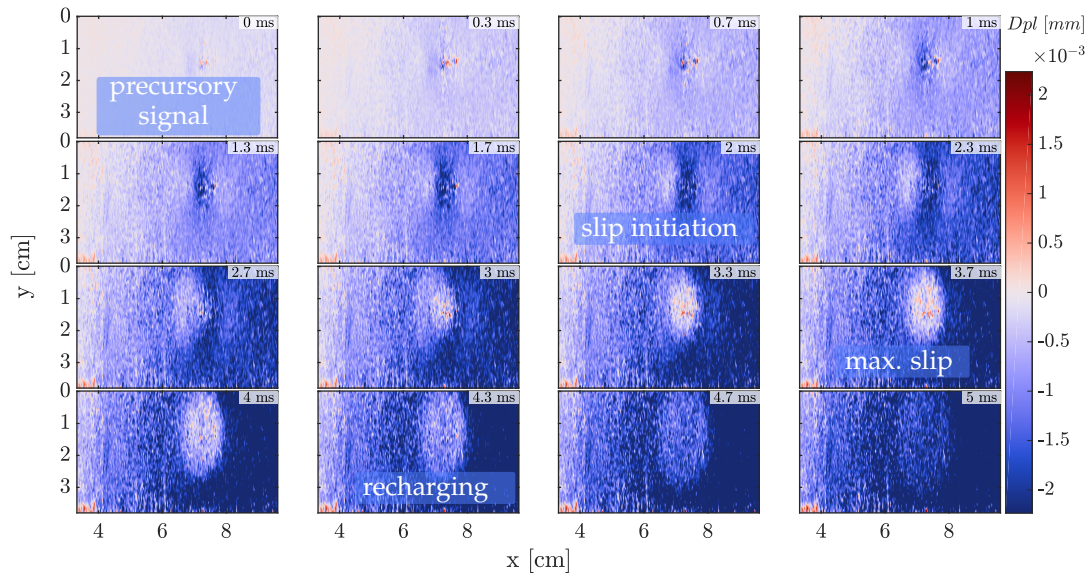
The particle velocity and displacement snapshots show that the gel is constantly deformed towards the probe (blue background). However, periods of global deformation in opposite direction exist in the full film of the experiment (see Fig. C.1.1). This indicates that sometimes the gel slowly slips back. At least one of these events appears to be initiated by a left-traveling rupture, which is shown in Fig. C.1.1. Note that the polarization of particle movement is the same as for the rupture presented above. The main front of left-, as well as Right-traveling ruptures is polarized with a particle velocity away from the probe. The movement of the slip is thus equal, independent of the side on which the rupture start. If we set a simple dipole force as the source mechanism, one case represents a dilatation mechanism, while the other represents a compressional mechanism<sup>14</sup>. The generation of ruptures traveling in both directions is probably favored by the setup of a small asperity that better equilibrates the stress conditions throughout the gel. However, left-traveling rupture propagation might also be promoted non-uniform shear stress induced by the motor. This effect of the imperfect alignment and unstable frame causing friction on the rails is shown in the next section, which analyses the long term evolution of the displacement.

**Source mechanism** Due to the symmetry of the Green's function towards the  $x - z$  plane, the simple line source was a sufficient equivalent to the frictional interface for the vertical observation plane. In the present experiment however, the experimental data does reveals the extension of  $\approx 5$  mm in  $y$  of the asperity. Furthermore the nucleation of the asperity rupture is resolved in space and time. The simulation of the  $x$ -component of the wavefield in the  $x - y$  plane through a line source is thus less evident than the previous was the case for the previous simulations in the  $x - z$  plane. Fig. 4.4.22 shows two exemplary simulations using the singular-force and the double-couple solution in the fault-parallel observation plane, 1 mm above the fault. For the singular-force, the same parameters as in Fig. 4.4.4 were used, but with a shorter source-line of 2.6 cm. The nucleation phase of the experimental ruptures (see also Fig. C.1.1) is not well retrieved. The rupture and consequent wave propagation match better: The amplitudes of the shear wave are larger orthogonal to the rupture direction and an overall negative polarization of the particle velocity in the wake of the rupture is observed.

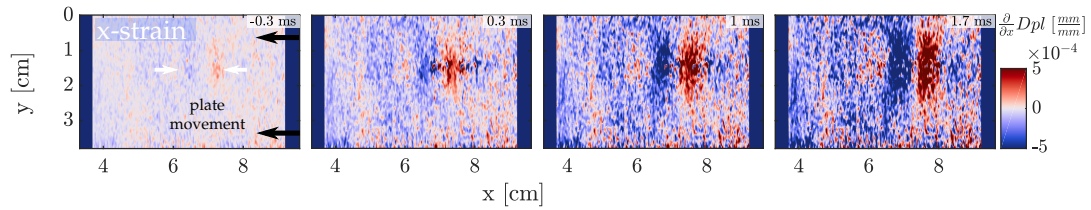
<sup>14</sup>In the case of a wrinkle-like rupture the dilatation can be visualized by the pulling of a carpet wrinkle and the compression as the pushing of a carpet wrinkle



a: Particle velocity snapshots.



b: Displacement relative to 0 ms.

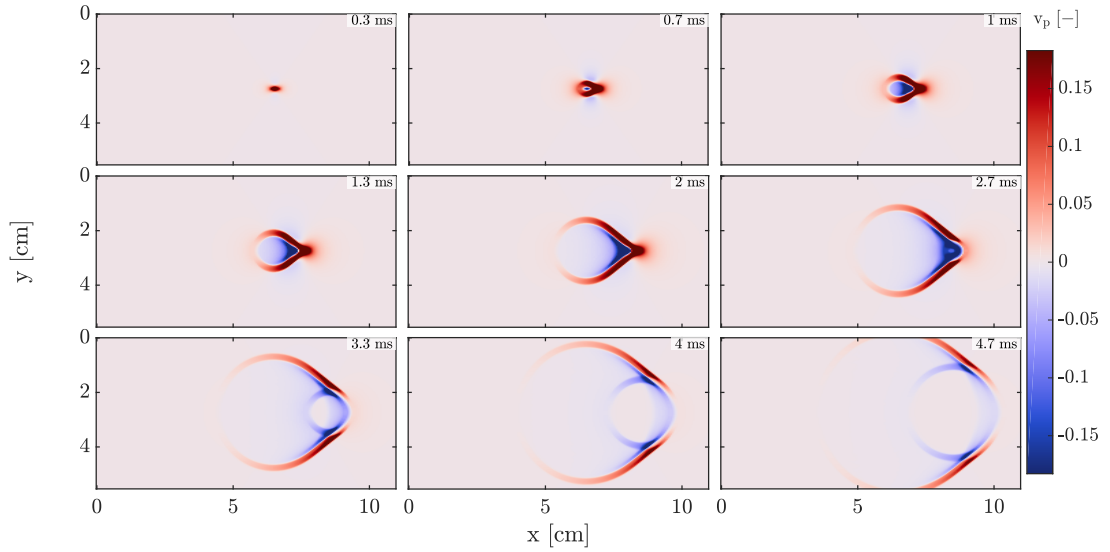


c: x-gradient of the displacement.

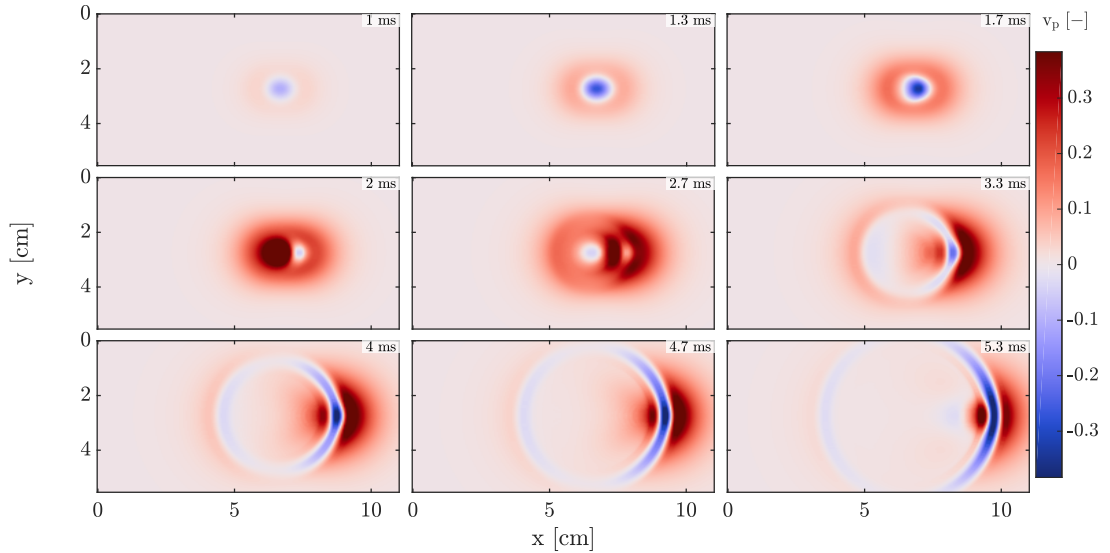
Figure 4.4.21: One cycle in the horizontal observation plane. Black arrows indicate plate movement and the schematic inset visualizes the experimental setup.



For the DC-simulation the best match was found for a rupture starting at  $3 \times v_s$  and decelerating to  $v_s$  ( $6.9 \text{ m s}^{-1}$ ). The nucleation phase matches the experimental results slightly better, especially compared to Fig. C.1.1a. I hypothesize that during the experimental rupture nucleation different forces are present, possibly containing a  $y$ -component. The true mechanism is thus more complex than a single-force but not a pure double-couple either. For a numerical analysis corresponding to the complexity of the experimental setup, a parameter sweep over the source types rise time and rupture speed including the  $y$ -extension of the asperity would be needed.



a: A singular-force rupture at constant ( $1.6v_s$ ) speed.



b: A DC rupture starting at  $3v_s$  and decelerating to shear wave speed.

Figure 4.4.22: Moving sources of the single-force and DC type. The fault parallel particle velocity is simulated 1 mm above and parallel to the frictional interface. Note that while the experimental asperity has a width  $y$ , the simulated source is a line of discrete point sources.

**Temporal evolution** In the horizontal observation plane the accumulated displacement should give us an idea of the long term dynamics of deformation and the slip of the bottom part of the gel and potentially of the sand patch. Fig. 4.4.23 shows the displacement curves for selected points (see inset on the left) on the asperity. Two main features are observed.

- The deformation approaches a plateau at about 1.5 s.
- The deformation shows an oscillation pattern throughout the whole experiment.

The oscillation is very likely due to the imperfect alignment and fixation of the preliminary friction bench. We will see that in the first experiments undertaken with the new friction bench, the oscillations vanish. Even though the experimental setup is flawed, the plateau indicates that the system develops into a stable state of stick-slip. The short term dynamics become evident in the time-zoom of the inset on the right. Each long-term oscillations contains several ruptures comparable to the one shown in Fig. 4.4.21. In total, there are more than 200 ruptures, propagating in both directions (see Fig. C.1.1).

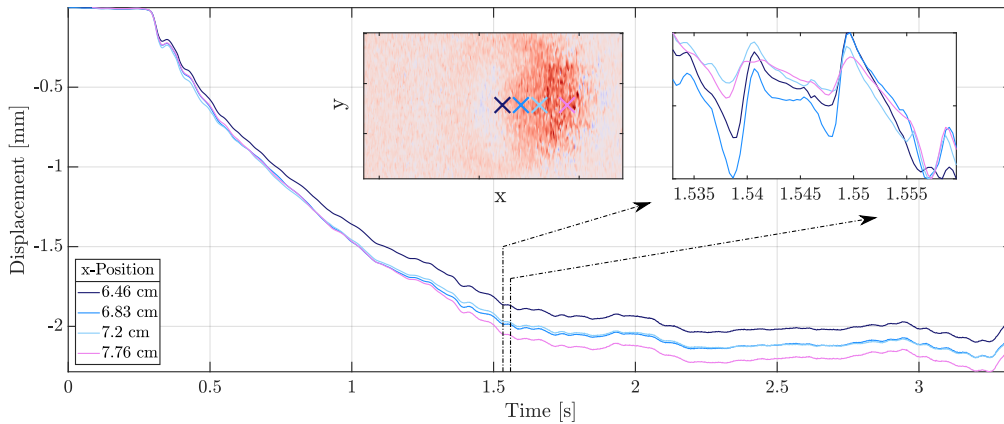


Figure 4.4.23: Displacement against time. The main plot shows the displacement in the indicated points of the left inset. The right inset shows a time-zoom of the same displacement curves.

**Image detection** As was the case for the vertical plane, the wavefield data in the horizontal plane, which is shown in Fig. 4.4.21, is highly resolved and shows a variety of phenomena. However, the cycle represents just 2 % of the experiment, and longer experiments are possible. Thus, automated or semi-automated data analysis is crucial for exploitation of the entire potential of the experimental setup. Ideally, the entire  $x - y$  data is analyzed, Here we will start with a simplification and represent the

central part of the asperity as a seismogram. We thus average over a few probe elements along  $y$  at the  $y$ -position of the asperity and plot the data along  $x$  and time. The rupture nucleation point and the wavefield traveltime can easily be identified in Fig. 4.4.24. Similar to Section 4.4.1.a we use image segmentation and the Hough transform to extract the rupture velocity from the wave-field. In contrast to the vertical observation plane however, where we investigate the elastic wave-field in the gel, the events close to the rupture surface in the horizontal plane bear a strong signature of the source. This is reflected in inclination changes in the seismogram.

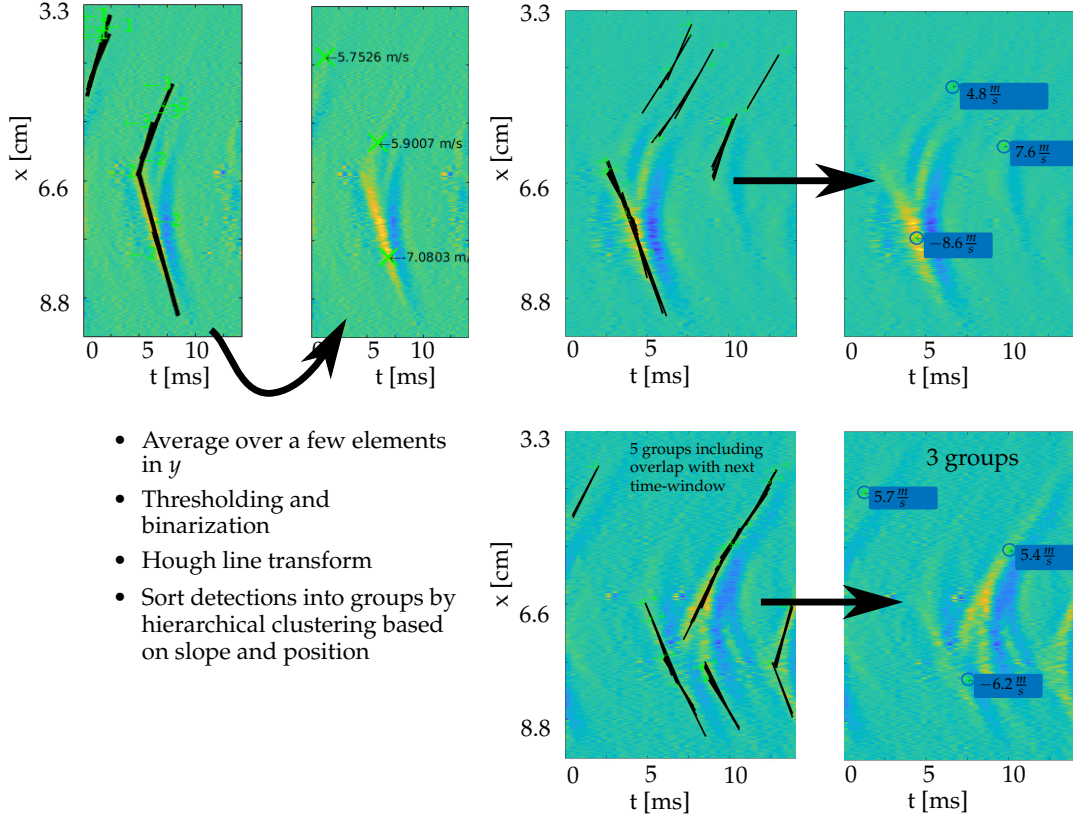


Figure 4.4.24: Detection examples of  $x - t$  seismograms.

Events get clustered by their spatial position and inclination by help of hierarchical clustering to prevent double detections. The results are shown in Fig. 4.4.25. Each point represents a speed measurement. The  $x$ -location indicates the central point of the segment on which the speed was measured and the  $y$ -location the measured speed. Each point does thus represent a speed measurement of a segment of a rupture. A rupture and its associated shear wave field can thus be represented by more than one point. Large dots signify left-traveling events and small dots signify right-traveling events. Red color characterizes super-shear speed and blue color speeds below the shear-wave speed of  $6.9 \text{ m s}^{-1}$ . The histogram on the right shows results measured with the same methodology but in  $y$ -direction, along the line indicated in Fig. 4.4.21a. Due to the large ratio  $\frac{x}{y}$  of the asperity, the measurements along this

line are expected to be close to the shear wave speed of the medium. The histogram confirms that on average the shear wave speed is well reproduced.

While false detections and over- or under-estimations cannot be excluded, the plot reproduces the essential characteristics of the full wave propagation film.

- Ruptures propagate in both directions (see Appendix C.1 for snapshots).
- Ruptures starting from a central point as well as reflecting ruptures from the end of the asperity exist. Ruptures propagating very fast or propagating both ways appear as nearly straight lines in the seismograms. In the last case the center point of the segment is also the nucleation point. These ruptures are represented as  $>20 \text{ m s}^{-1}$ .
- Shear waves speeds are measured nearly entirely outside the rupture zone, indicating that no or very few sub-Rayleigh ruptures exist.
- The pyramidal form of the supershear speeds reflects the deceleration of ruptures traveling from one end of the asperity to the other or from the center of the asperity.

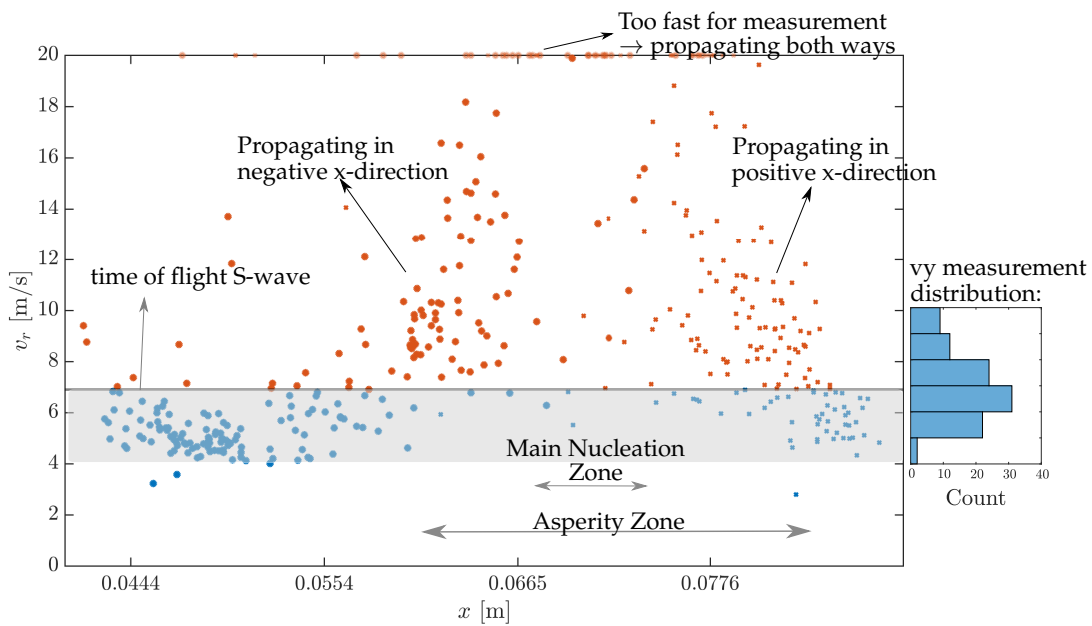


Figure 4.4.25: Speed profile of all detected rupture events. Each point represents the speed measured for a segment that has its center in the  $x$ -position against which it is plotted. Large dots represent events traveling to the left, small dots represent events traveling to the right. The histogram on the right shows the speeds measured with the same technique orthogonal to the rupture direction, starting in the center of the asperity.

The precursory signal visible in Fig. 4.4.21 is of an interesting nature. It exposes high amplitudes and very localized polarity changes. Thus, in a local region of interest comprising the precursory signal, the Variance of the signal is higher than in the



rest of the imaging plane comprising background noise or coherent wavefronts. The main rupture events also have a characteristic footprint in their statistical moments. I took advantage of this to automatically classify events into ruptures and precursors based on the geometric distribution of their statistical moments. Fig. 4.4.26 shows the results for 1.5 ms. Although false positive and missed events cannot be excluded, a pattern is clearly identifiable. The precursory signal start at exactly the same time lag (3 ms) before the main rupture event traverses the asperity for most detections. Combining this knowledge with the fact that the signal seems to move along the asperity line in rupture direction leads to several possible interpretations.

- The asperity emits pulsed high frequency acoustic signals that disturb the ultrasonic signal, leading to a decorrelation between consecutive snapshots and thus to the localized high-amplitude events. For this, the signals would have to be  $>4$  MHz, the approximate cut-off frequency of the probe. The acoustic emissions observed by, e.g., Hulbert et al. (2019) and Goebel (2013) are in the kHz to MHz range. These are experiments with very high confining stresses though and to assume the same for the present setup would be highly speculative.
- Movement in the experimental setup of the preliminary friction bench moves the probe vertically and the ultrasonic beam hits the sand or glass plate, leading to decorrelation. However, this does not explain the coincidence of the signal with rupture events (see Fig. 4.4.26) and why a similar signal is observed with the new friction bench as we'll see in the next section.
- Grains move due to the vertical displacement in the gel that we have seen in Section 4.4.1
- Grains or patches of grains move or get rearranged due to a redistribution of force chains.

⇒ In the last two cases the movement would be in the sand layer, below the idealized imaging plane of the probe. The ultrasonic beam however is not a perfectly flat plane and at the distance of 7 cm from the probe at which the precursors are observed, it is quite likely that sand movement might be sensed by the beam. This interpretation would also explain why some precursors expose weak diffraction mustaches.

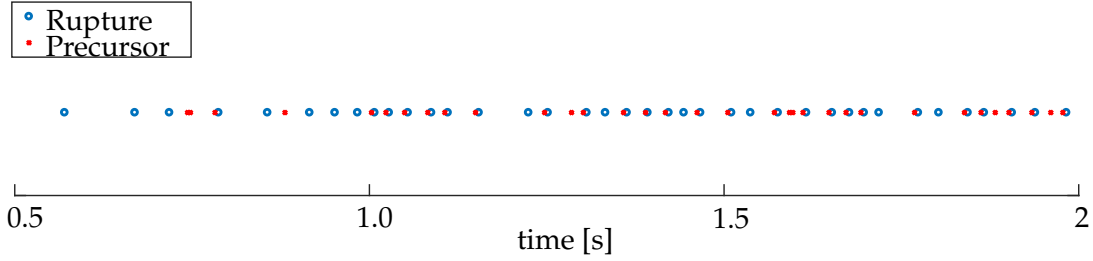


Figure 4.4.26: Variance based event classification into precursory events and main ruptures. The precursory events are detected nearly exclusively at one well-defined time-lag (3 ms) before the main ruptures.

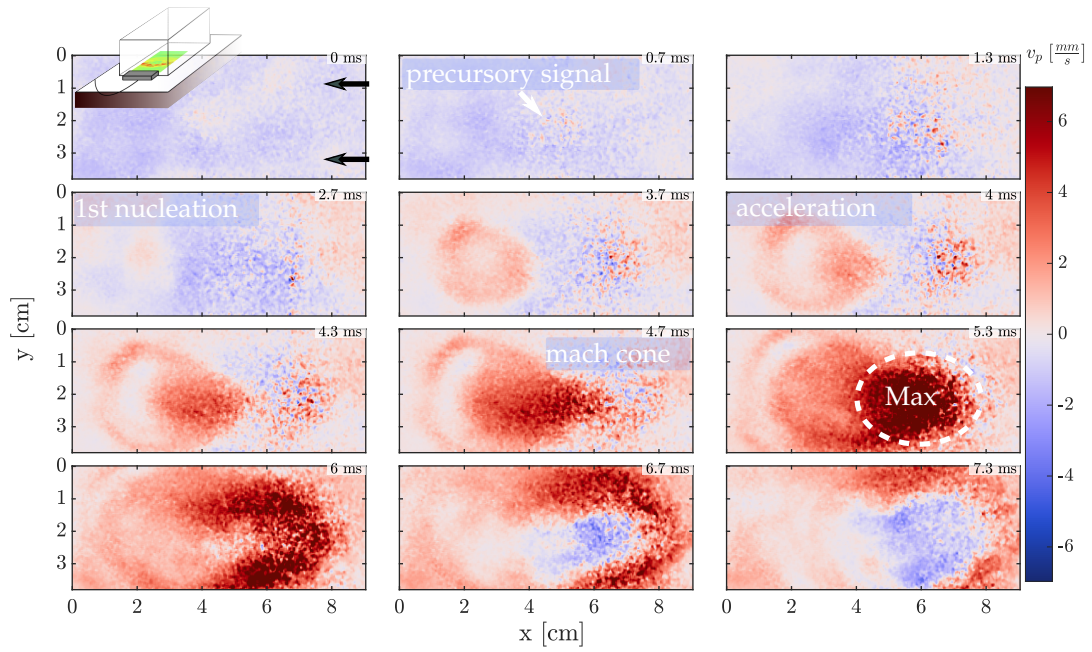
#### 4.4.2.b Experiment 2 - Larger asperity

**Setup** The setup is similar to the previous one. The main difference is that the sand path is now  $\approx 4$  cm long and initially 0.5 cm wide<sup>15</sup>. Furthermore, the initial sand patch is thicker ( $< 3$  mm), ensuring several layers of grains in between the gel and the plate. Consequently, the type and shape of the rupture events changes. Furthermore, the new, stabilized and well aligned friction bench was used.

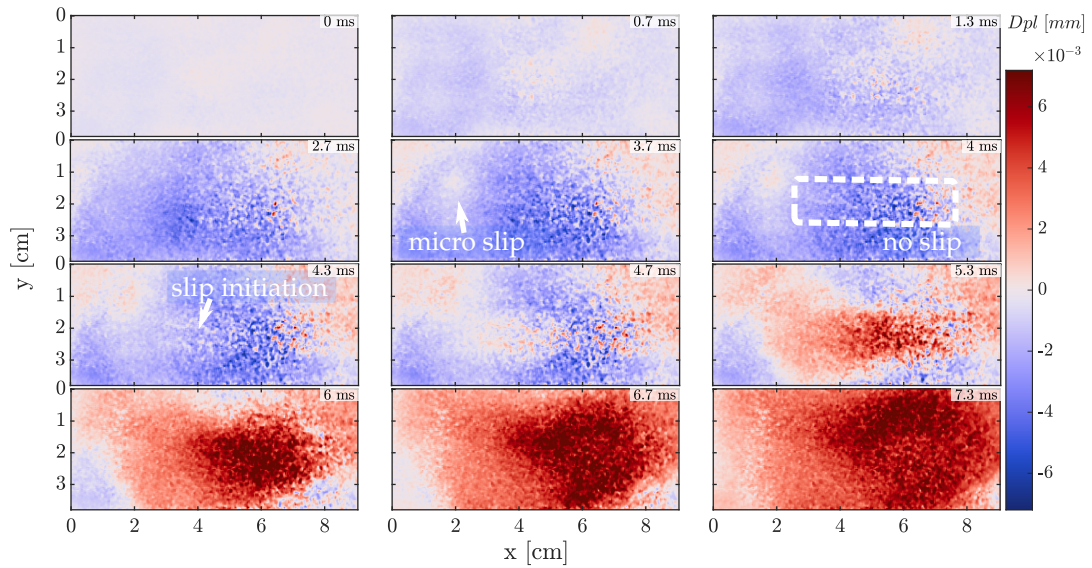
**Wavefield** Fig. 4.4.27 and Fig. 4.4.28 show the particle velocity and displacement in  $x$ -direction of two rupture events. Fig. 4.4.27 additionally shows an extract of the  $x$ -derivative of the displacement. In both setups, the main rupture clearly propagates along the sand patch. It is preceded by a singular event nucleating at about 2 cm. As the event propagates, it transform into or triggers the main rupture. The main rupture is a supershear event which is clearly identified by the transformation of the circular shape into a cone-shape. The displacement snapshots on which the continuous movement on the asperity becomes visible confirm further confirm the interpretation. A comparison of the wavefields after the rupture traversed the entire interface of both examples (Fig. 4.4.27 and Fig. 4.4.28) shows qualitatively different radiation patterns. They indicate not only the rupture speeds but also the rupture direction varies between events. While the rupture in Fig. 4.4.28 seems to advance in a straight line, the wavefield of the rupture in Fig. 4.4.27 indicates a slightly deviated path: directed downwards-right in the beginning and upwards-right in the end. Furthermore, the event in Fig. 4.4.28, which clearly is right-traveling in the beginning (2 millis), has its maximum of radiated energy at  $\approx 7$  cm while the event in Fig. 4.4.27 has its maximum at  $\approx 8$  cm. The earlier maximum in Fig. 4.4.28 could be either induced by rupture arrest or a re-rupturing of the surface from left to right.

The  $x$ -gradient of the displacement in Fig. 4.4.27c is an indicator for the  $x$ -component of the strain. It suggests, that stress is concentrating at 4-5 cm, at the approximate center of the asperity.

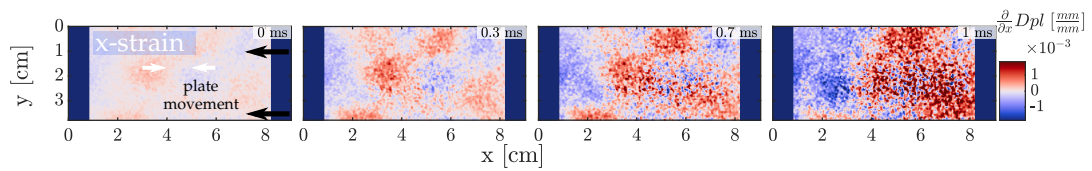
<sup>15</sup>Due to the larger extension in  $z$  of the sand layer it gets spread during the experiment



a: Particle velocity snapshots of an exemplary rupture

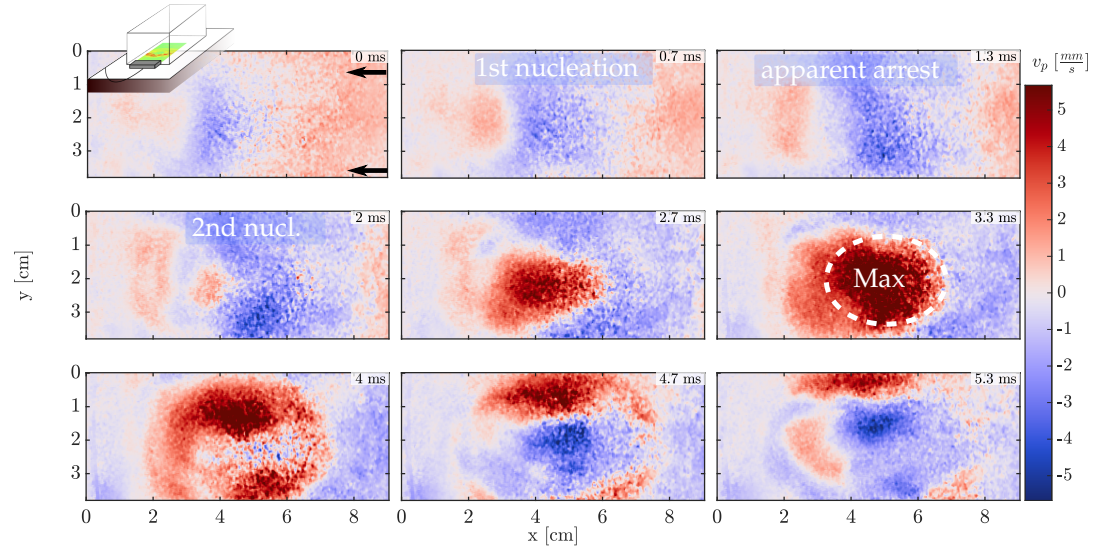


b: Displacement snapshots relative to  $t_0$ .

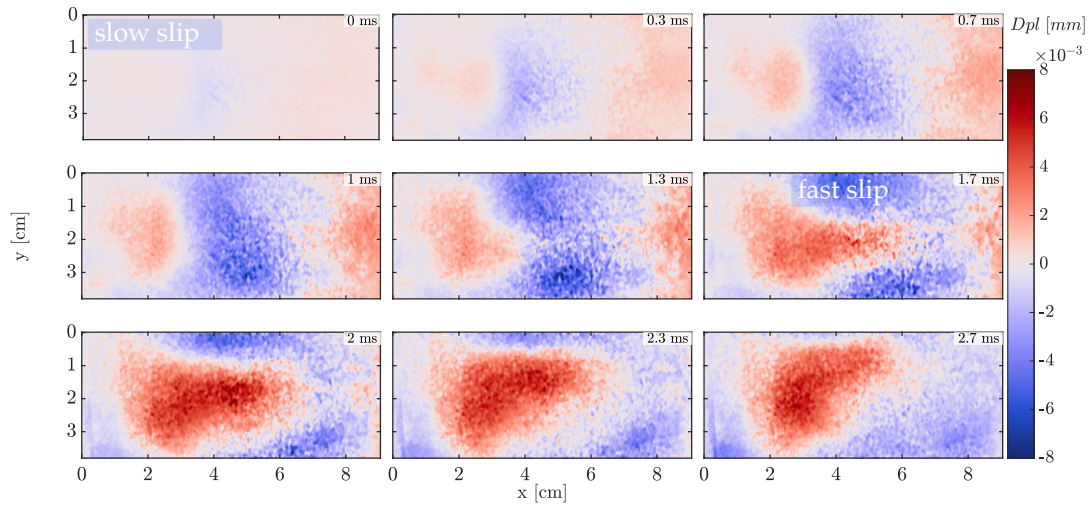


c: x-component of gradient of displacement.

Figure 4.4.27: One cycle in the horizontal observation plane. Black arrows indicate plate movement and the schematic inset visualizes the observation plane. Annotations in the wavefield are interpretations.



a: Particle velocity snapshots of an exemplary rupture



b: Displacement snapshots relative to  $t_0$ .

Figure 4.4.28: A second cycle showing slightly different rupture dynamics



The high-amplitude events of changing polarity which I interpreted as possible movement in the granular layer in the previous experiment are now spatially more extended. This becomes more evident by subtraction of the continuous deformation present in the gel. Fig. 4.4.29 shows the acceleration of a third rupture and visualizes that these precursory events are present on the asperity prior to arrival of the supershear wavefront.

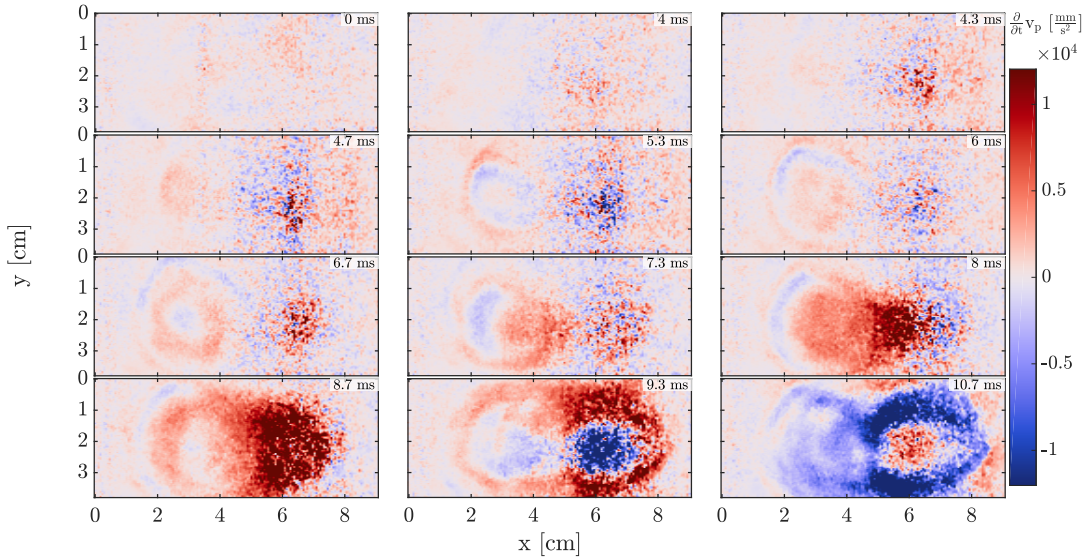


Figure 4.4.29: Particle acceleration snapshots of a third rupture. Note that the time interval between the snapshots is not regular.

**Temporal evolution** Fig. 4.4.30 shows the accumulated displacements in three regions of interest (ROI), indicated on the snapshot in the top right of the same Figure. The red curves show the displacement as measured with the ultrasonic probe and the blue curve shows the normalized response of the force gauge. While the displacements curves are very localized characteristic of specific ROIs in the gel, the force gauge response is the average response of the system, e.g., the force exerted on the glass plate. In both curves the oscillations, present in the old motor, are absent. The saw-teeth visible in the displacement curves and representing stick-slip events get flattened in the force gauge response and are not discernible from the noise. Both measures exhibit the same trend. This confirms the value of the displacement measurements, which strictly speaking are always taken from an Eulerian viewpoint and are thus not true point displacements. Hence, it appears that the particle velocity of approximately the same speckle is measured, and the error introduced by the Eulerian viewpoint is negligible. Fig. 4.4.31 shows a zoom on the force gauge response and the displacement curve of ROI2 for the time interval of Fig. 4.4.28. It can be seen that the main slip, visible in the high peak with a rise time of 1 ms is preceded

by a slower slip of a rise time of 3 ms. As Fig. 4.4.28a shows, this first slip does not produce a discernible wavefield, it appears aseismic.

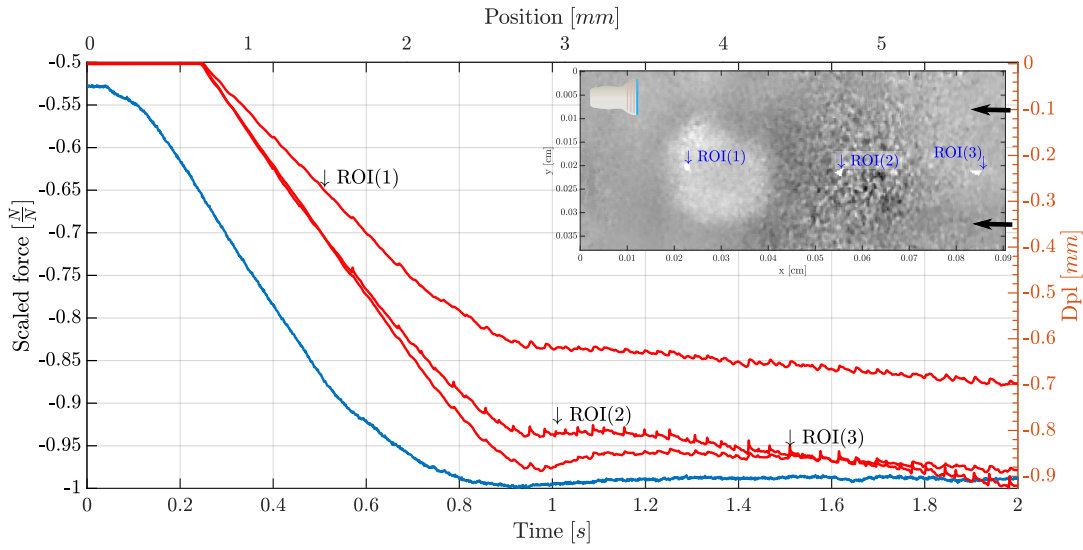


Figure 4.4.30: Red curves: Displacement throughout the whole experiment at specified regions of interest (ROI) on the imaging plane shown in the inset. Each sawtooth represents a rupture event similar to the one shown in Fig. 4.4.27. Blue curve: Normalized response of the force gauge against time. At constant driving speed the force gauge response is a direct indicator for the stress of the driving system.

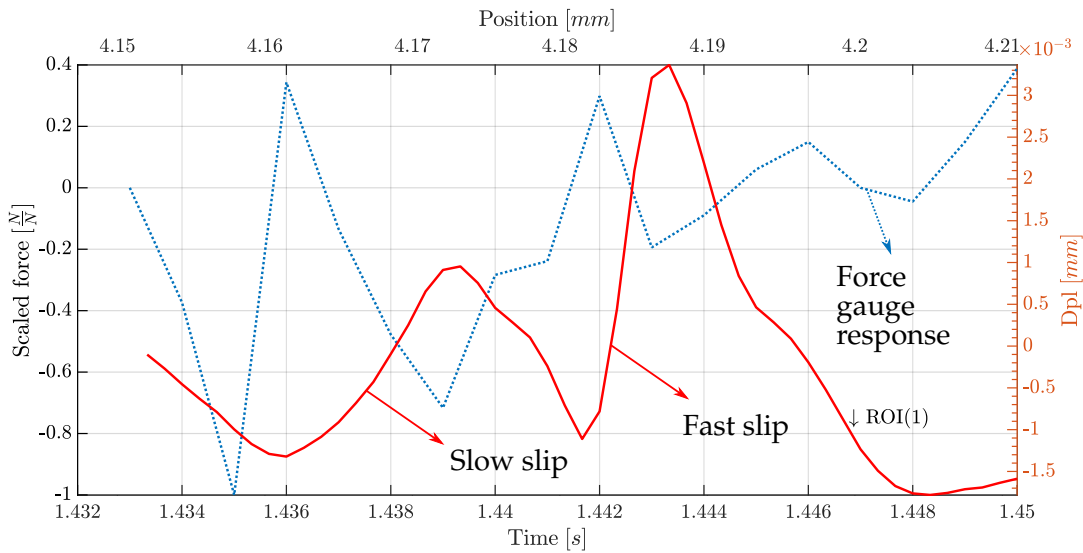
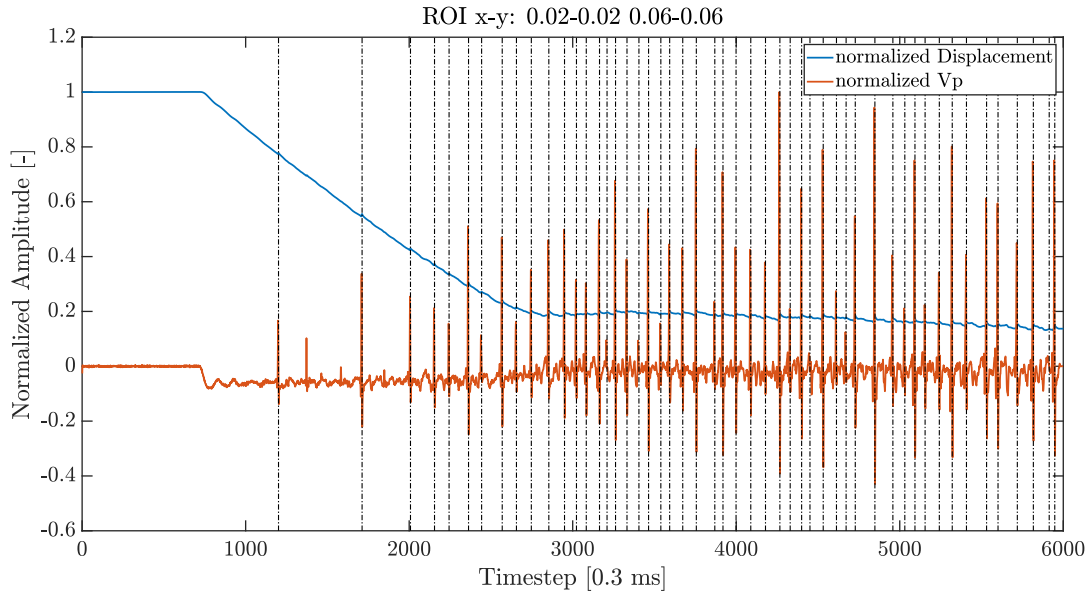


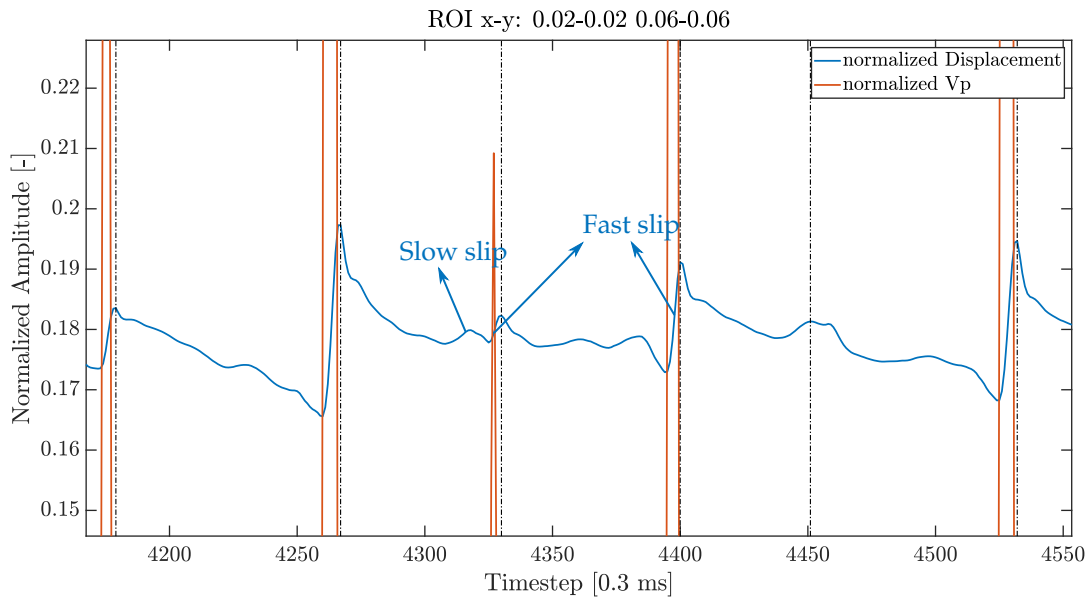
Figure 4.4.31: Zoom on the displacement data of Fig. 4.4.30 for the event in Fig. 4.4.27.

**Event detection** The image detection of Section 4.4.2.a demanded a lot of time-consuming manual adjustment of filtering and segmentation parameters. Here I show a detailed workflow for user-guided analysis to include more general, easily

available parameters less prone to false positives and false negatives. The data quality of the new friction bench facilitates this task. In a first step a combination of peak detection on the velocity and displacement data is used to identify the main rupture events. Fig. 4.4.32 shows the resulting detections and a zoom on the detections, including the time-interval of Fig. 4.4.31. In total, 52 events are detected with no false positives.



*a*: Entire experiment.

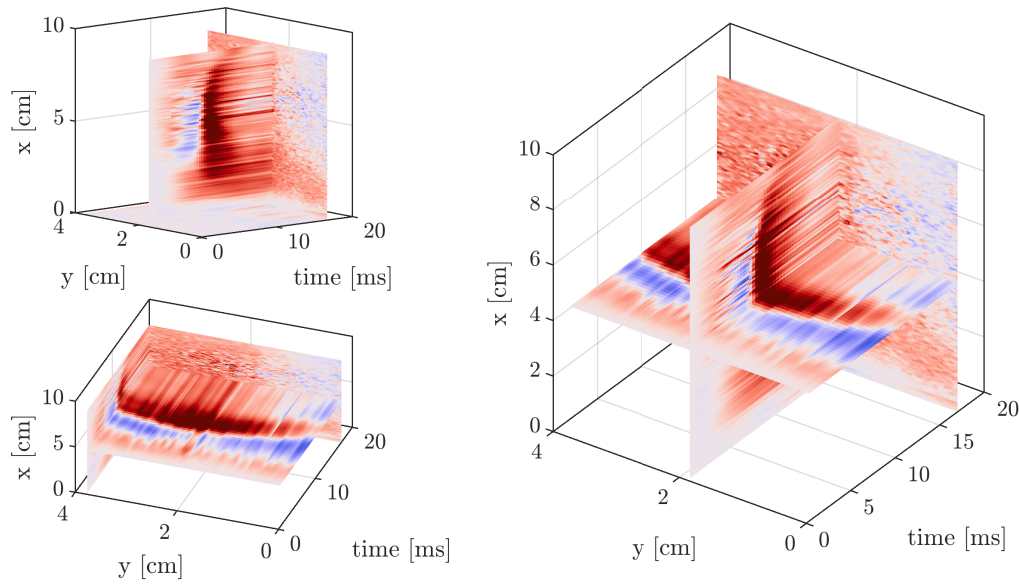


*b*: Zoom on the event in Fig. 4.4.27.

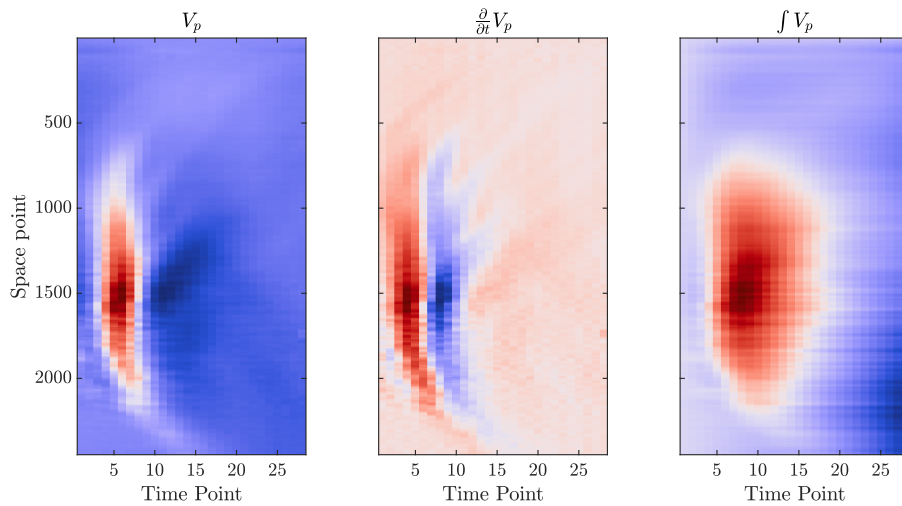
Displacement, particle velocity and rupture detections by a combined maximum finder. The vertical dashed lines indicate the events classified as ruptures.

Figure 4.4.32

In a second step, one detected event is chosen by the user to define the filter and detection parameters for speed measurements in the  $x - t$  space as presented in the Section 4.4.2.a. If the asperity was more complex, this would have to be done in the complete  $x - y - t$  space. Fig. 4.4.33a shows the displacement data in such a 3D space for one rupture. For the asperity extending mainly in  $x$ -direction, a  $x - t$  representation is sufficient. Fig. 4.4.33b shows exemplary space-time representations for one rupture. Depending on which dynamics one is interested in, displacement, particle velocity or acceleration can be chosen.



a: 3D representation of seismograms in  $x$  and  $y$ .



b: 2D representation of seismograms in  $x - t$

Figure 4.4.33: Exemplary input data for detection.



Once the user has chosen a satisfying set of parameter for the detection by the Hough transform, the detection algorithm is run on the whole data using the chosen parameters.

Fig. 4.4.34 shows a result using an edge detector on the displacement data for image segmentation. Four groups can be identified in the plot.

- Very fast supershear ruptures between 2.5 and 6.7 cm. They are represented by the main rupture events in Figs. 4.4.27 and 4.4.28.
- Very slow events of  $\approx 2 \text{ m s}^{-1}$  between 1 and 2 cm. They are probably corresponding to the first events in Figs. 4.4.27 and 4.4.28. The very low speeds are explained by the fact that the edge detection is done on the displacement time-space data. Hence, the slow nucleation phase is retrieved.
- Left-traveling supershear ruptures  $< 20 \text{ m s}^{-1}$ . They probably represent ruptures that nucleate in the center and propagate both ways. The fact that these speeds are nearly absent in positive  $x$ -direction shows a clear speed dichotomy between left- and right-traveling ruptures.
- Speeds between 2 and  $6 \text{ m s}^{-1}$ . They might be a sign of rupture slow down and arrest at the asperity borders.

I hypothesize that the very slow events between 1 and 2 cm are due to a secondary asperity. This secondary asperity is most likely formed by undissolved PVA particles that expose different frictional properties than the rest of the gel. The stark contrast of the propagation speed at this asperity with the rupture speed on the main asperity could be related to the difference in friction between the glass-gel and gel-sand-glass interfaces. Indeed, the slow rupture propagation of the first type reminds the slow slip with depinning events observed by Latour et al. (2011b) for sandpaper friction. The fast propagation of the second type are then associated with the properties of the granular interface. In a second paper, Latour et al. (2013b) noted that an asperity can modify the velocity of a propagating rupture, e.g., trigger a transition from subshear to supershear rupture velocity. The dichotomy between the events at 1 to 2 cm and 2.5 to 6.7 cm could reflect a similar mechanism. The first, sub-Rayleigh event triggers a delayed supershear rupture on the main asperity.

**K-means clustering** As a proof-of-concept I employed the standard Matlab k-means<sup>16</sup> algorithm (Arthur et al., 2007) to test the performance of this machine learning algorithm on rupture event classification. By using skewness, variance and mean of one ROI on the asperity and one ROI outside of the asperity as the input data for each timestep, classification into snapshots containing early and late ruptures and

<sup>16</sup>K-means clustering sorts the observations of the input data into a specified number of groups based on, e.g., Euclidian distance calculation of the observations.

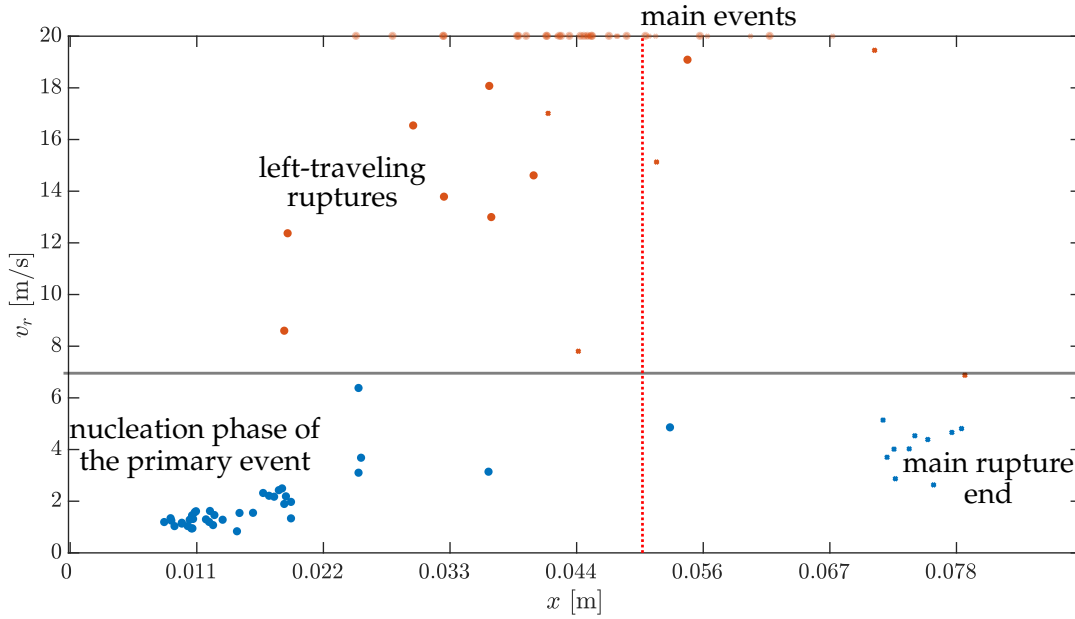


Figure 4.4.34: Speed profile of the detected rupture events. Each point represents the speed measured for a segment that has its center in the  $x$ -position against which it is plotted. Large dots represent events traveling to the left, small dots represent events traveling to the right. In contrast to Fig. 4.4.25 the image segmentation has been performed with an edge detector on the displacement  $x - t$  map.

snapshots containing no events was successful. Very few false negatives or positives were present for the experiments of Section 4.4.2.a and this section<sup>17</sup>. Appendix C.4 contains an example of classification for several groupnumbers as well as exemplary snapshots from three different k-means groups.

#### 4.4.2.c Experiment 3 - Coarse sand

**Setup** The gel and observation plane are the same as in Section 4.4.2.b. However, the asperity is now 7 cm long and the sand used is much coarser, with a diameter of  $\approx 2-3$  mm. In contrast to the previous experiments, a thicker layer of sand ( $\approx 4$  mm) is used. At the start of the experiment, the asperity ends about 4.5 cm from the probe<sup>18</sup>.

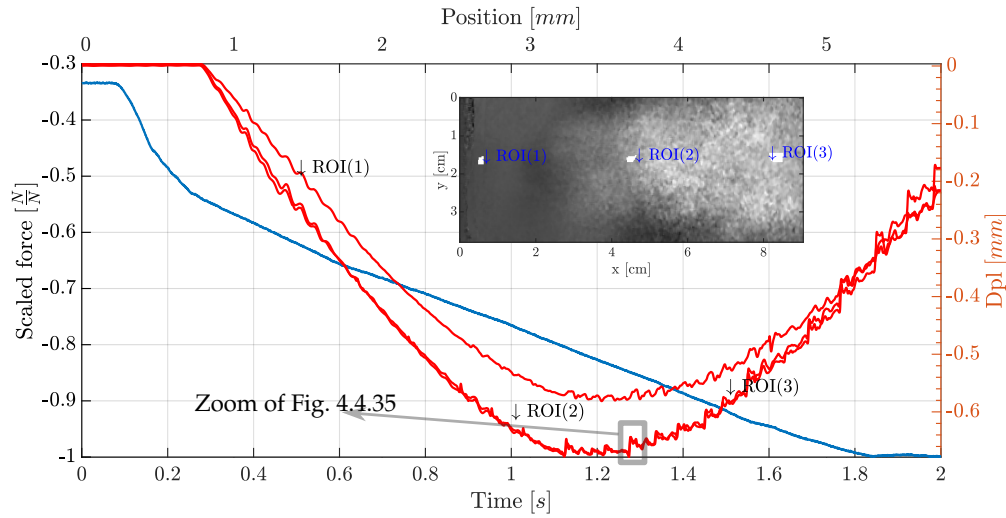
**Temporal evolution** Fig. 4.4.35a shows the displacement and force gauge response against time. In contrast to the previous experiments, the curves are qualitatively different. While the force gauge response reaches a plateau at  $\approx 1.8$  s, the displacement curves show an inverted trend from 1.2 ms onward. Thus, while the force exerted on the glass plate increases, the gel slides more than it gets deformed in-between two slide-events. One reason could be alteration of the sand layer. Indeed, after experiment we observe that the sand patch has been displaced. During the experiment it

<sup>17</sup>Verification was done by manual investigation of the particle velocity film.

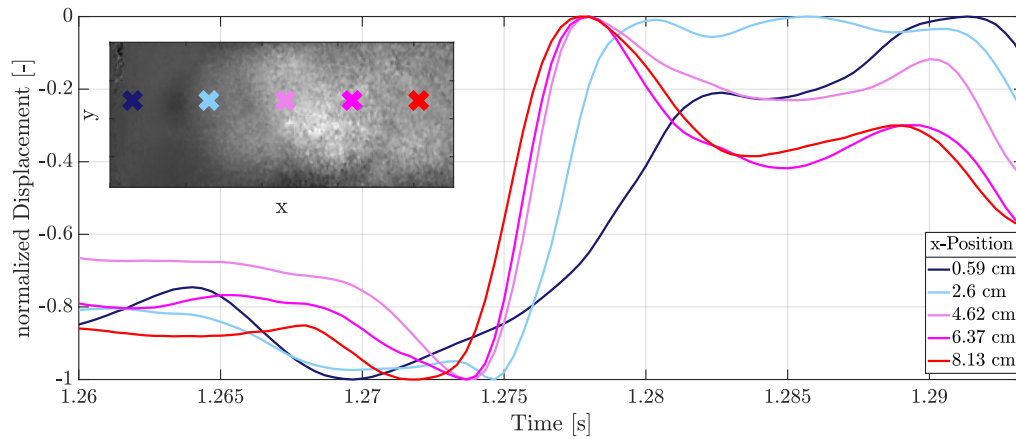
<sup>18</sup>The displacement of the glass plate of  $3 \text{ mm s}^{-1}$  might entrail the asperity.

probably gets spread out and flattened. Due to the difference in grain size, the coarse sand shows less cohesion than the fine sand which is likely to change the frictional properties further.

Fig. 4.4.35 shows a zoom on the displacement during one rupture event of four points on the asperity and two points outside of the asperity. The rupture advances from right to left, shown on the snapshot inset into Fig. 4.4.35. Note that sand asperity extends several centimeters further than the imaging plane and the rupture could nucleate in the center of the asperity. Due to the continuous charging it is difficult to make a definite statement on the nature of the observed rupture. Nevertheless, several important observations are made. The points on the asperity and the first points outside exhibit a similar inclination of the displacement curve at the approximate time of the rupture 1.274 ms. The curves of the points at 4.6 and 6.3 cm coincide indicating synchronous slip. In contrast, the point at 8 cm sets in earlier. All three however finish displacement in slip directions at the same time, indicating either crack-like propagation or a wide pulse. The point at 2 cm, which is located outside the sand asperity shows a delayed onset of motion in slip directions but nearly the same inclination. This indicates that sliding speed on the smooth interface behind the asperity only slightly decreases and that the rupture either changes pulse width or changes from crack- to pulse-like rupture. The point at 0.59 cm exposes much slower dynamics, justified by the fact that it is several centimeters away from the asperity, on the smooth part of the interface.



*a*: Red curves: Displacement throughout the whole experiment at specified regions of interest (ROI) on the imaging plane shown in the inset. Blue curve: Normalized response of the force gauge against time. At constant driving speed the force gauge response is a direct indicator for the stress of the driving system.



*b*: Zoom on the event at 1.3 s for five points along the  $x$ -dimension. 0.59 cm is outside the asperity, all the other points are within. Each point's displacement curve is scaled by its maximum to facilitate the interpretation of the temporal dynamics.

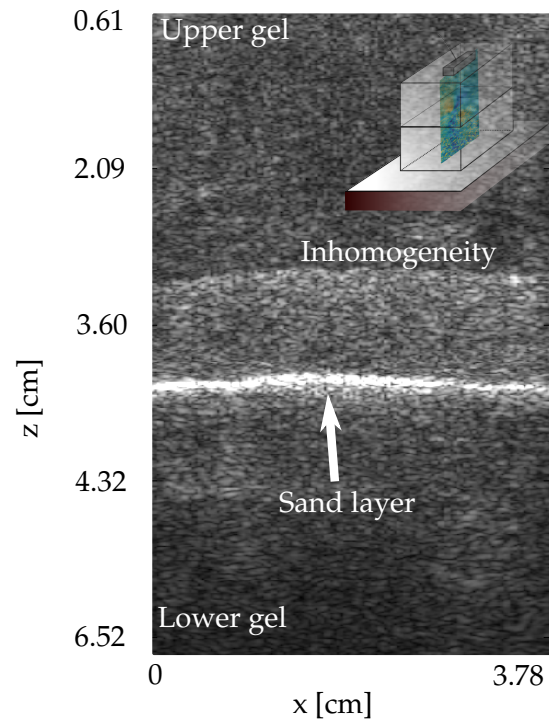
Figure 4.4.35: Displacement curves for the coarse sand.

### 4.4.3 Gel-gel rupture

The aforementioned experiments are all glass-sand-gel friction. Hence, they expose a huge material contrast in terms of shear elasticity. For example, glass exposes a shear modulus of approximately 26.2 GPa (Crandall, Dahl, 1959), but the used PVA gels differ by 5 orders of magnitude (Genisson et al., 2007). This material contrast explains the prevalent supershear nature of the present ruptures (Shlomain et al., 2016). In the following we overcome this limitation of the previous setup by producing a gel-sand-gel rupture.

**Setup** Instead of sliding a gel on a glass plate, the gel is sliding on another gel. The sandpatch is positioned between the two gels. Thus, the material contrast between the two half-spaces is reduced by orders of magnitude and elastic deformation is allowed in both half-spaces. The probe is positioned on top, permitting to retrieve the vertical component of the particle velocity. Fig. 4.4.36 shows the ultrasound reflection image of this setup. The sand patch can clearly be discerned from the high intensity spot in the center. There is sufficient ultrasound reflection from below the sand to allow for imaging in both half-spaces. In the ultrasound reflection image, both gels show an inhomogeneity, as if each gel would consist of two layers. This can be explained by the gel production process. During the first freeze-thaw cycle needed for solidification of the PVA gels, graphite accumulates at the bottom of the gel, which is still in a viscous fluid state. This graphite leads to higher ultrasound reflection intensity. Furthermore, in the production of these relatively large gels we observe incomplete solution of PVA particles that also deposit at the bottom.

*Figure 4.4.36: Ultrasound reflection image of the gel-gel setup. Dark spots indicate low reflectivity and white spots indicate high reflectivity. The sand layer can be discerned from the highest reflectivity in the center of the image. Above and below, a small layer of increased reflectivity compared to the rest of the gel reflects the fact that the gel is not perfectly homogeneous. Gavity leads to an accumulation of graphite at the bottom of the gel during gel production.*



**Wavefield** Fig. 4.4.37 shows an extract of 5 ms from the experiment. Wave propagation can be observed in both half-spaces, although image quality is largely deteriorated in the lower half-space. At 0 and 3.7-4.0 ms a noisy layer at the approximate position of the sand layer can be identified. The noisy layer is thinning towards its center, reminding a diffraction mustache. It is possibly induced by local failure of the correlation algorithm due to varying strong diffraction of the ultrasound in the sand. The varying diffraction could be induced by rapid movement of the sand, which results in different diffraction between two images.

Three events of two types can be discerned in the snapshots. Event 1 starts at 0 ms. It is nucleating at about 2.6 cm and followed by wavefronts advancing in both directions in the upper half-space. The bad image quality in the lower half-space does not allow identification of sharp wavefronts, but the smeared image still shows that the polarization of the propagating wave in the lower half-space stays the same as in the upper half-space. The particle velocity snapshots of Fig. 4.4.37 don't show a full wave cycle, only the downgoing component (red) can be identified in the upper half-space. In the lower half-space, the upgoing component can be identified at 0, 1 and 1.3 ms. The upgoing component of the particle velocity probably gets masked in the upper layer by the continuous deformation of the gel. The right- and left-travelling waves expose a different inclination, with the left-traveling wave exposing a larger angle to the vertical. Since the right-traveling wave has a higher amplitude, a supershear rupture is unlikely for the left-traveling waves. A possible explanation is, that we observe a right-traveling sub-Rayleigh rupture and the corresponding left-traveling shear waves. Event 2 exposes a different radiation pattern than event 1. From 3 to 4 ms, a quadripolar radiation pattern whose upper and lower lobes get displaced along  $x$  relative to one another is observed. At 4.3-4.7 ms, the event is followed or transforms into an event 3, which shows a similar radiation pattern as event 1. In contrast to event 2 however, event 3 appears to be left-traveling.

**Rupture type** The 1D analysis in Fig. 4.4.38 confirms the sub-Rayleigh hypothesis. Fig. 4.4.38a shows the waveforms at nucleation depth and time (indicated on the inset) against  $x$ . The nucleation position in  $x$  can clearly be discerned by the growing peak at 0 and 0.3 ms. The diffraction mustaches do not allow to follow the event at nucleation depth further in time. Fig. 4.4.38b shows thus the associated waveforms a few millimeters above along the  $x$ -axis. The maxima of the right- and left-traveling waves at each timestep show the exact same distance to the nucleation position. However, the right-traveling wave exposes a larger amplitude and its peak is more narrow. This is a strong indicator for a right-traveling sub-Rayleigh rupture. Furthermore, the form of the waveforms qualitatively reminds the signature of the source time function of a unilateral rupturing fault depicted in Fig. 4.2.15b: One can imagine that without the varying noise underlying the signal, the integral of the left- and right-traveling waves could be identical.

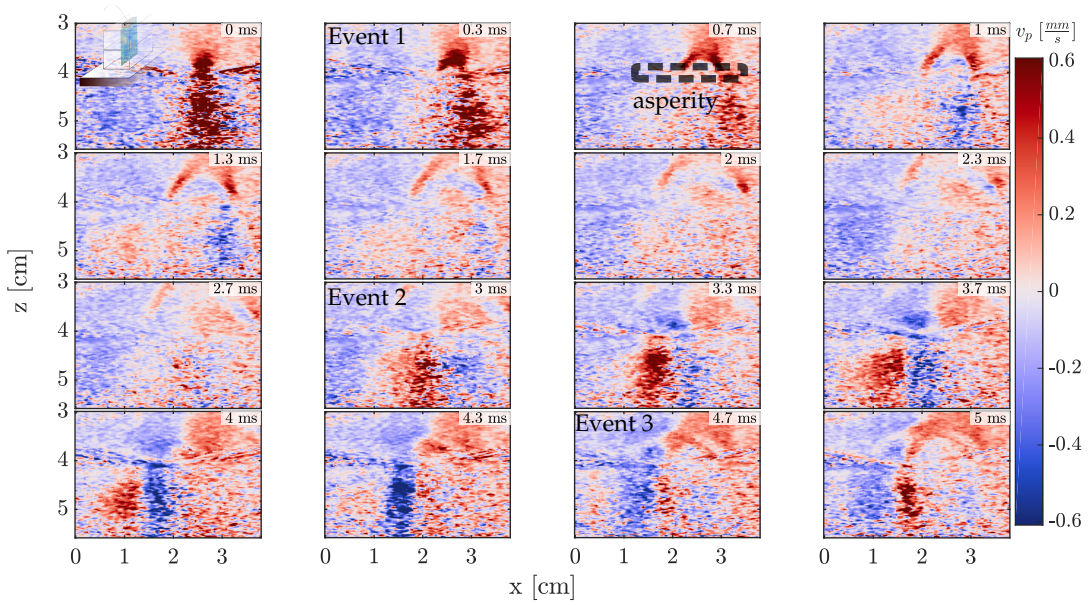
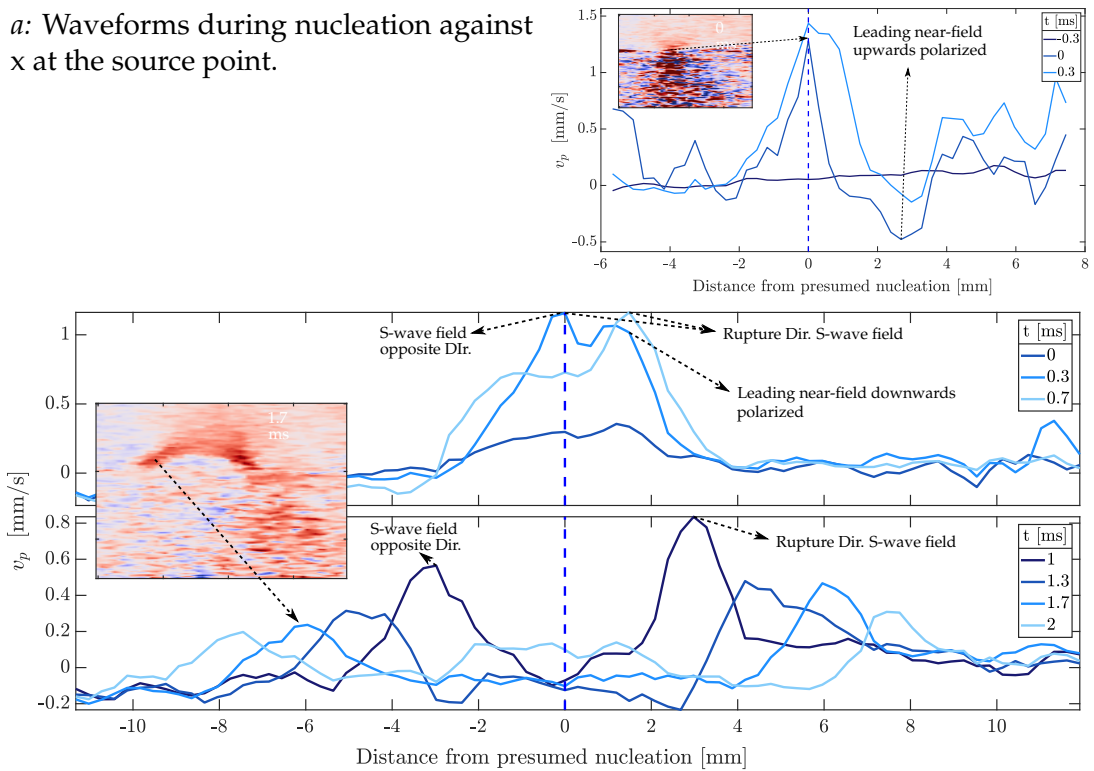


Figure 4.4.37: Particle velocity snapshots for the gel-gel rupture.

*a*: Waveforms during nucleation against  $x$  at the source point.



*b*: Waveforms after nucleation against  $x$ . The  $z$ -position is indicated in the insert.

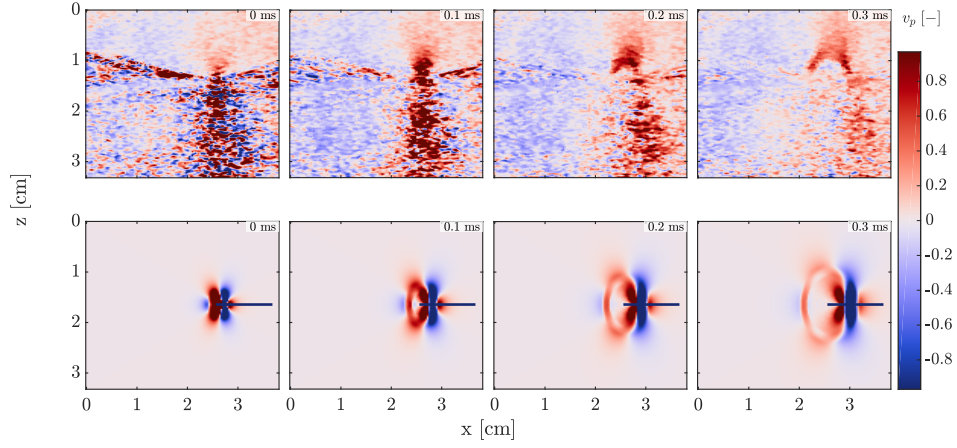
Figure 4.4.38: Particle velocity evolution for the event at 0 ms in Fig. 4.4.37.

Fig. 4.4.39a shows a qualitative comparison of the event with a right-traveling DC-source at sub-Rayleigh speed ( $0.6v_s$ ). Considering that the downwards component of the near-field is masked in the experimental data and that inhomogeneities in the sand layer or gel, as well as the local stress-field at the nucleation point, might lead to a rupture exposing a slight angle to the  $x$ - or even  $z$ -axis, the DC-source qualitatively maps the rupture quite well.

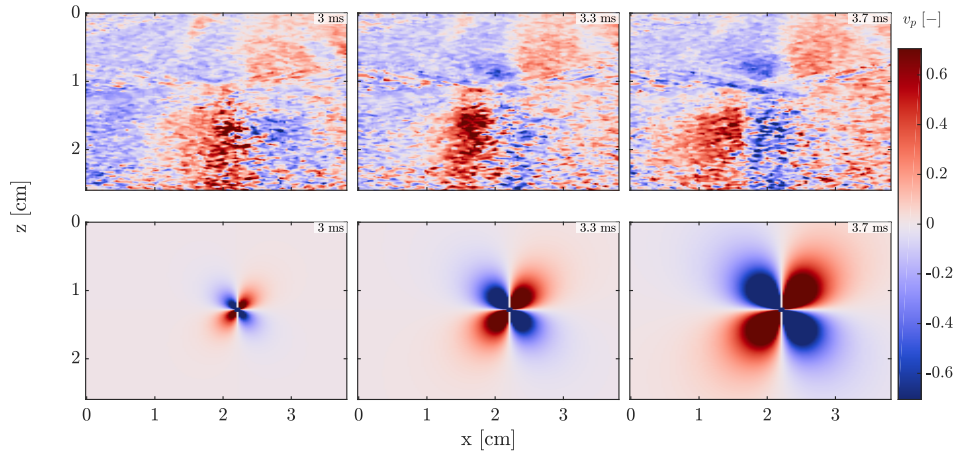
This type of event, a right-traveling sub-Rayleigh rupture, seems to be repeated at 4.3/4.7 ms. However, this second occurrence is preceded by another event which strongly resembles the near-field of a Gaussian force source function. Fig. 4.4.39b shows a comparison of the experimental snapshots with the snapshots of a 4 ms long Gaussian source. The main qualitative difference is that the experimental lobes seem to be offset from 3 to 3.3 ms. There are two possible explanations. Either the half-spaces have slipped against each other or the rupture exposes a diagonal offset to the  $x$ -axis and or the nucleation point exposes an offset in  $y$  to the imaging plane. In combination with the speed difference of the two half-spaces, this deviation from an idealized  $x - z$  geometry could produce the observed effect.

A visual investigation of the whole particle velocity film (3 s) shows that most events start at the central part of the imaging plane and thus the central part of the sand patch. Fig. 4.4.37 is an extract at around 2.4 s, quite late in the experiment. The lower gel already moved 5 mm, explaining why the nucleation happens shifted slightly to the right of the center of the image.





*a*: Top row: Experimental particle velocities for the event at 0 ms in Fig. 4.4.37. Bottom row: Right-traveling sub-Rayleigh DC rupture. The upwards component of  $u_z$  as well as the leading near-field seem non-existent or masked in the experimental results. The dark blue line denotes the rupture extension simulated by the superposition of DC-sources traveling along  $x$ -direction.



*b*: Top row: Experimental results for the event at 3 ms in Fig. 4.4.37. Bottom row: Left-directional Gaussian point source. The Source duration is 4 ms. Note that the simulation is done in a homogeneous medium while the two gels of the experiment expose a small material contrast. Furthermore, the experimental rupture might not be perfectly aligned in  $x$ -direction and nucleate at  $y = 0$ .

Figure 4.4.39: Comparison of the two events in Fig. 4.4.37 with analytical solutions.

## 4.5 Work in progress: 2D wavefield detection

Because in a kinematic framework a rupture is a moving source, the shape of the waveforms vary with rupture speed. For example, the wavefield superposition observed for a decelerating source changes from cone-like to elliptical, as the simulation in Fig. 4.4.22b shows.

I thus started investigating parabolic fits in the  $x - y$ -plane. The crucial part which has prevented a successful implementation so far is the image segmentation, which has also been the biggest challenge in the analysis of the space-time representations. In comparison to these representations, which were averaged along a few probe elements in the direction orthogonal to propagation, the Signal to Noise ratio in one 2D snapshot is much lower (see Appendix C.2 for an example). Recently, I started exploiting the use of wavelet transforms. These facilitated largely the processing of the  $x - t$ -seismograms as well as the  $x - y$ -snapshots. Fig. 4.5.1 shows the results for the phase congruency (top,  $x - t$ ) and phase symmetry (bottom,  $x - y$ ) methods. The improvement in terms of Signal to Noise ratio and segmentation is obvious. From these preliminary results I strongly suggest to include the wavelets into the detection workflow in future studies. Both results are achieved through Matlab functions by Peter Kovési<sup>19</sup> (Kovács, 1997; Kovési, 1999).

---

<sup>19</sup><https://www.peterkovesi.com/matlabfns/index.html#phasecong>

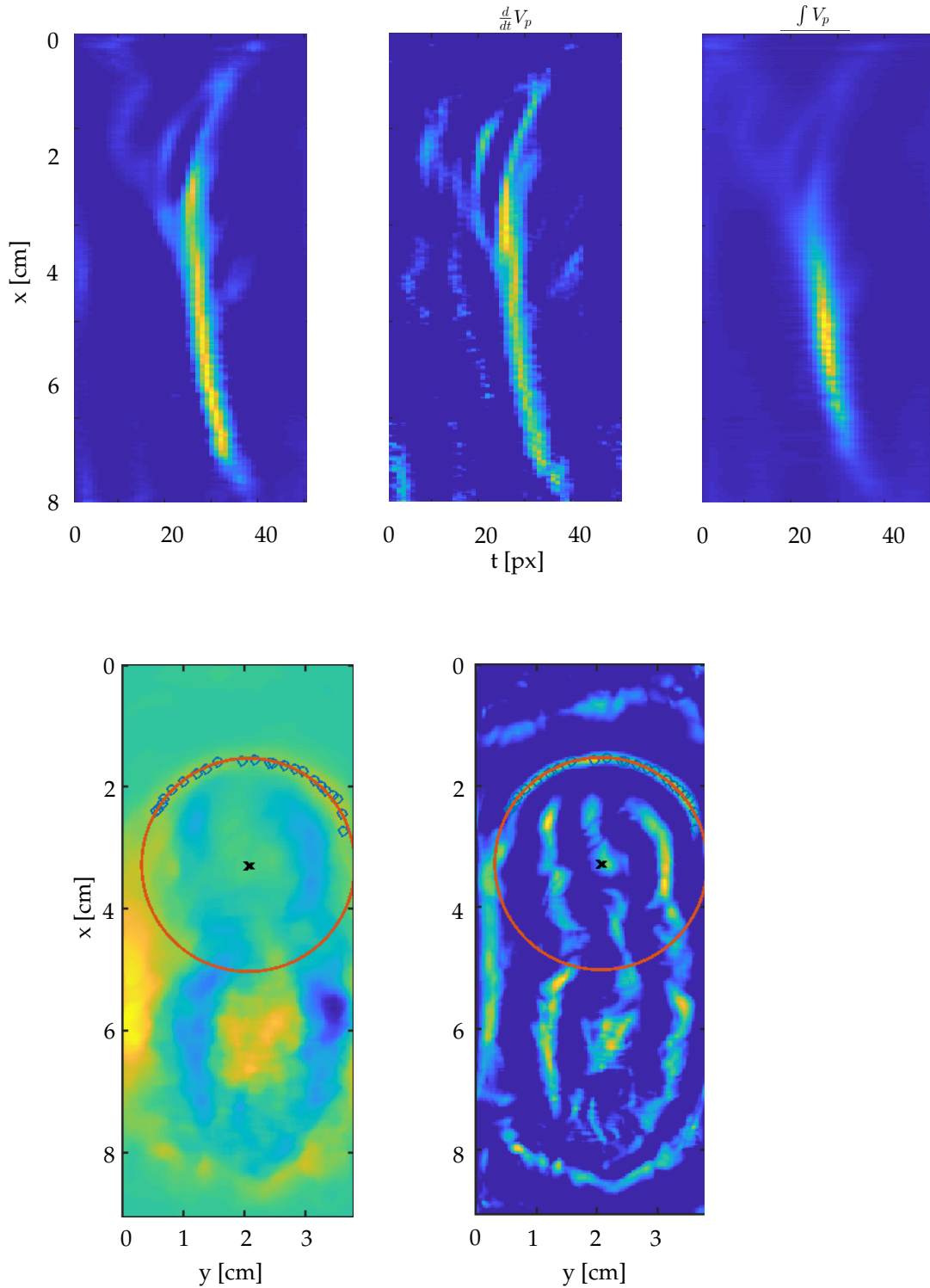


Figure 4.5.1: Wavelet transform methods applied on the  $x-t$  (top) and  $x-y$  (bottom) data of Section 4.4.2.b. The transformations allow more robust segmentation, opening up the possibility for further automated analysis.

## 4.6 Conclusion

The experimental setup initiated by Latour et al. (2011a) was successfully reproduced, improving data quality as well as manageability of the experiment. We notably introduced local displacement measurement inside the sliding body, which was made possible by a change of the correlation algorithm. Section 4.4 illuminates the richness of phenomenons observed and the potential of ultrafast ultrasound imaging for rupture observation. Using particle velocity, acceleration and displacement, different aspects of the physics of rupture are investigated through the dense grid of virtual in situ sensors provided by the ultrasound image correlation.

The five gel-on-glass experiments I have presented confirm the conclusions already drawn by Latour et al. (2011a). For the gel-on-glass setup, rupture preferably propagates from the blocked side to the free side of the gel. However, spontaneously nucleating as well as reflected ruptures are observed in the opposite direction as well. The results indicate that the setup most likely favors pulse-like ruptures, which is in accordance with previous observations. While the gel-on-glass setup exposes a strong bimaterial contrast and favors supershear ruptures, the newly introduced gel-on-gel sliding allows for equal order of magnitude deformation in both half-spaces. As a result we observe the nucleation of sub-Rayleigh and the associated radiation pattern in both half-spaces.

The goal of automated detection, identification and analysis on a large number of controlled experiments has not been reached, yet. The strength of the setup is the observation of 3D rupture effects at very high spatial resolution. In terms of automated data analysis this is also its weakness. The quantity of the data and number of different phenomena observed have been an obstacle which has not been fully overcome so far. However, I have shown that despite the use of non perfectly homogeneous hydrogels and varying experimental conditions, rupture events are reproducible. By reducing the spatial complexity to a small asperity, the rupture type, interval and direction develop into a stable pattern for the gel-on-glass setups. In terms of event detection thus I suggest two paths to be taken in the future:

First, image segmentation and computer vision for 2D-waveforms can further identify and classify rupture fronts, rupture arrest fronts and precursory events. The change of shape of the rupture wave-front for example gives information on acceleration, de-acceleration as well as nucleation position.

The second approach is a purely data-driven one. Since the wavefield data is highly resolved, each phenomenon bears specific characteristics in terms of its statistical modes. The data seems thus predestined for detection and classification of events by machine learning algorithms. The application of a simple k-means algorithm has shown the effectiveness of such an approach. In combination, the two approaches would be a powerful tool to statistically analyze experimental results.

In a further step, numerical modeling using either dynamic rupture or kinematic models could be compared to the experimental data. The access to the near-field would allow for inversion of the full<sup>20</sup> transverse wave field. Ideally, the experiment would be performed with two or three observation planes simultaneously. In such a 3D-setup, schematically shown in Fig. 4.6.1, fault-parallel and fault-normal particle velocities could be compared. Apart from the already presented observation modes, the fault-parallel particle velocity in the vertical plane and the fault-orthogonal particle velocity could be investigated. The retrieval of two or more components of the gradient of displacement might allow for a better estimation of the strain tensor. Thus, the stress-strain conditions under which ruptures nucleate could possibly be better characterized.

Once these methods are sufficiently developed, the experimental setup offers many possibilities to change the initial conditions. For example, the shear stress can be varied through the driving speed, e.g., inducing accelerations, pauses and oscillations. Shape and material of the asperity are also highly variable. Varying grain sizes, layer thicknesses and asperity geometries should be investigated. The limitation for the phantom material is a soft elastic solid. Apart from PVA, more brittle hydrogels such as Agar- or Polyacrylamide could be used. This would be particularly interesting combined with monitoring of the elastic properties of the gel, e.g., through passive elastography. If the wavefield in the wake of the rupture is not sufficiently diffuse and long, the gels could be probed continuously with low amplitude waves to create a diffuse wave-field. At last, the experimental setup could always be extended by, e.g., adding acoustical sensors for P-wave monitoring or optical sensors for monitoring of the granular layer.

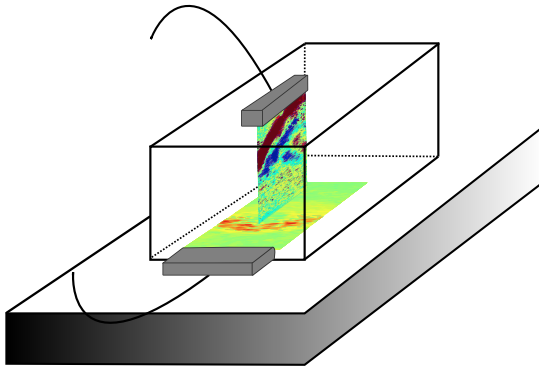


Figure 4.6.1: Schematic setup for a pseudo 3D - configuration with crossing observation planes. Fault-parallel and fault-normal particle velocity can be measured simultaneously.

## 4.7 Relevance for real-world cases

The presented experiments illustrate several phenomena that have been shown for hard elastic materials in the laboratory and real-world earthquakes as well. These include for example supershear and rupture arrest fronts and a slow nucleation phase

<sup>20</sup>Full in the sense that near- and far-field components are inverted for

prior to rupture propagation. However, it is clear that the strong bimaterial contrast present in the gel on glass experiments is difficult to scale to natural faults. While the use of hydrogels is not uncommon, Corbi et al. (2013) for example use a gelatin hydrogel to model a seismic subduction zone, this apparent contrast with a natural earthquake setting is the most obvious weakness of our setup. A situation much closer to our experimental setup is the sliding of ice on rock. As detailed in Section 4.2.2, many phenomena known to occur on earthquake faults have also been observed for glacial sliding. In this comparison, the glass plate mimics the rock, the sand the glacial till and the hydrogel the ice mass. The geometry of the frictional interface chosen in this work might be another parallel. I have named it an asperity on a smooth fault. Nettles et al. (2003) report that icequakes have been linked to sliding motion on so-called sticky spots - *patches of resistance to slip along the glacier base* and Winberry et al. (2013) associate the observed frequency spectrum of ice stick-slip with the repeated rupturing of a single asperity. This description fits our asperity setup astonishingly well. Nettles et al. (2003) further note that pore pressure<sup>21</sup> variations or nonlinear weakening of deforming till may be responsible for the growth of a slipping patch and the consequent motion of the glacier. In the case of the Whillains ice plain in the Antarctica, Winberry et al. (2013) state that “the elastic strain is stored primarily within the ice, and motion is concentrated just beneath in a narrow (<10m) fault zone of unconsolidated sediments (functionally and genetically a fault gouge)”. Again, the similarity with the gel-sand-glass setup is apparent. Nettles et al. (2003) report another feature of glacial sliding that resonates well with the here presented results. Using a standard moment tensor inversion (Harvard-CMT) they do not manage to match the observed phases. Following Kawakatsu (1989), who modeled landslide ruptures, they employed a single force centroid inversion (CSF) and improved their inversion results. My comparisons of a double-couple and singular-force source mechanism to the experimental data have been purely qualitative, but have the unique advantage of being compared to the full transverse field, including the near-field. While an inversion would be needed to cover the possible range of rise times and rupture kinematics, let us summarize what the comparisons have shown so far. Both source mechanisms qualitatively explain different aspects of the observed ruptures. Both solutions reproduce the near-field lobe, supershear rupture front and rupture arrest front of the gel-on-glass experiments. The complexity of a double-couple seems to better reflect the nucleation phase, while the simplicity of the singular-force describes the wave field of the advancing rupture sufficiently well. In the gel-gel setup we observe one event with a radiation pattern best described by a one singular-force point source but the continuity of the rupture front in both half-spaces of another event is only described by the double-couple. All experimental near-fields seem to miss a near-field phase present in the double-couple solution, which might be masked in the global deformation of the gel. The true mechanism

most likely varies in the gel-on-gel and gel-on-glass setups and is a different combination of forces, possibly including tensile opening. I hypothesize that due to the elastic deformation of both half-spaces the gel-gel rupture mechanism is a double-couple, while the gel-on-plate mechanism is best described by a simpler mechanism, e.g., a combination of two forces. A next step could be to use the radiation patterns of the non- double-couple sources of, e.g., Kwiatek et al. (2013), in a full shear wave field inversion.

Due to the just mentioned similarities between our experimental setup and glacial sliding, I further suggest to compare the source mechanisms and rupture types of glaciers to a well-designed laboratory friction experiment. An ideal natural study object would be the Argentière glacier, which has recently been equipped with a dense array of seismic and electric sensors in the course of the RESOLVE project<sup>22</sup>. This is probably as close as we can get in terms of data richness in the field to the ultrafast ultrasound experiment.

---

<sup>22</sup><https://resolve.osug.fr/?lang=fr>

<sup>22</sup>While the role of pore pressure in hydrogel is beyond the scope of this work, it should be emphasized that during the experiments the hydrogels are observed to slowly become dryer and the sand is wet after the experiment. In Section 3.3 I noted that Tanaka et al. (1973) reported a slow wave similar to Biot's secondary compression wave for hydrogels. It is thus suggesting to regard the hydrogel-sand ensemble under the imposed normal and shear stress in our experiment as porous.

## Chapter 5

# Conclusion

In the present work I have shown that by its unique feature of in situ wave-field observation shear wave imaging can be used to tackle various questions in distinct fields of research.

First, the existence of three elastic waves in porous melamine foams was experimentally demonstrated and their attenuation and dispersion was analyzed. The possible implications for characterization of soft porous organs in medical imaging are straightforward: The consideration of fluid viscosity in elasticity characterization of soft porous tissues.

Second, the nucleation of laboratory earthquake ruptures was directly imaged in the near field. By comparing the analytic solution for kinematic rupture propagation to the experimental wave field it has been shown that the presented laboratory experiment combined with shear wave imaging is an excellent tool to investigate the dynamics of rupture propagation.

Apart from the scientific results that were reported and already summarized in the conclusion of each chapter I aimed to establish how the physics of wave propagation underlay such varying applications as rupture propagation and porous characterization. Furthermore, it was my intention to make the work accessible to readers from different backgrounds. Since many methods in medical and geophysical imaging share a common basis, both fields can highly profit from each other. For example, without the works of early seismologists shear wave elastography would probably not be a standard practice in hospitals today. Namely the book by Aki et al. (2009) has been an invaluable source in understanding the elastic wave field. Without the exchange between seismology, ultrasound imaging and biophysics the present work would not have been achieved.

Chapter 3 introduces Biot's theory of elastic wave propagation for the characterization of soft tissues. The theory is yet another example of knowledge transfer across the disciplines. It was originally developed in the earth sciences to characterize soils and hydrocarbon reservoirs and later extended for different applications. Our experimental results confirm that it is applicable to soft tissues as well.



In medical imaging the scientist's ultimate goal is to acquire in-vivo results, thus imaging human tissue under the conditions which the medical practitioner encounters. Likewise, the seismologist aims to analyze real earthquake data at the global scale. In medical imaging, the controlled laboratory scale is a necessary and useful prerequisite to in-vivo imaging. Chapter 4 shows that stepping down a scale in seismology does not have to mean to take a step back. Imaging at the laboratory scale using spatially dense arrays, as is common practice in the medical field, adds unique insights to seismology as well.

Finally, I want to present another linkage of chapters Chapter 3 and Chapter 4 as an outlook for further research. Poro-elasticity plays an important role in different rupture nucleation scenarios. While it is investigated for landslides (Viesca et al., 2010) and fault slip (Scuderi et al., 2015), its most prominent role is in induced seismicity - small earthquakes triggered by geothermal or hydrocarbon reservoir exploitation (Shapiro et al., 2009; Galis et al., 2017). For the presented Poly-Vinyl-Alcohol samples and at the wavelengths typically encountered in shear wave imaging, classic elasticity was assumed. However, at the micro-scale hydrogels are poro-elastic materials and different types of porous hydrogels can be designed (Ahmed, 2015). Maybe in the future, a poro-elastic rupture experiment using ultrafast ultrasound imaging can be thought of.

## Appendix A

# Biot theory

### A.1 Idealized fluid: Wave propagation in the absence of viscosity

Similar to the wave equation in an elastic solid, the wave equation for a porous aggregate can be defined. First, the equations of motion are developed for a fluid-solid aggregate represented by an elementary cube (REV). In contrast to classical linear elasticity, inertial coupling has to be taken into account. For simplicity, we start with an ideal fluid and will derive the role of viscosity at a later point.

As for the notation:

$$\mathbf{u} = u(\mathbf{r}) = (u_x \ u_y \ u_z) = u_i \text{ and } \sum_{i=1}^3 u_i U_i = u_i U_i = u_1 U_1 + u_2 U_2 + u_3 U_3.$$

#### A.1.1 Stress-strain relations

The total displacement of the elementary cube is divided into two components: the average displacements of the solid  $u(\mathbf{r}, t)$  and of the fluid  $U(\mathbf{r}, t)$ . The forces acting on each side of the solid parts of the cube give the solid nine element stress tensor  $(\sigma_{ij}) \in \mathbb{R}^{3 \times 3}$ . The fluid stress tensor resulting from the forces acting on the fluid parts of the cube is a diagonal tensor comprising the fluid pressure  $p$  scaled by porosity:  $(\phi p \delta_{ij})$ . The strain tensor in the solid is defined as  $(e_{ij}) \in \mathbb{R}^{\times}$ , where  $e_{ij} = \frac{1}{2}(\frac{\partial u_i}{\partial x_j} + \frac{\partial u_j}{\partial x_i})$  and  $e_{ij} = e_{ji}$ . In the fluid the strain is  $\epsilon_{kk} = \frac{\partial U_x}{\partial x} + \frac{\partial U_y}{\partial y} + \frac{\partial U_z}{\partial z}$ <sup>1</sup>

Next, similar to classic linear elasticity, a poroelastic strain-energy function  $W$ , which relates stress and strain and is exact differentiable is posited (Biot, 1956c; Biot, 1962):

$$\begin{aligned} W &= W(e_{ij}, \epsilon) \\ \sigma_{ij} &= \sigma_{ji} = \frac{\partial W}{\partial e_{ij}} \\ \phi p &= \frac{\partial W}{\partial \epsilon}. \end{aligned} \tag{A.1}$$

---

<sup>1</sup>We use the Einstein summation convention, where repeated indices are summed over, except if specified otherwise. The indices  $i, j, k$  take the values of the cartesian coordinates  $x, y, z$ .

For isotropic materials the stress-strain relations can then be expressed as:

$$\begin{aligned}\sigma_{ij}^s &= 2Ne_{ij} + Ae_{kk}\delta_{ij} + Q\epsilon_{kk}\delta_{ij} \quad ; \quad A = P - 2N \\ \sigma_{ij}^f &= -\phi p\delta_{ij} = (Qe_{kk} + Re_{kk})\delta_{ij}\end{aligned}\tag{A.2}$$

$P, Q$  and  $N$  are the Biot's poroelastic coefficients and are a function of the fluid as well as the solid properties.  $P - 2N$  and  $N$  represent the Lamé parameters.  $R$  expresses the pressure needed for the fluid to enter the aggregate without change in total volume.  $Q$  expresses the coupling between volume of solid and fluid phase. Deriving a potential energy of interaction for a linear model  $E_{fl/s} = Q(\nabla \cdot \mathbf{u}_s)(\nabla \cdot \mathbf{u}_f)$  results in  $Q$  appearing in both stress-strain relations. In practice, the coefficients are calculated using the Gedankenexperiments presented by Biot et al. (1957) (see Appendix A.1.2). Since fluids do not support shear motion,  $N$  is equal to the shear modulus. The other coefficients are defined in terms of the solid, frame and fluid bulk moduli as presented in.

### A.1.2 Poroelastic coefficients - Gedankenexperimente

The Gedankenexperimente are presented as in Allard et al. (2009) based on (Biot, 1956c; Biot et al., 1957). An equivalent derivation can be found in Carcione (2015).

Gedankenexperiment 1: If the aggregate is sheared, only the frame is sheared because the fluid does not support any shear motion. Hence, the poroelastic second Lamé parameter  $N$  equals the shear modulus of the frame.

Gedankenexperiment 2: The solid-fluid aggregate is surrounded by a flexible jacket (jacket in the sense of covering structure). The pressure in the fluid is  $p_0$ . The jacket is then subjected to a hydrostatic pressure  $p_1$ . The jacket allows the pressure of the fluid inside the jacket to remain constant at  $p_0$ . Hence, only the solid frame is deformed by the pressure increase. Consequently, the frame bulk modulus  $K_{fr}$  is defined as:

$$K_{fr} = \frac{-p_1}{e_{kk}}\tag{A.3}$$

The stresses in the solid are equal to  $-p_1$  and the stress-strain relation can be redefined:

$$\begin{aligned}-p_1 &= (P - \frac{4}{3}N)\epsilon_{kk} \\ 0 &= Qe_{kk1} + Re_{kk}.\end{aligned}\tag{A.4}$$

Gedankenexperiment 3: No jacket is present. The pressure in the fluid is increased by  $p_1$  and transmitted to the solid. The frame stress tensor is subject to the pressure

change and becomes:

$$\sigma_{ij}^s = -p_f(1 - \phi)\delta_{ij}. \quad (\text{A.5})$$

The stress-strain relations for this case are:

$$\begin{aligned} -p_f(1 - \phi) &= (P - \frac{4}{3}N)e_{kk} + Q\epsilon_{kk} \\ -\phi p_f &= Q\epsilon_{kk} + R\epsilon_{kk}. \end{aligned} \quad (\text{A.6})$$

Equivalent to the frame bulk modulus, the solid bulk modulus  $K_s$  (bulk modulus of the material which makes up the frame) and fluid bulk modulus  $K_f$  are defined:

$$\begin{aligned} K_s &= \frac{-p_f}{e_{kk}} \\ K_f &= \frac{-p_f}{\epsilon_{kk}}. \end{aligned} \quad (\text{A.7})$$

Through rearranging the equations resulting from the Gedankenexperiments, a system of three equations is written, which can be solved for the unknown parameters:

$$\begin{aligned} P &= \frac{(1 - \phi)(1 - \phi - \frac{K_{fr}}{K_s})K_s + \frac{\phi K_s K_{fr}}{K_{fl}}}{1 - \phi - \frac{K_{fr}}{K_s} + \frac{\phi K_s}{K_{fl}}} + \frac{4}{3}\mu_{fr} \\ Q &= \frac{(1 - \phi - \frac{K_{fr}}{K_s})\phi K_s}{1 - \phi - \frac{K_{fr}}{K_s} + \frac{\phi K_s}{K_{fl}}} \\ R &= \frac{\phi^2 K_s}{1 - \phi - \frac{K_{fr}}{K_s} + \frac{\phi K_s}{K_{fl}}}. \end{aligned} \quad (\text{A.8})$$

The common denominator  $1 - \phi - \frac{K_{fr}}{K_s} + \frac{\phi K_s}{K_{fl}}$  is also known as effective porosity.

### A.1.3 Inertial coupling - nonviscous fluid

For a solid-fluid aggregate the acceleration of one phase creates an inertial force or a drag on the other element. This effect holds true for an idealized fluid without viscosity as well and is known as added mass or apparent weight. It states that a body moving in a fluid moves in the same way that the same body, but with an added mass, would move in vacuum (Landau et al., 1987; Oman et al., 2016). The added mass has to be taken into account in energy considerations and consequently the kinetic energy of a porous material cannot simply be expressed by the sum of the

fluid and solid macroscopic accelerations. Instead:

$$E_c = \frac{1}{2}\rho_{11}|\dot{\mathbf{u}}|^2 + \rho_{12}\dot{\mathbf{u}}\dot{\mathbf{U}} + \frac{1}{2}\rho_{22}|\dot{\mathbf{U}}|^2. \quad (\text{A.9})$$

The added mass and thus the mass coefficients  $\rho_{11}, \rho_{12}, \rho_{22}$  depend on the density of the porous aggregate and geometry of the pores.  $\rho_{22}$  represents the total effective mass of the solid moving in the fluid,  $\rho_{22}$  that of the fluid in the solid and  $\rho_{12}$  is the coupling coefficient or the negative apparent mass. Its negative sign becomes apparent if we picture the following Gedankenexperiment: We induce solid displacement but prevent fluid displacement. To do so we need a force working on the fluid in direction opposite to the solid acceleration. Hence, the sign of the mass coupling coefficient  $\rho_{12}$  is negative. Expressed in terms of the kinetic energy, the force exerted on the solid respectively fluid equals the change in energy of the fluid respectively solid and hence:

$$\begin{aligned} f_i^s &= \frac{\partial}{\partial t} \frac{\partial E_c}{\partial \dot{\mathbf{u}}_i} = \rho_{11}\ddot{\mathbf{u}}_i + \rho_{12}\ddot{\mathbf{U}}_i \\ f_i^f &= \frac{\partial}{\partial t} \frac{\partial E_c}{\partial \dot{\mathbf{U}}_i} = \rho_{12}\ddot{\mathbf{u}}_i + \rho_{22}\ddot{\mathbf{U}}_i. \end{aligned} \quad (\text{A.10})$$

In the idealized case that both phases move together at the same particle velocity  $\dot{\mathbf{u}}_i = \dot{\mathbf{U}}_i$  the kinetic energy can be simplified to:

$$E_c = \frac{1}{2}(\rho_{fr} + \phi\rho_{fl})|\dot{\mathbf{u}}_{s/f}|^2. \quad (\text{A.11})$$

The force exerted on the fluid can be expressed as:

$$f_i^f = \phi\rho_{fl} \frac{\partial^2 \mathbf{U}_i}{\partial t^2}. \quad (\text{A.12})$$

It follows from Eq. (A.10) and A.12 that:

$$\begin{aligned} \phi\rho_{fl} &= \rho_{22} + \rho_{12} \\ \rho_{fr} &= \rho_{11} + \rho_{12}. \end{aligned} \quad (\text{A.13})$$

The three mass coefficients can thus be expressed in terms of the frame density, fluid density and the porosity.

#### A.1.4 Equations of motion

Expressing the forces in Eq. (A.10) as stress gradients yields the porous equations of motion:

$$\begin{aligned}\nabla_j \sigma_{ij}^s &= \frac{\partial^2}{\partial t^2} (\rho_{11} u_i + \rho_{12} U_i) ; \quad \nabla_j = \frac{\partial}{\partial x_j} \\ \nabla \sigma_{ij}^f &= \frac{\partial^2}{\partial t^2} (\rho_{12} u_i + \rho_{22} U_i).\end{aligned}\tag{A.14}$$

Making use of Eq. (3.1) which relates stress  $\sigma$  to displacement  $u$  we retrieve:

$$\begin{aligned}N \nabla^2 u_i + (A + N) \frac{\partial e_{kk}}{\partial x_i} + Q \frac{\partial \epsilon_{kk}}{\partial x_i} &= \frac{\partial^2}{\partial t^2} (\rho_{11} u_i + \rho_{12} U_i) ; \quad A = P - 2N \\ Q \frac{\partial e_{kk}}{\partial x_i} + R \frac{\partial \epsilon_{kk}}{\partial x_i} &= \frac{\partial^2}{\partial t^2} (\rho_{12} u_i + \rho_{22} U_i).\end{aligned}\tag{A.15}$$

### A.1.5 Wave equations

Now we can proceed as in classical elasticity and apply the divergence and curl operators to retrieve dilatational and rotational wave motion. For simplicity we will use the vector notation for the rotational equations with  $\mathbf{u} = (u_x \ u_y \ u_z)$  and  $\mathbf{U} = (U_x \ U_y \ U_z)$

**Shear wave** Taking the curl, Eq. (A.15) becomes:

$$\begin{aligned}\frac{\partial}{\partial t^2} (\rho_{11} \nabla \times \mathbf{u} + \rho_{12} \nabla \times \mathbf{U}) &= N \nabla \nabla \times \mathbf{u} \\ \Rightarrow \left[ \frac{N}{\rho_{11} (1 - \frac{\rho_{12}^2}{\rho_{11} \rho_{22}})} \right] \nabla^2 \nabla \times \mathbf{u} &= \frac{\partial^2 \nabla \times \mathbf{u}}{\partial t^2} \\ \frac{\partial}{\partial t^2} (\rho_{12} \nabla \times \mathbf{u} + \rho_{22} \nabla \times \mathbf{U}) &= 0 \\ \Rightarrow \nabla \times \mathbf{U} &= \frac{\rho_{12}}{\rho_{22}} \nabla \times \mathbf{u}\end{aligned}\tag{A.16}$$

Hence, only one rotational equation remains and the fluid rotation is proportional to the solid rotation scaled by  $\frac{\rho_{12}}{\rho_{22}}$ .

$$\sqrt{\frac{N}{\rho_{11} (1 - \frac{\rho_{12}^2}{\rho_{11} \rho_{22}})}} = V_s\tag{A.17}$$

By comparing Eq. (A.17) to the purely elastic shear wave velocity  $\sqrt{\frac{\mu}{\rho}}$ , we see that the difference stems not only from the additional mass of the fluid ( $\rho_{11} = \rho_{solid} + \rho_{apparent}$ ) but the apparent mass effect gets weakened due to a rotation induced in the fluid.

**Compression waves** Applying the divergence operator to Eq. (A.15), two equations remain, explaining mathematically the existence of two dilatational waves:

$$\begin{aligned}\nabla^2(Pe_{kk} + Q\epsilon_{kk}) &= \frac{\partial^2}{\partial t^2}(\rho_{11}e_{kk} + \rho_{12}\epsilon_{kk}) \\ \nabla^2(Qe_{kk} + R\epsilon_{kk}) &= \frac{\partial^2}{\partial t^2}(\rho_{12}e_{kk} + \rho_{22}\epsilon_{kk})\end{aligned}\quad (\text{A.18})$$

Reformulating Eq. (A.18) using a reference velocity  $V_{ref}$ , the coefficient  $H = P + R + 2Q$  and the mass of the aggregate  $\rho = (1 - \phi)\rho_s + \phi\rho_{fl} = \rho_{fr} + \phi\rho_{fl}$  we get:

$$\begin{aligned}\nabla^2(Pe_{kk} + Q\epsilon_{kk}) &= \frac{1}{V_{ref}^2} \frac{\partial^2}{\partial t^2} \left( \frac{\rho_{11}}{\rho} e_{kk} + \frac{\rho_{12}}{\rho} \epsilon_{kk} \right); \quad V_{ref}^2 = \frac{H}{\rho}; \quad P = A + 2N \\ \nabla^2\left(\frac{Q}{H}e_{kk} + \frac{R}{H}\epsilon_{kk}\right) &= \frac{1}{V_{ref}^2} \frac{\partial^2}{\partial t^2} \left( \frac{\rho_{12}}{\rho} e_{kk} + \frac{\rho_{22}}{\rho} \epsilon_{kk} \right).\end{aligned}\quad (\text{A.19})$$

Assuming plane wave propagation, the solutions of Eq. (A.19) are in the isotropic case:

$$\begin{aligned}e_{kk} &= \nabla \cdot \mathbf{u} = A_{p1}e^{i(kx + \omega t)} \\ \epsilon_{kk} &= \nabla \cdot \mathbf{U} = A_{p2}e^{i(kx + \omega t)}\end{aligned}\quad (\text{A.20})$$

with a wave velocity  $v = \frac{\omega}{k}$ , which can be determined by substituting the solutions of Eq. (A.20) into Eq. (A.19) and solving the resulting system. The two resulting roots have each two amplitudes associated. Biot notes, that these satisfy an orthogonality such that the amplitudes  $A_{p1s}, A_{p1f}$  of the first waves are in phase and the amplitudes of the second wave  $A_{p2s}, A_{p2f}$  are out of phase<sup>2</sup>. The solutions for the compression wave velocities will be given at the end of the next section, including the effect of viscosity.

## A.2 Viscous fluid: Wave propagation in the presence of dissipation

To account for dissipation Biot assumes Poiseuille flow to hold true in a low frequency regime defined by a cross-over frequency  $f_c$  (see Appendix A.3). Above, Poiseuille flow breaks down. Assuming isotropy and that the flow in microscopic pores is completely determined by the velocities  $\mathbf{u}_i$  and  $\mathbf{U}_i$ , Biot defines a dissipation function

<sup>2</sup>A physical explanation for the secondary longitudinal wave is due to out of phase motion of the solid and fluid constituent. Fluid flow balances local pressure gradients induced by the primary p-wave. The pressure gradients develop because the pore size is much smaller than the wavelength of the primary seismic wave.

$D_{visc}$ :

$$2D_{visc} = b \left[ \sum_{i=1}^3 (\dot{u}_i - \dot{U}_i)^2 \right] \quad (A.21)$$

$$b = \eta_f \frac{\phi^2}{\kappa}$$

where  $\eta_f$  is fluid viscosity and  $\kappa$  is permeability. The permeability characterizes how well the solid allows for fluid flow. It is independent of the fluid and measured in  $m^2$ . The equations for the purely viscous fluid flow and consequently Darcy's equation are defined as follows:

$$\frac{\partial \sigma_{ij}^f}{\partial x_j} = b \frac{\partial}{\partial t} (U_i - u_i) \quad (A.22)$$

$$\nabla_i (Q e_{kk} + R \epsilon_{kk}) = b \frac{\partial}{\partial t} (U_i - u_i).$$

Since the Poiseuille flow depends only on relative fluid-solid motion the dissipation vanishes in its absence. The same reasoning we applied to Eq. (A.11) is applied to the dissipation function, leading to the new equations of motion, now including viscosity:

$$N \nabla^2 u_i + (A + N) \frac{\partial e_{kk}}{\partial x_i} + Q \frac{\partial \epsilon_{kk}}{\partial x_i} = \frac{\partial^2}{\partial t^2} (\rho_{11} u_i + \rho_{12} U_i) + b \frac{\partial}{\partial t} (u_i - U_i) ; A = P - 2N$$

$$Q \frac{\partial e_{kk}}{\partial x_i} + R \frac{\partial \epsilon_{kk}}{\partial x_i} = \frac{\partial^2}{\partial t^2} (\rho_{12} u_i + \rho_{22} U_i) - b \frac{\partial}{\partial t} (u_i - U_i). \quad (A.23)$$

Spatially differentiating the equations of motion leads to the dilatational wave equations:

$$\nabla^2 (P e_{kk} + Q \epsilon_{kk}) = \frac{\partial^2}{\partial t^2} (\rho_{11} e_{kk} + \rho_{12} \epsilon_{kk}) + b \frac{\partial}{\partial t} (e_{kk} - \epsilon_{kk}) \quad (A.24)$$

$$\nabla^2 (Q e_{kk} + R \epsilon_{kk}) = \frac{\partial^2}{\partial t^2} (\rho_{12} e_{kk} + \rho_{22} \epsilon_{kk}) - b \frac{\partial}{\partial t} (e_{kk} - \epsilon_{kk}).$$

because  $\nabla u = e_{kk}$ ;  $\nabla U = \epsilon_{kk}$

The rotational wave equation is retrieved by applying the curl operation and in vector notation we get:



$$\begin{aligned}
N\nabla^2\nabla \times \mathbf{u} &= \frac{\partial^2}{\partial t^2}(\rho_{11}\nabla \times \mathbf{u} + \rho_{12}\nabla \times \mathbf{U}) + b\frac{\partial}{\partial t}(\nabla \times \mathbf{u} - \nabla \times \mathbf{U}) \\
&= \frac{\partial^2}{\partial t^2}(\rho_{11}\nabla \times \mathbf{u}) + b\frac{\partial}{\partial t}(\nabla \times \mathbf{u}) \\
0 &= \frac{\partial^2}{\partial t^2}(\rho_{12}\nabla \times \mathbf{u} + \rho_{22}\nabla \times \mathbf{U}) - b\frac{\partial}{\partial t}((\nabla \times \mathbf{u} - \nabla \times \mathbf{U})) \\
&= \frac{\partial^2}{\partial t^2}(\rho_{12}\nabla \times \mathbf{u}) - b\frac{\partial}{\partial t}((\nabla \times \mathbf{u})).
\end{aligned} \tag{A.25}$$

### A.2.1 Wavespeed calculation

For the calculation of Biot's wavespeed in this manuscript we use a formulation that employs a slightly different notation from Biot's original paper. For practical applications Biot (1956a) and Biot et al. (1957) introduce a new set of variables. Biot et al. (1957) gives a linear strain energy formulation, which for uniform porosity results in equations of motion equivalent to Eq. (A.23). The wave equations then depend on the new coefficients  $H, M, C, \mu_{fr}$  instead of  $P, Q, R, N$ . Instead of the mass coefficients  $p_{11}, p_{12}, p_{22}$ , the mass of the fluid ( $\rho_{fl}$ ) and solid ( $\rho_s$ ) or frame ( $\rho_{fr}$ ) as well as the tortuosity ( $\alpha$ ) are used. Furthermore,  $\zeta$ , which is the volumetric change of fluid content is introduced (Biot, 1956a):

$$\begin{aligned}
H &= P + 2Q + R \\
\mu_{fr} &= N \\
M &= \frac{R}{\phi^2} \\
C &= B_W M \\
B_W &= \left(\frac{Q+R}{R}\phi\right) \\
\zeta &= \phi\nabla \cdot (\dot{\mathbf{u}} - \dot{\mathbf{U}}) \\
m &= \alpha \frac{\rho_{fl}}{\phi} \\
\rho &= (1 - \phi)\rho_s + \phi\rho_{fl}
\end{aligned} \tag{A.26}$$

where  $B_W$  is known as the Biot-Willis coefficient. Note that the purely geometric tortuosity factor can be related to the mass coupling coefficient by  $\rho_{12} = -(\alpha - 1)\phi\rho_f$  (Berryman, 1980).  $\alpha$  generally varies between 1 (uniform cylindrical pores) and 3 (random pore orientations).

Following Biot (1962), Stoll et al. (1970), Buchanan (2005), and Berryman (1980) the dilatational equations read:

$$\begin{aligned}\nabla^2(He_{kk} - C\zeta) &= \frac{\partial}{\partial t^2}(\rho e_{kk} - \rho_{fl}\zeta) \\ \nabla^2(Ce_{kk} - M\zeta) &= \frac{\partial}{\partial t^2}(\rho_{fl}e_{kk} - m\zeta) - \frac{\eta}{\kappa} \frac{\partial \zeta}{\partial t}\end{aligned}\tag{A.27}$$

and the rotational wave equations read:

$$\begin{aligned}\mu \nabla^2 \nabla \times \mathbf{u} &= \frac{\partial}{\partial t^2}(\rho \nabla \times \mathbf{u} - \rho_{fl} \nabla \times \mathbf{U}) \\ -\frac{\eta}{\kappa} \frac{\partial \nabla \times \mathbf{U}}{\partial t} &= \frac{\partial^2}{\partial t^2}(\rho_{fl} \nabla \times \mathbf{u} + m \nabla \times \mathbf{U})\end{aligned}\tag{A.28}$$

Considering plane waves, the deformation due to a rotation or dilatation and consequently the solution to Eqs. (A.27) and (A.28) can be expressed as:

$$\begin{aligned}\nabla \cdot \mathbf{u} &= A_{p1} e^{i(kx + \omega t)} \\ \nabla \cdot \mathbf{U} &= A_{p2} e^{i(kx + \omega t)} \\ \nabla \times \mathbf{u} &= A_{s1} e^{i(kx + \omega t)} \\ \nabla \times \mathbf{U} &= A_{s2} e^{i(kx + \omega t)} = 0.\end{aligned}\tag{A.29}$$

with  $A$  being the respective constant for each solution. The frequency dependent velocity  $v = \frac{\omega}{k}$  is calculated from the the dispersion relation (Berryman, 1980; Mavko et al., 2009; Stoll, 1974) in the frequency domain:

$$\begin{vmatrix} \rho - \frac{H}{(\omega_p/k_p)^2} & \rho_{fl} - \frac{C}{(\omega_p/k_p)^2} \\ \rho_{fl} - \frac{C}{(\omega_p/k_p)^2} & q_f - \frac{M}{(\omega_p/k_p)^2} \end{vmatrix} = 0\tag{A.30}$$

$$\begin{vmatrix} \rho - \frac{\mu_{fr}}{(\omega_s/k_s)^2} & \rho_{fl} \\ \rho_{fl} & q_f \end{vmatrix} = 0.\tag{A.31}$$

The velocities can then be expressed as solutions of the exponential function  $v = \text{Re} \sqrt{(\frac{\omega}{k})^{-2}}$ :

$$\left(\frac{\omega_p}{k_p}\right)^{-2} = \frac{-(Hq + M\rho - 2C\rho_{fl}) \pm \sqrt{(Hq + M\rho - 2C\rho_{fl})^2 - 4(C^2 - MH)(\rho_{fl}^2 - \rho q)}}{2(C^2 - MH)}\tag{A.32}$$

$$\left(\frac{\omega_s}{k_s}\right)^{-2} = \frac{q\rho - \rho_{fl}^2}{q\mu_{fr}}\tag{A.33}$$

where the different terms can be expressed in term of the solid, fluid and porous parameters as:

$$\begin{aligned}
 q &= \frac{\alpha \rho_{fl}}{\phi} - \frac{i\eta F(\zeta)}{\omega \kappa} \\
 H &= \frac{(K_s - K_{fr}) * (K_s - K_{fr})}{D - K_{fr}} + K_{fr} + \frac{4}{3} \mu_{fr} \\
 C &= K_s \frac{K_s - K_{fr}}{D - K_{fr}} \\
 M &= K_s \frac{K_s}{D - K_{fr}} \\
 D &= K_s (1 + \phi (\frac{K_s}{K_f} - 1)),
 \end{aligned} \tag{A.34}$$

where  $\kappa$  is permeability,  $\alpha$  is tortuosity and  $F(\zeta)$  expresses the frequency dependence of the viscosity (see Appendix A.4). Under the assumption of Poiseuille flow, which we have assumed until now  $F(\zeta)$  is one. The frequency dependence becomes relevant for frequencies larger than Biot's crossover frequency (see Appendix A.3).

### A.3 Crossover frequency between high and low frequency range

The theory distinguishes two frequency dependent flow regimes separated by Biot's critical or crossover frequency  $\omega_c$

$$\omega_c = \frac{\eta \phi}{\rho_{fl} \kappa_0 \alpha_\infty} \tag{A.35}$$

where  $\alpha_\infty$  is dynamic tortuosity,  $\eta$  is fluid viscosity and  $\kappa$  is permeability. In the low frequency regime the viscous skin depth

$$\delta_{skin} = \frac{2\eta}{\omega \rho_{fl}}^{1/2} \tag{A.36}$$

is smaller than the pore radius and Poiseuille dominates inertial flow. Above the critical frequency however, inertial forces dominate and the viscosity becomes frequency dependent (Biot, 1956b). Further extensions also assume a frequency dependence for permeability and tortuosity values (Champoux et al., 1991; Johnson et al., 1994).

### A.4 High frequency approximation

For high frequencies above the crossover frequency given in Eq. (A.35), the flow profile of the fluid deviates from a classic Poiseuille flow. In other words, the higher the frequency, the more inertial effects dominate over viscous effects. Hence, the

viscosity needs to be corrected by a frequency dependent factor, which is given by  $F(\zeta)$ :

$$\begin{aligned}
 F(\zeta) &= \frac{1}{4} \left( \frac{\zeta T(\zeta)}{1 + 2i \frac{T(\zeta)}{\zeta}} \right) \\
 T(\zeta) &= \frac{ber'(\zeta) + i bei'(\zeta)}{ber(\zeta) + i bei(\zeta)} \\
 \zeta &= \sqrt{\frac{\omega}{\omega_c}}.
 \end{aligned} \tag{A.37}$$

with  $ber()$  the real part of the Kelvin function and  $bei()$  the imaginary part of the Kelvin function and  $\omega_c$  being the angular crossover frequency.



## Appendix B

# Appendix Sensitivity Analysis

To verify the influence of the two free parameters within the given literature bounds, we ran a global sensitivity analysis of the Sobol type, using the SALib library (Herman et al., 2017). Our sensitivity measure is the misfit of the experimental values and Biot's prediction. We performed it separately for the shear wave and the PII-wave (see Table B.1). The resulting sensitivity indexes are Sobol's first and total order indexes, which give the dependence of the misfit for each parameter (first order index) and the level of interactions between the parameters (ratio of total order index and first order index).

*Table B.1:* Results for a global sensitivity analysis of the Sobol type using the SALib library (Iooss et al., 2015; Wainwright et al., 2014; Herman et al., 2017). The misfit of the experimental wave speeds and Biot's prediction is the sensitivity measure and gives the sensitivity indexes. If the total order index approximately equals the first order index, the dependence is linear. If the total order index is higher than the first order index, the joint effect on the output is different from the sum of the individual effects and higher order interactions are present.

	S-wave		P-wave	
	Young	Poisson	Young	Poisson
First order	0.97640753	0.00095548	-0.000055294	0.91035
Total order	1.00208442	0.03074983	0.000293239	1.45568

The results presented in Table B.1 show that there is a difference in sensitivity for the S-wave and the PII-wave. While the misfit of the S-wave is predominately dependent on changes in the Young's modulus (high first order index), the misfit of the PII-wave is predominately dependent on changes in Poisson's modulus. For the S-wave, first order indexes approximately equal second order indexes and thus the misfit is linear dependent on changes in the parameters. For the PII-wave, the total order index of Poisson is higher than its first order index and consequently higher order interactions are present.<sup>1</sup>

The sensitivity analysis shows that our result for the shear wave fit is robust with regard to Young's modulus but less robust for Poisson's ratio. At the same time, the Biot's PII-wave dispersion at the measured low frequencies is dominated by a non-linear dependence on the variation of Poisson's modulus. However, changes in

Poisson's modulus do not alter the general trend of the PII-wave. The predictions by Biot theory are still overestimating our experimental measures.

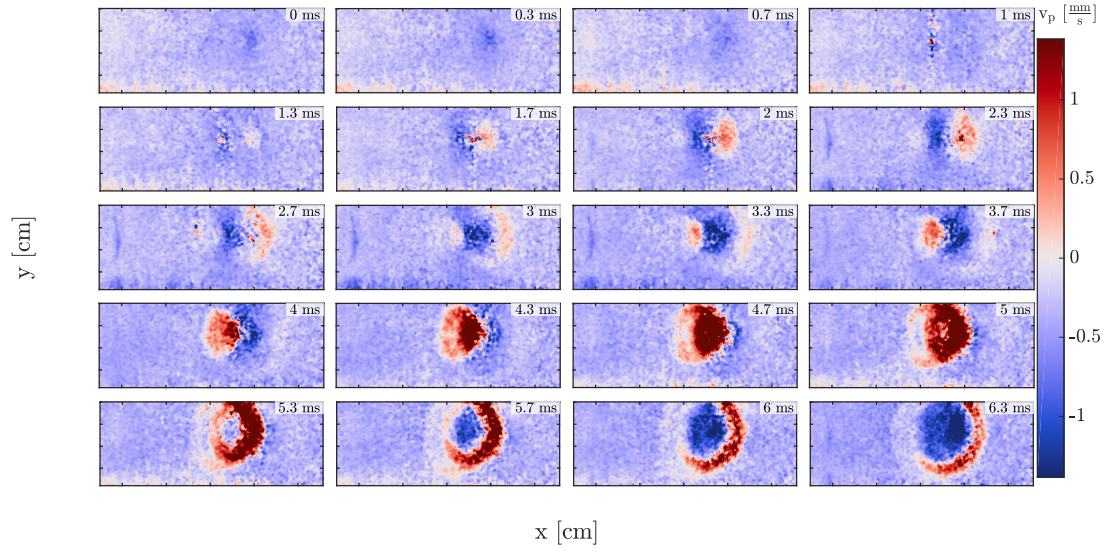
## Appendix C

# Further experimental results

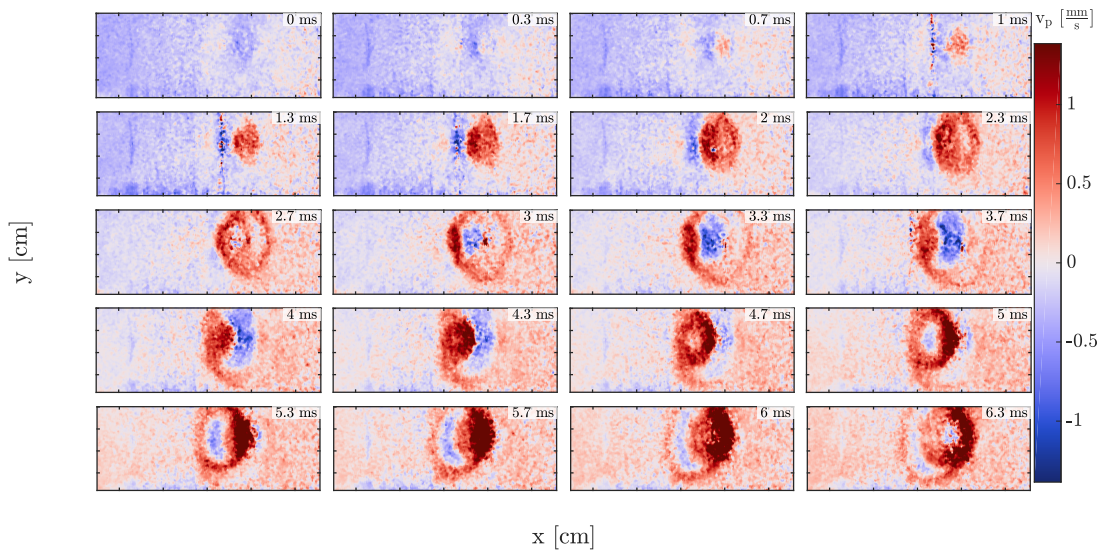
### C.1 Further rupture examples

The following two Figures show snapshots from the experiment in Section 4.4.2.a. They exemplify the presence of left-going ruptures as well as reflected ruptures.





*a*: Right-traveling

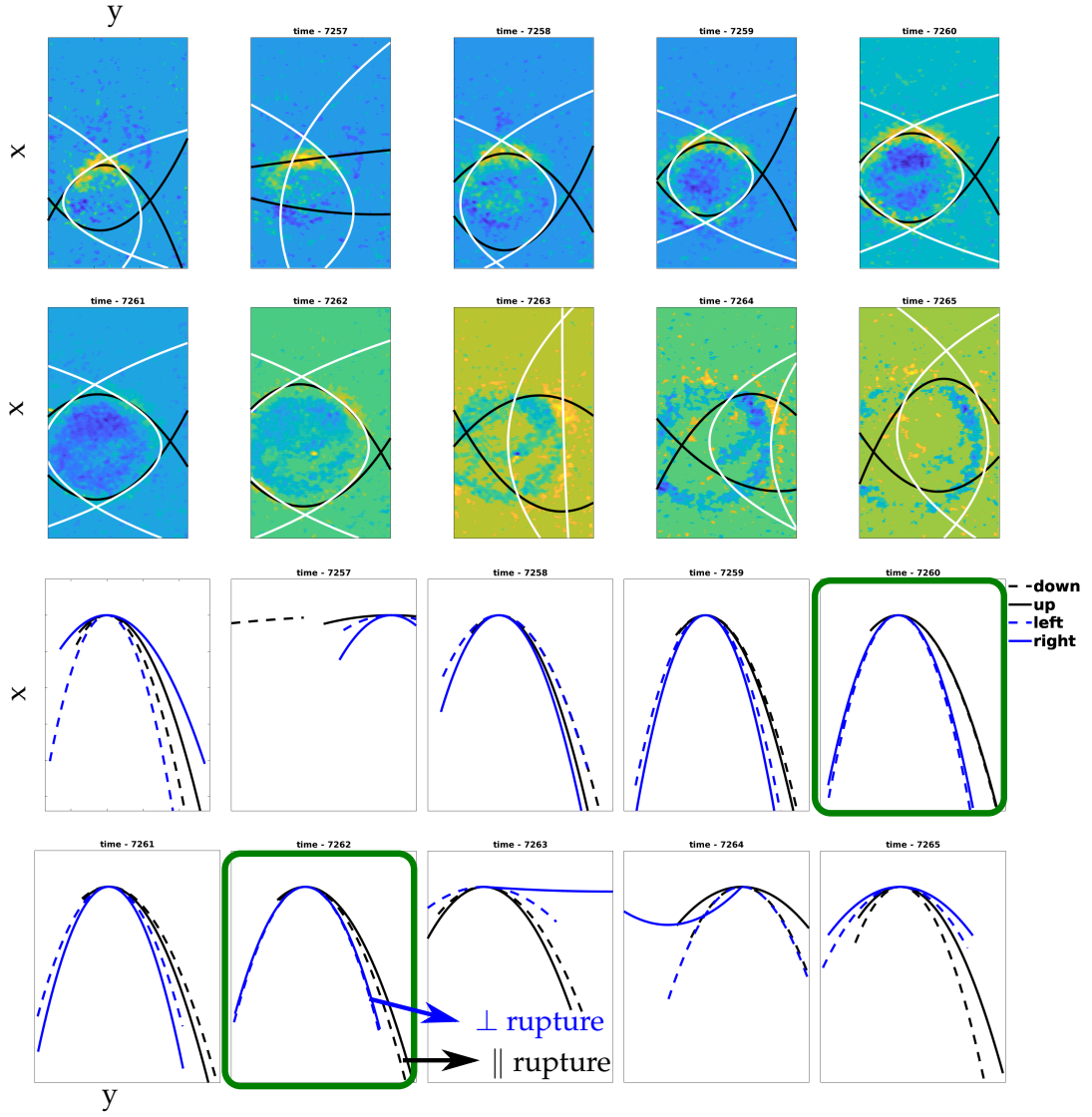


*b*: Left-traveling and reflected rupture

Figure C.1.1: Further rupture examples from Section 4.4.2.a.

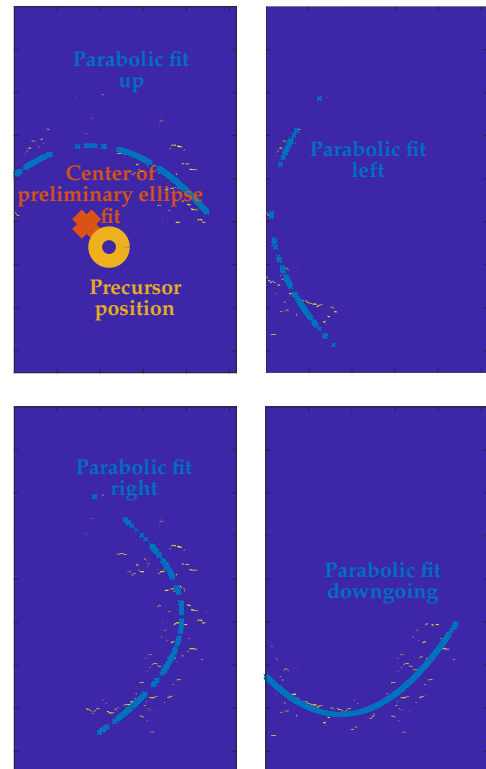
## C.2 2D wavefield detection

Fig. C.2.1a shows two examples of filtered snapshots and superimposed parabolic fits. The right shows the parabolic fits for each snapshot superimposed. Only for the central part of the rupture, the fits appear reliable and expose a clear dichotomy between fault-parallel and fault-orthogonal propagation direction. Fig. C.2.1b shows an example of the binarized data the fit is performed on. We notice, that the binarized data scarcely resembles the segmentation we would have performed by eye.



*a:* Left: Parabolic fits on a wavefield from Section 4.4.2.a. Right: The four fits of each snapshot superimposed.

*b:* Example of the binary data retrieved through image segmentation used as input for the parabolic fit.



### C.3 Frequency content

In the present manuscript I have analyzed the space and time properties of the wavefield. In the future it would be interesting to analyze the frequency content of the observed ruptures. In the following I show several examples of the frequencies present in two experiments.

Fig. C.3.1 shows the spectrograms of one measurement point inside and one measurement point outside the asperity for the rupture in Section 4.4.2.a. With the onset of asperity ruptures, the point inside the asperity exposes a higher frequency content than the point outside. This feature in combination with other could facilitate automatic detection in the future. It is probably due to the undersampled precursory events.

Figs. C.3.2 to C.3.4 show the frequency content of Section 4.4.2.b for the ROIs indicated in Fig. C.3.2. The rupture starts at the top and travel downwards. Fig. C.3.3 shows that the power spectra of two ROIs on the asperity expose a more bell-like shape, while the points outside and on the edge of the asperity two distinctive peaks. It is interesting to note that from ROI3 to ROI4 the frequency increases with the power.

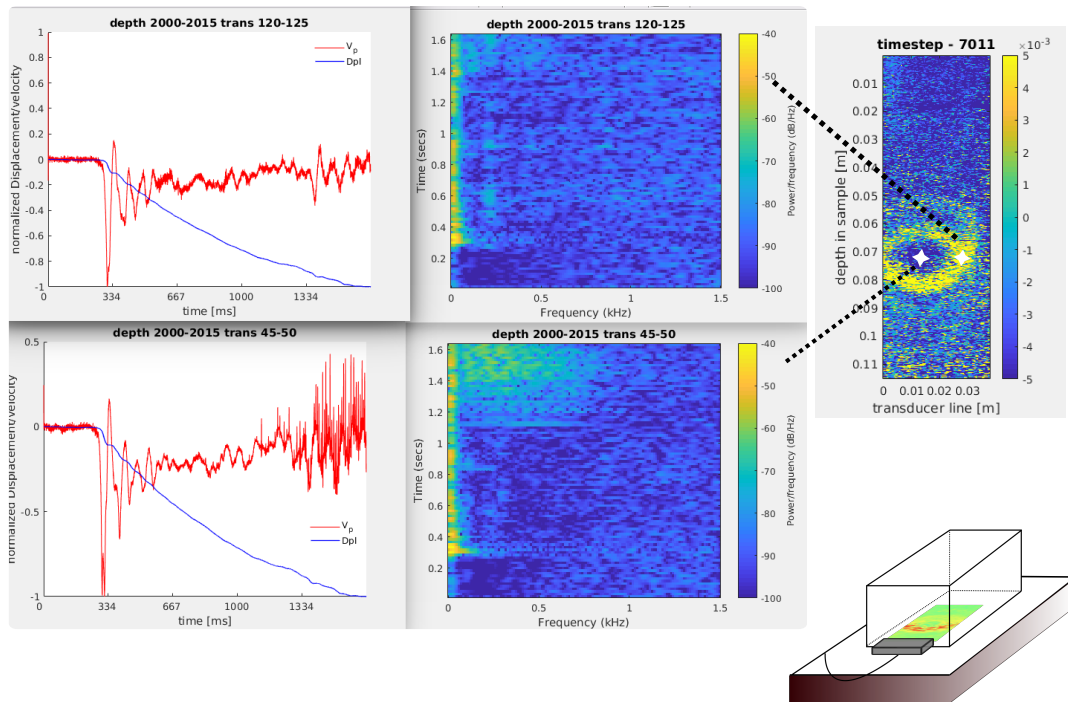


Figure C.3.1: Frequency analysis of two points from the experiment presented in Section 4.4.2.a. On the right, the particle velocity and displacement curves of the two indicated points in the imaging plane on the right are shown. The middle part shows a spectrogram. The frequency content from 1.1 s onwards is only increasing for the point on the asperity.

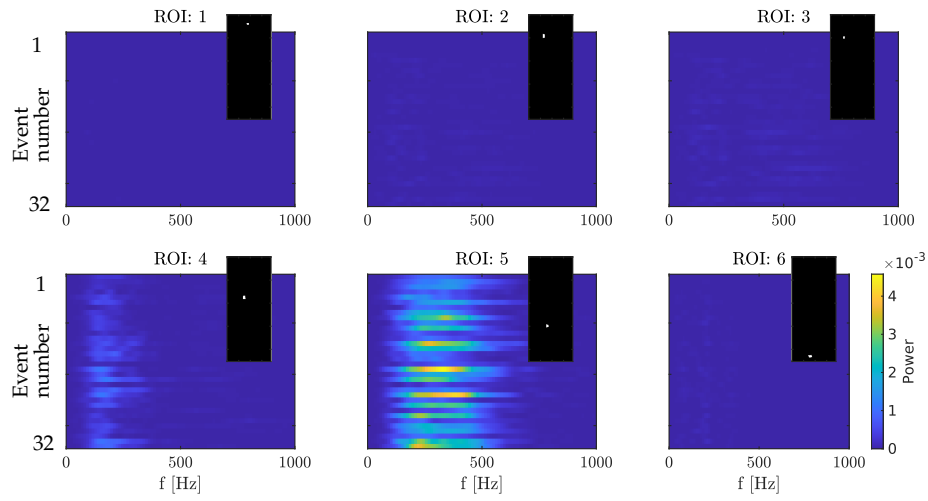


Figure C.3.2: Power spectra for all ruptures and different ROIs of Section 4.4.2.b. The time vector for each rupture is 30 ms, with the main event at the center. The inset schematically shows the ROI position on the imaging plane. Top left is  $x = 0, y = 3.8$  cm and bottom right is  $x = 8.5, y = 0$  cm

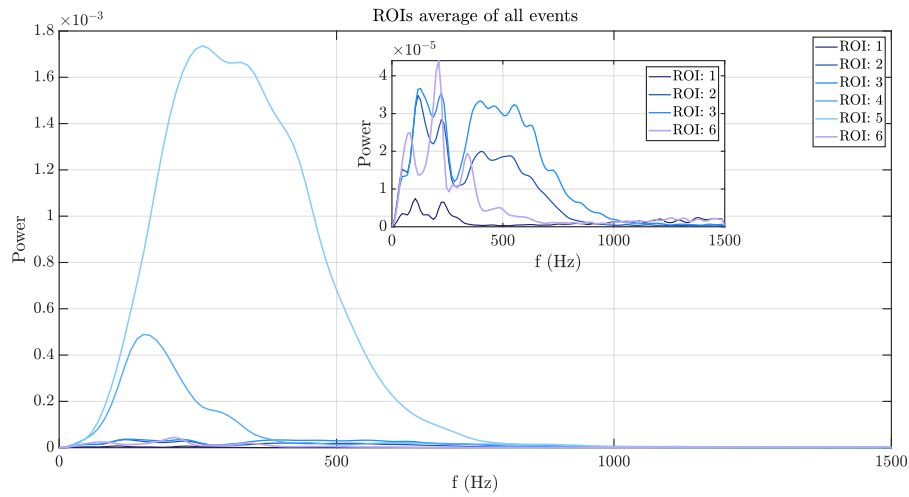


Figure C.3.3: Power spectra of the average of all detected ruptures for each ROI of Section 4.4.2.b. The time vector for each rupture is 30 ms, with the main event at the center.

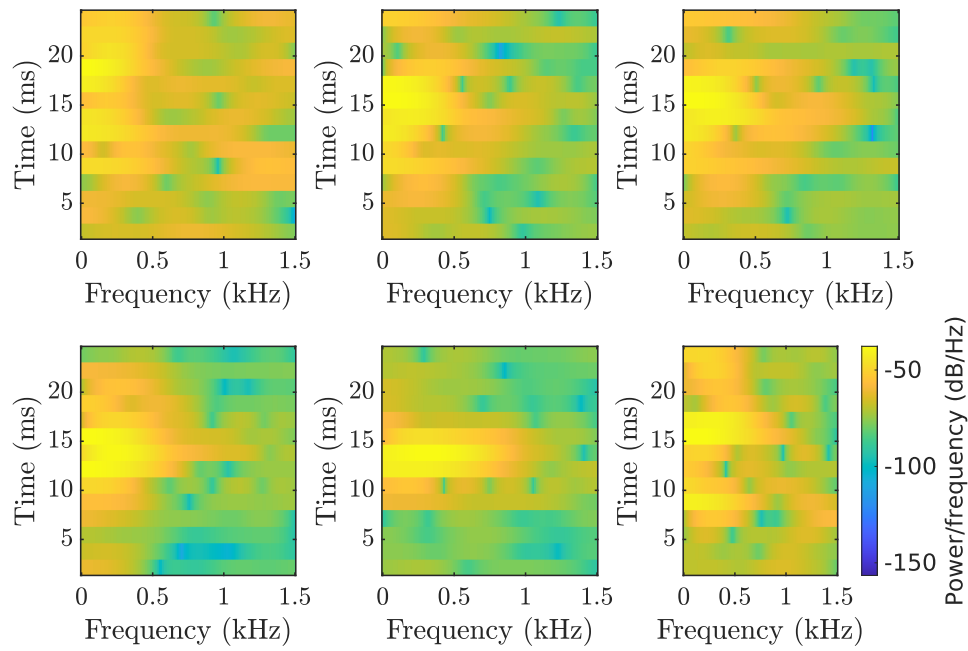


Figure C.3.4: Spectrograms for each ROI in Section 4.4.2.b. The input data is the particle-velocity data of 30 ms around the rupture detection. For each ROI all ruptures get averaged and the average spectrogram is calculated.

The high frequency radiation during laboratory earthquakes has been the topic of a recent study by Marty et al. (2019). One key finding is that the sources of high frequency radiation travel with and are located just behind the rupture front. It would be worth investigating if the conclusions they draw from acoustic emissions hold true for the here presented experiments and their characteristic frequencies as well.

## C.4 K-means

I quickly mentioned the testing of a K-means algorithm for classification of rupture events in Section 4.4.2.a. In Fig. C.4.1 the results for different numbers of clustering groups applied on the results of Section 4.4.2.b are shown. The input parameters for the K-means algorithm are skewness, variance and mean for one large region on the asperity as well as one small region outside of the asperity. Fig. C.4.2 shows examples of snapshots that got sorted into the same group.

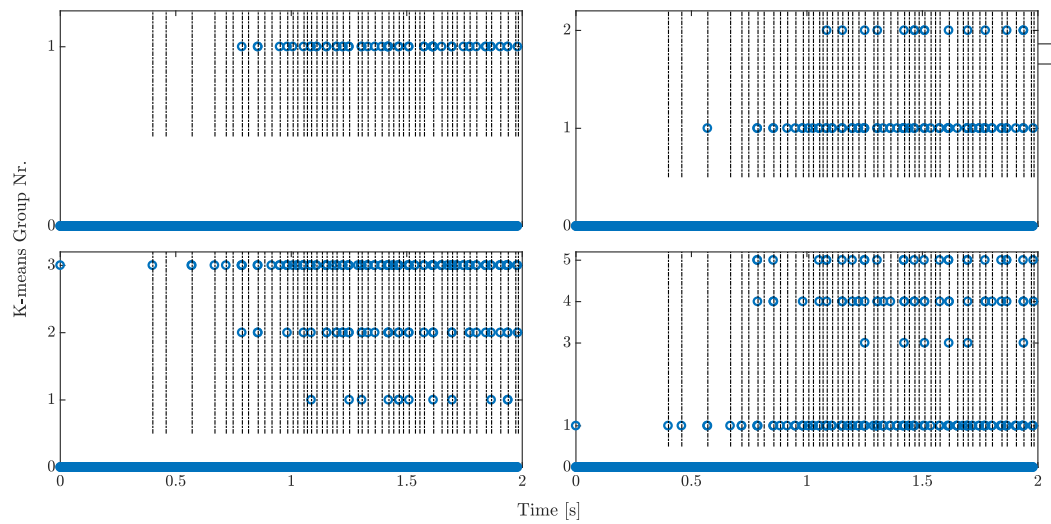
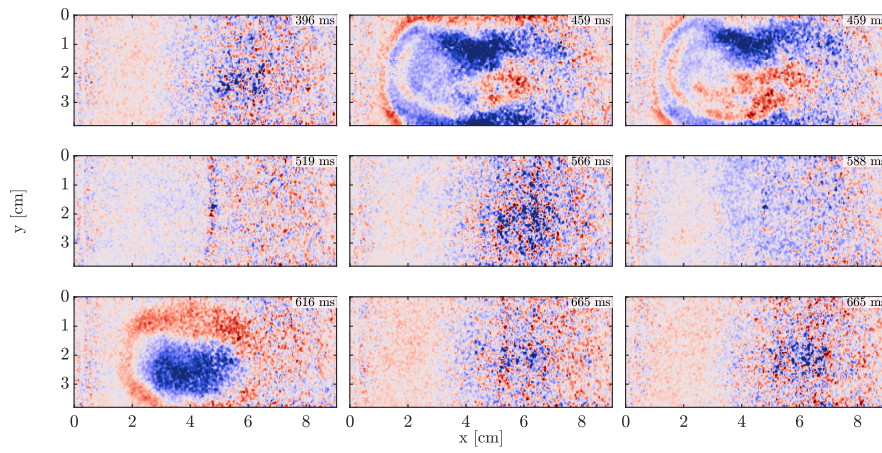
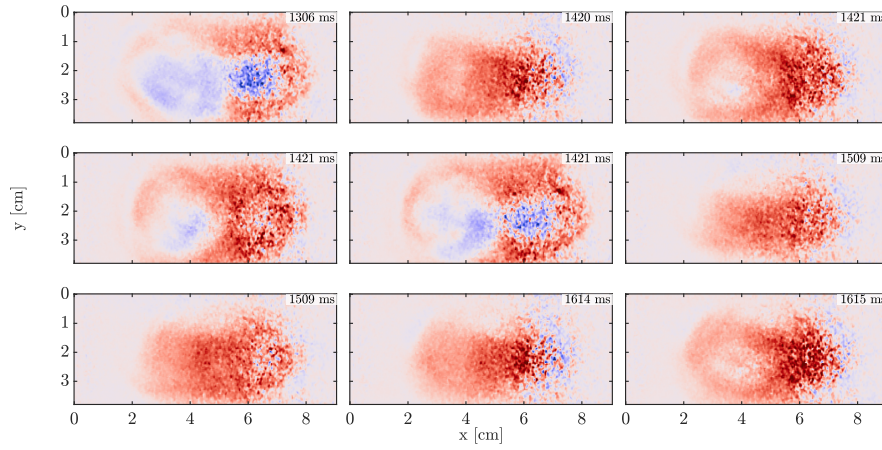


Figure C.4.1: K-means classifications for different group numbers for the experiment in Section 4.4.2.b.

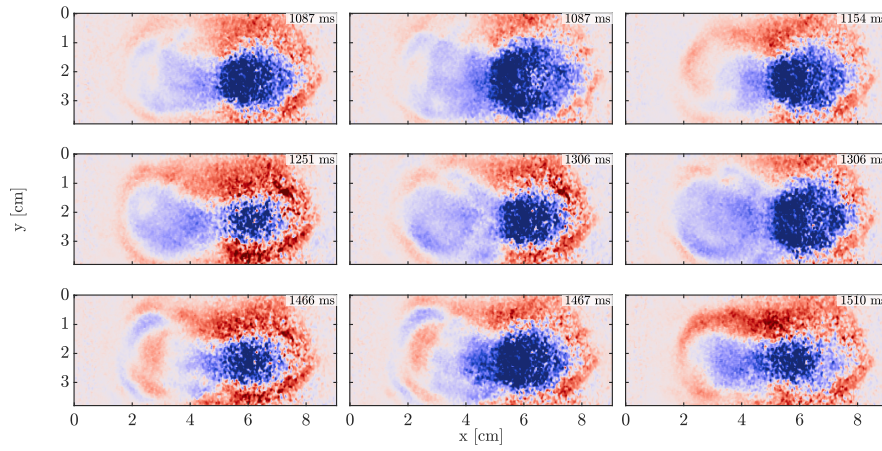




a: Examples for snapshots classified into the same group by kMeans,



b: Examples for snapshots classified into the same group by kMeans,



c: Examples for snapshots classified into the same group by kMeans,

Figure C.4.2: Snapshots from the experiment presented in Section 4.4.2.b which got classified into the same group by the K-means clustering algorithm.





## Appendix D

### Simulation sources

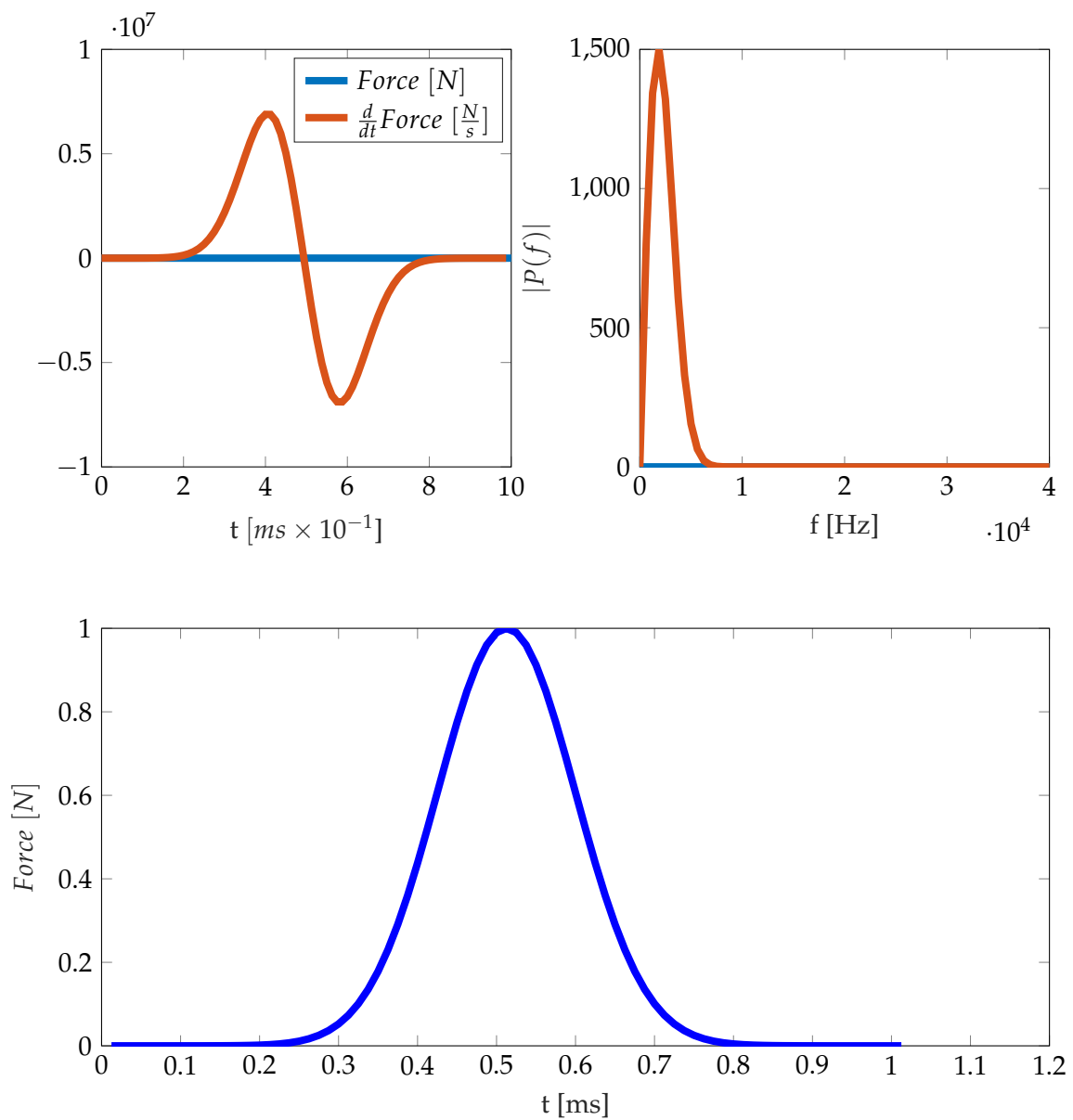
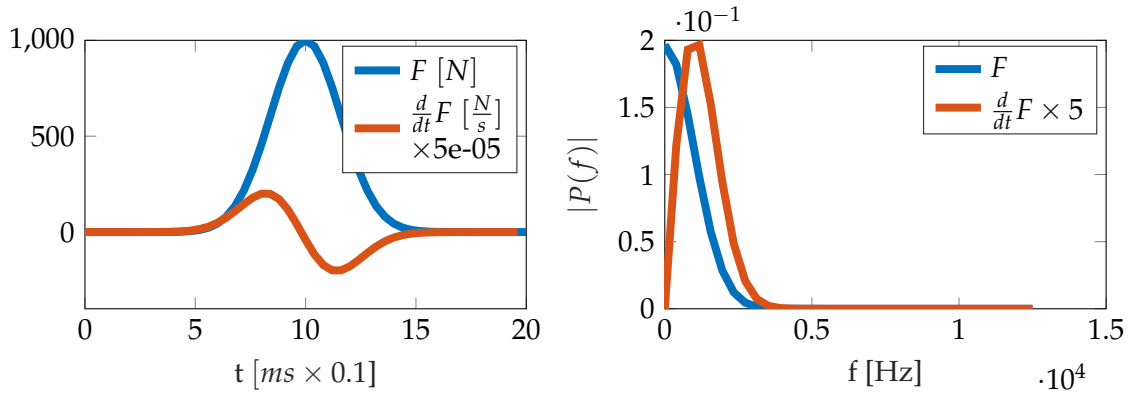
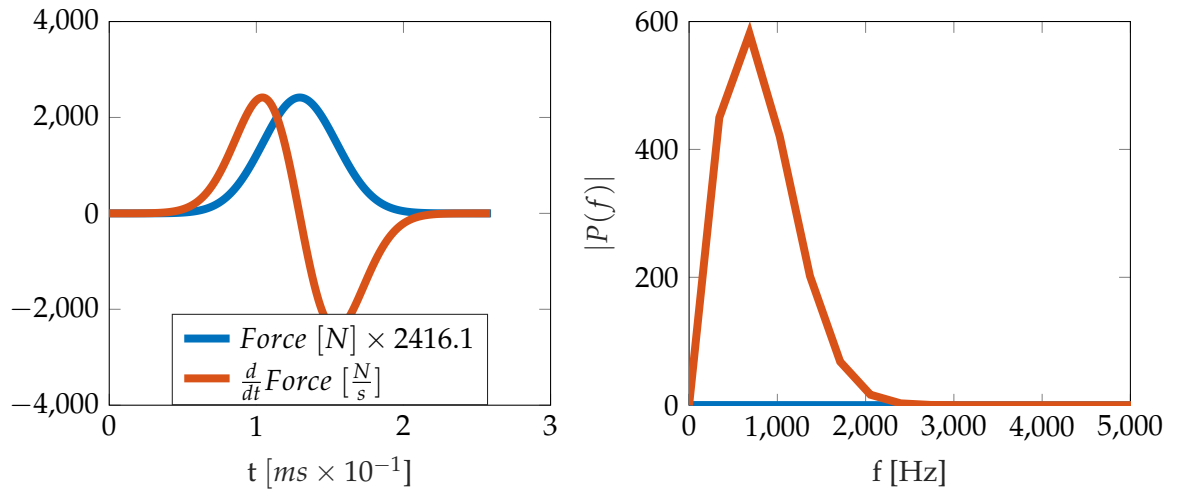


Figure D.0.1: Source function for Fig. 4.4.19

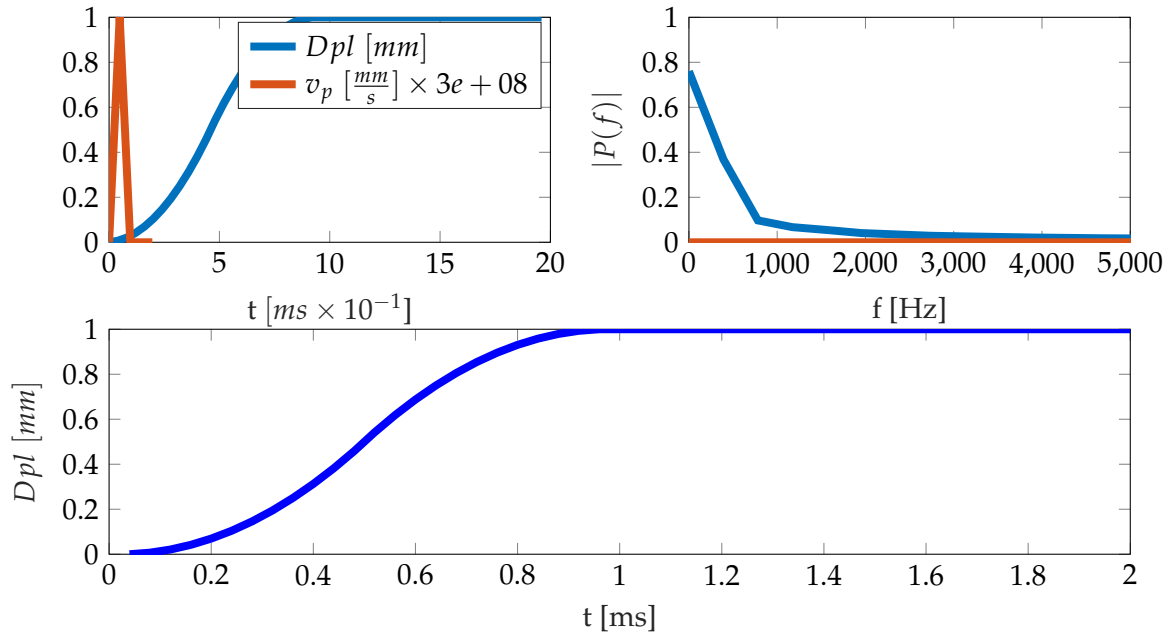


a: Source function for Fig. 4.4.3

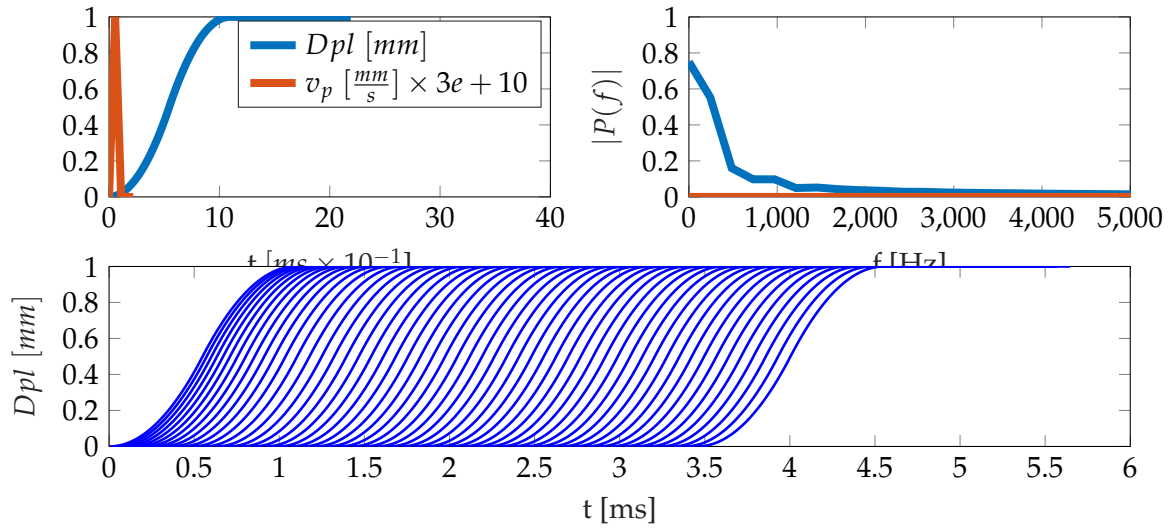


b: Source function for Fig. 4.4.4

Figure D.0.2: Source function for the singular-force simulations in Section 4.4.1.a

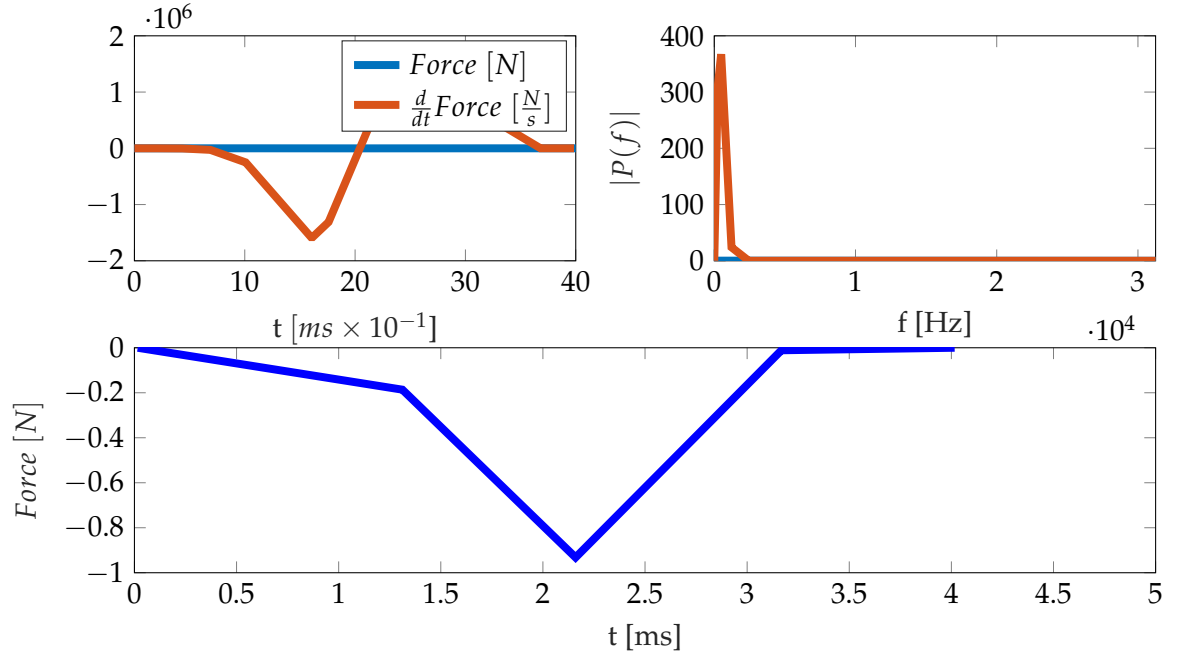


a: Source function for Fig. 4.4.17

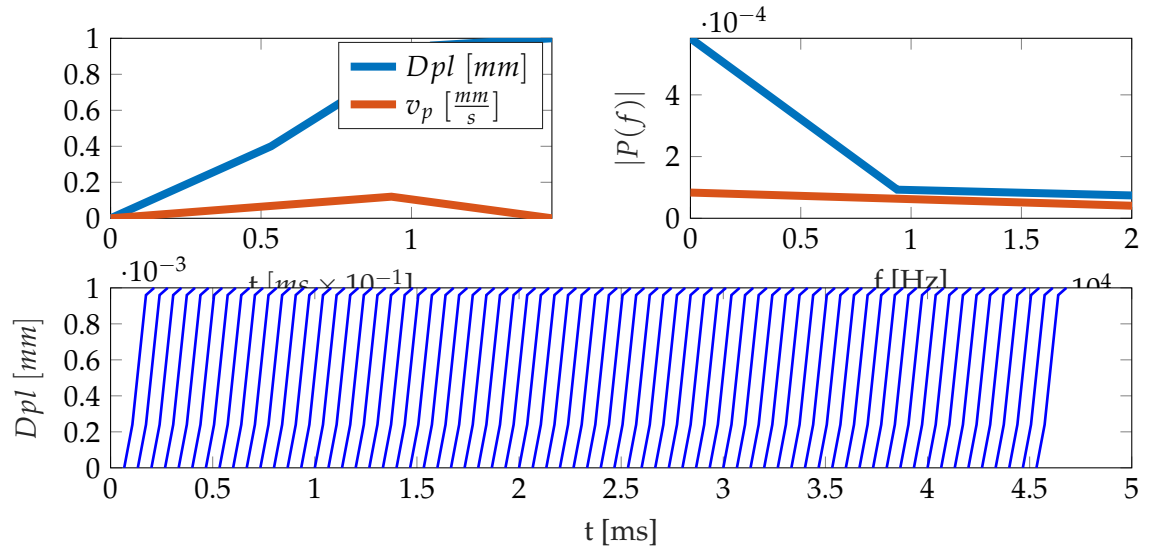


b: Source function for Fig. 4.4.5

Figure D.0.3: Source function for the DC simulations in Section 4.4.1.a



a: Source function for Fig. 4.4.39b



b: Source function for Fig. 4.4.39a

Figure D.0.4: Source function for the simulations in Section 4.4.3

## Appendix E

# Accepted article - <https://arxiv.org/abs/1907.11276>

### Capturing the shear and secondary compression wave: High frame rate ultrasound imaging in saturated foams

Aichele J.,<sup>1</sup> Giammarinaro B.,<sup>1</sup> Reinwald M.,<sup>2</sup> Le Moign G.,<sup>3</sup> and Catheline S.<sup>1</sup>

<sup>1</sup>Laboratory of Therapeutic Applications of Ultrasound, INSERM & University of Lyon, Lyon, France

<sup>2</sup>Department of Biomedical Engineering, School of Biomedical Engineering & Imaging Sciences, King's College London, London, UK

<sup>3</sup>CREATIS Medical Imaging Research Center & University of Lyon, Lyon, France & GAUS, University of Sherbrooke, Sherbrooke, Canada

(Dated: July 24, 2019)

We experimentally observe the shear and secondary compression wave inside soft porous water-saturated melamine foams by high frame rate ultrasound imaging. Both wave speeds are supported by the weak frame of the foam. The first and second compression waves show opposite polarity, as predicted by Biot theory. Our experiments have direct implications for medical imaging: Melamine foams exhibit a similar microstructure as lung tissue. In the future, combined shear wave and slow compression wave imaging might provide new means of distinguishing malignant and healthy pulmonary tissue.

The characterization of wave propagation in porous materials has a wide range of applications in various fields at different scales. In contrast to classical elastic materials, poroelastic materials support three types of elastic waves and exhibit a distinctive dispersion in the presence of viscous fluids [1–3]. The first thorough theoretical description of poroelasticity that included dispersion was developed by M. Biot [1, 4]. He predicted a secondary compressional wave (PII-wave), which is often named Biot slow wave. His theory was soon applied in geophysics at large scale for hydrocarbon exploration [5]. It was later extended to laboratory scale for bone and lung characterization through numerical modeling and medical imaging [6–11]. While poroelastic models have been used to characterize materials and fabrics such as textiles [12], anisotropic composites [13], snow [14] and sound absorbing materials [15], experimental detection of the PII-wave remains scarce [2, 16]. In medical imaging, the characterization of the porous lung surface wave has only recently been emphasized [17–19, 27]. Experimental detection of poroelastic waves is difficult due to their strong attenuation and the diffuse PII-wave behaviour below a critical frequency [1, 16, 20]. We overcome this challenge by using in situ measurements from medical imaging. We apply high frame rate (ultrafast) ultrasound for wave tracking [21], the technique underlying transient elastography [21–24], on saturated, highly porous melamine foams. A very dense grid of virtual receivers is placed inside the sample through correlation of backscattered ultrasound images, reconstructing the particle velocity field of elastic waves. The resolution is thus only determined by the wavelength of the tracking ultrasound waves, which is several orders of magnitude lower than the wavelength of the tracked low-frequency waves [24, 25]. Two factors allow us thusly to visualize S- and PII-wave propagation and measure phase speed

and attenuation, which, to the best of our knowledge, has not been done before. Firstly, simple scattering of ultrasound at the foam matrix ensures the reflection image. Secondly, the imaged elastic waves propagate several times slower ( $< 40 \text{ m s}^{-1}$ ) than the ultrasonic waves ( $\approx 1500 \text{ m s}^{-1}$ ). The measured low-frequency speeds are in agreement with a first approximation that views the foam as a biphasic elastic medium. To take solid-fluid coupling into account, we compare the measured speeds and attenuations with the analytic results of Biot's theory. The S-wave results show a good quantitative prediction, while the PII-wave speeds show a qualitative agreement. Melamine foams have already been used to simulate the acousto-elastic properties of pulmonary tissue due to their common highly porous, soft structure [3, 19, 26]. We thus postulate that our results have possible future implications for lung characterization by ultrasound imaging.

We use a rectangular Basotect® melamine resin foam of dimensions  $x = 30 \text{ cm}$ ,  $y = 18 \text{ cm}$ ,  $z = 12 \text{ cm}$ , which is fully immersed in water to ensure complete saturation. The foam exhibits a porosity between 96.7 and 99.7%, a tortuosity between 1 and 1.02, a permeability between  $1.28 \times 10^{-9}$  and  $2.85 \times 10^{-9} \text{ m}^2$  and a density of  $8.8 \text{ kg m}^{-3} \pm 1 \text{ kg m}^{-3}$ . The viscous length  $\sigma$  is between  $11.24 \times 10^{-5}$  and  $13.02 \times 10^{-5} \text{ m}$ , as indicated in the microscopic photo at the top of Fig. 1. The foam parameters were independently measured using the acoustic impedance tube method [28] and a Johnson-Champoux-Allard-Lafarge model [7, 8, 28, 29]. These measurements serve as input to the analytic Biot model. Figure 1 shows the setups for the S-wave (a) and PII-wave (b) experiments. A piston (ModalShop Inc. K2004E01), displayed at the top, excites the waves. In a), a rigid metal rod which is pierced through the sponge ensures rod-foam coupling, as well as transverse polarization

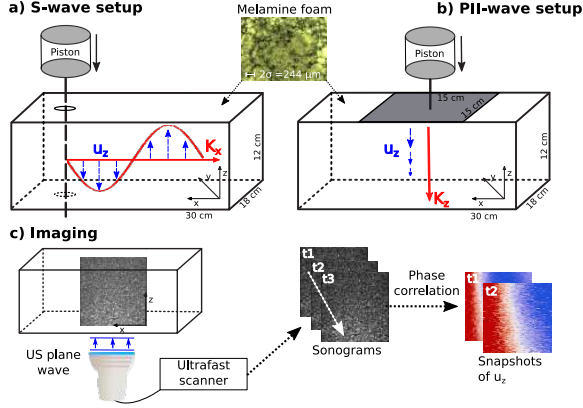


FIG. 1. Schematic experimental setups of the S-wave (a) and PII-wave excitation (b). Blue arrows signify the polarization of particle motion and red arrows the direction of wave propagation. At the center top, a microscopic photo of the investigated melamine foam is displayed. c) Ultrafast ultrasound imaging principle: The particle velocity maps are retrieved through correlation of subsequent ultrasound images.

( $u_z$ ) of the wave. Excitation is achieved in two ways. Firstly, through a pulse and secondly, through a frequency sweep from 60 to 650 Hz. The excited S-wave propagates along x-dimension ( $k_x$ ) exposing a slight angle due to imperfect alignment of the rod. In b), a rigid plastic plate at the end of a rod excites the compression wave on the upper foam surface and ensures longitudinal polarization. The induced vibration is a Heaviside step function. We undertake three experiments with different excitation amplitudes. In both setups, particle and rod motion are along the z-dimension. The imaging device is a 128-element L7-4 (Philips) ultrasound probe centered at 5 MHz. Fig. 1c) schematically indicates the probe position below the foam and the z-polarization of the ultrasonic waves. The probe is connected to an ultrafast ultrasound scanner (Verasonics Vantage™) which works at 3000 (S-wave) and 2000 (PII-wave) frames per second. Each frame is obtained through emission of plane waves as in [21] and beamforming of the backscattered signals. In order to visualize the wave propagation, we apply phase-based motion estimation [30] on subsequent ultrasound frames. Similar to Doppler ultrasound techniques, the retrieved phase difference gives the relative displacement on the micrometer scale. Due to the finite size of our sample, reflections from the opposite boundary can occur. Therefore, we apply a directional filter [31] in the  $k_x - k_y - f$  domain of the full 2D wavefield [34]. For setup 1a) (S-wave) the filter effect is negligible, but for setup 1b) (P-wave), a reflection at the boundary opposite of the excitation plate is

attenuated (see Ref. [32] and [33]). The resulting relative displacement for setup 1b) is a superposition of the primary compression wave (PI) and the PII-wave. Thus, we additionally apply a spatial gradient in z-direction to isolate the PII-wave displacement.

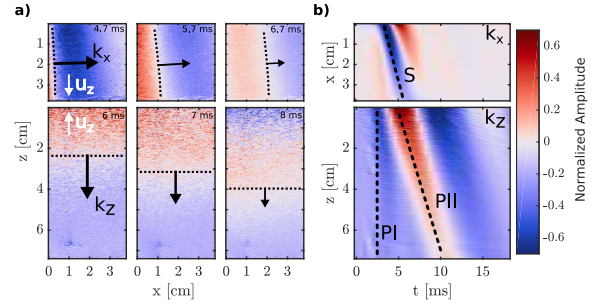


FIG. 2. Experimental wave-fields for the setups in Fig. 1. a) Snapshots at three time-steps of a propagating S-wave pulse (top) and PII-wave step (bottom). The top row shows the particle velocity and the bottom row its z-gradient. b) Corresponding time-space representation by summation orthogonal to x (top) and z (bottom). In the top row, the S-wave (S) and in the bottom row, the first (PI) and secondary compression wave (PII) can be identified.  $u_z$  - Direction of particle motion.  $k_x/z$  - Direction of wave propagation. The displacement films are in Ref. [32] and the unfiltered PII-wave snapshots in Ref. [33].

Three displacement snapshots of the S- and PII-wave are shown in Fig. 2a). The top row is an example of the wave propagation induced by shear excitation as schematically shown in Fig. 1a). The blue color signifies particle motion  $u_z$  towards the probe. A comparison of the wave-fields shows that the plane wave front propagates in the positive x-direction ( $k_x$ ). The bottom row displays the PII-wave for 6, 7 and 8 ms. It is excited at the top and propagates with decreasing amplitude in positive z-direction ( $k_z$ ). A summation along the z-dimension for the transverse setup, and along the x-dimension for the longitudinal setup, result in the space-time representations of Fig. 2b). They show, that the S- and PII-wave are propagating over the whole length at near constant speed. The PII-wave (PII) is well separated and of opposite polarity from the direct arrival (PI) at 2.5 ms. A time-of-flight measurement through slope fitting gives a group velocity of  $14.7 \text{ m s}^{-1}$  (S-wave) and  $14.4 \text{ m s}^{-1}$  (PII-wave). The central frequency is approximately 220 Hz for the S-wave, and 120 Hz for the PII-wave. These values suggest that both speed are governed by the low elastic modulus of the foam. The simplest porous foam model is an uncoupled biphasic medium with a weak frame supporting the S- and PII-wave. In this case, the PI-wave is supported by an in-compressible fluid, which circulates freely through the open pores.

The porous compressibility is that of the foam matrix, and its first Lamé parameter  $\lambda_0$  is very small compared to the shear modulus  $\mu_0$ . Hence, the compression wave speeds  $v_{p1,2}$  become:

$$\begin{cases} v_{p1} = \sqrt{\frac{\lambda_f}{\rho_f}} & ; \lambda_f \gg \mu_f \\ v_{p2} = \sqrt{\frac{(\lambda_0 + 2\mu_0)}{\rho_0}} \approx \sqrt{\frac{2\mu_0}{\rho_0}} \approx \sqrt{2}v_s & ; \lambda_0 \ll \mu_0 \end{cases} \quad (1)$$

with  $\lambda_0$ ,  $\mu_0$  and  $\lambda_f$ ,  $\mu_f$  being the first and second Lamé parameters of the drained sponge and the fluid.  $\rho_0 = \rho_{\text{mineral}}(1 - \phi)$  is the density of the the drained sponge,  $\rho_f$  the fluid density,  $v_s$  the S-wave speed and  $\phi$  is porosity. This approximation is in accordance with Ref. [35] who investigated the quasi-static behavior of hydrogels. To assess the dispersion of the observed waves, we apply a fast Fourier transformation and recover the phase velocity and attenuation from the imaginary and real part of the complex signal. For the S-wave, we use a frequency sweep. For the PII-wave, reflections from the boundaries and mode conversions prohibit the exploitation of a chirp, hence we use the Heaviside displayed in Fig. 2. Its  $-10$  dB bandwidth is limited from 50 to 150 Hz. The phase velocity is directly deduced from a linear fit of the phase value along the propagation dimension. We use a Ransac algorithm [36] and display values with a  $R^2$  of 0.98 and minimum 70 % inliers. The speed measurements of the S- and PII-wave in their shared frequency band are displayed in Fig. 3a). Both curves are monotonously increasing with frequency. To verify Equation 1 we use a sixth-order polynomial fit (blue line) and its 95 % confidence interval as input data. The resulting PII-wave speeds (black line) and its 95 % confidence interval (gray zone) show that the PII-wave experimental data lie within the prediction of Equation 1, with a ratio of approximately  $\sqrt{2}$  with the S-wave speeds. Figure 3b) shows the entire frequency range of the measured S-wave speeds.

The elastic model for Equation 1 cannot account for viscous dissipation. Consequently, we compare the measured dispersion with a second approach, the Biot theory [1]. This theory uses continuum mechanics to model a solid matrix saturated by a viscous fluid. The Biot dispersion and PII-wave result from the coupling of fluid and solid displacement [1, 4, 6, 38–42]. One drawback is that the theory requires nine parameters. We reduced the degrees of freedom to two by fixing the porous parameters to the values measured by the acoustic impedance tube method in air:  $\phi = 0.99\%$ ,  $\alpha_\infty = 1.02$ ,  $k_0 = 12.76 \times 10^{-10} \text{ m}^2$ ,  $\rho = 8.8 \text{ kg m}^{-3} \pm 1 \text{ kg m}^{-3}$ ,  $BW = \phi$  (Biot-Willis coefficient), and the fluid parameters to literature values for water:  $E_{fl} = 2.15 \times 10^9 \text{ kPa}$  (fluid Young's modulus) and fluid viscosity  $\eta_f = 1.3 \times 10^{-3} \text{ Pa s}$ . We optimize the

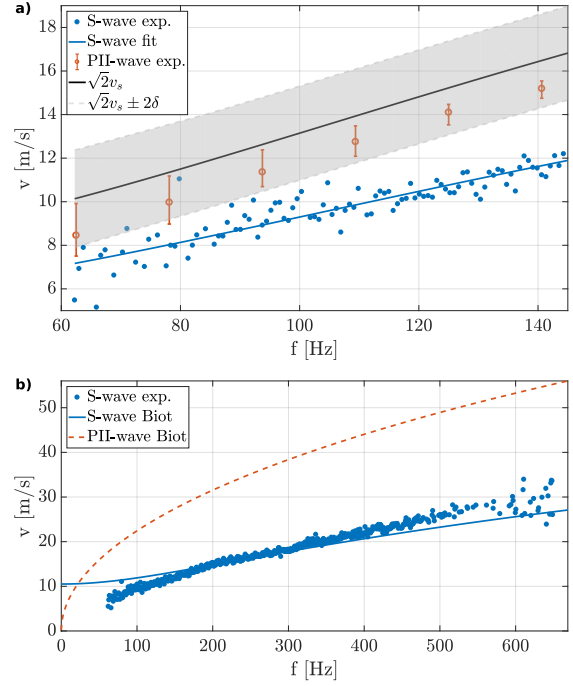


FIG. 3. Experimental and theoretical dispersion. a) Experimental S-wave (blue dots) and PII-wave (red circles) speeds. A sixth-order polynomial fit (blue solid line) of the full frequency band and its 95 % confidence interval give  $v_s$  for Equation 1. The resulting PII-wave speeds (black solid line) and its 95 % confidence interval (gray zone) are displayed. The PII-wave results are the average of three experiments with the maximum deviation indicated by the error bars. b) Experimental S-wave (blue dots) and analytic Biot S- (blue line) and PII-wave (red dashed line).

two remaining elastic parameters within literature values of 0.276 to 0.44 for Poisson's ratio and 30 to 400 kPa for Young's modulus [6, 15, 43–45]. To avoid local minima, we first run a parameter sweep in the literature bounds and use the best fit as input to an unconstrained least squares optimization, described in [46]. The resulting Poisson's ratio is 0.39 and the Young's modulus 303 kPa. However, it should be noted that the optimization is not very sensitive to the Poisson's ratio. For example, a 10 % increase in Poisson's ratio, results in a  $R^2$  of 0.998 between the optimal S-wave solution and the deviation. However, the PII-wave is sensitive to the Poisson's ratio with a  $R^2$  of 0.783. In contrast, both waves exhibit a similar sensitivity with a  $R^2$  of 0.975 (S-wave) and 0.979 (PII-wave) for a 10 % increase in Young's modulus. For a detailed sensitivity analysis see Ref. [47]. The analytic S-wave curve resulting from the minimization is displayed in Fig. 3b). It shows good agreement ( $R^2 = 0.808$ ) with



the experimental values between 120 and 600 Hz. Below this frequency, wave guiding, present if the wavelength exceeds the dimension of particle motion [37], and not taken into account by Biot's infinite medium, might lower the measured speeds. Biot's model overestimates the experimental PII-speeds, but exhibits the same trend. Furthermore, it predicts that the PII-displacements of the solid and fluid constituent are of opposite sign while they are phase locked for the PI-wave [1, 48]. This leads the PI and PII arrivals to be out-of-phase [49, 50], which is confirmed by the time-space representation of Fig. 2b). Ultrasound imaging measures the solid displacement only, hence the displacement of PI (blue) and PII (red) is out-of-phase. The phase opposition [49] and the measured positive PII-dispersion are strong arguments to exclude the presence of a bar wave ( $S_0$ -mode). It should be pointed out, that there is a crucial difference between previous interpretations of the PII-wave [2, 49, 50] and this study. In geophysics and bone characterization, the PII-wave travels close to the fluid sound speed and the PI-wave close to the sound speed of the rigid skeleton. In contrast to that, our results indicate that the PII-wave speed is governed by the weak frame of the foam and the PI-wave propagates at the speed of sound in water. An equivalent interpretation was given by Ref. [16] for experiments in porous granular media [51].

To verify the dispersion results we compare them to attenuation, which for plane waves is described by [25]:

$$A(x + \Delta x) = A(x)e^{-\alpha(\omega)\Delta x} \quad (2)$$

where  $\omega$  is angular frequency,  $\alpha(\omega)$  is attenuation coefficient,  $A$  is amplitude and  $x$  is measurement direction. The top left inset in Fig. 4 shows the logarithmic amplitude decrease with distance at one frequency of the S-wave. The bottom right inset shows the decrease at the central frequency of the PII-wave. The difference between these experimental curves and the expected linear decrease reflects the difficulties to conduct attenuation measurement by ultrafast ultrasound imaging [25]. We apply a logarithmic fit of the amplitude with distance to retrieve the attenuation coefficient at each frequency, using the RANSAC algorithm described earlier. The resulting attenuation, displayed in Fig. 4, monotonously increases with frequency.

Attenuation and velocity of plane waves can be related through the bidirectional Kramers-Kronig (K-K) relations. They relate the real and imaginary part of any complex causal response function [52], which we use to verify our experimental results. While the original relations are integral functions that require a signal of infinite bandwidth, Ref. [53–55] developed a derivative form that is applicable on bandlimited data and has previously been applied by Ref. [56] on S-wave disper-

sion. Following Ref. [25, 57], the attenuation in complex media is observed to follow a frequency power law:

$$\alpha(\omega) = \alpha_0 + \alpha_1 \omega^y \quad (3)$$

and can be related to velocity by [54, 55]:

$$\frac{1}{c(\omega)} - \frac{1}{c(\omega_0)} = \begin{cases} \alpha_1 \tan(\frac{\pi}{2}y)(\omega^{y-1} - \omega_0^{y-1}) & ; 0 \leq y \leq 2 \\ \frac{-2}{\pi}\alpha_1 \ln \frac{\omega}{\omega_0} & ; y = 1 \end{cases} \quad (4)$$

where  $\omega_0$  is a reference frequency,  $\alpha_1$  and  $y$  are fitting parameters and  $\alpha_0$  is an offset, typically observed in soft tissues [56, 58]. Since velocity measurements by ultrafast ultrasound imaging are less error prone than attenuation measurements [25], we use Equation 4 to predict attenuation from velocity. A least squares fit gives the exponent  $y$  and the attenuation constant  $\alpha_1$  that minimizes Equation 4 for different reference frequencies. The resulting attenuation model is  $\alpha(\omega) = 21 * \omega^{0.29}$  [ $\text{Np m}^{-1}$ ], with a reference frequency of 413 Hz and a  $R^2$  larger 0.98 for frequencies between 120 Hz and 650 Hz. The attenuation exponent  $y = 0.29$  is an expected value for S-waves in biological tissues [57, 59]. The K-K relations do not take into account the offset  $\alpha_0$ . It is introduced by minimizing the least squares of Equation 3 and the attenuation measurements. The resulting attenuation curve with  $\alpha_0 = -119 \text{ Np m}^{-1}$  is displayed in Fig. 4. It shows a significant agreement with the attenuation measurements ( $R^2 = 0.9016$ ) and Biot predictions ( $R^2 = 0.9274$ ). The successful K-K prediction implies that guided waves have little influence on our measurements above 120 Hz. The remaining misfit might stem from out-of-plane particle motion, which can introduce an error on amplitude measures by ultrafast ultrasound imaging [25]. Furthermore, the low-frequency elastic wave is imaged in the near-field, where it does not show a power law amplitude decrease due to the coupling of transverse and rotational particle motion [60]. The good agreement between the experimental and theoretical S-wave dispersion and attenuation indicates that the observed S-wave attenuation is due to the interaction between the solid and the viscous fluid. The PII-wave attenuation of the three experiments converges only at the central frequency of 120 Hz ( $\approx 16 \text{ Np m}^{-1}$ ). Below this frequency, the measurements are taken on less than two wavelengths of wave propagation and consequently, the exponential amplitude decrease cannot be ensured [60]. A reason for the failure of the Biot theory to quantitatively predict the observed PII-wave dispersion could be viscoelasticity and anisotropy of the foam matrix itself [44, 61]. The Biot theory and the model of Equation 1 have different implications at low frequencies. The

Biot PII-wave disappears, whereas it persists as a decoupled frame-borne wave in Equation 1. Our velocity measurements support the decoupling hypothesis, but measurements at lower frequencies would be needed to make a definite statement.

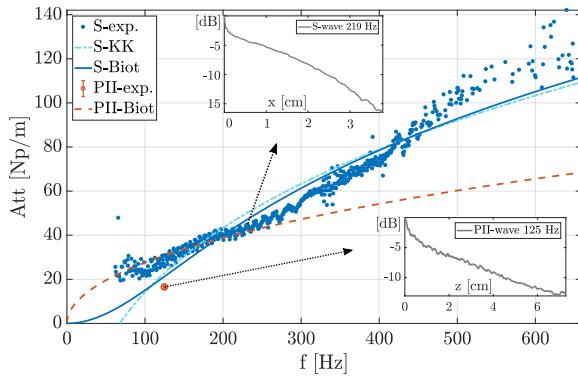


FIG. 4. Attenuation measurements, K-K and Biot predictions. The insets show the exemplary amplitude decrease of the S-wave (left) and PII-wave (right). Dots are attenuation measurements, solid blue and dashed red lines are the Biot predictions and the dashed blue line is the S-wave K-K prediction for Equation 3:  $\alpha(\omega) = -119 + 21 * \omega^{0.29} \text{ [Np m}^{-1}\text{]}$ .

In conclusion, we have showed the first direct observation of elastic wave propagation inside a poroelastic medium. The recorded compression wave of the second kind (PII-wave) propagates at  $\sqrt{2}$  times the shear wave speed and is of opposite polarization compared to the first compression wave (PI-wave). Finally, the measured shear wave dispersion (S-wave) and attenuation are closely related to the fluid viscosity. These results might have important consequences in medical physics for characterizing porous organs such as the lung or the liver.

We are grateful to Aroune Duclos and Jean-Philippe Groby of the university of Le Mans for introducing us to the world of foams and for measuring the acoustic parameters of the Melamine foam. The project has received funding from the European Union's Horizon 2020 research and innovation programme under the Marie Skłodowska-Curie grant agreement No 641943 (ITN WAVES).

- [1] M. A. Biot, Theory of Propagation of Elastic Waves in a Fluid-Saturated Porous Solid. I. Low-Frequency Range, *J. Acoust. Soc. Am.* **28**, 168 (1956).
- [2] T. J. Plona, Observation of a second bulk compressional wave in a porous medium at ultrasonic frequencies, *Appl. Phys. Lett.* **36**, 259 (1980).

- [3] W. Lauriks, L. Boeckx, and P. Leclaire, Characterization of porous acoustic materials, in *Sapem* (Lyon, 2005) pp. 0–14.
- [4] M. A. Biot, Theory of Propagation of Elastic Waves in a Fluid-Saturated Porous Solid. II. Higher Frequency Range, *J. Acoust. Soc. Am.* **28**, 179 (1956).
- [5] J. Geerstma, Younane Abousleiman, and A. H. Cheng, Maurice Biot - I remember him well, in *Proc. 3rd Biot Conf. Poromechanics* (2005) pp. 3–6.
- [6] J. Allard and N. Atalla, *Propagation of Sound in Porous Media: modelling sound absorbing materials*, 2nd ed. (John Wiley & Sons, Ltd Registered, 2009).
- [7] D. L. Johnson, J. Koplik, and R. Dashen, Theory of dynamic permeability and tortuosity in fluid saturated porous media, *J. Fluid Mech.* **176**, 379 (1987).
- [8] Y. Champoux and J. F. Allard, Dynamic tortuosity and bulk modulus in air-saturated porous media, *J. Appl. Phys.* **70**, 1975 (1991).
- [9] Z. E. Fella, N. Sebaa, M. Fella, F. G. Mitri, E. Ogam, W. Lauriks, and C. Depollier, Application of the biot model to ultrasound in bone: Direct problem, *IEEE Trans. Ultrason. Ferroelectr. Freq. Control* **55**, 1508 (2008).
- [10] K. Mizuno, M. Matsukawa, T. Otani, P. Laugier, and F. Padilla, Propagation of two longitudinal waves in human cancellous bone: An in vitro study, *J. Acoust. Soc. Am.* **125**, 3460 (2009).
- [11] Z. Dai, Y. Peng, B. M. Henry, H. A. Mansy, R. H. Sandler, and T. J. Royston, A comprehensive computational model of sound transmission through the porcine lung, *J. Acoust. Soc. Am.* **136**, 1419 (2014).
- [12] T. E. Álvarez-Arenas, P. Y. Apel, and O. Orelovitch, Ultrasound attenuation in cylindrical micro-pores: Nondestructive porometry of ion-track membranes, *IEEE Trans. Ultrason. Ferroelectr. Freq. Control* **55**, 2442 (2008).
- [13] B. Castagnede, A. Aknine, M. Melon, and C. Depollier, Ultrasonic characterization of the anisotropic behavior of air-saturated porous materials, *Ultrasonics* **36**, 323 (1998).
- [14] B. Gerling, H. Löwe, and A. van Herwijnen, Measuring the Elastic Modulus of Snow, *Geophys. Res. Lett.* **44**, 11,088 (2017).
- [15] L. Boeckx, P. Leclaire, P. Khurana, C. Glorieux, W. Lauriks, and J. F. Allard, Guided elastic waves in porous materials saturated by air under Lamb conditions, *J. Appl. Phys.* **97**, 094911 (2005).
- [16] D. M. Smeulders, Experimental Evidence for Slow Compressional Waves, *J. Eng. Mech.* **131**, 908 (2005).
- [17] Z. Dai, Y. Peng, H. A. Mansy, R. H. Sandler, and T. J. Royston, Comparison of Poroviscoelastic Models for Sound and Vibration in the Lungs, *J. Vib. Acoust.* **136**, 051012 (2014).
- [18] M. M. Nguyen, H. Xie, K. Paluch, D. Stanton, and B. Ramachandran, Pulmonary ultrasound elastography: a feasibility study with phantoms and ex-vivo tissue, in *Proc. SPIE*, Vol. 8675, edited by J. G. Bosch and M. M. Doyley (2013) p. 867503.
- [19] J. Zhou and X. Zhang, Effect of a Thin Fluid Layer on Surface Wave Speed Measurements: A Lung Phantom Study, *J. Ultrasound Med.* , 1 (2018).
- [20] D. Yang, Q. Li, and L. Zhang, Propagation of pore pressure diffusion waves in saturated dual-porosity media (II), *J. Appl. Phys.* **119**, 154901 (2016).

- [21] L. Sandrin, S. Catheline, M. Tanter, X. Hennequin, & M. Fink, Time-resolved pulsed elastography with ultrafast ultrasonic imaging, *Ultrason. Imaging* **21**, 259 (1999).
- [22] J.-L. Gennisson, S. Catheline, S. Chaffai, and M. Fink, Transient elastography in anisotropic medium: Application to the measurement of slow and fast shear wave speeds in muscles, *J. Acoust. Soc. Am.* **114**, 536 (2003).
- [23] S. Catheline, *Etudes experimentales en acoustique : de l'elastographie aux cavites reverberantes*, Habilitation, Universite Paris-Diderot - Paris VII (2006).
- [24] J. Gennisson, T. Defieux, M. Fink, and M. Tanter, Ultrasound elastography: Principles and techniques, *Diagn. Interv. Imaging* **94**, 487 (2013).
- [25] S. Catheline, J. L. Gennisson, G. Delon, M. Fink, R. Sinkus, S. Abouelkaram, and J. Culioli, Measuring of viscoelastic properties of homogeneous soft solid using transient elastography: an inverse problem approach., *J. Acoust. Soc. Am.* **116**, 3734 (2004).
- [26] K. Mohanty, J. Blackwell, T. Egan, and M. Muller, Characterization of the lung parenchyma using ultrasound multiple scattering, *Acoust. Soc. Am.* **140**, 3186 (2016).
- [27] X. Zhang, T. Osborn, and S. Kalra, A noninvasive ultrasound elastography technique for measuring surface waves on the lung, *Ultrasonics* **71**, 183 (2016).
- [28] M. Niskanen, J. Groby, A. Duclos, O. Dazel, J. C. Le Roux, N. Poulain, T. Huttunen, and T. Lähivaara, Deterministic and statistical characterization of rigid frame porous materials from impedance tube measurements, *J. Acoust. Soc. Am.* **2407**, 14255 (2017).
- [29] D. Lafarge, P. Lemarini, J. F. Allard, and V. Tarnow, Dynamic compressibility of air in porous structures at audible frequencies, *J. Acoust. Soc. Am.* **102**, 1995 (1997).
- [30] G. F. Pinton, J. J. Dahl, and G. E. Trahey, Rapid tracking of small displacements using ultrasound, *Proc. - IEEE Ultrason. Symp.* **4**, 2062 (2005).
- [31] D. B. Buttkus, B. Buttkus: *Spectral Analysis and Filter Theory in Applied Geophysics*, 1st ed. (Springer-Verlag, Berlin-Heidelberg, 2000).
- [32] See Supplemental Material at ... for the video files., .
- [33] See Supplemental Material at ... for the figure., .
- [34] T. Defieux, J.-L. Gennisson, and J. Bercoff, On the Effects of Reflected Waves in Transient Shear Wave Elastography, *IEEE Trans. Ultrason. Ferroelectr. Freq. Control* **58**, 2032 (2011).
- [35] T. Tanaka, L. O. Hocker, and G. B. Benedek, Spectrum of light scattered from a viscoelastic gel, *J. Chem. Phys.* **59**, 5151 (1973).
- [36] P. H. Torr and A. Zisserman, MLESAC: A new robust estimator with application to estimating image geometry, *Comput. Vis. Image Underst.* **78**, 138 (2000).
- [37] D. Royer and E. Dieulesaint, *Ondes Elastiques dans les Solides 1* (Masson, 1996).
- [38] M. A. Biot, Mechanics of deformation and acoustic propagation in porous media, *J. Appl. Phys.* **33**, 1482 (1962).
- [39] J. M. Carcione, *Wave Fields in Real Media*, 3rd ed. (Elsevier, 2015).
- [40] B. B. S. A. Vogelaar, *Fluid effect on wave propagation in heterogeneous porous media*, Ph.D. thesis, Delft University of Technology (2009).
- [41] C. Morency and J. Tromp, Spectral-element simulations of wave propagation in porous media, *Geophys. J. Int.* **175**, 301 (2008).
- [42] G. Mavko, T. Mukerji, and J. Dvorkin, *The rock physics handbook - Tools for seismic analysis of porous media*, 2nd ed. (Cambridge University Press, 2009).
- [43] N. Geebelen, L. Boeckx, G. Vermeir, W. Lauriks, J. F. Al-lard, and O. Dazel, Measurement of the rigidity coefficients of a melamine foam, *Acta Acust. united with Acust.* **93**, 783 (2007).
- [44] M. Deverge, A. Renault, and L. Jaouen, Elastic and damping characterizations of acoustical porous materials: Available experimental methods and applications to a melamine foam, *Appl. Acoust.* **69**, 1129 (2008).
- [45] E. Ogam, Z. E. A. Fellah, N. Sebaa, and J. Groby, Non-ambiguous recovery of Biot poroelastic parameters of cellular panels using ultrasonic waves, *J. Sound Vib.* **330**, 1074 (2011).
- [46] J. Nocedal and S. J. Wright, *Numerical Optimization*, volume 17, 136-143 (Springer New York, 2006).
- [47] See Supplemental Material at ... for the sensitivity analysis., .
- [48] T. W. Geerits, Acoustic wave propagation through porous media revisited, *J. Acoust. Soc. Am.* **100**, 2949 (1996).
- [49] K. Nakagawa, K. Soga, and J.K. Mitchell, Observation of Biot compressional wave of the second kind in granular soils, *Geotechnique* **20**, 19 (2001).
- [50] Y. Bouzidi and D. R. Schmitt, Measurement of the speed and attenuation of the Biot slow wave using a large ultrasonic transmitter, *J. Geophys. Res. Solid Earth* **114**, 1 (2009).
- [51] N. R. Paterson, Seismic wave propagation in porous granular media, *Geophysics* **XXI**, 691 (1956).
- [52] J. S. Toll, Causality and the dispersion relation: Logical foundations, *Phys. Rev.* **104**, 1760 (1956).
- [53] M. O'Donnel, E.T. Jaynes, and J.G. Miller, Kramers-Kronig relationship between ultrasonic attenuation and phase velocity, *J. Acoust. Soc. Am.* **69** (1981).
- [54] K. R. Waters, M. S. Hughes, J. Mobley, and J. G. Miller, Differential Forms of the Kramers-Kronig Dispersion Relations, *IEEE Trans. Ultrason. Ferroelectr. Freq. Control* **50**, 68 (2003).
- [55] K. Waters, J. Mobley, and J. Miller, Causality-imposed (Kramers-Kronig) relationships between attenuation and dispersion, *IEEE Trans. Ultrason. Ferroelectr. Freq. Control* **52**, 822 (2005).
- [56] M. W. Urban and J. F. Greenleaf, A Kramers-Kronig-based quality factor for shear wave propagation in soft tissue, *Phys. Med. Biol.* **54**, 5919 (2009).
- [57] S. Holm and S. P. Näsholm, Comparison of Fractional Wave Equations for Power Law Attenuation in Ultrasound and Elastography, *Ultrasound Med. Biol.* **40**, 695 (2014).
- [58] T. L. Szabo and J. Wu, A model for longitudinal and shear wave propagation in viscoelastic media, *J. Acoust. Soc. Am.* **107**, 2437 (2000).
- [59] S. P. Näsholm and S. Holm, On a Fractional Zener Elastic Wave Equation, *Fract. Calc. Appl. Anal.* **16**, 26 (2012).
- [60] L. Sandrin, The role of the coupling term in transient elastography, *J. Acoust. Soc. Am.* **115**, 73 (2004).
- [61] M. Melon, E. Mariez, C. Ayrault, and S. Sahraoui, Acoustical and mechanical characterization of anisotropic open-cell foams, *J. Acoust. Soc. Am.* **104**, 2622 (1998).

# Bibliography

- Abraham, Farid F. (2001). "The atomic dynamics of fracture". In: *J. Mech. Phys. Solids* 49.9, pp. 2095–2111. ISSN: 00225096. DOI: 10.1016/s0022-5096(01)00028-x.
- Abraham, Farid F. and Huajian Gao (2000). "How fast can cracks propagate?" In: *Phys. Rev. Lett.* 84.14, pp. 3113–3116. ISSN: 10797114. DOI: 10.1103/PhysRevLett.84.3113.
- Ahlborn, F. (1902a). *Über den Mechanismus des hydrodynamischen Widerstandes*, ed. by L. Friederichsen & Co. Vol. 17. Hamburg.
- (1902b). "Über den Mechanismus des Widerstandes flüssiger Medien". In: *Phys. Zeitschrift* 3.6, pp. 120–124.
- Ahmed, Enas M. (2015). "Hydrogel: Preparation, characterization, and applications: A review". In: *J. Adv. Res.* 6.2, pp. 105–121. ISSN: 20901232. DOI: 10.1016/j.jare.2013.07.006. arXiv: arXiv:1011.1669v3.
- Aki, Keiiti (1968). "Seismic displacements near a fault". In: *J. Geophys. Res.* 73.16, pp. 5359–5376. ISSN: 01480227. DOI: 10.1029/JB073i016p05359.
- Aki, Keiiti and Paul G Richards (2009). "Quantitative seismology". In: *Book*. 2nd. University Science Books, p. 700.
- Allard, Jean and Noureddine Atalla (2009). *Propagation of Sound in Porous Media: modelling sound absorbing materials*. Second. John Wiley & Sons, Ltd Registered. ISBN: 9780470746615.
- Álvarez-Arenas, Tomás E. Gómez, Pavel Yu Apel, and Oleg Orelovitch (2008). "Ultrasound attenuation in cylindrical micro-pores: Nondestructive porometry of ion-track membranes". In: *IEEE Trans. Ultrason. Ferroelectr. Freq. Control* 55.11, pp. 2442–2449. ISSN: 08853010. DOI: 10.1109/TUFFC.951.
- Amontons, M. (1699). "De la resistance causee dans les machines". In: *Hist. l'academie R. des Sci.* Pp. 206–226.
- Anandakrishnan, S. and C. R. Bentley (1993). "Micro-earthquakes beneath ice streams B and C, West Antarctica: observations and implications". In: *J. Glaciol.* 39.133, pp. 455–462. ISSN: 00221430.
- Andrews, D J (1976). "Rupture velocity of plane strain shear cracks". In: 81.32.
- Andrews, D. J. and Yehuda Ben-Zion (1997). "Wrinkle-like slip pulse on a fault between different materials". In: *J. Geophys. Res. Solid Earth* 102.B1, pp. 553–571. ISSN: 01480227. DOI: 10.1029/96JB02856.

- Anuta, Paul E. (1970). "Spatial Registration of Multispectral and Multitemporal Digital Imagery Using Fast Fourier Transform Techniques". In: *IEEE Trans. Geosci. Electron.* 8.4, pp. 353–368. ISSN: 00189413. DOI: 10.1109/TGE.1970.271435.
- Archuleta, B Y Ralph J (1982). "Analysis of near-source static and dynamic measurements from the 1979 imperial valley earthquake". In: 72.6, pp. 1927–1956. DOI: 10.1.1.1025.5203.
- Aristotle and W.D. Ross (1936). *Aristotle's Physics. Text and Commentary*. Oxford: Oxford University Press.
- Arthur, David and Sergei Vassilvitskii (2007). "K-Means++: The Advantages of Careful Seeding". In: *Proc. Eighteenth Annu. ACM-SIAM Symp. Discret. Algorithms*. New Orleans, Louisiana, USA. DOI: 10.1145/1283383.1283494.
- Astm and Astm International (2006). *Standard Practice for Classification of Soils for Engineering Purposes (Unified Soil Classification System)*. DOI: 10.1520/D2487-11. arXiv: arXiv:1011.1669v3.
- Bardot, Anne, Bruno Brouard, and Jean-François Allard (1996). "Frame decoupling at low frequency in thin porous layers saturated by air". In: *J. Appl. Phys.* 79.11, p. 8223. ISSN: 00218979. DOI: 10.1063/1.362462.
- Barenblatt, G.I. (1962). *The Mathematical Theory of Equilibrium Cracks in Brittle Fracture*. Institute of Geology and Development of Combustible Minerals of the U.S.S.R. Academy of Sciences. Moscow. U.S.S.R., pp. 55–129. DOI: 10.1016/S0065-2156(08)70121-2.
- Barry, Christopher T., Bradley Mills, Zaegyoo Hah, Robert A. Mooney, Charlotte K. Ryan, Deborah J. Rubens, and Kevin J. Parker (2012). "Shear wave dispersion measures liver steatosis". In: *Ultrasound Med. Biol.* 38.2, pp. 175–182. ISSN: 03015629. DOI: 10.1016/j.ultrasmedbio.2011.10.019.
- Baumberger, T., P. Berthoud, and C. Caroli (1999). "Physical analysis of the state- and rate-dependent friction law. II. Dynamic friction". In: *Phys. Rev. B* 60.6, pp. 3928–3939. ISSN: 0163-1829. DOI: 10.1103/PhysRevB.60.3928.
- Baumberger, T, C Caroli, and O Ronsin (2003). "Self-healing slip pulses and the friction of gelatin gels." In: *Eur. Phys. J. E. Soft Matter* 11.1, pp. 85–93. ISSN: 1292-8941. DOI: 10.1140/epje/i2003-10009-7. arXiv: 0303129 [cond-mat].
- Ben-David, Oded, Gil Cohen, Jay Fineberg, Shmuel M Rubinstein, and Jay Fineberg (2010). "The Dynamics of the Onset of Frictional Slip". In: *Science (80-. )*. 330.6001, pp. 211–214. ISSN: 0036-8075. DOI: 10.1126/science.1194777.
- Ben-David, Oded and Jay Fineberg (2011). "Static friction coefficient is not a material constant". In: *Phys. Rev. Lett.* 106.25, pp. 1–4. ISSN: 00319007. DOI: 10.1103/PhysRevLett.106.254301.
- Ben-Menahem, Ari (1961). "Radiation of seismic surface-waves from finite moving sources". In: *Bull. Seismol. Soc. Am.* 51.3, pp. 401–435. ISSN: 0037-1106.

- Ben-zion, Yehuda and Jean-paul Ampuero (2009). "Seismic radiation from regions sustaining material damage". In: pp. 1351–1356. DOI: 10.1111/j.1365-246X.2009.04285.x.
- Beranek, Leo L. (1947). "Acoustical Properties of Homogeneous, Isotropic Rigid Tiles and Flexible Blankets". In: *J. Acoust. Soc. Am.* 19.4, pp. 556–568. ISSN: 0001-4966. DOI: 10.1121/1.1916521.
- Beroza, Gregory C. and William L. Ellsworth (1996). "Properties of the seismic nucleation phase". In: *Tectonophysics* 261.1-3, pp. 209–227. ISSN: 00401951. DOI: 10.1016/0040-1951(96)00067-4.
- Berryman, James G (1980). "Confirmation of Biot's theory Confirmation of Biot's theory". In: *Appl. Phys. Lett.* 37.4. DOI: 10.1063/1.91951.
- Biot, M. A. (1955). "Theory of elasticity and consolidation for a porous anisotropic solid". In: *J. Appl. Phys.* 26.2, pp. 182–185. ISSN: 00218979. DOI: 10.1063/1.1721956.
- (1956a). "General Solutions of the Equations of Elasticity and Consolidation for a Porous Material". In: *J. Appl. Mech.* 78, pp. 91–96.
- (1956b). "Theory of Propagation of Elastic Waves in a Fluid-Saturated Porous Solid. II. Higher Frequency Range". In: *J. Acoust. Soc. Am.* 28.2, pp. 179–191. ISSN: 0001-4966. DOI: 10.1121/1.1908241.
- (1962). "Mechanics of deformation and acoustic propagation in porous media". In: *J. Appl. Phys.* 33.4, pp. 1482–1498. ISSN: 00218979. DOI: 10.1063/1.1728759.
- Biot, M. A. and D.G. Willis (1957). "Theory of consolidation". In: *J. Appl. Mech.* Vol. December, pp. 594–601. DOI: 10.1016/B978-0-444-98950-5.50011-3.
- Biot, M.a. (1956c). "Theory of propagation of elastic waves in a fluid saturated porous solid. I. Low frequency range". In: *J. Acoust. Soc. Am.* 28.2, pp. 168–178. ISSN: 00014966. DOI: 10.1121/1.1908239.
- Birnholz, J C and E E Farrell (1985). "Fetal lung development: compressibility as a measure of maturity." In: *Radiology* 157.2, pp. 495–498. ISSN: 0033-8419. DOI: 10.1148/radiology.157.2.3901109.
- Bizzarri, Andrea (2011). "ON THE DETERMINISTIC DESCRIPTION OF EARTH-QUAKES". In: *Rev. Geophys.* 49.3, RG3002. ISSN: 8755-1209. DOI: 10.1029/2011RG000356.
- Boccon-Gibod, L., M. Berthier-Falissard, N. Ben-Lagha, P. Josset, and C. Courpotin (1997). "Bronchoalveolar lavage". In: *Pediatr. Pulmonol.* 23.S16, pp. 192–193. ISSN: 87556863. DOI: 10.1002/ppu1.19502308102.
- Boeckx, L., P. Leclaire, P. Khurana, C. Glorieux, W. Lauriks, and J. F. Allard (2005). "Guided elastic waves in porous materials saturated by air under Lamb conditions". In: *J. Appl. Phys.* 97.9, p. 094911. ISSN: 0021-8979. DOI: 10.1063/1.1886885.
- Bonfiglio, Andrea, Kritsada Leungchavaphongse, Rodolfo Repetto, and Jennifer H. Siggers (2010). "Mathematical Modeling of the Circulation in the Liver Lobule". In: *J. Biomech. Eng.* 132.11, p. 111011. ISSN: 01480731. DOI: 10.1115/1.4002563.

- Bouchon, Michel and Ares J Rosakis (2001). "New Insights from the 1999 Turkey Earthquakes". In: 28.14, pp. 2723–2726.
- (2002). "Reply to comment on 'How fast is rupture during an earthquake? New insights from the 1999 Turkey earthquakes'" in: 29.8, pp. 1999–2000.
- Bouchon, Michel and Martin Vallée (2003). "Observation of Long Supershear Rupture During the Magnitude 8.1 Kunlunshan Earthquake". In: 301.August, pp. 824–826.
- Bouchon, Michel, Hayrullah Karabulut, Marie-paule Bouin, Jean Schmittbuhl, Martin Vallée, Ralph Archuleta, Shamita Das, François Renard, and David Marsan (2010). "Faulting characteristics of supershear earthquakes". In: *Tectonophysics* 493.3-4, pp. 244–253. ISSN: 0040-1951. DOI: 10.1016/j.tecto.2010.06.011.
- Bouchon, Michel, Hayrullah Karabulut, Mustafa Aktar, Serdar Oezalaybey, Jean Schmittbuhl, and Marie Paule Bouin (2011). "Extended nucleation of the 1999 Mw7.6 Izmit earthquake". In: *Science* (80-. ). 331.6019, pp. 877–880. ISSN: 00368075. DOI: 10.1126/science.1197341.
- Boué, Tamar Goldman, Roi Harpaz, Jay Fineberg, and Eran Bouchbinder (2015). "Failing softly: A fracture theory of highly-deformable materials". In: pp. 3812–3821. ISSN: 1744-683X. DOI: 10.1039/C5SM00496A. arXiv: 1502.04848.
- Bouzidi, Youcef and Douglas R. Schmitt (2009). "Measurement of the speed and attenuation of the Biot slow wave using a large ultrasonic transmitter". In: *J. Geophys. Res. Solid Earth* 114.8, pp. 1–14. ISSN: 21699356. DOI: 10.1029/2008JB006018.
- Bowden, Frank Philip and David Tabor (1939). "The area of contact between stationary and moving surfaces". In: *Proc. R. Soc. London. Ser. A. Math. Phys. Sci.* 169.938, pp. 391–413. ISSN: 2053-9169. DOI: 10.1098/rspa.1939.0005.
- Brune, James N. and Abdolrasool Anooshehpour (1991). "Foam Rubber Modeling of the El Centro Terminal Substation Building". In: *Earthq. Spectra* 7.1, pp. 45–79. ISSN: 8755-2930. DOI: 10.1193/1.1585612.
- Brune, James N., Stephen Brown, and Peggy A. Johnson (1993). "Rupture mechanism and interface separation in foam rubber models of earthquakes: a possible solution to the heat flow paradox and the paradox of large overthrusts". In: *Tectonophysics* 218.1-3, pp. 59–67. ISSN: 00401951. DOI: 10.1016/0040-1951(93)90259-M.
- Buchanan, James L. (2005). *An Assessment of the Biot-Stoll Model of a Poroelastic Seabed*. Tech. rep. August. Wahington DC: Naval Research Laboratory.
- Burridge, R. and L. Knopoff (1967). "MODEL AND THEORETICAL SEISMICITY". In: *Bull. Seismol. Soc. Am.* 57.3, pp. 341–371.
- (2003). "Body Force Equivalents for Seismic Dislocations". In: *Seismol. Res. Lett.* 74.2, pp. 154–162. ISSN: 0895-0695. DOI: 10.1785/gssr1.74.2.154.
- Burridge, Robert (1973). "Admissible Speeds for Plane-Strain Self-Similar Shear Cracks with Friction but Lacking Cohesion". In: *Geophys. J. R. Astron. Soc.* 35.4, pp. 439–455. ISSN: 1365246X. DOI: 10.1111/j.1365-246X.1973.tb00608.x.

- Buttkus, Dr. Burkhard (2000). *B. Buttkus: Spectral Analysis and Filter Theory in Applied Geophysics*. 1st ed. Berlin-Heidelberg: Springer-Verlag, p. 667. ISBN: 9783642629433. DOI: 10.1007/9783642570162.
- Byerlee, James D and William F Brace (1966). "Stick-Slip as a Mechanism for Earthquakes". In: *Science* (80-. ). 153.3739, pp. 990–992.
- Cadman, J. D. and R. E. Goodman (1967). "Landslide Noise". In: *Science* (80-. ). 158.3805, pp. 1182–1184. ISSN: 0036-8075. DOI: 10.1126/science.158.3805.1182.
- Cantisani, Vito et al. (2014). "Ultrasound elastography in the evaluation of thyroid pathology. Current status". In: *Eur. J. Radiol.* 83.3, pp. 420–428. ISSN: 0720048X. DOI: 10.1016/j.ejrad.2013.05.008.
- Carcione, Jose M. (2015). *Wave Fields in Real Media*. 3rd ed. Elsevier. ISBN: 9780080999999.
- Castagnede, Bernard, Achour Aknine, Manuel Melon, and Claude Depollier (1998). "Ultrasonic characterization of the anisotropic behavior of air-saturated porous materials". In: *Ultrasonics* 36.1-5, pp. 323–341. ISSN: 0041624X. DOI: 10.1016/S0041-624X(97)00093-0.
- Catheline, S., J. L. Gennisson, M. Tanter, and M. Fink (2003). "Observation of shock transverse waves in elastic media". In: *Phys. Rev. Lett.* 91.16, pp. 1–4. ISSN: 10797114. DOI: 10.1103/PhysRevLett.91.164301.
- Catheline, S, J L Gennisson, G Delon, M Fink, R Sinkus, S Abouelkaram, and J Culioli (2004). "Measuring of viscoelastic properties of homogeneous soft solid using transient elastography: an inverse problem approach." In: *J. Acoust. Soc. Am.* 116.6, pp. 3734–3741. ISSN: 00014966. DOI: 10.1121/1.1815075.
- Catheline, S., R. Souchon, M. Rupin, J. Brum, A. H. Dinh, and J. Y. Chapelon (2013). "Tomography from diffuse waves: Passive shear wave imaging using low frame rate scanners". In: *Appl. Phys. Lett.* 103.1. ISSN: 00036951. DOI: 10.1063/1.4812515.
- Catheline, Stefan (1998). "INTERFEROMETRIE-SPECKLE ULTRASONORE : APPLICATION A LA MESURE D'ELASTICITE". PhD thesis. UNIVERSITE PARIS VII.
- (2006). "Etudes experimentales en acoustique : de l'elastographie aux cavites reverberantes". Habilitation. Universite Paris-Diderot - Paris VII. DOI: tel-00378138.
- Catheline, Stefan, François Wu, and Mathias Fink (1999). "A solution to diffraction biases in sonoelasticity: The acoustic impulse technique". In: *J. Acoust. Soc. Am.* 105.5, pp. 2941–2950. ISSN: 0001-4966. DOI: 10.1121/1.426907.
- Champoux, Yvan and Jean F Allard (1991). "Dynamic tortuosity and bulk modulus in air-saturated porous media". In: *J. Appl. Phys.* 70.4, pp. 1975–1979. ISSN: 00218979. DOI: 10.1063/1.349482.
- Chui, Cheekong, E. Kobayashi, X. Chen, T. Hisada, and I. Sakuma (2004). "Combined compression and elongation experiments and non-linear modelling of liver tissue for surgical simulation". In: *Med. Biol. Eng. Comput.* 42.6, pp. 787–798. ISSN: 0140-0118. DOI: 10.1007/BF02345212.



- Corbi, F, F Funiciello, M Moroni, Y. van Dinther, P M Mai, L A Dalguer, and C Faccenna (2013). "The seismic cycle at subduction thrusts: 1. Insights from laboratory models". In: *J. Geophys. Res. Solid Earth* 118.4, pp. 1483–1501. ISSN: 21699313. DOI: 10.1029/2012JB009481.
- Coulomb, C A (1781). "Théorie des machines simples, en ayant égard au frottement de leurs parties, et à la roideur des cordages". In:
- Cox, M. and P. H. Rogers (1987). "Automated Noninvasive Motion Measurement of Auditory Organs in Fish Using Ultrasound". In: *J. Vib. Acoust. Stress Reliab. Des.* 109.1, pp. 55–59. ISSN: 07393717. DOI: 10.1115/1.3269395.
- Crandall, Dahl, Lardner (1959). *An Introduction to the Mechanics of Solids*. Boston.
- Dai, Zoujun, Ying Peng, Brian M Henry, Hansen A Mansy, Richard H Sandler, and Thomas J Royston (2014a). "A comprehensive computational model of sound transmission through the porcine lung". In: *J. Acoust. Soc. Am.* 136.3, pp. 1419–1429. ISSN: 0001-4966. DOI: 10.1121/1.4890647.
- Dai, Zoujun, Ying Peng, Hansen A Mansy, Richard H Sandler, and Thomas J Royston (2014b). "Comparison of Poroviscoelastic Models for Sound and Vibration in the Lungs". In: *J. Vib. Acoust.* 136.5, p. 51012. ISSN: 0739-3717. DOI: 10.1115/1.4026436.
- Daniels, Karen E. and Nicholas W. Hayman (2008). "Force chains seismogenic faults visualized with photoelastic granular shear experiments". In: *J. Geophys. Res. Solid Earth* 113.11, pp. 1–13. ISSN: 21699356. DOI: 10.1029/2008JB005781.
- Daub, Eric G and Jean M Carlson (2010). "Friction, Fracture, and Earthquakes". In: *Annu. Rev. Condens. Matter Phys.* 1.1, pp. 397–418. ISSN: 1947-5454. DOI: 10.1146/annurev-conmatphys-070909-104025.
- Debbaut, Charlotte, Jan Vierendeels, Christophe Casteleyn, Pieter Cornillie, Denis Van Loo, Paul Simoens, Luc Van Hoorebeke, Diethard Monbaliu, and Patrick Segers (2012). "Perfusion Characteristics of the Human Hepatic Microcirculation Based on Three-Dimensional Reconstructions and Computational Fluid Dynamic Analysis". In: *J. Biomech. Eng.* 134.1, p. 011003. ISSN: 01480731. DOI: 10.1115/1.4005545.
- Debbaut, Charlotte, Jan Vierendeels, Jennifer H. Siggers, Rodolfo Repetto, Diethard Monbaliu, and Patrick Segers (2014). "A 3D porous media liver lobule model: the importance of vascular septa and anisotropic permeability for homogeneous perfusion". In: *Comput. Methods Biomech. Biomed. Engin.* 17.12, pp. 1295–1310. ISSN: 14768259. DOI: 10.1080/10255842.2012.744399.
- Deffieux, Thomas, Jean-luc Gennisson, and Jeremy Bercoff (2011). "On the Effects of Reflected Waves in Transient Shear Wave Elastography". In: *IEEE Trans. Ultrason. Ferroelectr. Freq. Control* 58.10, pp. 2032–2035.
- Deverge, Mickael, Amélie Renault, and Luc Jaouen (2008). "Elastic and damping characterizations of acoustical porous materials: Available experimental methods

- and applications to a melamine foam". In: *Appl. Acoust.* 69, pp. 1129–1140. DOI: 10.1016/j.apacoust.2007.11.008.
- Dickinson, R. J. and C. R. Hill (1982). "Measurement of soft tissue motion using correlation between A-scans". In: *Ultrasound Med. Biol.* 8.3, pp. 263–271. ISSN: 03015629. DOI: 10.1016/0301-5629(82)90032-1.
- Dieterich, James H. (1972). "Time-dependent friction in rocks". In: *J. Geophys. Res.* 77.20, pp. 3690–3697. DOI: 10.1029/jb077i020p03690.
- (1978). "Time-dependent friction and the mechanics of stick-slip". In: *Pure Appl. Geophys. PAGEOPH* 116.4-5, pp. 790–806. ISSN: 0033-4553. DOI: 10.1007/BF00876539.
- Dolnikoff, Marisa, Thais Mauad, and Mara S. Ludwig (1999). "Extracellular Matrix and Oscillatory Mechanics of Rat Lung Parenchyma in Bleomycin-induced Fibrosis". In: *Am. J. Respir. Crit. Care Med.* 160.5, pp. 1750–1757. ISSN: 1073-449X. DOI: 10.1164/ajrccm.160.5.9812040.
- Duda, Richard O. and Peter E. Hart (1972). "Use of the Hough Transformation to Detect Lines and Curves in Pictures". In: *Comm. ACM* 15.1, pp. 11–15. ISSN: 00010782. DOI: 10.1145/361237.361242.
- Dugdale, D.S. (1960). "Yielding of steel sheets containing slits". In: *J. Mech. Phys. Solids* 8.2, pp. 100–104. ISSN: 00225096. DOI: 10.1016/0022-5096(60)90013-2. arXiv: 0021-8928(59)90157-1 [10.1016].
- Eisenscher, A, E Schweg-Toffler, G Pelletier, and P Jacquemard (1983). "Rhythmic echographic palpation. Echosisomography. A new technic of differentiating benign and malignant tumors by ultrasonic study of tissue elasticity". In: *J. Radiol.* 64.4, pp. 255–261.
- Eshelby, J. D. (1949). "Uniformly moving dislocations". In: *Proc. Phys. Soc. Sect. A* 62.5, pp. 307–314. ISSN: 03701298. DOI: 10.1088/0370-1298/62/5/307.
- Fedosov, D. A., W. Pan, B. Caswell, G. Gompper, and G. E. Karniadakis (2011). "Predicting human blood viscosity in silico". In: *Proc. Natl. Acad. Sci.* 108.29, pp. 11772–11777. ISSN: 0027-8424. DOI: 10.1073/pnas.1101210108.
- Feeny, Brian and Ardeshir Guran (1997). "Friction as a nonlinearity in dynamics: A historical review". In: *Nonlinear Dyn. Richard Rand 50th Anniv. Vol.* Vol. 2, pp. 24–59.
- Feeny, Brian, Ardeshir Guran, Nikolaus Hinrichs, and Karl Popp (1998). "A Historical Review on Dry Friction and Stick-Slip Phenomena". In: *Appl. Mech. Rev.* 51.5, pp. 321–341. ISSN: 0003-6900. DOI: 10.1115/1.3099008.
- Fellah, Zine E A, Naima Sebaa, Mohamed Fellah, Farid G Mitri, Erick Ogam, Walter Lauriks, and Claude Depollier (2008). "Application of the biot model to ultrasound in bone: Direct problem". In: *IEEE Trans. Ultrason. Ferroelectr. Freq. Control* 55.7, pp. 1508–1515. ISSN: 08853010. DOI: 10.1109/TUFFC.2008.826.
- Ferdowsi, B., M. Griffo, R. A. Guyer, P. A. Johnson, C. Marone, and J. Carmeliet (2013). "Microslips as precursors of large slip events in the stick-slip dynamics of sheared

- granular layers: A discrete element model analysis". In: *Geophys. Res. Lett.* 40.16, pp. 4194–4198. ISSN: 00948276. DOI: 10.1002/grl.50813.
- Frenkel, J. (1944). "On the theory of Seismic and Seismoelectric Phenomena in a Moist Soil". In: *J. Phys.* III.5, pp. 230–241.
- (2005). "On the Theory of Seismic and Seismoelectric Phenomena in a Moist Soil". In: *J. Eng. Mech.* 131.9, pp. 879–887. ISSN: 0733-9399. DOI: 10.1061/(ASCE)0733-9399(2005)131:9(879).
- Freund, L. B. (1979). "The mechanics of dynamic shear crack propagation". In: *J. Geophys. Res. Solid Earth* 84.B5, pp. 2199–2209. ISSN: 21699356. DOI: 10.1029/JB084iB05p02199.
- Galis, Martin, Jean Paul Ampuero, P. Martin Mai, and Frédéric Cappa (2017). "Induced seismicity provides insight into why earthquake ruptures stop". In: *Sci. Adv.* 3.12. ISSN: 23752548. DOI: 10.1126/sciadv.aap7528.
- Gallot, Thomas, Stefan Catheline, Philippe Roux, Javier Brum, Nicolas Benech, and Carlos Negreira (2011). "Passive Elastography: Shear-Wave Tomography From Physiological-Noise Correlation in Soft Tissues". In: 58.6, pp. 1122–1126.
- Gallot, Thomas, Christophe Perge, Vincent Grenard, Marc-Antoine Fardin, Nicolas Taberlet, and Sébastien Manneville (2013). "Ultrafast ultrasonic imaging coupled to rheometry: Principle and illustration". In: *Rev. Sci. Instrum.* 84.4, p. 045107. ISSN: 0034-6748. DOI: 10.1063/1.4801462.
- Gao, H, Y Huang, P Gumbsch, and A J Rosakis (1999). "ScienceDirect.com - Journal of the Mechanics and Physics of Solids - On radiation-free transonic motion of cracks and dislocations". In: {...} *Mech. Phys.* {...} 47.9, pp. 1941–1962. ISSN: 0022-5096.
- Gao, Huajian, Yonggang Huang, and Farid F. Abraham (2001). "Continuum and atomistic studies of intersonic crack propagation". In: *J. Mech. Phys. Solids* 49.9, pp. 2113–2132. ISSN: 00225096. DOI: 10.1016/S0022-5096(01)00032-1.
- Geebelen, N., L. Boeckx, G. Vermeir, W. Lauriks, Jean F. Allard, and Olivier Dazel (2007). "Measurement of the rigidity coefficients of a melamine foam". In: *Acta Acust. united with Acust.* 93.5, pp. 783–788. ISSN: 16101928.
- Geerits, Tim W (1996). "Acoustic wave propagation through porous media revisited". In: *J. Acoust. Soc. Am.* 100.5, p. 2949. ISSN: 00014966. DOI: 10.1121/1.417106.
- Geerstma, Jan, Younane Abousleiman, and Alexander H.D. Cheng (2005). "Maurice Biot - I remember him well". In: *Proc. 3rd Biot Conf. Poromechanics*. Leiden / London / New York / Philadelphia / Singapore: A.A. BALKEMA, pp. 3–6.
- Genisson, J.-L., S Catheline, J Bercoff, M Tanter, and M Fink (2007). "Acoustoelasticity in soft solids: Assessment of the nonlinear shear modulus with the acoustic radiation force". In: December, pp. 3211–3219. DOI: 10.1121/1.2793605.
- Gennisson, J, T Deffieux, M Fink, and M Tanter (2013). "Ultrasound elastography: Principles and techniques". In: *Diagn. Interv. Imaging* 94.5, pp. 487–495. ISSN: 2211-5684. DOI: 10.1016/j.diii.2013.01.022.

- Gennisson, Jean-Luc, Stefan Catheline, Sana Chaffai, and Mathias Fink (2003). "Transient elastography in anisotropic medium: Application to the measurement of slow and fast shear wave speeds in muscles". In: *J. Acoust. Soc. Am.* 114.1, pp. 536–541. ISSN: 0001-4966. DOI: 10.1121/1.1579008.
- Gerling, B., H. Löwe, and A. van Herwijnen (2017). "Measuring the Elastic Modulus of Snow". In: *Geophys. Res. Lett.* 44.21, pp. 11,088–11,096. ISSN: 00948276. DOI: 10.1002/2017GL075110.
- Gierke, Henning E. von, Hans L. Oestreicher, Ernst K. Franke, Horace O. Parrack, and Wolf W. von Wittern (1952). "Physics of Vibrations in Living Tissues". In: *J. Appl. Physiol.* 4.12, pp. 886–900. ISSN: 8750-7587. DOI: 10.1152/jappl.1952.4.12.886.
- Goebel, T (2013). "MICROSEISMICITY , FAULT STRUCTURE , & THE SEISMIC CYCLE : INSIGHTS FROM LABORATORY STICK-SLIP EXPERIMENTS by". In: August, p. 204.
- Gomberg, J., P. A. Reasenberg, P. Bodin, and R. A. Harris (2001). "Earthquake triggering by seismic waves following the Landers and Hector Mine earthquakes". In: *Nature* 411.6836, pp. 462–466. ISSN: 0028-0836. DOI: 10.1038/35078053.
- Griffith, A. A. (1921). "The Phenomena of Rupture and Flow in Solids". In: *Philos. Trans. R. Soc. A Math. Phys. Eng. Sci.* 221.582-593, pp. 163–198. ISSN: 1364-503X. DOI: 10.1098/rsta.1921.0006.
- Gu, Yaojun and Teng fong Wong (1994). "Development of shear localization in simulated quartz gouge: Effect of cumulative slip and gouge particle size". In: *Pure Appl. Geophys. PAGEOPH* 143.1-3, pp. 387–423. ISSN: 00334553. DOI: 10.1007/BF00874336.
- Haire, T J and C M Langton (1999). "Biot theory: a review of its application to ultrasound propagation through cancellous bone". In: *Bone* 24.4, pp. 291–295. ISSN: 87563282. DOI: 10.1016/S8756-3282(99)00011-3.
- Haskell, N A (1964). "ENERGY WAVE AND ENERGY FROM BY DENSITY OF ELASTIC RADIATION PROPAGATING FAULTS". In: *Bull. Seismol. Soc. Am.* 54.6, pp. 1811–1841.
- Heaton, Thomas H. (1990). "Evidence for and implications of self-healing pulses of slip in earthquake rupture". In: *Phys. Earth Planet. Inter.* 64.1, pp. 1–20. ISSN: 00319201. DOI: 10.1016/0031-9201(90)90002-F.
- Helmstetter, Agnès, Barbara Nicolas, Pierre Comon, and Michel Gay (2015). "Basal icequakes recorded beneath an alpine glacier (Glacier d'Argentière, Mont Blanc, France): Evidence for stick-slip motion?" In: *J. Geophys. Res. Earth Surf.* 120.3, pp. 379–401. ISSN: 21699011. DOI: 10.1002/2014JF003288.
- Herman, Jon and Will Usher (2017). "SALib: An open-source Python library for Sensitivity Analysis". In: *J. Open Source Softw.* 2.9, p. 97. ISSN: 2475-9066. DOI: 10.21105/joss.00097.

- Herwijnen, A. van and J. Schweizer (2011). "Monitoring avalanche activity using a seismic sensor". In: *Cold Reg. Sci. Technol.* 69.2-3, pp. 165–176. ISSN: 0165232X. DOI: 10.1016/j.coldregions.2011.06.008.
- Heslot, F., T. Baumberger, B. Perrin, B. Caroli, and C. Caroli (1994). "Creep, stick-slip, and dry-friction dynamics: Experiments and a heuristic model". In: *Phys. Rev. E* 49.6, pp. 4973–4988. ISSN: 1063-651X. DOI: 10.1103/PhysRevE.49.4973.
- Hidalgo, Raúl Cruz, Christian U. Grosse, Ferenc Kun, Hans W. Reinhardt, and Hans J. Herrmann (2002). "Evolution of Percolating Force Chains in Compressed Granular Media". In: *Phys. Rev. Lett.* 89.20, pp. 1–4. ISSN: 10797114. DOI: 10.1103/PhysRevLett.89.205501.
- Holen, Jarle, Robert C. Waag, and Raymond Gramiak (1985). "Representations of rapidly oscillating structures on the Doppler display". In: *Ultrasound Med. Biol.* 11.2, pp. 267–272. ISSN: 03015629. DOI: 10.1016/0301-5629(85)90125-5.
- Holm, Sverre and Sven Peter Näsholm (2014). "Comparison of fractional wave equations for power law attenuation in ultrasound and elastography". In: *Ultrasound Med. Biol.* 40.4, pp. 695–703. ISSN: 03015629. DOI: 10.1016/j.ultrasmedbio.2013.09.033. arXiv: 1306.6507v1.
- Hough, Paul V C (1962). *US3069654A - Method and means for recognizing complex patterns*.
- Hulbert, Claudia, Bertrand Rouet-Leduc, Paul A. Johnson, Christopher X. Ren, Jacques Rivière, David C. Bolton, and Chris Marone (2019). "Similarity of fast and slow earthquakes illuminated by machine learning". In: *Nat. Geosci.* 12.1, pp. 69–74. ISSN: 17520908. DOI: 10.1038/s41561-018-0272-8.
- Hutchings, Ian M. (2016). "Leonardo da Vinci's studies of friction". In: *Wear* 360-361, pp. 51–66. ISSN: 00431648. DOI: 10.1016/j.wear.2016.04.019.
- Ide, Satoshi (2014). "Modeling fast and slow earthquakes at various scales". In: *Proc. Japan Acad. Ser. B* 90.8, pp. 259–277. ISSN: 13492896. DOI: 10.2183/pjab.90.259.
- Igel, H. (2017). *Computational Seismology*. 1st ed. Oxford: Oxford University Press. ISBN: 978-0-19-871740-9.
- Iio, Yoshihisa (1995). "Observations of the slow initial phase generated by microearthquakes: Implications for earthquake nucleation and propagation". In: *J. Geophys. Res. Solid Earth* 100.B8, pp. 15333–15349. ISSN: 01480227. DOI: 10.1029/95JB01150.
- Iooss, Bertrand and Paul Lemaître (2015). "A Review on Global Sensitivity Analysis Methods". In: vol. 59, pp. 101–122. ISBN: 978-1-4899-7546-1. DOI: 10.1007/978-1-4899-7547-8\_5.
- Jang, Bohyun, Ji Won Han, Pil Soo Sung, Jeong Won Jang, Si Hyun Bae, Jong Young Choi, Young I. Cho, and Seung Kew Yoon (2016). "Hemorheological alteration in patients clinically diagnosed with chronic liver diseases". In: *J. Korean Med. Sci.* 31.12, pp. 1943–1948. ISSN: 15986357. DOI: 10.3346/jkms.2016.31.12.1943.
- John Leslie (1804). *An experimental inquiry into the nature and propagation of heat*. Printed for London. ISBN: 3663537137.

- Johnson, David Linton, Joel Koplik, and Roger Dashen (1987). "Theory of dynamic permeability and tortuosity in fluid saturated porous media". In: *J. Fluid Mech.* 176.1987, pp. 379–402. ISSN: 14697645. DOI: 10.1017/S0022112087000727.
- Johnson, David Linton, Thomas J. Plona, and Haruo Kojima (1994). "Probing porous media with first and second sound. II. Acoustic properties of water-saturated porous media". In: *J. Appl. Phys.* 76.1, pp. 115–125. ISSN: 00218979. DOI: 10.1063/1.358438.
- Johnson, P A, B Ferdowsi, B M Kaproth, M Scuderi, M Griffa, J Carmeliet, R A Guyer, P-Y. Le Bas, D T Trugman, and C Marone (2013). "Acoustic emission and microslip precursors to stick-slip failure in sheared granular material". In: *Geophys. Res. Lett.* 40.21, pp. 5627–5631. ISSN: 00948276. DOI: 10.1002/2013GL057848.
- Johnson, P A, J Carmeliet, H M Savage, M Scuderi, B M Carpenter, R A Guyer, E G Daub, and C Marone (2016). "Dynamically triggered slip leading to sustained fault gouge weakening under laboratory shear conditions". In: DOI: 10.1002/2015GL067056. Received.
- Johnson, T., F. T. Wu, and C. H. Scholz (1973). "Source Parameters for Stick-Slip and for Earthquakes". In: *Science* (80-. ). 179.4070, pp. 278–280. ISSN: 0036-8075. DOI: 10.1126/science.179.4070.278.
- Johnson, T. L. and C. H. Scholz (1976). "Dynamic properties of stick-slip friction of rock". In: *J. Geophys. Res.* 81.5, pp. 881–888. DOI: 10.1029/jb081i005p00881.
- Joseph-Léonard-Marie Poiseuille (1835). *Recherches sur les causes du mouvement du sang dans les vaisseaux capillaires 1835*.
- Julian, Bruce R, D Miller, and G R Foulger (1998). "Non-Double-Couple Earthquakes". In: *Rev. Geophys.* 36.4, pp. 551–568.
- Kanamori, Hiroo and Emily E. Brodsky (2004). "The physics of earthquakes". In: *Proc. Japan Acad. Ser. B* 80.7, pp. 297–316. ISSN: 0386-2208. DOI: 10.1088/0034-4885/67/8/R03.
- Kaproth, B. M. and C. Marone (2013). "Slow Earthquakes, Preseismic Velocity Changes, and the Origin of Slow Frictional Stick-Slip". In: *Science* (80-. ). 341.6151, pp. 1229–1232. ISSN: 0036-8075. DOI: 10.1126/science.1239577.
- Kato, A., K. Obara, T. Igarashi, H. Tsuruoka, S. Nakagawa, and N. Hirata (2012). "Propagation of Slow Slip Leading Up to the 2011 Mw 9.0 Tohoku-Oki Earthquake". In: *Science* (80-. ). 335.6069, pp. 705–708. ISSN: 0036-8075. DOI: 10.1126/science.1215141.
- Kato, Naoyuki, Kinichiro Kusunose, Kiyohiko Yamamoto, and Tomowo Hirasawai (1991). "Slowly Propagating Slip Events in a Composite Sample of Granite and Marble." In: *J. Phys. Earth* 39.2, pp. 461–476. ISSN: 1884-2305. DOI: 10.4294/jpe1952.39.461.
- Kawakatsu, Hitoshi (1989). "Centroid single force inversion of seismic waves generated by landslides". In: *J. Geophys. Res.* 94.B9, p. 12363. ISSN: 0148-0227. DOI: 10.1029/JB094iB09p12363.

- King, C.-Y., R. D. Nason, and D. Tocher (1973). "Kinematics of Fault Creep". In: *Philos. Trans. R. Soc. A Math. Phys. Eng. Sci.* 274.1239, pp. 355–360. ISSN: 1364-503X. DOI: 10.1098/rsta.1973.0063.
- Koerner, R M, A E Lord Jr, W M McCabe, and J W Curran (1976). "Acoustic emission behavior of granular soils". In: *J. Geotech. Geoenvironmental Eng.* 102N.GT7, pp. 761–773.
- Komatsu, Hirokazu, Anthony Koo, and Paul H. Guth (1990). "Leukocyte flow dynamics in the rat liver microcirculation". In: *Microvasc. Res.* 40.1, pp. 1–13. ISSN: 10959319. DOI: 10.1016/0026-2862(90)90002-9.
- Kovesi, P. (1999). "Image Features from Phase Congruency". In: *Videre* 1.3, pp. C3–C3. ISSN: 1041-1135.
- Kovesi, Peter (1997). "Symmetry and asymmetry from local phase". In: *Tenth Aust. Jt. Convergence Artif. Intell.* Pp. 2–4. DOI: 10.1.1.40.4146.
- Krouskop, T A, D R Dougherty, and F S Vinson (1987). "A pulsed Doppler ultrasonic system for making noninvasive measurements of the mechanical properties of soft tissue". In: *J. Rehabil. Res. Dev.* 24.10, pp. 1–8.
- Kuglin, C. D. and D. C. Hines (1975). "The Phase Correlation Image Alignment Method". In: *Proceeding IEEE Int. Conf. Cybern. Soc.* New York, NY, USA, pp. 163–165.
- Kwiatek, Grzegorz and Yehuda Ben-Zion (2013). "Assessment of P and S wave energy radiated from very small shear-tensile seismic events in a deep South African mine". In: *J. Geophys. Res. Solid Earth* 118.7, pp. 3630–3641. ISSN: 21699313. DOI: 10.1002/jgrb.50274.
- Lafarge, Denis, Pavel Lemarinier, Jean F. Allard, and Viggo Tarnow (1997). "Dynamic compressibility of air in porous structures at audible frequencies". In: *J. Acoust. Soc. Am.* 102.4, pp. 1995–2006. ISSN: 0001-4966. DOI: 10.1121/1.419690.
- Landau, L.D. and E. M. Lifshitz (1986). *Theory of elasticity*.
- Landau, L.D and E.M. Lifshitz (1987). *Fluid Mechanics*.
- Latour, S., Michel Campillo, Christophe Voisin, and Stefan Nielsen (2011a). "Effets de l'hétérogénéité des failles sur la dynamique de la rupture : étude numérique et expérimentale". In:
- Latour, S., T. Gallot, S. Catheline, C. Voisin, F. Renard, E. Larose, and M. Campillo (2011b). "Ultrafast ultrasonic imaging of dynamic sliding friction in soft solids: The slow slip and the super-shear regimes". In: *EPL (Europhysics Lett.)* 96.January 2016, p. 59003. ISSN: 0295-5075. DOI: 10.1209/0295-5075/96/59003.
- Latour, S., A. Schubnel, S. Nielsen, R. Madariaga, and S. Vinciguerra (2013a). "Characterization of nucleation during laboratory earthquakes". In: *Geophys. Res. Lett.* 40.19, pp. 5064–5069. ISSN: 0094-8276. DOI: 10.1002/grl.50974.
- Latour, S., C. Voisin, F. Renard, E. Larose, S. Catheline, and M. Campillo (2013b). "Effect of fault heterogeneity on rupture dynamics : An experimental approach using

- ultrafast ultrasonic imaging". In: *J. Geophys. Res. Solid Earth* 118.11, pp. 5888–5902. ISSN: 21699313. DOI: 10.1002/2013JB010231.
- Lauriks, Walter, Laurens Boeckx, and Philippe Leclaire (2005). "Characterization of porous acoustic materials". In: *Sapem*. Lyon, pp. 0–14.
- Lay, Thorne and Terry C. Wallace (1995). *Modern Global Seismology*. c, pp. 2–6. ISBN: 9780127328706.
- Leeman, J. R., R. D. Valdez, R. B. Alley, S. Anandakrishnan, and D. M. Saffer (2016). "Mechanical and hydrologic properties of Whillans Ice Stream till: Implications for basal strength and stick-slip failure". In: *J. Geophys. Res. Earth Surf.* 121.7, pp. 1295–1309. ISSN: 21699011. DOI: 10.1002/2016JF003863.
- Lerner, Robert M., S. R. Huang, and Kevin J. Parker (1990). "'Sonoelasticity' images derived from ultrasound signals in mechanically vibrated tissues". In: *Ultrasound Med. Biol.* 16.3, pp. 231–239. ISSN: 03015629. DOI: 10.1016/0301-5629(90)90002-T.
- Lieou, Charles K C, Eric G Daub, Robert A Guyer, Robert E Ecke, Chris Marone, and Paul A Johnson (2017). "Simulating stick-slip failure in a sheared granular layer using a physics-based constitutive model". In: DOI: 10.1002/2016JB013627.
- Linde, Alan T., Michael T. Gladwin, Malcolm J.S. Johnston, Ross L. Gwyther, and Roger G. Bilham (1996). *A slow earthquake sequence on the San Andreas fault*. DOI: 10.1038/383065a0.
- Lipovsky, Bradley Paul and Eric M. Dunham (2017). "Slow-slip events on the Whillans Ice Plain, Antarctica, described using rate-and-state friction as an ice stream sliding law". In: *J. Geophys. Res. Earth Surf.* 122.4, pp. 973–1003. ISSN: 21699011. DOI: 10.1002/2016JF004183.
- Liu, Fei and Daniel J. Tschumperlin (2011). "Micro-Mechanical Characterization of Lung Tissue Using Atomic Force Microscopy". In: *J. Vis. Exp.* 54, pp. 1–7. ISSN: 1940-087X. DOI: 10.3791/2911.
- Livne, Ariel, Eran Bouchbinder, and Jay Fineberg (2008). "Breakdown of Linear Elastic Fracture Mechanics near the Tip of a Rapid Crack". In: *Phys. Rev. Lett.* 101.26, p. 264301. ISSN: 0031-9007. DOI: 10.1103/PhysRevLett.101.264301.
- Lu, Xiao, Ares J. Rosakis, and Nadia Lapusta (2010). "Rupture modes in laboratory earthquakes: Effect of fault prestress and nucleation conditions". In: *J. Geophys. Res. Solid Earth* 115.12, pp. 1–25. ISSN: 21699356. DOI: 10.1029/2009JB006833.
- Mach, L. (1896). "Über die Sichtbarmachung von Luftstromlinien. Zeitschrift für Luftschiffahrt und Physik der Atmosphäre". In: *Zeitschrift für Luftschiffahrt und Phys. der Atmosphäre* 15.6, pp. 129–139.
- Mair, Karen and Chris Marone (1999). "Friction of simulated fault gouge for a wide range of velocities and normal stresses". In: *J. Geophys. Res. Solid Earth* 104.B12, pp. 28899–28914. ISSN: 01480227. DOI: 10.1029/1999JB900279.
- Marey, E.J. (1893). "Le mouvement des liquides étudié par la chronophotographie". In: *Comptes Rendus Hebd. des Séances l'Académie des Sci.* 117, pp. 913–924.



- (1901). “Le mouvement des liquides étudié par la chronophotographie”. In: *La Nat.* 49, pp. 252–254.
- Marone, Chris (1998). “Laboratory-Derived Friction Laws and Their Application To Seismic Faulting”. In: *Annu. Rev. Earth Planet. Sci.* 26.1, pp. 643–696. ISSN: 0084-6597. DOI: 10.1146/annurev.earth.26.1.643.
- Marty, S, F X Passelègue, J Aubry, H S Bhat, A Schubnel, and R Madariaga (2019). “Origin of High-Frequency Radiation During Laboratory Earthquakes”. In: *Geophys. Res. Lett.* 46.7, pp. 3755–3763. ISSN: 0094-8276. DOI: 10.1029/2018GL080519.
- Mavko, Gary, Tapan Mukerji, and Jack Dvorkin (2009). *The rock physics handbook - Tools for seismic analysis of porous media*. 2nd ed. Cambridge University Press. ISBN: 9780521861366.
- Mello, Michael, Harsha S Bhat, and Ares J Rosakis (2016). “Spatiotemporal properties of Sub-Rayleigh and supershear rupture velocity fields: Theory and experiments”. In: *J. Mech. Phys. Solids* 93, pp. 153–181. ISSN: 00225096. DOI: 10.1016/j.jmps.2016.02.031.
- Melon, M, E Mariez, C Ayrault, and S Sahraoui (1998). “Acoustical and mechanical characterization of anisotropic open-cell foams”. In: *J. Acoust. Soc. Am.* 104.5, pp. 2622–2627. ISSN: 0001-4966. DOI: 10.1121/1.423897.
- Meyer, Enno (2013). “Beurteilung der Pfortader mittels endoskopischen Ultraschall (EUS) bei Patienten mit Leberzirrhose und einem Kontrollkollektiv”. PhD thesis. Ruhr – Universität Bochum.
- Meyer, Keith C. et al. (2012). “An official American Thoracic Society clinical practice guideline: The clinical utility of bronchoalveolar lavage cellular analysis in interstitial lung disease”. In: *Am. J. Respir. Crit. Care Med.* 185.9, pp. 1004–1014. ISSN: 1073449X. DOI: 10.1164/rccm.201202-0320ST.
- Michlmayr, Gernot, Denis Cohen, and Dani Or (2012). “Sources and characteristics of acoustic emissions from mechanically stressed geologic granular media - A review”. In: *Earth-Science Rev.* 112.3-4, pp. 97–114. ISSN: 00128252. DOI: 10.1016/j.earscirev.2012.02.009.
- Mizuno, K, M Matsukawa, T Otani, P Laugier, and F Padilla (2009). “Propagation of two longitudinal waves in human cancellous bone: An in vitro study”. In: *J. Acoust. Soc. Am.* 125.5, pp. 3460–3466. ISSN: 1520-8524. DOI: 10.1121/1.3111107.
- Mohanty, Kaustav, John Blackwell, Thomas Egan, and Marie Muller (2016). “Characterization of the lung parenchyma using ultrasound multiple scattering”. In: *Acoust. Soc. Am.* 140, pp. 3186–3187. DOI: 10.1016/j.ultrasmedbio.2017.01.011.
- Morency, Christina and Jeroen Tromp (2008). “Spectral-element simulations of wave propagation in porous media”. In: *Geophys. J. Int.* 175.1, pp. 301–345. ISSN: 0956540X. DOI: 10.1111/j.1365-246X.2008.03907.x.

- Muller, Marie, Jean-Luc Gennisson, Thomas Deffieux, Mickaël Tanter, and Mathias Fink (2009). "Quantitative Viscoelasticity Mapping of Human Liver Using Supersonic Shear Imaging: Preliminary In Vivo Feasibility Study". In: *Ultrasound Med. Biol.* 35.2, pp. 219–229. ISSN: 03015629. DOI: 10.1016/j.ultrasmedbio.2008.08.018.
- Nakagawa, K., K. Soga, and J.K. Mitchell (2001). "Observation of Biot compressional wave of the second kind in granular soils". In: *Geotechnique* 20.1, pp. 19–22.
- Nasholm, Sven Peter and Sverre Holm (2012). "On a Fractional Zener Elastic Wave Equation". In: *Fract. Calc. Appl. Anal.* 16.1, pp. 26–50. ISSN: 1311-0454. DOI: 10.2478/s13540-013--0003-1. arXiv: 1212.4024.
- Nettles, Meredith and Geoffrey A Abers (2003). "Glacial Earthquakes". In: *Science* (80-). 302.September 2000, pp. 2001–2003. ISSN: 0036-8075. DOI: 10.1126/science.1088057.
- Nguyen, Man Minh, Hua Xie, Kamila Paluch, Douglas Stanton, and Bharat Ramachandran (2013). "Pulmonary ultrasound elastography: a feasibility study with phantoms and ex-vivo tissue". In: *Proc. SPIE*. Ed. by Johan G Bosch and Marvin M Dooley. Vol. 8675, p. 867503. ISBN: 9780819494498. DOI: 10.1117/12.2007354.
- NI (2018). *What is I/Q Data ? - National Instruments Tutorial*. <http://www.ni.com/tutorial/4805/en/>.
- Nightingale, Kathryn, Ned Rouze, Stephen Rosenzweig, Michael Wang, Manal Abdelmalek, Cynthia Guy, and Mark Palmeri (2015). "Derivation and analysis of viscoelastic properties in human liver: impact of frequency on fibrosis and steatosis staging". In: *IEEE Trans. Ultrason. Ferroelectr. Freq. Control* 62.1, pp. 165–175. ISSN: 0885-3010. DOI: 10.1109/TUFFC.2014.006653.
- Niskanen, M., J. Groby, A. Duclos, O. Dazel, J. C. Le Roux, N. Poulain, T. Huttunen, and T. Lähivaara (2017). "Deterministic and statistical characterization of rigid frame porous materials from impedance tube measurements". In: *J. Acoust. Soc. Am.* 2407.142, p. 14255. ISSN: 00014966. DOI: 10.1121/1.5008742.
- O'Donnell, M., E. T. Jaynes, and J. G. Miller (1981). "Kramers–Kronig relationship between ultrasonic attenuation and phase velocity". In: *J. Acoust. Soc. Am.* 69.3, pp. 696–701. ISSN: 0001-4966. DOI: 10.1121/1.385566.
- Oestreicher, Hans L. (1951). "Field and Impedance of an Oscillating Sphere in a Viscoelastic Medium with an Application to Biophysics". In: *J. Acoust. Soc. Am.* 23.6.
- Ogam, Erick, Z E A Fellah, Naima Sebaa, and J Groby (2011). "Non-ambiguous recovery of Biot poroelastic parameters of cellular panels using ultrasonic waves". In: *J. Sound Vib.* 330.6, pp. 1074–1090. ISSN: 0022-460X. DOI: 10.1016/j.jsv.2010.09.032.
- Ohnaka, Mitiyasu (2004a). "Earthquake cycles and physical modeling of the process leading up to a large earthquake". In: *Earth, Planets Sp.* 56.8, pp. 773–793. ISSN: 1880-5981. DOI: 10.1186/BF03353085.

- (2004b). “GEOPHYSICS: Rupture in the Laboratory”. In: *Science* (80-. ). 303.5665, pp. 1788–1789. ISSN: 0036-8075. DOI: 10.1126/science.1095765.
- (2013). *The Physics of Rock Failure and Earthquakes*. Cambridge University Press. ISBN: 9781107030060.
- Ohnaka, Mitiyasu and Yasuto Kuwahara (1990). “Characteristic features of local breakdown near a crack-tip in the transition zone from nucleation to unstable rupture during stick-slip shear failure”. In: *Tectonophysics* 175.1-3, pp. 197–220. ISSN: 00401951. DOI: 10.1016/0040-1951(90)90138-X.
- Ohnaka, Mitiyasu and Lin-feng Shen (1999a). “Scaling of the shear rupture process from nucleation to dynamic propagation: Implications of geometric irregularity of the rupturing surfaces”. In: *J. Geophys. Res. Solid Earth* 104.B1, pp. 817–844. ISSN: 01480227. DOI: 10.1029/1998JB900007.
- (1999b). “Scaling of the shear rupture process from nucleation to dynamic propagation: Implications of geometric irregularity of the rupturing surfaces”. In: *J. Geophys. Res.* 104.1998, p. 817. ISSN: 0148-0227. DOI: 10.1029/1998JB900007.
- Oldham, R. D. (1906). “The Constitution of the Interior of the Earth, as Revealed by Earthquakes”. In: *Q. J. Geol. Soc.* 62.1-4, pp. 456–475. ISSN: 0370-291X. DOI: 10.1144/GSL.JGS.1906.062.01-04.21.
- Olsen, Kim B and R Madariaga (2002). “Earthquake dynamics”. In: *Int. Geophys. {...}* 1989.
- Oman, Daniel Milton and Robert Milton Oman (2016). *How to solve Physics problems*. 2. ISBN: 9780071849326.
- Ophir, Jonathan, I. Cespedes, H. Ponnekanti, Y. Yazdi, and X. Li (1991). “Elastography: A quantitative method for imaging the elasticity of biological Tissues”. In: *Ultrason. Imaging* 13, pp. 111–134. DOI: 10.1016/B978-0-12-396487-8.00016-1.
- Oura, H. (1952). “Sound velocity in the snow cover.” In: *Low Temp. Sci. Ser. A, Phys. Sci.* A.9, pp. 171–178.
- Parker, K.J., S.R. Huang, R.A. Musulin, and R.M. Lerner (1990). “Tissue response to mechanical vibrations for “sonoelasticity imaging””. In: *Ultrasound Med. Biol.* 16.3, pp. 241–246. ISSN: 03015629. DOI: 10.1016/0301-5629(90)90003-U.
- Passelegue, F. X., A. Schubnel, S. Nielsen, Harsha S Bhat, and Raúl Madariaga (2013). “From Sub-Rayleigh to Supershear Ruptures During Stick-Slip Experiments on Crustal Rocks”. In: *Science* (80-. ). 340.6137, pp. 1208–1211. ISSN: 0036-8075. DOI: 10.1126/science.1235637.
- Paterson, Norman R. (1956). “Seismic wave propagation in porous granular media”. In: *Geophysics* XXI.3, pp. 691–714.
- Pawluś, Aleksander et al. (2016). “Shear wave elastography of the spleen: evaluation of spleen stiffness in healthy volunteers”. In: *Abdom. Radiol.* 41.11, pp. 2169–2174. ISSN: 23660058. DOI: 10.1007/s00261-016-0834-4.
- Peeters, Geert, Charlotte Debbaut, Pieter Cornillie, Thomas De Schryver, Diethard Monbaliu, Wim Laleman, and Patrick Segers (2015). “A Multilevel Modeling

- Framework to Study Hepatic Perfusion Characteristics in Case of Liver Cirrhosis". In: *J. Biomech. Eng.* 137.5, p. 051007. ISSN: 0148-0731. DOI: 10.1115/1.4029280.
- Peng, Zhigang and Joan Gomberg (2010). "An integrated perspective of the continuum between earthquakes and slow-slip phenomena". In: *Nat. Geosci.* 3.9, pp. 599–607. ISSN: 1752-0894. DOI: 10.1038/ngeo940.
- Persson, Bo N. J. (2000). *Sliding Friction*. 2nd. NanoScience and Technology. Berlin, Heidelberg: Springer Berlin Heidelberg, p. 367. ISBN: 978-3-642-08652-6. DOI: 10.1007/978-3-662-04283-0.
- Pinton, G.F., J.J. Dahl, and G.E. Trahey (2005). "Rapid Tracking of Small Displacements with Ultrasound". In: *IEEE Ultrason. Symp. 2005*. Vol. 4. 6. IEEE, pp. 2062–2065. ISBN: 0-7803-9382-1. DOI: 10.1109/ULTSYM.2005.1603285.
- Plona, Thomas J. (1980). "Observation of a second bulk compressional wave in a porous medium at ultrasonic frequencies". In: *Appl. Phys. Lett.* 36.4, pp. 259–261. ISSN: 00036951. DOI: 10.1063/1.91445.
- Pujol, Jose (2003). *Elastic Wave Propagation and Generation in Seismology*. Cambridge University Press, p. 444. ISBN: 9780521817301.
- Quirk, Bryden C., Robert A. McLaughlin, Andrea Curatolo, Rodney W. Kirk, Peter B. Noble, and David D. Sampson (2011). "In situ imaging of lung alveoli with an optical coherence tomography needle probe". In: *J. Biomed. Opt.* 16.3, p. 036009. ISSN: 10833668. DOI: 10.1117/1.3556719.
- Raffael, M, C Willert, S T Wereley, and J Kompenhans (2007). *Particle Image Velocimetry*. 3. Springer-Verlag. ISBN: 978-3-540-72307-3. DOI: 10.1007/978-3-540-72308-0.
- Rand, Peter W., Eleanor Lacombe, Hamilton E. Hunt, and William H. Austin (1963). "Viscosity of normal human blood". In: *J. Appl. Physiol.* 19.1, pp. 117–122. ISSN: 0021-8987.
- Rattanadecho, Phadungsak and Pornthip Keangin (2013). "Numerical study of heat transfer and blood flow in two-layered porous liver tissue during microwave ablation process using single and double slot antenna". In: *Int. J. Heat Mass Transf.* 58.1-2, pp. 457–470. ISSN: 00179310. DOI: 10.1016/j.ijheatmasstransfer.2012.10.043.
- Reid, H. G. (1910). "The mechanics of the earthquake". In: *Calif. Earthq. April 18, 1906, Rep. State Earthq. Investig. Comm.* Pp. 3–55. ISSN: 0022-1120. DOI: 10.1533/9780857099211.2.177.
- Rice, J R (1980). "The mechanics of earthquake rupture". In: *Phys. Earth's Inter.* Pp. 555–649. DOI: 10.1.1.161.3251.
- Rice, J. R. and A. L. Ruina (1983). "Stability of Steady Frictional Slipping". In: *J. Appl. Mech.* 50.2, p. 343. ISSN: 00218936. DOI: 10.1115/1.3167042.
- Robinson, D P, C Brough, and S Das (2006). "The Mw 7.8, 2001 Kunlunshan earthquake: Extreme rupture speed variability and effect of fault geometry". In: *J. Geophys. Res.* 111.B8, B08303. ISSN: 0148-0227. DOI: 10.1029/2005JB004137.

- Rogers, Garry and Herb Dragert (2003). "Episodic Tremor and Slip on the Cascadia Episodic Tremor and Slip on the Cascadia Subduction Zone : The". In: *Science* (80-. ). 300.2003, pp. 1942–1943. DOI: 10.1126/science.1084783.
- Rosakis, A J and D Coker (1999). "Cracks Faster than the Shear Wave Speed". In: *Science* (80-. ). 284.May, pp. 1337–1340.
- Rosakis, Ares J, Omprakash Samudrala, Raman P Singh, and A Shukla (1998). "Intersonic crack propagation in bimaterial systems". In: *J. Mech. Phys. Solids* 46.10, pp. 1789–1814. ISSN: 00225096. DOI: 10.1016/s0022-5096(98)00036-2.
- Rosakis, Ares J., Kaiwen Xia, G. Lykotrafitis, and Hiroo Kanamori (2007). "Dynamic shear rupture in frictional interfaces: speeds, directionality and modes". In: *Treatise Geophys. Vol 4, Earthq. Seismol.* Pp. 153–192.
- Rosenau, Matthias, Fabio Corbi, and Stephane Dominguez (2017). "Analogue earthquakes and seismic cycles: Experimental modelling across timescales". In: *Solid Earth* 8.3, pp. 597–635. ISSN: 18699529. DOI: 10.5194/se-8-597-2017.
- Royer, Daniel and E. Dieulesaint (1996). *Ondes Elastiques dans les Solides 1*. Masson.
- Rubinstein, S M, G Cohen, and J Fineberg (2009). "Visualizing stick-slip: experimental observations of processes governing the nucleation of frictional sliding". In: *J. Phys. D. Appl. Phys.* 42.21, p. 214016. ISSN: 0022-3727. DOI: 10.1088/0022-3727/42/21/214016.
- Rubinstein, Shmuel M., Gil Cohen, and Jay Fineberg (2004). "Detachment fronts and the onset of dynamic friction". In: *Nature* 430.August, pp. 1005–1009. DOI: 10.1038/nature02861.1..
- Rubinstein, Shmuel M., Meni Shay, Gil Cohen, and Jay Fineberg (2006). "Crack-like processes governing the onset of frictional slip". In: *Int. J. Fract.* 140.1-4, pp. 201–212. ISSN: 03769429. DOI: 10.1007/s10704-006-0049-8. arXiv: 0603528 [cond-mat].
- Sabra, Karim G., Stephane Conti, Philippe Roux, and W. A. Kuperman (2007). "Passive in vivo elastography from skeletal muscle noise". In: *Appl. Phys. Lett.* 90.19. ISSN: 00036951. DOI: 10.1063/1.2737358.
- Sambursky, Samuel (1962). *The Physical World of Late Antiquity*. Princeton Legacy Library. ISBN: 9783540773405.
- Sandrin, L., S. Catheline, M. Tanter, X. Hennequin, and M. Fink (1999a). "Time-Resolved Pulsed Elastography with Ultrafast Ultrasonic Imaging". In: *Ultrason. Imaging* 21.4, pp. 259–272. ISSN: 0161-7346. DOI: 10.1177/016173469902100402.
- Sandrin, Laurent (2004). "The role of the coupling term in transient elastography". In: *J. Acoust. Soc. Am.* 115.January 2004, pp. 73–83. DOI: 10.1121/1.1635412.
- Sandrin, Laurent, Stefan Catheline, and Mathias Fink (1999b). "Transient elastography in biological tissues". In: *J. Acoust. Soc. Am.* 105.2, pp. 1014–1015. ISSN: 0001-4966. DOI: 10.1121/1.425852.
- Sarvazyan, Armen, Tj Timothy J Hall, Mw Matthew W Urban, Mostafa Fatemi, Salavat R Aglyamov, and Brian S Garra (2011). "an Overview of Elastography - an

- Emerging Branch of Medical Imaging." In: *Curr. Med. Imaging Rev.* 7.4, pp. 255–282. ISSN: 1573-4056. DOI: 10.2174/157340511798038684.
- Sarvazyan, Armen P, Oleg V Rudenko, Scott D Swanson, J.Brian Fowlkes, and Stanislav Y Emelianov (1998). "Shear wave elasticity imaging: a new ultrasonic technology of medical diagnostics". In: *Ultrasound Med. Biol.* 24.9, pp. 1419–1435. ISSN: 03015629. DOI: 10.1016/S0301-5629(98)00110-0.
- Schallamach, A. (1971). "How does rubber slide?" In: *Wear* 17.4, pp. 301–312. ISSN: 00431648. DOI: 10.1016/0043-1648(71)90033-0.
- Scholz, C.~H. (1998). "Earthquakes and friction laws". In: *Nature* 391, pp. 37–42.
- Scholz, Christopher H (2002). *The Mechanics of Earthquakes and Faulting*. 2nd. Cambridge University Press. ISBN: 9780521652230.
- Scottl, David R, Southern California, Los Angeles, Chris J Marone, Planetary Sciences, and Charles G Sammis (1994). "The apparent friction of granular fault gouge". In: *Sci. York* 99.93, pp. 7231–7246.
- Scuderi, Marco M., Brett M. Carpenter, Paul A. Johnson, and Chris Marone (2015). "Poromechanics of stick-slip frictional sliding and strength recovery on tectonic faults". In: *J. Geophys. Res. Solid Earth* 120.10, pp. 6895–6912. ISSN: 21699313. DOI: 10.1002/2015JB011983.
- Selin, Helaine (2016). *Encyclopaedia of the History of Science, Technology and Medicine in Non-Western Cultures*. Ed. by Helaine Selin. Third. Springer-Verlag, p. 4706. ISBN: 9789400777460.
- Shapiro, S. A. and C. Dinske (2009). "Fluid-induced seismicity: Pressure diffusion and hydraulic fracturing". In: *Geophys. Prospect.* 57.2, pp. 301–310. ISSN: 13652478. DOI: 10.1111/j.1365-2478.2008.00770.x.
- Shearer, P. M. (2009). *Introduction to seismology*. 2nd. Cambridge University Press. ISBN: 978-0-511-58010-9.
- Shlomai, Hadar and Jay Fineberg (2016). "The structure of slip-pulses and supershear ruptures driving slip in bimaterial friction". In: *Nat. Commun.* 7.1, pp. 1–7. ISSN: 2041-1723. DOI: 10.1038/ncomms11787.
- Smeulders, D. M. (2005). "Experimental Evidence for Slow Compressional Waves". In: *J. Eng. Mech.* 131.9, pp. 908–917. ISSN: 0733-9399. DOI: 10.1061/(ASCE)0733-9399(2005)131:9(908).
- Smye, S. W., C. J. Evans, M. P. Robinson, and B. D. Sleeman (2007). "Modelling the electrical properties of tissue as a porous medium". In: *Phys. Med. Biol.* 52.23, pp. 7007–7022. ISSN: 00319155. DOI: 10.1088/0031-9155/52/23/016.
- Stefanescu, Horia, Mircea Grigorescu, Monica Lupsor, Bogdan Procopet, Anca Maniu, and Radu Badea (2011). "Spleen stiffness measurement using fibroscan for the noninvasive assessment of esophageal varices in liver cirrhosis patients". In: *J. Gastroenterol. Hepatol.* 26.1, pp. 164–170. ISSN: 14401746. DOI: 10.1111/j.1440-1746.2010.06325.x.

- Steinbrugge, Karl V, Edwin G Zacher, Don Tocher, C A Whitten, and C N Claire (1960). "Creep on the San Andreas fault". In: *Bull. Seismol. Soc. Am.* 50.3, pp. 389–415. ISSN: 0037-1106.
- Stoll, Robert D. (1974). "Acoustic waves in saturated sediments". In: *Phys. sound Mar. sediments*. Ed. by Ronald J. Gibbs and Loyd Hampton. Austin, Texas: Plenum Press, pp. 19–39.
- Stoll, Robert D. and George M. Bryan (1970). "Wave Attenuation in Saturated Sediments". In: *J. Acoust. Soc. Am.* 47.5B, pp. 1440–1447. ISSN: 0001-4966. DOI: 10.1121/1.1912054.
- Sutera, S P and R Skalak (1993). "The History of Poiseuille's Law". In: *Annu. Rev. Fluid Mech.* 25.1, pp. 1–20. ISSN: 0066-4189. DOI: 10.1146/annurev.fl.25.010193.000245.
- Svetlizky, Ilya, Elsa Bayart, and Jay Fineberg (2019). "Brittle Fracture Theory Describes the Onset of Frictional Motion". In: *Annu. Rev. Condens. Matter Phys.* 10.1, pp. 253–273. ISSN: 1947-5454. DOI: 10.1146/annurev-conmatphys-031218-013327.
- Szabo, Thomas L. and Junru Wu (2000). "A model for longitudinal and shear wave propagation in viscoelastic media". In: *J. Acoust. Soc. Am.* 107.5, pp. 2437–2446. ISSN: 0001-4966. DOI: 10.1121/1.428630.
- T, Maruyama (1963). "On the Force Equivalents of Dynamically Elastic Dislocations with Reference to the Earthquake Mechanism". In: *Bull. Seismol. Soc. Am.* 41, pp. 467–486.
- Tanaka, Toyochi, Lon O Hocker, and George B Benedek (1973). "Spectrum of light scattered from a viscoelastic gel". In: *J. Chem. Phys.* 59.9, pp. 5151–5159. ISSN: 0021-9606. DOI: 10.1063/1.1680734.
- Tang, An, Guy Cloutier, Nikolaus M. Szeverenyi, and Claude B. Sirlin (2015). "Ultrasound elastography and MR elastography for assessing liver fibrosis: Part 1, principles and techniques". In: *Am. J. Roentgenol.* 205.1, pp. 22–32. ISSN: 15463141. DOI: 10.2214/AJR.15.14552.
- Tanter, Mickael and Mathias Fink (2014). "Ultrafast imaging in biomedical ultrasound". In: *IEEE Trans. Ultrason. Ferroelectr. Freq. Control* 61.1, pp. 102–119. ISSN: 0885-3010. DOI: 10.1109/TUFFC.2014.6689779.
- TenCate, James A. (2011). "Slow Dynamics of Earth Materials: An Experimental Overview". In: *Pure Appl. Geophys.* 168.12, pp. 2211–2219. ISSN: 0033-4553. DOI: 10.1007/s00024-011-0268-4.
- Thielicke, William (2014). "The Flapping Flight of Birds Analysis and Application". PhD thesis. University of Groningen. ISBN: 9789036772419.
- Thielicke, William and Eize J. Stamhuis (2019). *PIVlab Time-Resolved Digital Particle Image Velocimetry Tool for MATLAB*. DOI: 10.6084/m9.figshare.1092508.v12.

- Thoduka, Santosh, Frederik Hegger, Gerhard K. Kraetzschmar, and Paul G. Plöger (2017). "Motion Detection in the Presence of Egomotion Using the Fourier-Mellin Transform". In: *Proc. 21st Rob. Int. Symp.*
- Tocher, D (1960). "Creep on the San Andreas fault-Creep rate and related measurements at Vineyard, California". In: *Bull. Seism. Soc. Am.* 50, pp. 394–404.
- Toll, John S (1956). "Causality and the dispersion relation: Logical foundations". In: *Phys. Rev.* 104.6, pp. 1760–1770. ISSN: 0031899X. DOI: 10.1103/PhysRev.104.1760.
- Torr, P. H.S. and A. Zisserman (2000). "MLE-SAC: A new robust estimator with application to estimating image geometry". In: *Comput. Vis. Image Underst.* 78.1, pp. 138–156. ISSN: 10773142. DOI: 10.1006/cviu.1999.0832.
- Trømborg, Jørgen Kjoshagen, Henrik Andersen Sveinsson, Julien Scheibert, Kjetil Thøgersen, David Skålid Amundsen, and Anders Malthe-Sørenssen (2014). "Slow slip and the transition from fast to slow fronts in the rupture of frictional interfaces." In: *Proc. Natl. Acad. Sci. U. S. A.* 111.24, pp. 8764–9. ISSN: 1091-6490. DOI: 10.1073/pnas.1321752111.
- Urban, Matthew W and James F Greenleaf (2009). "A Kramers–Kronig-based quality factor for shear wave propagation in soft tissue". In: *Phys. Med. Biol.* 54.19, pp. 5919–5933. ISSN: 0031-9155. DOI: 10.1088/0031-9155/54/19/017.
- Van Veen, B.D. and K.M. Buckley (1988). "Beamforming: a versatile approach to spatial filtering". In: *IEEE ASSP Mag.* 5.2, pp. 4–24. ISSN: 0740-7467. DOI: 10.1109/53.665.
- Viesca, R. C. and J. R. Rice (2010). "Modeling slope instability as shear rupture propagation in a saturated porous medium". In: *Submar. Mass Movements Their Consequences - 4th Int. Symp.* 28.November 2009, pp. 215–225.
- Vogelaar, Bouko Barteld Sytze Adriaan (2009). "Fluid effect on wave propagation in heterogeneous porous media". PhD thesis. Delft University of Technology. ISBN: 9789090240510.
- Voisin, Christophe, Jean Robert Grasso, Eric Larose, and François Renard (2008). "Evolution of seismic signals and slip patterns along subduction zones: Insights from a friction lab scale experiment". In: *Geophys. Res. Lett.* 35.8, pp. 2–6. ISSN: 00948276. DOI: 10.1029/2008GL033356.
- Wainwright, Haruko M., Stefan Finsterle, Yoojin Jung, Quanlin Zhou, and Jens T. Birkholzer (2014). "Making sense of global sensitivity analyses". In: *Comput. Geosci.* 65, pp. 84–94. ISSN: 00983004. DOI: 10.1016/j.cageo.2013.06.006.
- Walter, Jacob I., Ilya Svetlizky, Jay Fineberg, Emily E. Brodsky, Slawek Tulaczyk, C. Grace Barcheck, and Sasha P. Carter (2015). "Rupture speed dependence on initial stress profiles: Insights from glacier and laboratory stick-slip". In: *Earth Planet. Sci. Lett.* 411, pp. 112–120. ISSN: 0012821X. DOI: 10.1016/j.epsl.2014.11.025.



- Wasserman, Karlman, Norman Blank, and Grant Fletcher (1968). "Lung lavage (alveolar washing) in alveolar proteinosis". In: *Am. J. Med.* 44.4, pp. 611–617. ISSN: 00029343. DOI: 10.1016/0002-9343(68)90062-4.
- Waters, K.R., M.S. Hughes, Joel Mobley, and J.G. Miller (2003). "Differential forms of the Kramers-Kronig dispersion relations". In: *IEEE Trans. Ultrason. Ferroelectr. Freq. Control* 50.1, pp. 68–76. ISSN: 0885-3010. DOI: 10.1109/TUFFC.2003.1176526.
- Waters, K.R., Joel Mobley, and J.G. Miller (2005). "Causality-imposed (Kramers-Kronig) relationships between attenuation and dispersion". In: *IEEE Trans. Ultrason. Ferroelectr. Freq. Control* 52.5, pp. 822–823. ISSN: 0885-3010. DOI: 10.1109/TUFFC.2005.1503968.
- Weber, B., T. Suhina, A. M. Brouwer, and D. Bonn (2019). "Frictional weakening of slip interfaces". In: *Sci. Adv.* 5.4, pp. 1–8. ISSN: 23752548. DOI: 10.1126/sciadv.aav7603.
- Weertman, J (1980). "Unstable slippage across a fault that separates elastic media of different elastic constants". In: *J. Geophys. Res. Solid Earth* 85.B3, pp. 1455–1461. ISSN: 01480227. DOI: 10.1029/JB085iB03p01455.
- Wells, P. N. T. and H.-D. Liang (2011). "Medical ultrasound: imaging of soft tissue strain and elasticity". In: *J. R. Soc. Interface* 8.64, pp. 1521–1549. ISSN: 1742-5689. DOI: 10.1098/rsif.2011.0054.
- White, Diana, Dennis Coombe, Vahid Rezaia, and Jack Tuszynski (2016). "Building a 3D virtual liver: Methods for simulating blood flow and hepatic clearance on 3D structures". In: *PLoS One* 11.9, pp. 1–24. ISSN: 19326203. DOI: 10.1371/journal.pone.0162215.
- Williamson, Jonathan P. et al. (2011). "Elastic properties of the central airways in obstructive lung diseases measured using anatomical optical coherence tomography". In: *Am. J. Respir. Crit. Care Med.* 183.5, pp. 612–619. ISSN: 1073449X. DOI: 10.1164/rccm.201002-01780C.
- Wilson, L.S. and D.E. Robinson (1982). "Ultrasonic measurement of small displacements and deformations in tissue". In: *Ultrason. Imaging* 4, pp. 71–82.
- Winberry, J. Paul, Sridhar Anandakrishnan, Douglas A. Wiens, and Richard B. Alley (2013). "Nucleation and seismic tremor associated with the glacial earthquakes of Whillans Ice Stream, Antarctica". In: *Geophys. Res. Lett.* 40.2, pp. 312–315. ISSN: 00948276. DOI: 10.1002/grl.50130.
- Wundenbuch Papyrus Smith.*
- Xia, Kaiwen, Ares J Rosakis, and Hiroo Kanamori (2004). "Laboratory earthquakes: the sub-Rayleigh-to-supershear rupture transition." In: *Science* (80-. ). 303.March, pp. 1859–1861. ISSN: 0036-8075. DOI: 10.1126/science.1094022.
- Xiang, Jun Xi, Xing Long Zheng, Rui Gao, Wan Quan Wu, Xu Long Zhu, Jian Hui Li, and Yi Lv (2015). "Liver regeneration using decellularized splenic scaffold: A

- novel approach in tissue engineering". In: *Hepatobiliary Pancreat. Dis. Int.* 14.5, pp. 502–508. ISSN: 14993872. DOI: 10.1016/S1499-3872(15)60423-4.
- Yang, Duoxing, Qi Li, and Lianzhong Zhang (2016). "Propagation of pore pressure diffusion waves in saturated dual-porosity media (II)". In: *J. Appl. Phys.* 119.15, p. 154901. ISSN: 0021-8979. DOI: 10.1063/1.4946832.
- Yu, Kai jiang, Mei jie Zhang, Ying Li, and Rui tao Wang (2014). "Increased whole blood viscosity associated with arterial stiffness in patients with non-alcoholic fatty liver disease". In: *J. Gastroenterol. Hepatol.* 29.3, pp. 540–544. ISSN: 14401746. DOI: 10.1111/jgh.12368.
- Zhang, Xiaoming, Thomas Osborn, and Sanjay Kalra (2016). "A noninvasive ultrasound elastography technique for measuring surface waves on the lung". In: *Ultrasonics* 71.June, pp. 183–188. ISSN: 0041624X. DOI: 10.1016/j.ultras.2016.06.012.
- Zhou, Jinling and Xiaoming Zhang (2018). "Effect of a Thin Fluid Layer on Surface Wave Speed Measurements: A Lung Phantom Study". In: *J. Ultrasound Med.* Pp. 1–5. ISSN: 02784297. DOI: 10.1002/jum.14802.
- Zoback, Mary Lou (2006). "The 1906 earthquake and a century of progress in understanding earthquakes and their hazards". In: *GSA Today* 16.4, p. 4. ISSN: 1052-5173. DOI: 10.1130/gsat01604.1.
- Zwikker and Kosten (1949). *Sound absorbing materials*. New York: Elsevier, p. 56.
- Zwikker, C and C.W. Kosten (1941). "Extended theory of the adsorption of sound by compressible wall-coverings". In: *Physica* 8.9, pp. 968–978.